Politecnico di Milano

Department of Structural Engineering
Doctoral School in Structural, Earthquake and Geotechnical Engineering
XXIV Cycle

NEAR-FIELD EARTHQUAKE GROUND MOTION ROTATIONS AND RELEVANCE ON CIVIL ENGINEERING STRUCTURES

Doctoral Dissertation of

Roberto Guidotti
738619

Supervisor

Prof. Alberto Castellani

Co-supervisors

Prof. Roberto Paolucci
Dr. Marco Stupazzini

The Chair of the Doctoral Program

Prof. Roberto Paolucci

March 2012

Doctoral School in Structural, Earthquake and Geotechnical Engineering
Department of Structural Engineering
Politecnico di Milano
XXIV cycle

Supervisor

Prof. Alberto Castellani

Co-supervisors

Prof. Roberto Paolucci

Dr. Marco Stupazzini

Board committee

Prof. Roberto Paolucci (Coordinator)

Prof. Fabio Biondini

Prof. Gabriella Bolzon

Prof. Claudia Comi

Prof. Alberto Corigliano

Prof. Maria Laura Costantino

Prof. Claudio di Prisco

Prof. Marco di Prisco

Prof. Roberto Felicetti

Prof. Attilio Frangi

Prof. Pietro Gambarova

Prof. Anna Pandolfi

Prof. Federico Perotti

Prof. Alberto Taliercio

Prof. Pasquale Vena

To Emilia

I cannot honestly say I am confident
as to the exact shape of the once-seen,
oft-regretted Cube;
and in my nightly visions the mysterious precept,
"Upward, not Northward",
haunts me like a soul-devouring Sphinx.

Edwin A. Abbott
Flatland: A Romance in Many Dimensions
1884

ABSTRACT

The growing interest in the study of rotational ground motions induced by earthquakes, explosions, and ambient vibrations has led in recent years to the development of an emerging field of inquiry, referred to as *Rotational Seismology*. The main idea of the rotational seismology is that for a complete and proper characterization of strong ground motions, measurements should be no longer limited to only the three components of translational motion, but should simultaneously include the three components of rotational motion, especially in the near field of an earthquake. Accelerations recorded by translational sensors could themselves be affected by rotations and collecting translational and rotational information together can yield a more complete description of the wave field, providing a substantial improvement in studies of velocity heterogeneity, source complexity, and media nonlinearity in strong ground motions. From a civil engineering perspective, the relevance for structures is still under debate by the scientific community and the notion that the rotational component of strong motion could contribute significantly to the overall structural response has only recently been recognized, driven by a growing interest in performance-based design and structural health monitoring. Nevertheless, studies of recorded rotational strong ground motion are limited to a few examples and, consequently, the knowledge of the rotational wave field is still insufficient.

The goal of this work is to make a contribution to the study of rotational ground motion in near-field region, referring to a realistic earthquake scenario, as with the M_W 6.3 Christchurch earthquake of 22 February 2011. The exceptionally high vertical acceleration recorded together with the widespread liquefaction, suggests that rotational motions could have played a significant role in the damage of the area, and especially in the Central Business District (CBD) of the city, characterized by a dense urban setting with closely spaced high rise buildings. Aiming to further understanding of

the rotational wave field and its relation with the translational wave field, rotational ground motions are evaluated: i) semi-empirically, starting from measured translational records in closely-spaced arrays of stations, relying on the mathematical relation between the cross power spectrum and the power spectrum of rotation; and ii) numerically, considering the prediction of the variability of strong ground motion (translational and rotational) in near-fault conditions obtained through three-dimensional models of the Christchurch earthquake, testing their reliability by exploiting the availability of an unprecedented dataset of near-fault strong ground motion. Values of estimated peak ground torsional rates in the epicentral region range up to around 20 mrad/s with maximum peak ground rotations higher than 1 mrad. The relevance of the rotational strong ground motions is then evaluated for a series of civil engineering structures: i) buried pipeline and lifeline networks, assessing some implications of the effect of a different ground motion from point to point (wave passage effect); ii) tall wind towers; iii) high rise buildings, such as those that constitute and characterize the Christchurch CBD; and iv) pounding-prone compounds of buildings, considering the complex interaction between the topography and the characteristics of the soil and geometry of foundations and buildings of a densely urbanized city (Site-City interaction). In particular, to disregard rotational effect in buildings, could result, according to the considered models, in an underestimation of interstory drift up to 15%, and, consequently, higher levels of damage than expected.

Keywords: Rotational Seismology, Rotational Ground Motions, Three-dimensional Ground Motions Simulations, Near-field of an earthquake, Structural Response.

ACKNOWLEDGEMENTS

This work is the conclusion of my PhD experience and I wish to thank all the people who have contributed to my growth, both professional and personal, during these years.

In particular I deeply thank my supervisor Prof. Alberto Castellani, for his invaluable experience and wisdom, for the confidence he put in me and for his passion for engineering he passed on me. I wish to thank also Prof. Roberto Paolucci, for his precious suggestions and comments that contributed to enhance this work. Work that would have been not possible without the support (scientific and human) of Marco Stupazzini that I gratefully thank for introducing me with his enthusiasm in the field of numerical modelling. Special thanks to Prof. Heiner Igel, for his warm welcome and for his precious teachings during the six months of my experience as a visiting student at the Ludwig Maximilians Universitaet in Munich, Germany. A particular thanks to Prof. Zbigniew Zembaty for the detailed, constructive criticism he devoted to the work.

Special thanks to Chiara Smerzini and Ilario Mazzieri: this work fruitfully benefits from their expertises and their precious availability. Thanks to Andrea Titi, that shared with me the difficulties and the best moments since the beginning of our PhD experience. The Consorzio Interuniversitario Lombardo per L'Elaborazione Automatica (CILEA), in Milan, in particular Paolo Ramieri and Paride Dagna, is greatly acknowledged for the extensive use of supercomputing facilities and for providing technical assistance. This work has been supported by Regione Lombardia and CILEA Consortium through a LISA Initiative (Laboratory for Interdisciplinary Advanced Simulation) 2010 grant [http://lisa.cilea.it]. I wish to thank Marco Valente for his valuable assistance and support in the passage between the Master Degree Program and the Doctoral Program.

Thanks, my parents, Lidia and Alfredo, and my family, for your moral support in this chapter of my life. This experience would have been not possible without your efforts, and I would like to ensure you that despite of the distance I always feel your closeness.

Thanks, my darling Emilia, for the strength of your encouragements, for the sweetness of your patience and for the beauty of your love. Thanks to that I found the force to reach this goal, that I heartily dedicate to you.

TABLE OF CONTENTS

ABSTRACT ..... **i**

ACKNOWLEDGEMENTS ..... **iii**

LIST OF FIGURES ..... **xi**

LIST OF TABLES ..... **xxiii**

PREFACE **1**

Rotational Seismology 1

Engineering motivation, purpose and organization of the work 2

CHAPTER 1
ROTATIONAL SEISMOLOGY: THEORY, OBSERVATION, AND ENGINEERING IMPLICATIONS **9**

1.1 Introduction 9

1.2 Historical background of Rotational Seismology 11

1.3 Theoretical background of rotational ground motion 12

1.3.1 The Torsional motion from incident waves 14

1.3.2 The Rocking motion from incident waves 15
1.4. The challenge of the estimation and measurement of rotational ground motions 17
1.4.1 Dense array estimation of ground rotational motions 19
1.4.2 Direct earthquake-induced measurements of rotational ground motions in Taiwan and Japan 20
1.5 Relevance of rotational strong ground motion for civil engineering structures 22

CHAPTER 2.
FREE-FIELD ROTATIONS DURING EARTHQUAKES:
A CLASSICAL SEMI-EMPIRICAL APPROACH 27

2.1 Introduction 27
2.2 Relevance of free-field rotation for building: role of the coherence and of the vertical input motion 28
2.3 Mathematical relation between the Cross-power spectrum and the Power spectrum of rotations 31
2.3.1 Horizontal and vertical components 36
2.3.2 Relevance of the interpolation function in the estimation of cross-power spectra 37
2.3.3 Dependence of the measurements on the separation distance 38
2.4 Evaluation of rotational accelerograms on the basis of measured vertical accelerograms 38
2.4.1 Rotational Response Spectra 41
2.4.2 Results and comparison with available measured data 42
2.5 Concluding remarks 44

CHAPTER 3
A CHALLENGING CASE STUDY: THE M_W 6.3 CHRISTCHURCH EARTHQUAKE ON 22 FEBRUARY 2011, NEW ZEALAND.....45

3.1. Introduction 45
3.2. Geology of the Christchurch region 48
3.3 1D Analytical transfer function for the Canterbury Plains 50
3.3.1 Transfer function for a system of N layers over elastic half-space 50
3.3.2 Transfer function for the Canterbury Plains model 53
3.4. 3D Numerical simulations of the seismic response of the Canterbury Plains 53

3.5 Role of the basin geometry and of the kinematic seismic source in the spatial variability of strong ground motion: Numerical results in the near source region 58
3.5.1 Dependence of results on the geometry of the Canterbury Plains 59
3.5.2 Effect of the kinematic seismic source 61
3.6 Comparison with observed Standard Spectral Ratios 66
3.7 Concluding remarks 67

CHAPTER 4
ROTATIONAL GROUND MOTION DURING THE M_W 6.3 CHRISTCHURCH EARTHQUAKE: SYNTHETICS vs. SEMI-EMPIRICAL RESULTS IN THE NEAR-FIELD REGION 69

4.1 Introduction 69
4.2 Correlation between rotational and translational ground motions 70
4.3 Semi-empiric and synthetic rotational wave field for the M_W 6.3 Christchurch earthquake 71
4.3.1 Semi-empirical vs. synthetic rotational wave field 74
4.3.2 Current vs. Past studies data of rotational ground motions 79
4.4 Spatial variability of peak ground rotation in the Canterbury Plains 81
4.5 Concluding remarks 84

CHAPTER 5
FREE FIELD ROTATIONS DURING EARTHQUAKES: RELEVANCE ON CIVIL ENGINEERING STRUCTURES 87

5.1 Introduction: rotations in structural response 87
5.2 Wave passage effect in buried pipelines: the Bazzano, L'Aquila, case. 88
5.2.1 Seismic effects on buried pipelines 89
5.2.2 Seismic behaviour of the buried pipeline network of Bazzano during the 2009 L'Aquila earthquake: direct observation of damages 92
5.2.3 Wave passage effect according to Eurocode 8 92
5.2.4 Variability of the apparent velocity and limit of the Eurocode approach 95
5.2.5 3D numerical study of the Bazzano pipeline network 96
5.2.6 Concluding remarks 98

5.3 The Gebbie Pass Wind Tower, Christchurch: relevance of rotational ground motion for simple oscillator structural models 99
5.3.1 Four degrees of freedom oscillator: the Chopin model 99
5.3.2 The Gebbie Pass wind tower: a Finite Element model 108
5.3.3 Concluding remarks 109
5.4 Grand Chancellor, Christchurch, Canterbury Business District. Relevance of rotational ground motion for a tall building 112
5.4.1 Observed damages in the Grand Chancellor Hotel 114
5.4.2 Three-dimensional model of the Grand Chancellor Hotel 114
5.4.3 Concluding remarks 116
5.5. The Christchurch Canterbury Business District. Relevance of site-city interaction effect in the spatial variability of motion 118
5.5.1 Site-City Interaction 118
5.5.2 Three-dimensional numerical model of the CBD 119
5.5.3 Results: Peak ground values, strong motion variability and wave passage effect 121
5.5.4 Concluding remarks 125

CHAPTER 6
CONCLUDING REMARKS 129

APPENDIX A
THE GRAN SASSO LABORATORY AS A POSSIBLE LOCATION FOR A RING-LASER GYROSCOPE: STUDY ON THE NOISE LEVEL 133

A.1 Introduction 133
A.2 Ring laser Gyro: Principles of operation 134
A.3 Ring Laser technology: the meaningful example of Wettzell, Germany 135
A.4 Study of the noise level of the Gran Sasso Laboratory, Italy 137
A.4.1 Cultural noise 137
A.4.2 Microseisms 138
A.4.3 Earthquakes 138
A.4.4 Power Spectral Density and Probability Density Function 138
A.5 Concluding remarks 140
A.6 Acknowledgements 140

APPENDIX B

HONORING vs. NOT-HONORING vs. NON-CONFORMING: THREE MESHING APPROACHES FOR 3D COMPLEX SEISMIC SCENARIOS 141

B.1 Introduction 141
B.2 The meshing problem 142
B.3 The study case: Valley of Grenoble 143
B.4 Honoring (H) meshing strategy 144
B.5 Not Honoring (NH) meshing strategy 146
B.6 Non-Conforming (NC) meshing strategy 148
B.7 Numerical simulation: Extended fault input 150
B.8 Concluding remarks 152

REFERENCES 153

LIST OF FIGURES

Figure I. Nomenclature and sign conventions for translational and rotational motions adopted in these work. X and Y axes point into the page and are normally in the horizontal plane, while Z axis points upward. Annotations u and ω are translational displacements and rotation angles. (Adapted from Evans and IWGoRS 2009). **p. 2**

Figure II. Response of buildings under high- (Left hand side) and low- (Right hand side) frequency content of the rotational ground motions. **p. 3**

Figure 1.1. Left hand side: Rotation of obelisk segments from the 1897 Assam earthquake. Right hand side: Rotated tombstones from the 1906 San Francisco earthquake, illustrated by Jenista (1906-1907). (From Kozak 2009). **p. 11**

Figure 1.2. From Top to Bottom, from Left to Right, incident P-, SV-, SH and Rayleigh waves on half space, with the sign convention adopted for retrieving the mathematical expression of torsional and rocking ground motions. (Adapted from Lee 2002). **p. 13**

Figure 1.3. Peak ground horizontal velocity (PGV_h) versus peak ground rotation ($PG\omega_z$) in logarithmic scale obtained from data in the literature, listed in Table 1.3, superimposed to synthetics obtained for a 3D model of Grenoble valley, France, considering earthquakes with M_W 6.0 and M_W 4.5. (From Stupazzini et al. 2009b). **p. 19**

Figure 1.4. Top: Left: Location of earthquakes with good rotational motions recorded at the HGSD station in eastern Taiwan from 8 May 2007 to 17 February 2008. The size of the dot is proportional to the magnitude (From Liu et al. 2009. Right: Peak torsional rate versus peak ground acceleration for the Taiwan earthquakes data set. (From Lee at al. 2009b). Bottom: Location of the epicentres of the 1998 Ito offshore swarm activity. (From Takeo 2009). Right: Peak torsional rate versus peak ground acceleration for the Japan earthquakes data set. (From Lee et al. 2009b). **p. 21**

Figure 1.5. Estimation of stress drop from near-field recording of strong motion (different symbols) and from equations 1.8a (solid line) and 1.18b (dotted line). The corresponding order-of-magnitude estimates of peak ground rotation at the fault (with cg = 1 km/s) and the order-of-magnitude of the expected drift in buildings (with cb = 0.1 km/s) are superimposed. (From Trifunac 2009a). **p. 23**

Figure 2.1. Top two rows: Acceleration response spectra for the records of four stations located in the Christchurch CBD during the event of the 22 February 2011. Bottom: Acceleration response spectra for the records collected at Station AQK during the 2009 earthquake event of L'Aquila, Italy. **p. 29**

Figure 2.2. Top: Real part of the coherency, Re[γ(f, d)], as a function of frequency (Left hand side) and inter-station distance (Right hand side), for stations aligned in the radial direction. Records of acceleration have been used (from Abrahamson et al. 1991). Bottom: Coherency of vertical components and that of horizontal components, evaluated for a same set of earthquakes records at SMART-1 array, and elaborated in Abrahamson et al. 1991. **p. 34**

Figure 2.3. Top: Square root of the ratio between rotation and translation power spectrum according three sources of data. Separation between stations d = 5 m. Bottom: (Left hand side) Square root of the ratio between power spectra. The cross-power spectrum established by Abrahamson et al. 1991 is used; (Right hand side) The same ratio, when the power spectrum established by EPRI (1992), focused on short separations d, has been used to evaluate $Su_z(f,0)$. **p. 37**

Figure 2.4. a) Vertical ground acceleration: Taiwan SMART-1(5) 29/01/1981 (M_L 6.3) (station C00); b) vertical power spectrum; c) Rotational power spectrum considering a separation distance d equal to 10 m; d) input ground rotational acceleration (d = 10 m). **p. 39**

Figure 2.5. a) Response spectra of accelerations of horizontal and vertical directions, for the event TAIWAN SMART-1(5):C00; b) comparison of rotational response spectra for different values of the separation d. **p. 41**

Figure 2.6. Definition of rotation response spectrum. The reference system is excited by a rotational motion. A single-degree-of-freedom rotational oscillator is shown by the crosshatched ring. The rotation response spectrum is the peak rotational acceleration, as a function of the natural period, and a given damping ratio. **p. 42**

Figure 2.7. Elaboration of data presented by Liu et al. 2009. Ratio between the peak rotation velocity PRV and the peak horizontal acceleration PGA, in [mrad s/m] as a function of the epicentral distance. Average value 1.43. **p. 43**

Figure 3.1. Aftershocks map of the Christchurch sequence from GNS website updated November 2011. Stars refer to events with $M_W \geq 6.0$. **p. 47**

Figure 3.2. Top: (Left hand side) Geological map of parts of the Canterbury Plains and Banks Peninsula from Forsyth et al. 2008. Yellow tones indicate alluvial soil, pink ones outcropping rock; (Right hand side) Corresponding schematization of the area for the model under study, along with the strong ground motion stations. Bottom: geological A-A' cross-section. **p. 49**

Figure 3.3. Top: Considered model of N plain, parallel layers with different mechanical properties; Bottom: 1D Analytical transfer function for the system of 4 layers of the Canterbury Plains, assuming either viscous-elastic damping or no damping. Mechanical characteristics of each layer are listed in Table 3.2. **p. 51**

Figure 3.4. Sketch of the "step-like" (top panel) and "smooth" (bottom panel) model, referred to as an approximation of the transition between the soft sediments of the Canterbury Plains and the rigid volcano materials. Note that the alluvial basin has a maximum thickness of 1.5 km and consists of three horizontal layers with V_s ranging from 300 m/s to 1,500 m/s. **p. 54**

Figure 3.5. Slip distribution according the INGV (left hand side) and the GNS (right hand side) fault solution. The superimposed star denotes the hypocenter location. **p. 55**

Figure 3.6. Adopted moment rate function (left hand side) and its spectrum (right hand side). **p. 56**

Figure 3.7. Top: 3D mesh of the Canterbury Plains relying on the GNS kinematic seismic source inversion. Bottom: (Left hand side) Corresponding "Step-like" model and (Right hand side) "Smooth" model, with depth contours of the contact between the alluvial soft sediments and the rigid volcanic materials (depth in meters). Position of the CBD is also shown. **p. 57**

Figure 3.8. Comparison of 3D numerical simulations by GeoELSE with strong ground motion observations, in terms of three components velocity time histories, obtained at stations: a) HVSC, at outcrop rock, b) REHS, on soft sediments in the CBD, c) SHLC, on soft sediments at R_e = 9 km, d) SLRC, on soft sediments at R_e = 33 km, in the south-western portion of the model. Observed and simulated data are band-pass filtered between 0.1 and 2.0 Hz. **p. 60**

Figure 3.9. As in Figure 3.8 but in terms of velocity amplitude Fourier spectra. **p. 61**

Figure 3.10. Misfit parameters (Anderson, 2004) of simulated ground motion for the three components of motion, evaluated at the 23 stations under consideration (see Table 3.1 and Figure 3.2) in the frequency band between 0.25 and 0.50 Hz. The results are shown for the INGV "step-like"(top panel), INGV "smooth" (centre panel) and GNS "smooth" model (bottom panel). **p. 62**

Figure 3.11. Comparison between recorded and simulated (GNS "smooth") velocity time histories (in cm/s), on the EW, NS and the UD component for the whole set of stations at R_e < 40 km. The label on the left vertical axis reports the peak value of the corresponding time history. **p. 63**

Figure 3.12. Spatial variability of Peak Ground Velocity (geometric mean of horizontal components) as estimated by 3D numerical simulations with the INGV "smooth" model (top panel) and GNS "smooth" model (bottom panel). The recorded PGV values (filled dots) are superimposed for comparison purposes. **p. 64**

Figure 3.13. Snapshots (t = 7, 9, 11 and 13 s, from top to bottom) of the simulated fault normal velocity wavefield with the INGV "smooth" model (left hand side) and GNS "smooth" model (right hand side). **p. 65**

Figure 3.14. Standard Spectral Ratios (SSRs) of the four stations of CBD: CCCC (top-left panel), REHS (top-right panel), CHHC (bottom-left panel), and CBGS (bottom-right panel) located on soft alluvial sediments, over the rock reference station LPCC. The SSRs obtained from strong ground motion recordings during Darfield earthquake are compared with the 1D analytical transfer function and with the SSRs computed with the 3D numerical simulations (GNS "smooth" model). **p. 67**

Figure 4.1. Top: Ratio between the semi-empirical peak rotation velocity PRV and the peak horizontal acceleration PGA, in [mrad s/m], evaluated for the 23 stations considered for the Christchurch earthquake, with separation d = 10 m in function of the epicentral distance. Average value is 1.486. Bottom: Semi-empirical peak rotational velocity vs. peak ground acceleration (black) in logarithmic scale, superimposed to available measured values from Liu et al. 2009 (red) and Takeo 2009 (blue). **p. 72**

Figure 4.2. Recorded velocity time history and semi-empirically retrieved rotational waveforms at stations: a) HVSC, on outcrop volcanic rock and b) CCCC on soft soil in the CBD. Rotation about horizontal axis (ω_h) are associated to vertical component of ground motion (UP), while to the two horizontal components EW and NS correspond rotational motions about the vertical axis (ω_{z1}, ω_{z2}). Data are band-pass filtered between 0.1 and 2.0 Hz. **p. 75**

Figure 4.3. Velocity and rotational waveforms obtained from the six-component synthetic seismograms located at stations: a) HVSC, on outcrop volcanic rock and b) CCCC on soft soil in the CBD. Data are band-pass filtered between 0.1 and 2.0 Hz. **p. 76**

Figure 4.4. Map of the 25,488 six-component synthetic seismograms located on the top surface of the numerical model. Grey dots refer to monitors placed on outcropping volcanic rock, black dots refer to monitors located on the alluvial soil. Superimposed in white are the coastline of the region and the projection of the fault. Star denotes the epicentre of the earthquake. **p. 77**

Figure 4.5. Top: Synthetic values of peak ground horizontal velocity (PGV_h) versus peak ground rotation around vertical axis ($PG\omega_z$) in logarithmic scale obtained for the M_W 6.3 Christchurch earthquake. Bottom: Synthetic values of peak ground vertical velocity (PGV_z) versus peak ground rotation around horizontal axis ($PG\omega_h$). **p. 78**

Figure 4.6. Peak ground vertical velocity (PGV_z) versus peak ground rocking ($PG\omega_z$) and peak ground horizontal velocity (PGV_h) versus peak ground torsion ($PG\omega_z$) in logarithmic scale. Semi-empiric values, obtained from translational records, are superimposed to synthetics values, as results of the 3D numerical model, considering both the whole set of 25,488 monitors (Top) and the 21 monitors located on the reference stations (Bottom). Values filtered between 0.1 and 2.0 Hz. **p. 79**

Figure 4.7. Superposition of peak ground horizontal velocity (PGV_h) versus peak ground rotation ($PG\omega_z$) in logarithmic scale of synthetic data on alluvial soil (green) and rock (red), semi-empirical data (blue) and data retrieved from literature, listed in Table 3.1 and described in Figure 1.3; in particular black and gray dots refer to synthetics (alluvial and rock, respectively) obtained for a 3D model of Grenoble valley, France (Stupazzini et al. 2009b). Magenta dots refer to the measured data from an earthquake swarm in 1998, offshore the city of Ito, Japan, from Takeo (2009). **p. 80**

Figure 4.8. Comparison of the decay with distance from the epicentral location of the horizontal and vertical component of peak ground velocities (Top; left hand side: PGV_z, right hand side: PGV_h) and corresponding peak ground rotations (Bottom; left hand side: $PG\omega_h$, right hand side: $PG\omega_z$). **p. 82**

Figure 4.9. Top: Left: Spatial variability of peak ground vertical velocity (PGV_z) as estimated by 3D numerical simulation; Right: Spatial variability of peak ground horizontal velocity (PGV_h, geometric mean of horizontal components). Middle: Left: Spatial variability of peak ground rotation around horizontal axis ($PG\omega_h$, geometric mean of horizontal components); Right: Spatial variability of peak ground rotation around vertical axis ($PG\omega_z$). Bottom: Left: Spatial variability of the ratio between PGV_z and $PG\omega_h$; Right: Spatial variability of the ratio between PGV_h and $PG\omega_z$. **p. 83**

Figure 5.1. Top: Fault of Bazzano and the anthitetical fault of Paganica. Middle: sketch the buried pipeline network of Bazzano, object of the visual inspection through remote-controlled camera; Bottom: pipeline network scheme superimposed to the aerial view of the urbanized area of Bazzano. **p. 90**

Figure 5.2. Pictures from the visual inspection through a moving remote-controlled camera of the buried pipeline network of Bazzano, L'Aquila. Pictures in Top and Middle row present an horizontal crack that could be explained with the increase of the pressure due to a landslide of a soil clod, while pictures in the Bottom row could be due to a different ground motion from point to point (wave passage effect) or to a fault movement. **p. 91**

Figure 5.3. Description of the wave passage effect. Top: A different ground motion from point to point maximizes the bending action in the longitudinal plane, imposing curvature and longitudinal action to the pipeline. Middle: Picture of a pipe and sketch of the curvature effect, producing an angle α between consequent elements. Bottom: sketch of the elongation effect with detachment of the gasket. **p. 93**

Figure 5.4. Top: 3D numerical model introduced, validated and described in Smerzini (2011) and Smerzini and Villani (2012), including the Aterno Valley and the causative Paganica fault. Bottom: set of 20 receivers located in correspondence of the Bazzano pipeline network (Figure 5.1). **p. 97**

Figure 5.5. Before (09/03/2010, left-hand side) and after (23/02/2011, right-hand side) earthquake satellite pictures of the 500 kilowatt wind turbine located at Gebbies Pass, around 15 km south west of the epicentre of the 22 February Christchurch earthquake. The two pictures show the good seismic response of the structure. **p. 100**

Figure 5.6. 4-DOF model for dynamic soil-structure interaction analyses taking into account rotational ground motion (left hand side) and its simplified version for SDOF with fixed base (right hand side). **p. 101**

Figure 5.7. Displacement of the mass at top of the wind tower located at station MQZ, on outcropping rock, considering the effect of the rotational component of motion, using as input numerical data (left column) and semi-empirical data (right column). First row refers to displacement along East-West direction, second row is along the North-South direction. In the third row, an odometric representation of displacement in the two direction is presented. **p. 105**

Figure 5.8. Displacement of the mass at top of the wind tower supposed located at station PRPC, on alluvial soil, considering the effect of the rotational component of motion, using as input numerical data (left column) and semi-empirical data (right column). First row refers to displacement along East-West direction, second row is along the North-South direction. In the third row, an odometric representation of displacement in the two direction is presented. **p. 106**

Figure 5.9. Picture of the Wind tower installed at Gebbie Pass (left hand side) and its numerical representation with FE code (right hand side). **p. 109**

Figure 5.10. Displacement of the mass at top of the wind tower located at station MQZ, on outcropping rock, obtained with the 3D model, considering the effect of the rotational component of motion, using as input numerical data (left column) and semi-empirical data (right column). First row refers to displacement along East-West direction, second row is along the North-South direction. In the third row an odometric representation of displacement in the two direction is presented. **p. 110**

Figure 5.11. Distribution of the envelope of longitudinal (top) and circumferential (bottom) stresses along the tower's height, and zoom on the tower's basis, where they reach their maximum values. Values are in MPa. **p. 111**

Figure 5.12. Top and middle row: Pictures of the damages occurred at the Grand Chancellor Hotel. It is particularly evident the wall failure on the south-eastern side, causing the building to slump in the corner. Bottom: graphical reconstruction of the inferred collapse sequence (source: Critical Buckling Group, NZ Herald). **p. 113**

Figure 5.13. Top: Picture of the Grand Chancellor Hotel in the Christchurch CBD, after the earthquake (left hand side) and its numerical model with FE code (right hand side). Bottom: Technical drawing of a typical building story, from level 1 to 14 (left hand side) and from level 15 to 28 (right hand side). **p. 115**

Figure 5.14. Interstory drift along the height of the Grand Chancellor Hotel, evaluated considering a pure translational input (black line) and a rotational input superimposed to the translational one (red line), considering the four stations of reference, namely CCCC, REHS, CBGS and CHHC, located in the neighbourhood of the CBD. **p. 116**

Figure 5.15. Top: Aerial view of the Christchurch CBD. The red contour defines the modelled area. Middle: Corresponding three-dimensional model, independently meshed with element size around 5 m. Also foundations and soil around foundations are meshed. In yellow significant building are highlighted. Bottom: Model of the CBD set into the model of the Canterbury Plains described in Chapter 3. **p. 120**

Figure 5.16. Time histories of velocity recorded for the three translational components of motion at the four reference stations located in the neighbouring of the Christchurch CBD, considering (red line) or not (black line) the presence of the densely urbanized cluster of buildings. Bottom: Location of the four monitors on the map, the red contour delimits the numerical model of the CBD. **p. 122**

Figure 5.17. Peak ground velocity taken along the four directions across the CBD, namely South-North (S-N), East-West (E-W), South West-North East (SW-NE) and South-East-North-West (SE-NW), considering (red line) or not (black line) the presence of the densely urbanized cluster of buildings. Bottom: Set of monitors located along the four aforementioned directions (red dots). Distance between monitors varies between 7.5 and 10 m. **p. 123**

Figure 5.18. Spatial variability of Peak Ground Velocity (geometric mean of horizontal components) as estimated by 3D numerical simulations without (top panel) and with the city (bottom panel). **p. 124**

Figure 5.19. Snapshots (t = 5.5, 6, 6.5 and 7 s, from top to bottom) of the simulated velocity wavefield without the city (left hand side) and with the city (right hand side). **p. 126**

Figure 5.20. Snapshots (t = 5, 6, 7, 8, 9, 10, 11 and 12 s, from top to bottom) of the simulated displacement of the buildings of the CBD. Displacements are considered in their absolute values. On the ground, between buildings, is visible the displacement wave-field. **p. 127**

Figure A.1. Top: Schematic section through the "G" underground lab located in Wettzell, Germany. Bottom: (Left hand side): Principle of operation of the ring Laser "G"; (Right hand side): Picture of the ring laser "G". **p. 136**

Figure A.2. Power spectral density (PSD) (Left hand column) and its corresponding probability density function (PDFPSD) (Right hand column) of the three component of acceleration (East-West, North-South, Up-Down from top to bottom) recorded between January and May 2008, by a broadband seismometer located in the Gran Sasso Laboratory. **p. 139**

Figure B.1. Receivers location along the valley, contour line of the outcropping bedrock and topography adopted during the ESG06 "Grenoble Benchmark". Dimensions and orientations of the extended fault S are listed above, together with the position of the receiver from R25 to R32 located along the 2D profile. **p. 144**

Figure B.2. 3D numerical model obtained with the H strategy and used for the simulations of ESG06 "Grenoble Benchmark". The computational domain is subdivided into small chunks and each is sequentially meshed starting from the alluvial basin down to the bedrock (a sketch of the meshing procedure is here presented). For simplicity, the spectral elements are shown without the GLL nodes. **p. 145**

Figure B.3. Three-steps, Not Honoring meshing strategy. (Top) Topography of the Grenoble area with highlighted the two surfaces adopted in the meshing strategy: a) The computational domain is subdivided into big regular chunks and each one is meshed with a "pave" scheme on the top and then swept down to the bottom. b) First refinement, provided automatically by CUBIT; element size goes from 900 m down to 300 m. c) Second refinement with an imposed depth; elements in the surroundings of the alluvial deposit have a typical size of 100 m. d) and e) Final NH mesh of Grenoble: the domain is fully unstructured. The dark volume in a), b) and c) is here extracted from the inner core of the mesh to better highlight the interior design of the mesh with its refinements. For simplicity only the spectral elements are shown without GLL nodes **p. 146**

Figure B.4. a) DEM of the alluvial basin, meshed with a triangle with a typical edge size of 300 m. Zoom of the triangular mesh: top view b) the generic point P is inside the projected 2D triangle with vertex P1-P2-P3. c) the depth of the bedrock from point P is computed as the distance between P and the plane passing through the points P1-P2-P3, along the z axis. **p. 147**

Figure B.5. Not Honoring meshing strategy: the mechanical properties are distributed node by node according to the depth of the bedrock previously computed, as shown in Figure B.4. **p. 147**

Figure B.6. Non-conforming mesh approach. Volumes with different mechanical properties are meshed independently (top) and subsequently re-aggregate (bottom). Non-conforming techniques allow the contact between faces different in shape and size. With the resulting mesh the NH strategy can be adopted, describing the shape of the alluvial basin through the DEM depicted in Figure B.4. **p. 149**

Figure B.7. Superimposed synthetics of EW, NS and UD velocity component excited by source S, obtained for the Honoring, conforming model (black line) and for the Not-Honoring-Non-Conforming model (red line) Receivers R25, R26, R27, R28, R29, R30, R31, R32 are recorded along the 2D profile (Figure B.1). **p. 151**

LIST OF TABLES

Table 1.1. A list of historical earthquakes with observed rotational effects. (From Kozak 2009). **p. 12**

Table 1.2. Rocking and torsion components of strong earthquake ground motion under closed-form solutions from the literature (Trifunac 1982, Lee and Trifunac 1985, 1987, Lee 2002). See Figure 1.2 for sign convention and definitions of the symbols. **p. 15**

Table 1.3. Data retrieved from literature of peak ground horizontal velocity (PGVh) ,peak ground rotation (PGωz) and peak ground rotational velocity (PGώz) around the vertical axis. Additional information about the source parameters includes SS strike slip, T thrust and R reverse source mechanism. In "Data type", 1 means array-derived data, 2 indicates numerical/semi-analytical data and 3 measured data. N.A. stands for "not available". (Adapted from Stupazzini et al. 2009b). **p. 18**

Table 1.4. Least square fit to a straight line with error estimates for the torsional observations of Liu et al. 2009 and Takeo 2009. (From Lee et al. 2009b). **p. 20**

Table 2.1. Peak rotation velocity PRV and the peak horizontal acceleration PGA. PRV is the maximum among the three components, assuming d = 10 m. PGA is the maximum between the two horizontal components. **p. 43**

Table 3.1. Peak ground acceleration (PGA) and peak ground velocity (PGV) values recorded for the stations within a 40 km radius of the epicentre. Stations located on rock are in italics (data from CESMD, Center for Engineering Strong Motion Data: http://www.strongmotioncenter.org/; band-pass filter transition bands are 0.1-0.25 Hz and 24.50-25.50 Hz). R_e denotes the epicentral distance. **p. 46**

Table 3.2. Soil profile adopted in the numerical simulations. The top three layers constitute the Canterbury Plains. **p. 54**

Table 3.3. Kinematic source parameters adopted for the simulation of the 22 February 2011 Christchurch earthquake. V_R denotes the velocity rupture and τ the rise time. **p. 55**

Table 3.4. 3D numerical models size and computational time. Data of CPU time refer to the Lagrange cluster located at CILEA. **p. 58**

Table 4.1. Values of semi-empirical peak rotational velocity and recorded peak ground accelerations for the 23 stations within a radius of 40 km from the epicentre of the 22 February Christchurch earthquake. Band-pass filter transition bands are 0.10-0.25 Hz and 24.50-25.50 Hz (data of PGA from www.strongmotioncenter.org). PRV is the maximum among the three components, assuming d = 10 m. PGA is the maximum between the two horizontal components. In italic are typed stations located on outcropping rock. **p. 71**

Table 4.2. Values of semi-empirically retrieved peak rotation and peak rotational velocity for a set of stations within a radius of 40 km from the epicentre of the 22 February Christchurch earthquake. Data filtered between 0.1 and 2.0 Hz. In italic are typed stations located on outcropping rock. **p. 73**

Table 4.3. Values of synthetic peak rotation and peak rotational velocity for a set of stations within a radius of 40 km from the epicentre of the 22 February Christchurch earthquake. Data filtered between 0.1 and 2.0 Hz. In italic are typed stations located on outcropping rock. **p. 74**

Table 5.1. Soil maximum displacement, in meters, as a function of the local seismicity and the soil mechanical characteristics. In bold the value that refers to Bazzano. **p. 94**

Table 5.2. Strain ε_r as a function of the local seismicity and of the mechanical characteristics of the soil. In bold the value that refers to Bazzano. **p. 94**

Table 5.3. Curvature, in m^{-1}, as a function of the local seismicity and of the mechanical characteristics of the soil, considering values of apparent velocity C from the literature (Castellani and Boffi, 1989). In bold the value that refers to Bazzano. **p. 95**

Table 5.4. Peak Ground Velocity (geometric mean of the horizontal components) and strain ε_r in correspondence of the 20 sections of the pipeline network depicted in Figure 5.1, retrieved from the 3D numerical model of L'Aquila (data filtered between 0.1 and 2.0 Hz). **p. 98**

Table 5.5. Repair Rate - Peak Ground Velocity pipelines fragility relations proposed in the literature, together with the estimated Repair-Rate range of values for the Bazzano pipeline network, corresponding to the synthetically retrieved PGV range of values, between 18.35 and 23.9 cm/s. **p. 98**

Table 5.6. Main characteristic values of the three different wind towers lumped mass models adopted in the parametric analysis, together with the values adopted for the mass, stiffness and damping matrix. **p. 103**

Table 5.7. Top displacement obtained with synthetically and semi-empirically retrieved rotational accelerations, considering the two horizontal direction of motion and a translational (T) and a roto-translational (R-T) input, for the Wind Tower 1 model (see Table 5.6). **p. 104**

Table 5.8. Top displacement obtained with synthetically and semi-empirically retrieved rotational accelerations, considering the two horizontal direction of motion and a translational (T) and a roto-translational (R-T) input, for the Wind Tower 2 model (see Table 5.6). **p. 107**

Table 5.9: Top displacement obtained with synthetically and semi-empirically retrieved rotational accelerations, considering the two horizontal direction of motion and a translational (T) and a roto-translational (R-T) input, for the Wind Tower 3 model (see Table 5.6). **p. 107**

Table 5.10. Main structural technical specifications of the 500 kilowatt wind turbine located at Gebbies Pass. **p. 108**

Table 5.11. Modal properties of the wind tower model, considering the first 8 modes of vibration. z denotes the vertical axis and Ux, Uy, Uz, Rx, Ry and Rz represent the cumulative of the participation factor of the mode to the respective component of motion. **p. 108**

Table 5.12: Interstory drift obtained by the numerical model of the 28 story Grand Chancellor Hotel, considering a translational (T) and a roto-translational (R-T) input motion, considering the set of four strong motion seismometers located in the neighbourhood of the CBD. Percentage difference between interstory drifts is provided. **p. 117**

Table 5.13. Size and Computational time of the 3D aggregated numerical model of the CBD and Canterbury Plains in comparison with the parameters of the model described in Chapter3. Data of CPU time refer to the Lagrange cluster located at CILEA. **p. 121**

Table B.1. 3D numerical models produced with the different meshing strategies. **p. 144**

PREFACE

Rotational Seismology

"An emerging field of inquiry for studying all aspects of rotational ground motions induced by earthquakes, explosions and ambient vibrations". With these words W. H. K. Lee defines the term "rotational seismology" in the glossary he compiled for the special issue on rotational seismology and engineering application of the Bulletin of the Seismological Society of America (BSSA, Volume 99-2B, May 2009). Alphabetizing the key words of this emerging field of inquiry, the glossary responds to the double need to clarify and explain new technical terms without the delay typical of standard dictionaries, and, at the same time, to foster collaborations among different disciplines and researchers with dissimilar backgrounds. Rotational seismology, indeed, embraces a considerable range of disciplines and research areas, including strong motion seismology, broadband seismology, earthquake engineering, earthquake physics, seismic instrumentation, seismic hazard, seismotectonics and geodesy, and any other research fields linked with the observation and monitoring of earthquake induced ground motion. With the same spirit, J. Evans and the International Working Group on Rotational Seismology (IWGoRS) (2009) suggested a common notation and convention for translational and rotational motions, adopted for this work and depicted in Figure I. A Cartesian right-handed translational system, with z pointing upward, has been adopted. In this notation, "tilt", or rocking, denotes rotations about one of the horizontal axis, while rotation about the vertical axis is indicated as "torsion".

The core concept of rotational seismology, that appears as a common feature of almost the totality of the scientific papers on the topic, is that strong ground motions measurements should no longer be limited to only the three components of translational motion, but should simultaneously include

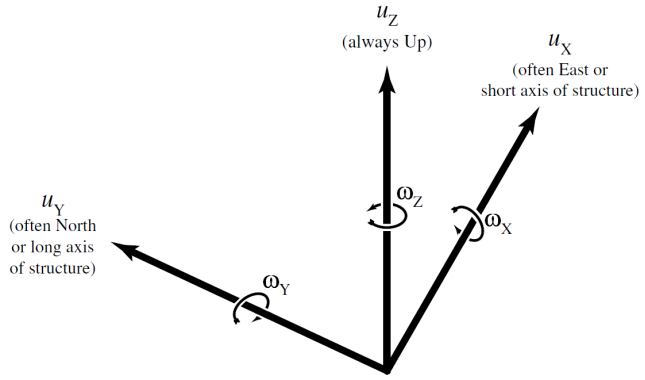

Figure I. Nomenclature and sign conventions for translational and rotational motions adopted in these work. X and Y axes point into the page and are normally in the horizontal plane, while Z axis points upward. Annotations u and ω are translational displacements and rotation angles. (Adapted from Evans and IWGoRS 2009).

the three components of rotational motion, especially in the near field of earthquakes, where soil response influences ground motions in a complex way, as pointed out in the introductory paper of the BSSA vol. 99-2B by Lee et al. (2009a).

Engineering motivation, purpose and organization of the work

Rotational seismology embraces a wide range of disciplines, from strong-motion seismology and earthquake engineering to seismic instrumentation and earthquake physics. Among these different topics, the main implications of rotational ground motions are the following:

i) In Strong-motion programs it is difficult to obtain accurate displacement for engineering purposes from the near-field records. Several studies have shown that acceleration recorded by translational sensors could be affected by rotations and therefore this effect should be reliably quantified and corrected (e.g., Trifunac and Todorovska, 2001, Graizer, 2005). Furthermore, to collect translational and rotational information together can yield a more complete description of the wave field, allowing a substantial improvement in studies of velocity heterogeneity, source complexity and media nonlinearity in strong ground motions (e.g. Takeo and Ito, 1997, Langston, 2007, Langston and Liang, 2008).

ii) From a civil engineering prospective, rotations could play an active role in the damaging of several categories of structures, e.g. pipelines or high-rise buildings, especially when soil-structure interaction effects should be taken into account. If a vertical motion differing from point to point is superimposed on a translational motion, indeed, there are two possible consequences for buildings (Castellani et al. 2012a):

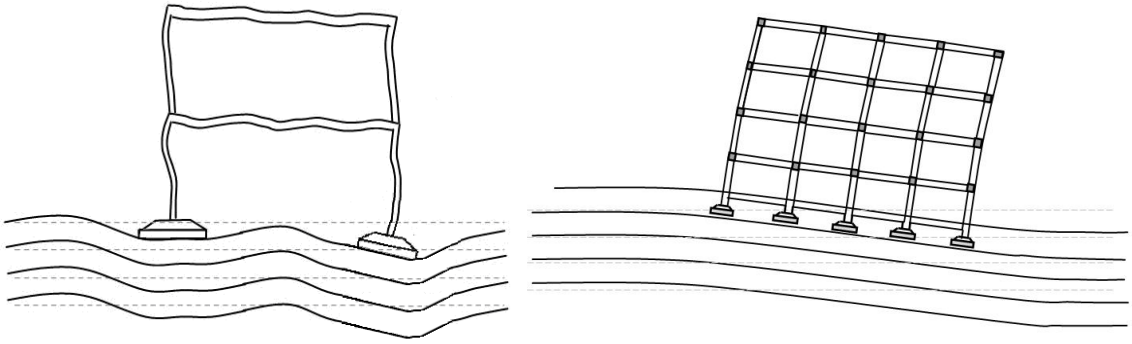

Figure II. Response of buildings under high- (Left hand side) and low- (Right hand side) frequency content of the rotational ground motions.

a) a local vibration along beams and columns (figure IIa), without the important motion of the building centre of mass, promoted by the high frequency content of the rotation motion;

b) an overall rotation of the base of the structure (Figure IIb), with an overturning motion, involving horizontal displacement of the centre of mass, provided by the low frequency content of the rotation motion.

It is important to underline that only direct, kinematic rotational effects on structures are pointed out (Figure II). Since the first mode of single, stiff, massive foundations (e.g. of high, slender towers) is rocking, the rocking excitations will always be difficult to distinguish from rocking soil-structure interaction effects, as the torsional seismic effects caused by structural, planar irregularities, versus torsional excitations. Relevance on civil engineering structures is still under debate by the scientific community and the recognition that the rotational component of strong motion could contribute significantly to the overall structural response appeared only recently (Trifunac 2006, Trifunac 2008). The main use of rotations in engineering design concerned the area of interstory drifts, associating the maximum drifts with damage levels (Trifunac and Ivanovic 2003, Ghobarah 2004, Trifunac 2009a). Fostered by a growing interest in performance-based design and structural health monitoring, studies of the rotational component in excitation and in response are now beginning to appear (Gicev and Trifunac 2008, Trifunac 2009b).

Despite the recent growth of interest in the field, there are only a few studies of recorded rotational strong ground motion and, consequently, the knowledge of the rotational wave field is still insufficient. Under these premises, this work aims to contribute to the study of rotational ground motion in the near-field region, addressing the basic questions about the magnitude of rotations

and their relevance for civil engineering structures, referring to a realistic earthquake scenario, as with the M_W 6.3 Christchurch earthquake of 22 February 2011, the deadliest and most damaging earthquake of the seismic chain that struck the Southern Island of New Zealand since September 2010 (Darfield M_W 7.1). The exceptionally high vertical acceleration recorded by many seismographs suggested that rotational motions could have played a significant role in the widespread damage of the area, and especially in the Central Business District (CBD), characterized by a dense urban setting with closely spaced high rise buildings.

In the first chapter, some bibliographic references are given, in order to briefly reconstruct the history and the main features of rotational seismology, since effects of rotational components of ground motion on obelisks, grave stones or similar vertically oriented objects have been observed since the middle of the nineteenth century by many scientists, who described these motions to better understand the physical nature of rotations. The fundamental theory for rotational components of seismic ground motion is reviewed, relying on the elastic wave theory. The chapter then describes the challenging topic of the evaluation of rotational strong ground motion, recalling and presenting empirical or semi-empirical results from past studies as well as direct measurements available in the literature. Finally some preliminary consideration about the relevance for civil engineering structures is provided. The purpose of the chapter is to give a general overview of the state-of-the-art of the rotational seismology, mainly focusing on the issues of estimation and measurement and on the relevance for buildings.

The second chapter presents a semi-empirical procedure to evaluate rotational accelerograms starting from measured translational records in closely-spaced array of stations, relying on the mathematical relation between the cross power spectrum and the power spectrum of rotation (Castellani and Zembaty, 1996). To understanding the relevance for civil engineering structures, the procedure has two areas of concern: i) the coherence implicit in the cross power spectra, which depends on interpolation of the original records, collected with the arrays of instruments; and ii) the relative importance of the vertical to the horizontal motion. When the records in an area a few kilometres from the epicentre are considered, the response spectrum of vertical motion over a wide range of frequencies is comparable and in some records even higher than that of horizontal motion. This has been observed in several stations that recorded the 2011 Christchurch earthquake. When the response spectrum of vertical motion is comparable to that of horizontal motion, the effects of rotational motions on most engineering structures can be meaningful.

The third chapter presents a selected case-study, the 22 February 2011 M_W 6.3 Christchurch Earthquake, with the epicentre located south-east of Christchurch, part of the seismic sequence that has been occurring since September 2010 in the southern island of New Zealand. The earthquake,

killing more than 180 people and damaging or destroying more than 100,000 buildings, is the deadliest and most disastrous event in New Zealand's history since the earthquake that struck the Napier and Hastings area in 1931. Beyond the effects and the consequences of the seismic event, the attention of the scientific community was drawn primarily to two aspects of the Christchurch earthquake: i) the extremely severe strong ground shaking observed with the ground acceleration recorded within the city of Christchurch being among the largest ever recorded for a New Zealand earthquake, with exceptionally high vertical ground motion (Bradley and Cubrinovski 2011); and ii) the widespread liquefaction phenomena occurring across the city (Cubrinovski and Green, 2010; Green et al. 2011). The combination of these two aspects could have led to significant rotational ground motions and, therefore, relevant effects on structures. Several digital stations of the permanent network operated by the local Institute of Geological and Nuclear Sciences (GNS), recorded the seismic event. The availability of this unprecedented dataset of near-fault strong ground motion, combined with the peculiar geological configuration of the area, makes the Christchurch earthquake a relevant benchmark to test the effectiveness of three-dimensional numerical tools for the prediction of the variability of strong ground motion in near-fault conditions. Different three-dimensional numerical models were constructed for the Christchurch earthquake, to check the dependence of the results on: i) the kinematic source model, based on the information retrieved from recent available seismic source inversion studies; ii) the shape of the alluvial-bedrock interface within the Canterbury Plains. The synthetic results are compared against the recorded data and their misfit is evaluated in a quantitative way, in a format suitable for engineering applications, making use of the criteria proposed by Anderson (2004).

In Chapter 4 rotational ground motions obtained with the semi-empirical procedure introduced in Chapter 2 and retrieved from the numerical three-dimensional model described and validated in Chapter 3 are discussed and compared, between each other and with past studies data. With the aim of a further understanding of the rotational ground motion and its relation with translational wave field, semi-empirical and synthetics data are analyzed in terms of peak ground acceleration (PGA) and peak ground rotation velocity (or rate, PRV) or, analogously, in terms of peak ground velocity (PGV) and peak ground rotation (PGω). Results of semi-empirical and numerical simulations fit reasonably well with data from past studies, and, furthermore, the ratio between translational and rotational peak amplitudes show a trend correlated with the velocity of the system, already pointed out by several authors with measured data (Lee at al. 2009b, Takeo 2009). The three-dimensional numerical model also makes it possible to study and visualize the spatial variability of peak ground rotation values and of the PGV/PGω ratio in the near-field of the earthquake, highlighting their dependence on the local site conditions, topographical features, epicentral distance and source directivity.

Chapter 5 presents the relevance of the rotational strong ground motions obtained from the semi-empirical procedure and from the three-dimensional numerical model for a series of civil engineering structures:

i) The wave passage effect is studied for a buried pipeline network in terms of peak ground rotational velocity and acceleration and their ratio. The crucial role of pipelines and lifelines during the emergency management and in the recovery phase has been highlighted by disastrous seismic events, as the 22 February Christchurch earthquake, drawing the attention of the scientific community and of stakeholders. The visual detection of damage of a buried pipeline network in Bazzano, near the epicentre of the disastrous earthquake that struck L'Aquila in 2009, allows assessment of some implications of the effect of a different ground motions from point to point on these kinds of structures.

ii) A numerical study is presented on a 30 m tall wind tower, located at Gebbie Pass, Christchurch, 15 km south-west of the epicentre of the 22 February 2011 earthquake. This kind of structure, as well as broadcasting antennas, play a strategic role, especially soon after a seismic event, when the need for energy and communication is of crucial importance. A parametric analysis has been performed on a simple 4 degree of freedom model, taking into account the soil-structure interaction through a system of springs and dashpots, varying height, diameter and foundation width of the structure. A three-dimensional finite element model of a fixed base wind tower allows an insight in the variability of stresses along the tower's height, evaluating the effect of the rotational component of strong ground motion. Even if significant differences in terms of top displacement or stress value can be found, the overall well seismic response of this kind of structure is demonstrated by the pictures taken before and after the seismic event.

iii) High rise buildings constitute and characterize the Central Business District, social and economic heart of the city of Christchurch. This kind of buildings experienced collapse or heavy damages during the earthquake sequence. A numerical analysis on the Grand Chancellor Hotel, the tallest building in Christchurch with a height of 85 m has been performed, analyzing the possible role of rotational input motions on its seismic behaviour in terms of interstory drift. The effect on the structural response of a rotational motion superimposed to a translational one is shown considering both semi-empirical and numerical input. Combining this preliminary result with the effects of nonlinearity and differential excitation of columns in the first story for extended structures, it is possible to state that ignoring the contribution of the rotational components of strong ground motion could lead to underestimated drift (Trifunac, 2009a).

iv) While the variability of strong ground motion, in its translational and more recently rotational components, is widely studied by many scientist both with large scale with regional models having width and depth of several kilometres, and at a small scale, considering the earthquake effect on single buildings, relatively few models have been done at the medium scale, considering the interaction between the topography and the characteristics of the soil and complex geometry of foundations and buildings of a city. In the literature it is called "Site-City interaction". In this application, the complexity of the seismic input is fully considered at a site-city scale, where the Christchurch CBD is geometrically represented and numerically modelled. Naturally including all the six component of motion, the example aims to evaluate, at the same time, the seismic response of a pounding-prone compound of buildings and the effect of a densely urbanized area in the spatial variability of strong ground motion, trying to explain the observed damage variability in apparently homogeneous areas. Looking at the variability of surface earthquake ground motion through snapshots of the velocity and displacement wavefield, it is possible to observe the active role played by the buildings cluster, in substantial agreement with the words of Trifunac (2009a): "*In an urban setting, a distribution of buildings will act as an extended surface source area consisting of a large number of closely spaced sources of translational and rotational motions, which will cause the warping of the half-space surface in the near-field and a seemingly random distribution of strong, high-frequency surface waves in the far field*".

In Chapter 6, some concluding remarks are given. The main aspects of the work are summarized, discussing the main results obtained and future developments. Two appendixes close the work.

Appendix A presents the complex technology at the basis of the ring laser systems, that exploits optical interferometers to directly measure rotational velocity up to approximately 10^{-12} rad/s. The inner complexity of this high-precision monolithic instrument, together with the high installation cost (above 1 million US$) make diffusion extremely difficult, and the assessment of the level of noise at the installation location particularly important. With the prospect of a future installation of a ring laser system inside the Gran Sasso Laboratory, a study of the noise level there has been performed, plotting the probability density function of the power spectral density of the accelerations recorded for five months, between January and May 2008, by a broadband seismometer located in the laboratory. All three components show excellent behaviour for a short period, whereas they have unexpected behaviour at a long period, approaching or even overtaking the high noise model curve . This is mostly explainable by a lack of instrumental resolution, requiring further measurements before there is more debate about the ring laser installation, which is supposed to work in the range of frequency between 3 mHz and 10 Hz (Schreiber et al. 2004b).

Appendix B presents the evolution of the meshing strategy, at the basis of the three-dimensional hexahedral unstructured models largely adopted in the work. The task of reproducing complex,

sharp, topographic interfaces is tackled and discussed through the evolution of the meshing strategy in recent years, from the standard technique to a "not honoring" technique, to a "non-conforming" approach that allows different mesh sizes in neighbouring sub-domains. In this way it is possible to nimbly represent the complex alluvial soil-volcanic rock interface of the Canterbury Plains as well as to reduce the size of the elements where it is necessary, without considerably increasing the computational burden of the problem, as has been done in the modelling phase of the buildings cluster in the Christchurch CBD. Non-conforming techniques, allow the use of independently generated meshes, thus avoiding the generation of a huge number of transition elements, together with the possibility of adopting different spectral approximation degrees in different sub-domains. This offers the possibility of tackling the wave propagation problem from different scales, from far-field to near-field, from near-field to the site-city interaction.

CHAPTER 1

ROTATIONAL SEISMOLOGY: THEORY, OBSERVATION, AND ENGINEERING IMPLICATIONS

1.1 Introduction

From the classical theory of continuum, the general motion of a particles with six degree of freedom in a solid body is fully described by three translations (along three orthogonal axes x, y and z) and three rotations (about the axes x, y and z). Even if this is widely accepted by classical seismology (Bath, 1979), modern seismology is still based on the observation and measurement of translational motions.

There are two main reasons that, together, constitute the main obstacles to the development of rotational seismology: the intrinsic difficulty of reliably measuring rotational motions, and the widespread belief that these kinds of motions are, in any case, insignificant (Gutemberg, 1927). In 1958, Richter, in a footnote of its Elementary Seismology, stated that "*Perfectly general motion would also involve rotations about three perpendicular axes, and three more instruments for these. Theory indicates, and observation confirms, that such rotations are negligible*". This sentence synthesizes well the thought that the scientific and engineering community has long held about rotational motions and their relevance for structures.

As recalled by Lee at al. 2009b, according to Cochard et al. (2006), displacement u of a point x is related to the displacement of the neighbouring point x+dx by the following equation:

$$\mathbf{u}(\mathbf{x}+\delta\mathbf{x}) = \mathbf{u}(\mathbf{x}) + \boldsymbol{\varepsilon}\delta\mathbf{x} + \boldsymbol{\omega}\times\delta\mathbf{x}, \qquad (1.1)$$

where ε is the strain tensor, and ω is a pseudovector representing the infinitesimal angle of rigid rotation generated by the disturbance:

$$\boldsymbol{\omega} = \frac{1}{2}\nabla \times \mathbf{u}(\mathbf{x}). \qquad (1.2)$$

The three components of rotation about the horizontal and vertical axes are therefore given by the following equations for infinitesimal motions:

$$\begin{cases} \omega_x = \frac{1}{2}\left(\frac{\partial u_z}{\partial y} - \frac{\partial u_y}{\partial z}\right) \\ \omega_y = \frac{1}{2}\left(\frac{\partial u_x}{\partial z} - \frac{\partial u_z}{\partial x}\right) \\ \omega_z = \frac{1}{2}\left(\frac{\partial u_y}{\partial x} - \frac{\partial u_x}{\partial y}\right) \end{cases}. \qquad (1.3\ a, b, c)$$

Therefore, it is possible to measure rotational ground motions directly with gyroscopic sensors or complex ring laser systems (e.g., Igel et al. 2005, Schreiber et al. 2006), or indirectly infer them from an array of translational sensors, assuming the classical elasticity theory is valid. Several studies, indeed, through the years, deduced ground rotational motions indirectly, from closely spaced accelerometer arrays (e.g., Castellani and Boffi 1986, Niazi 1986, Oliveira and Bolt, 1989, Spudich et al. 1995, Bodin et al. 1997, Huang, 2003, Suryanto 2006, Ghayamghamian and Nouri 2007, Spudich and Fletcher 2008) or theoretically, by exploiting kinematic source models and linear elatodynamic theory of wave propagation in elastic solids (e.g., Bouchon and Aki, 1982, Trifunac, 1982, Lee and Trifunac, 1985, 1987).

In order to reliably describe the spatial variability of strong-ground motion, therefore fully taking into account at the same time translational and rotational components, in recent years an impressive development of large-scale-three dimensional simulations of seismic-wave propagation has arisen, able to include the mutual effects of the seismic source, shallow crustal model and near-surface complex geological and topographical irregularities (e.g. Stupazzini et al. 2009a, Igel et al. 2011, Peter et al. 2011). Three-dimensional numerical simulations, mainly relying on Finite Differences, Finite Elements or Spectral Elements methods, must involve millions of nodal points to be reliable, implying a heavy computational burden and technical resources that have limited their application to relatively few examples in recent years, mainly concentrated in well defined and studied areas, such as the West Coast of US (e.g. Olsen and Archuleta, 1996, Graves, 1998, Wald and Graves, 1998, Olsen, 2001, Graves and Wald, 2004, Komatitsch et al. 2004, Day et al. 2008, Wang et al. 2008) or Japan (Pitarka et al. 1998, Furumura and Hayakawa, 2007).

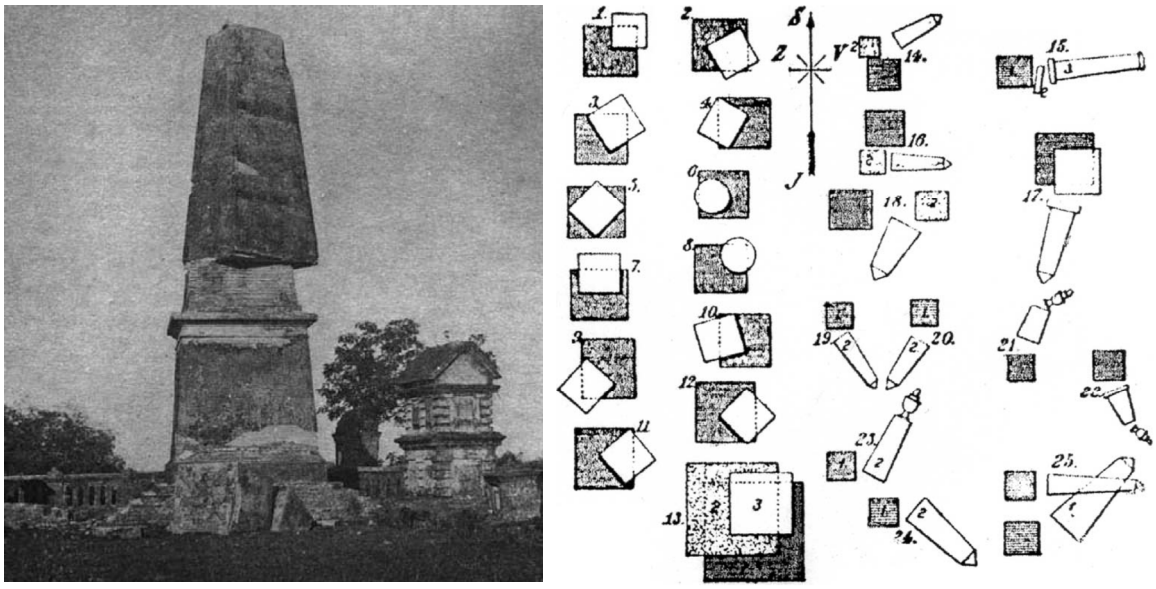

Figure 1.1. Left hand side: Rotation of obelisk segments from the 1897 Assam earthquake. Right hand side: Rotated tombstones from the 1906 San Francisco earthquake, illustrated by Jenista (1906-1907). (From Kozak 2009).

1.2 Historical background of Rotational Seismology

Earthquake rotational effects have been observed for centuries and several pioneers in different countries have tried to describe and measure rotational motions induced by earthquakes, starting with the work of P. Filippo Cecchi (1876) who, in the middle of the nineteenth century developed, with small success, an electrical seismograph with sliding smoked paper to record three-component translational motions together with the torsion movements from earthquakes (Ferrari, 2006). Table 1.1, taken from Kozak, 2009, contains a list of a group of historical earthquakes, documented by naturalists, geophysicists and seismologists, describing the rotational character of these earthquakes, while Figure 1.1a shows a characteristic example of rotation on a vertically oriented obelisk from the Assam earthquake (1897). Mallet (1862) in his analysis of the 1857 Basilicata earthquake reproduced numerous images of rotational effects and proposed that rotations could be due to a sequence of different seismic phases emerging under different angles. Reid, in 1910, observing the 1906 San Francisco earthquake, pointed out that the observed rotations are too large to be produced by waves of elastic distortion. A sketch showing displacement of tombstones in a San Francisco cemetery has been reproduced by Jenista (1906) and depicted in Figure 1.1b. In the same years brothers E. and F. Cosserat extensively treated the problem of rotations and in their "Theorie des Corps Deformables" (1909) introduced an elasticity theory incorporating a local rotation of continuum particles as well as the translational motion assumed in the classical theory and a couple stress (torque per unit area) as well as the force stress (force per unit area).

Table 1.1.A list of historical earthquakes with observed rotational effects. (From Kozak 2009).

Number	Date	Location	Intensity	Depth(km)	Rotational Effect
1	5 February 1783	Calabria	XI	13	Rotated San Bruno obelisk
2	26 July 1805	Baranello	X-XI	10	Visual description plus image
3	20 February 1818	Catanes	X	5	Visual description
4	23 October 1839	Comrie	VII	9	Rotated chimneys
5	1846	general	-	-	Visual description
6	16 December 1857	Basilicata	XI	2	Rotated columns, etc.
7	16 December 1857	Gera	VIII	9	Rotated wooden structure
8	29 June 1873	Belluno	X	25	Rotated tomb pyramid
9	22 October 1894	Shonai	M = 7 $^1/_4$	1	Rotated bell tower
10	12 June 1897	Assam	IX-X	1	Rotated obelisk
11	18 April 1906	San Francisco	XI	20	Rotated tombstones
12	8 May 1914	Linera	IX	2	Visual description

In the concluding remarks of his tutorial on earthquake rotational effects, Kozak comments that the majority of the rotational effects were observed in the epicentre zone of shallow events, that is the near field of earthquake, then in most cases, these effects were observed on vertically organized objects, such as chimneys, obelisks and tombstones. Thus, even if the explanation of the rotational effects is limited to few cases and relies on classical mechanical principle and visual description, these historic examples are already able to give some important hints about the relevance of rotational strong motion on structures in near-field.

1.3 Theoretical background of rotational ground motion

As described in the previous section, the rotational component of the seismic ground motion has been described and discussed since the early period of seismic engineering. Fostered by the lack of reliable measurements and with the slow diffusion at large scale of strong-motion instruments able to record rotational motions (Hudson 1983, Trifunac and Todorovska 2001), indirect methods for the assessment of strong ground rotations for engineering purposes have been developed. As pointed out by Zembaty (2009), since the 1980s two main groups of these methods have emerged in the literature:

i) Methods that utilize the synchronized measurements of translational ground motions at short distances (e.g. Niazi 1986, Oliveira and Bolt 1989, Spudich et al. 1995, Castellani and Zembaty 1996).

ii) Methods that rely on the analyses of the wave passage effects at the site, constructing and differentiating respective wave fields with respect to a spatial coordinate. Starting from the pioneer work of Trifunac 1982, these methods were subsequently developed by many authors, providing analytical solutions for the estimation of rocking and torsional components of motion at the

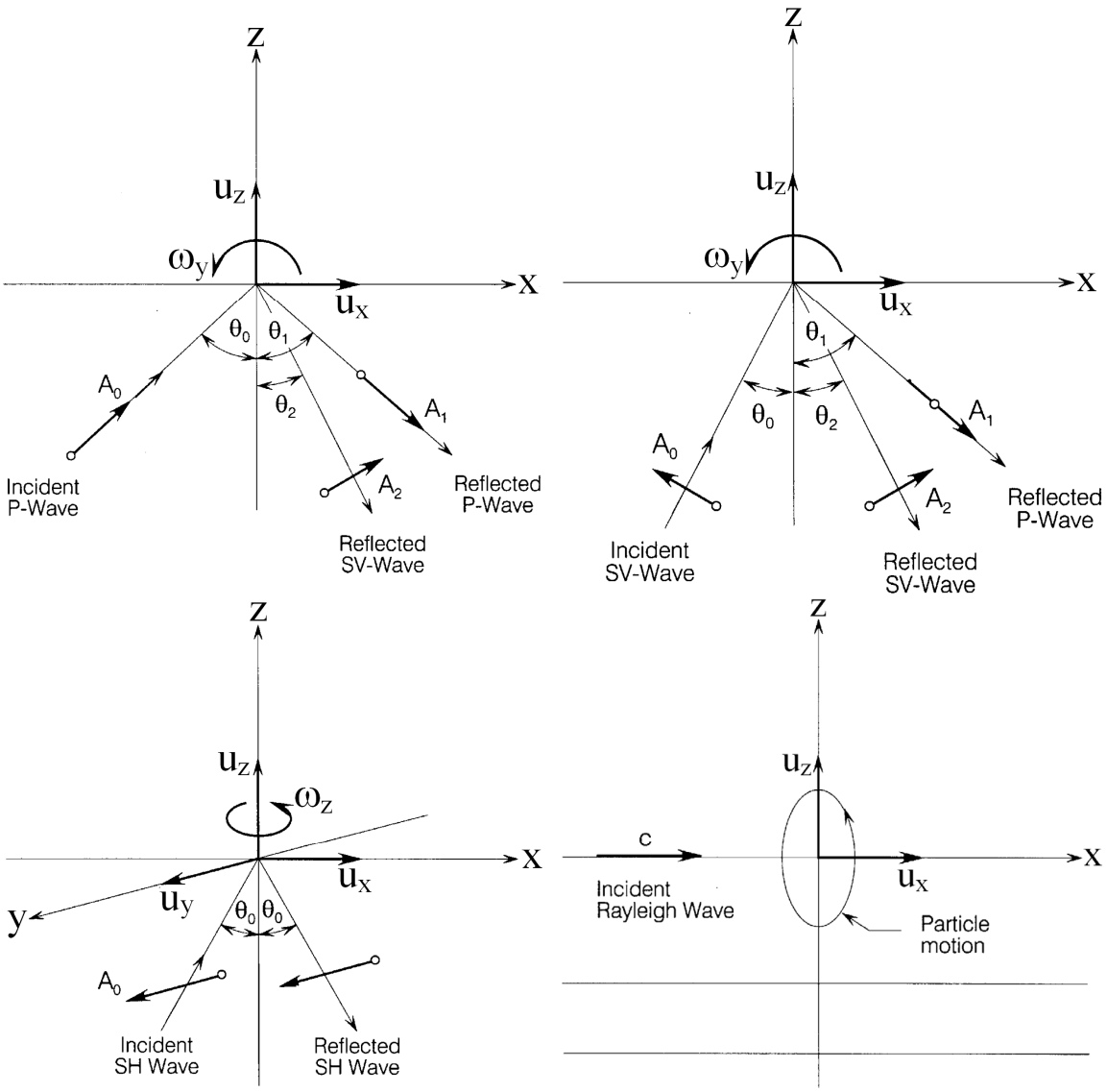

Figure 1.2. From Top to Bottom, from Left to Right, incident P-, SV-, SH and Rayleigh waves on half space, with the sign convention adopted for retrieving the mathematical expression of torsional and rocking ground motions. (Adapted from Lee 2002).

ground surface of an ideal elastic half-space, under harmonic plane P-SV, SH, Rayleigh and Love waves and computing synthetic torsion and rocking accelerograms from the corresponding translational components (e.g. Lee and Trifunac 1985, 1987, 2009, Rutemberg and Heidebrecht 1985, Castellani and Boffi 1989, Zembaty et al. 1993, Li et al. 1997, 2002, Lee 2002).

While Chapter 3 is extensively devoted to the first class of methods, the second one is briefly presented here, recalling the main mathematical expressions derived for the torsional and rocking component of earthquake ground motions. In Figure 1.2 are represented the rectangular coordinate systems (x, y, z) adopted by Lee (2002) and Trifunac (1982), in the presence of a stress-free

boundary at the surface of the elastic, homogeneous and isotropic half-space, with the incident and reflected rays associated with incident P-waves, incident SV-waves, incident SH-waves and incident Rayleigh waves.

1.3.1 The Torsional motion from incident waves

In Figure 1.2 the adopted coordinate system is represented, with the incident SH-wave having amplitude A_0 and angle of incidence θ_0. The frequency of the incoming wave is represented by f, β is the velocity and k their ratio, the motion is described by:

$$u_y = \left[A_0 e^{ik(x\sin\theta_0 + z\cos\theta_0)} + A_0 e^{ik(x\sin\theta_0 - z\cos\theta_0)} \right] e^{-ift} = 2A_0 \cos\left(kz\cos\theta_0\right) e^{ikx\sin\theta_0} e^{-ift}. \tag{1.4}$$

In the above and subsequent equations t represents time and i the square root of -1. The torsional component associated with the SH-waves at the half-space surface, according to Trifunac 1982, is:

$$\omega_z = \left(\frac{1}{2}\nabla \times \mathbf{u}\right) \times e_z = -\frac{1}{2}\frac{\partial u_y}{\partial x} = -A_0 ik\sin\theta_0 e^{ikx\sin\theta_0} = -\frac{1}{2} ik\sin\theta_0 u_y = \frac{k\sin\theta_0}{2} u_y e^{-i\pi/2}. \tag{1.5}$$

Therefore, it is possible to define the amplitude ratio as:

$$\left|\frac{\omega_z}{u_y}\right| = \frac{k\sin\theta_0}{2} = \frac{1}{2}\frac{f}{\beta}\sin\theta_0 = \frac{1}{2}\frac{f}{C}, \tag{1.6}$$

where C is the phase velocity in the horizontal x direction. Similar results can be obtained for the case of torsional motion associated with the translational component u_y of the Love waves at z = 0.

$$\left|\frac{\omega_z}{u_y}\right| = \frac{-i}{2}k = -\frac{i}{2}\frac{f}{C}, \tag{1.7}$$

where C is the phase velocity of Love waves.

Table 1.2. Rocking and torsion components of strong earthquake ground motion under closed-form solutions from the literature (Trifunac 1982, Lee and Trifunac 1985, 1987, Lee 2002). See Figure 1.2 for sign convention and definitions of the symbols.

Incident Wave type	Rotation	Amplitude
P-wave	$\omega_y = \frac{i}{2} A_2 k_\beta e^{[i(k_\alpha x \sin\theta_0 - ft)]}$	$\left\|\frac{\omega_y}{u_z}\right\| = \frac{\beta}{\alpha}\frac{f}{C}$
SV-wave	$\omega_y = \frac{ik_\beta}{2}\left(A_0 + A_2\right) e^{[i(k_\beta x \sin\theta_0 - ft)]}$	$\left\|\frac{\omega_y}{u_z}\right\| = \frac{f}{C}$
SH-wave	$\omega_z = -A_0 ik \sin\theta_0 e^{ikx\sin\theta_0}$	$\left\|\frac{\omega_z}{u_y}\right\| = \frac{1}{2}\frac{f}{C}$
Rayleigh	$\omega_y = -i\frac{f}{C} u_z\left(x,z,t\right)$	$\left\|\frac{\omega_y}{u_z}\right\| = i\frac{f}{C}$
Love	$\omega_z = -\frac{i}{2}\frac{f}{C} u_y\left(x,z,t\right)$	$\left\|\frac{\omega_z}{u_y}\right\| = -\frac{i}{2}\frac{f}{C}$

1.3.2 The Rocking motion from incident waves

In Figure 1.2 the coordinate system adopted is represented, with the incident P, SV and Rayleigh incident waves respectively. Considering the incident P-waves, A_0 denotes its amplitude, while A_1 and A_2 are the amplitudes of the reflected P-waves and of the reflected SV-waves, respectively. The two components of motion at the surface are described by:

$$\begin{cases} u_x = \left(A_0 \sin\theta_0 + A_1 \sin\theta_1 + A_2 \cos\theta_2\right) e^{[i(k_\alpha x \sin\theta_0 - ft)]} \\ u_z = \left(A_0 \cos\theta_0 - A_1 \cos\theta_1 + A_2 \sin\theta_2\right) e^{[i(k_\alpha x \sin\theta_0 - ft)]} \end{cases}. \qquad (1.8\ a, b)$$

The rocking component about the y axis is given by:

$$\omega_y = \frac{1}{2}\left(\frac{\partial u_z}{\partial x} - \frac{\partial u_x}{\partial z}\right) = \frac{i}{2} A_2 k_\beta e^{[i(k_\alpha x \sin\theta_0 - ft)]}, \qquad (1.9)$$

with, k_α and k_β respectively equal to the ratio between the circular frequency f and the respective velocities a and β of P- and SV-waves. Furthermore, Trifunac (1982) showed that the amplitude ratio of rocking in function of the translation u_z, being C being the horizontal phase velocity, is:

$$\left|\frac{\omega_y}{u_z}\right| = \frac{\beta}{\alpha}\frac{f}{C}. \qquad (1.10)$$

Considering the incident and reflected rays associated with plane SV-waves, depicted in Figure 1.2, being respectively A_0 the amplitude of the incident SV-waves, A_1 the amplitude of the reflected P-waves and A_2 the amplitudes of the reflected SV-waves, the two translational motions u_x and u_z are:

$$\begin{cases} u_x = \left(-A_0\cos\theta_0 + A_1\sin\theta_1 + A_2\cos\theta_2\right)e^{\left[i\left(k_\beta x\sin\theta_0 - ft\right)\right]} \\ u_z = \left(A_0\sin\theta_0 - A_1\cos\theta_1 + A_2\sin\theta_2\right)e^{\left[i\left(k_\beta x\sin\theta_0 - ft\right)\right]} \end{cases}. \qquad (1.11\ a,\ b)$$

Thus, the rocking component about the y axis is given by:

$$\omega_y = \frac{1}{2}\left(\frac{\partial u_z}{\partial x} - \frac{\partial u_x}{\partial z}\right) = \frac{ik_\beta}{2}\left(A_0 + A_2\right)e^{\left[i\left(k_\beta x\sin\theta_0 - ft\right)\right]}, \qquad (1.12)$$

while, in terms of translational component u_z, the amplitude of rotation is given by:

$$\left|\frac{\omega_y}{u_z}\right| = \frac{f}{C}. \qquad (1.13)$$

Considering, finally, the contribution of the incident Rayleigh waves on a half-space, Figure 1.2, being k the ratio between the circular frequency f and phase velocity C in the horizontal direction, it is possible to describe the rocking at the surface in function of the translational component u_z, in the following way:

$$\left|\frac{\omega_y}{u_z}\right| = ik = i\frac{f}{C}. \qquad (1.14)$$

Considering thus the maximum values of an harmonically propagating plane wave of arbitrary amplitude, and knowing the horizontal apparent velocity of propagation C, it is possible to have a first-order approximate estimation of the peak rocking and torsional values ($PG\omega_h$ and $PG\omega_z$) from the peak ground vertical and horizontal velocity, respectively (PGV_z and PGV_h).

$$\begin{cases} PG\omega_h = \dfrac{1}{C}PGV_z \\ PG\omega_z = \dfrac{1}{2C}PGV_h \end{cases}. \qquad (1.15\ a,\ b)$$

Starting with these expressions, many authors (e.g. Spudich and Fletcher 2008, Stupazzini et al. 2009b, Wang et al. 2009, Fichtner and Igel 2009), studied the ratio between peak rotations and velocity values. It can be interpreted as a slowness (Lee 2009b), the inverse of an apparent velocity, characterizing the seismic wavefield, even though in the near-field region this assumption could be too simplistic.

Results obtained in this way, on the basis of the elastic wave theory, are synthesized in Table 1.2. The idea of body and surface-waves decompositions has been recently revisited by Zembaty 2009, in order to formulate algorithms for constructing spectral densities of the rocking and torsional components in terms of translational spectra, their co-spectra and wave parameters.

1.4. The challenge of the estimation and measurement of rotational ground motions

Starting from the pioneering works of Cecchi, the issue of measuring or reliably estimating rotational motions induced by earthquakes has been a challenging topic. Only recently instruments sensitive enough to measure rotation motions at the level of microradians per second have developed.

In the first edition of "Quantitative Seismology" in 1980, Aki and Richards (1980) stated that "*the state-of-the-art sensitivity of the general rotation-sensor is not yet enough for a useful geophysical application*". The same statement is also made in the second edition, where Aki and Richards (2002) claim that "*seismology still awaits a suitable instrument for making such measurements*".

Graizer (1991) and Nigbor (1994) directly measured rotational and translational ground motions in the near field of large explosions using commercial rotational sensors sensitive to torsion, such as tilt meters or solid state devices. Rotational motions from tele-seismic and local earthquakes were recorded only recently, by sensitive rotational sensors, such as ring lasers or broadband rotation meters, in Poland, Germany, New Zealand and southern California (see e.g. Stedman et al.1995, McLeod et al. 1998, Pancha et al. 2000, Teisseyre et al. 2003, Igel et al. 2005, Schreiber et al. 2006, 2009a, Igel et al. 2007, Lin et al. 2009). In particular, the ring laser technology, extensively described in Appendix A, exploits highly sensitive optical interferometers, allowing the observation of earthquake-induced rotational ground motion over a wide magnitude and epicentral distance range (Cochard et al. 2006), even if the high installation cost and service requirements constitute a limit to its widespread diffusion.

A comparison between rotations from dense-arrays and point measurements, during the same event, and at the same location, has been provided by Suryanto et al. 2006. The overall fit is estimated by the authors to be satisfactory, although factors of 2 to 5 between such measurements have been observed. Authors explain them in terms of local site conditions. Nevertheless recent observations in the near field of earthquakes in Japan (Takeo 1998, Takeo 2009) and in Taiwan

Table 1.3. Data retrieved from literature of peak ground horizontal velocity (PGVh) ,peak ground rotation (PGωz) and peak ground rotational velocity (PGω̇z) around the vertical axis. Additional information about the source parameters includes SS strike slip, T thrust and R *reverse source mechanism. In "Data type", 1 means array-derived data, 2 indicates numerical/semi-analytical data and 3 measured data. N.A. stands for "not available". (Adapted from Stupazzini et al. 2009b).*

Reference	Number	Data type	M_W	R (km)	Source	PGV_h [m/s]	$PG\omega_z$ [rad]	$PG\dot{\omega}_z$ [rad/s]
Bouchon and Aki (1982	1	2	6.6	1	SS	1	$2x10^{-4}$	$1.2x10^{-3}$
	2	2	6.6	1	SS	1.6	$3x10^{-4}$	$1.5x10^{-3}$
Lee and Trifunac (1985)	3	2	6.6	10	N.A.	0.45	$1x10^{-4}$	$1.2x10^{-3}$
Niazi (1986)	4	1	6.6	5	SS	0.203	$2.75x10^{-4}$	$7x10^{-4}$
Oliveira and Bolt (1989)	5	1	5.6	6	N.A.	0.15	$7.4x10^{-6}$	N.A.
	6	1	5.7	30	N.A.	0.12	$8.5x10^{-6}$	N.A.
	7	1	5.8	22	N.A.	0.30	$1.46x10^{-5}$	N.A.
	8	1	6.7	84	N.A.	0.06	$6.8x10^{-6}$	N.A.
	9	1	7.8	79	N.A.	0.391	$3.93x10^{-5}$	N.A.
Castellani and Boffi (1986)	10	2	6.6	18	SS	0.0692	$3.06x10^{-5}$	$1.04x10^{-4}$
Nigbor (1994)	11	3	1 kton	1	Expl.	0.2780	$6.\ 6x10^{-4}$	$2.4x10^{-2}$
Bodin et al. (1997)	12	1	6.7	311	R	0.03	$5.6x10^{-5}$	N.A.
Singh et al. (1997)	13	1	7.5	305	R	0.11	$2.07x10^{-4}$	N.A.
Takeo (1998)	14	3	5.7	3.3	SS	0.29	N.A.	$3.3x10^{-3}$
	15	3	5.3	3.3	SS	0.20	N.A.	$8.1x10^{-3}$
Huang (2003)	16	1	7.7	6	T	0.33	$1.71x10^{-4}$	N.A.
Paolucci and Smerzini (2008)	17	1	4.2	81	N.A.	$4.06x10^{-4}$	$1.64x10^{-7}$	$2.4x10^{-4}$
	18	1	4.9	81	N.A.	$5.2x10^{-3}$	$2.25x10^{-6}$	$3.2x10^{-3}$
	19	1	6.0	11.6	SS	0.25	$8.98x10^{-5}$	$1.3x10^{-3}$
	20	1	6.5	65	SS	0.165	$7.68x10^{-5}$	$8.2x10^{-4}$
Spudich and Fletcher (2008)	21	1	6.0	8.8	SS	0.25	$8.81x10^{-5}$	$1.09x10^{-3}$
	22	1	4.7	14.0	SS	$1.19x10^{-2}$	$4.69x10^{-6}$	$9.44x10^{-5}$
	23	1	5.1	14.4	SS	$6.02x10^{-2}$	$2.0x10^{-5}$	$4.46x10^{-4}$
	24	1	4.9	18.3	SS	$2.74x10^{-2}$	$1.36x10^{-5}$	$2.47x10^{-4}$
Lin et al. (2009)	25	3	3 ton	0.25	Expl.	N.A.	N.A.	$2.74x10^{-3}$
	26	3	750 kg	0.25	Expl.	N.A.	N.A.	$1.75x10^{-3}$

(Huang et al. 2006, Liu et al. 2009) revealed that the recorded amplitude of rotations may be one to two orders of magnitude larger than expected from the classical linear elasticity theory.

Furthermore, additional rotations, beyond the classical elasticity theory could be generated in granular materials or cracked continua, by abrupt changes of fault slip, tensile fractures and asymmetries of the stress and strain fields (Vardoulakis 1989; Takeo and Ito 1997; Teisseyre and Boratynski 2003; Harris 2006; Grekova et al. 2009; Kulesh 2009). Many features of the theoretical and observational aspects of rotational motions recalled here are described comprehensively in two recent monographs edited by Teisseyre et al. (Teisseyre et al. 2006 and 2008).

These studies suggest that major discrepancy between observations and theoretical predictions may be the largest in the near field (within 30 km of fault ruptures) of earthquakes of magnitude M_W greater or equal to 6. Therefore, the goal of recording such ground motions is not trivial, requiring extensive and expensive seismic instrumentation along carefully-chosen active faults without the certainty of a strong seismic event in that area. An attempt to study near-field motions using explosions or rock-bursts in mines was introduced by Zembaty in 2004, while Wu et al. 2009 describe an ongoing project in south-western Taiwan promoted by their Central Weather Bureau,

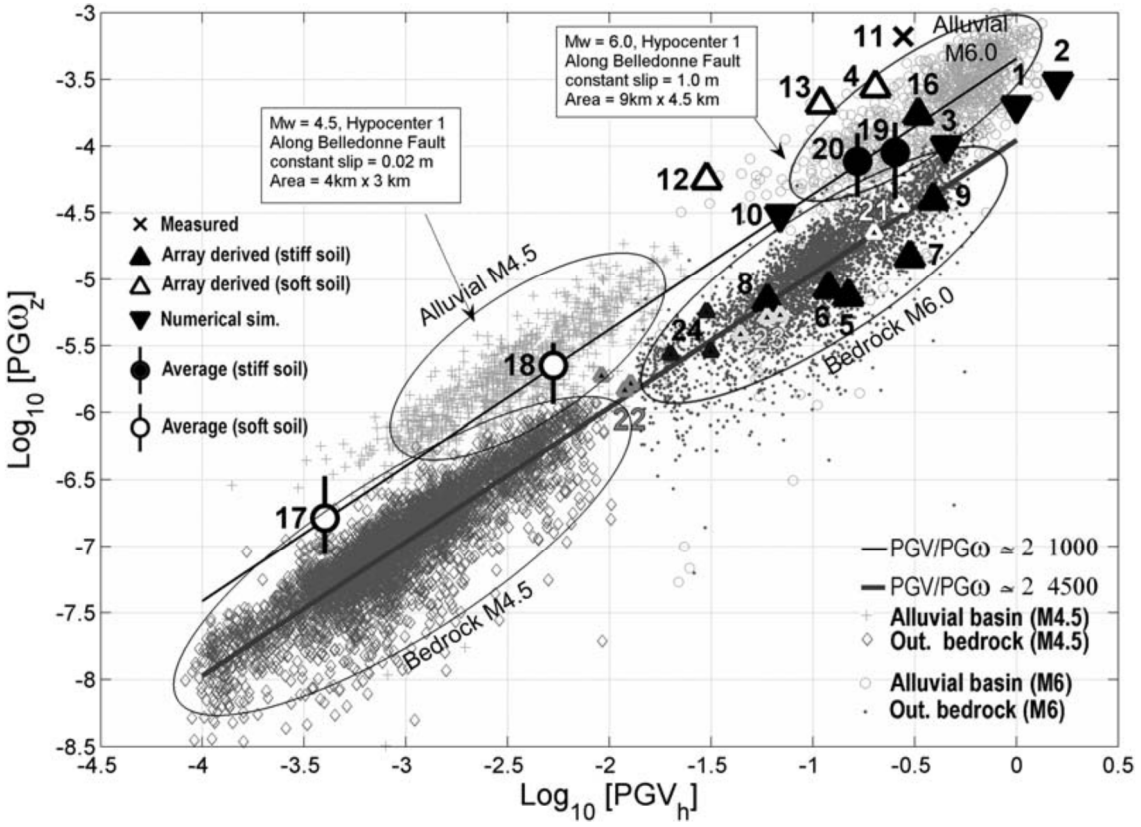

Figure 1.3. Peak ground horizontal velocity (PGV_h) versus peak ground torsion ($PG\omega_z$) in logarithmic scale obtained from data in the literature, listed in Table 1.3, superimposed to synthetics obtained for a 3D model of Grenoble valley, France, considering earthquakes with M_W 6.0 and M_W 4.5. (From Stupazzini et al. 2009b).

aimed at capturing a possible repeat of the 1906 Meishan earthquake with translational and rotational instruments.

1.4.1 Dense array estimation of ground rotational motions

As previously stated, specific devices for the direct observation of earthquake-induced rotational ground motion are not largely diffused and, most frequently, rotational motions are indirectly inferred from measurements of closely-spaced arrays of instruments. Through interpolation techniques (e.g. Paolucci and Smerzini 2008, Spudich and Fletcher 2008) it is possible to reconstruct the continuous three-component displacement wave field at the ground surface and consequently the rotation tensor Ω can be determined with its rotational components of motion:

$$\boldsymbol{\Omega}(x,y,z=0,t)=\begin{pmatrix} 0 & -\omega_z & \omega_y \\ \omega_y & 0 & -\omega_x \\ -\omega_y & \omega_x & 0 \end{pmatrix}. \qquad (1.16)$$

Table 1.4. Least square fit to a straight line with error estimates for the torsional observations of Liu et al. 2009 and Takeo 2009. (From Lee et al. 2009b).

Data set	Data samples	Location	$b \pm \varepsilon_b$ (s/km)	$a \pm \varepsilon_a$ (mrad/s)	ε (mrad/s)	r_{xy}
Liu et al. (2009)	52	Taiwan	1.301±0.028	0.002±0.003	0.028	0.988
Takeo (2009)	216	Japan	1.454±0.010	-0.036±0.004	0.060	0.995

Papers by Smerzini et al. (2009a) and Stupazzini et al. (2009b) present a comprehensive collection of rotational ground motion data from past studies available in the literature, here reported in Table 1.3 and represented, when possible, in Figure 1.3 in terms of peak ground horizontal velocity (PGV_h) over peak ground rotation ($PG\omega_z$) ratio, superimposed to the synthetic values obtained by a 3D numerical simulation of the Grenoble Valley, France (Stupazzini et al. 2009a, Stupazzini et al. 2009b).

For the sake of completeness, together with array-derived data, numerical and semi-analytical data as well as available measured data are also reported. Bouchon and Aki (1982) adopted a semi-analytical method in order to derive strains, tilts and rotations in the proximity of a 30 km long strike-slip fault. Different analysis followed this work, trying to indirectly estimate surface ground rotations from 2D seismic arrays (Castellani and Boffi 1986, Niazi 1986, Oliveira and Bolt, 1989, Bodin et al. 1997, Singh et al. 1997, Huang 2003, Paolucci and Smerzini 2008, Spudich and Fletcher 2008) or theoretically (Lee and Trifunac, 1985). As far as measured data are concerned, explosive sources have been measured by Nigbor (1994) and Lin et al. (2009). Earthquake-induced rotational ground motion measurements available from Liu et al. (2009) and Takeo (2009) are extensively described in next section.

1.4.2 Direct earthquake-induced measurements of rotational ground motions in Taiwan and Japan

At present, the richest set of available earthquake-induced rotational measurements is provided by two projects in Taiwan and Japan.

Liu et al. (2009) present observations between May 2007 and February 2008 of 52 earthquakes recorded at the HGSD station, in eastern Taiwan (Figure 1.4a). They observed good rotational velocity signals, together with excellent translational acceleration signals, exploiting a high-resolution triaxial rotational velocity sensor (Model R-1 made by eentec/PMD, http://www.eentec.com/) incorporated in well-known and tested accelerographs (Model K2 made by Kinemetrics, http://www.kinemetrics.com). Within the nine months of observations, local magnitudes ranging from 2.6 up to 6.6 were measured, with the hypocentral distance from the HGSD station from 14 km to 260 km. The peak ground acceleration recorded reaches 0.47 m/s^2, with much higher amplitudes for the two horizontal directions, while the peak rotation rate is

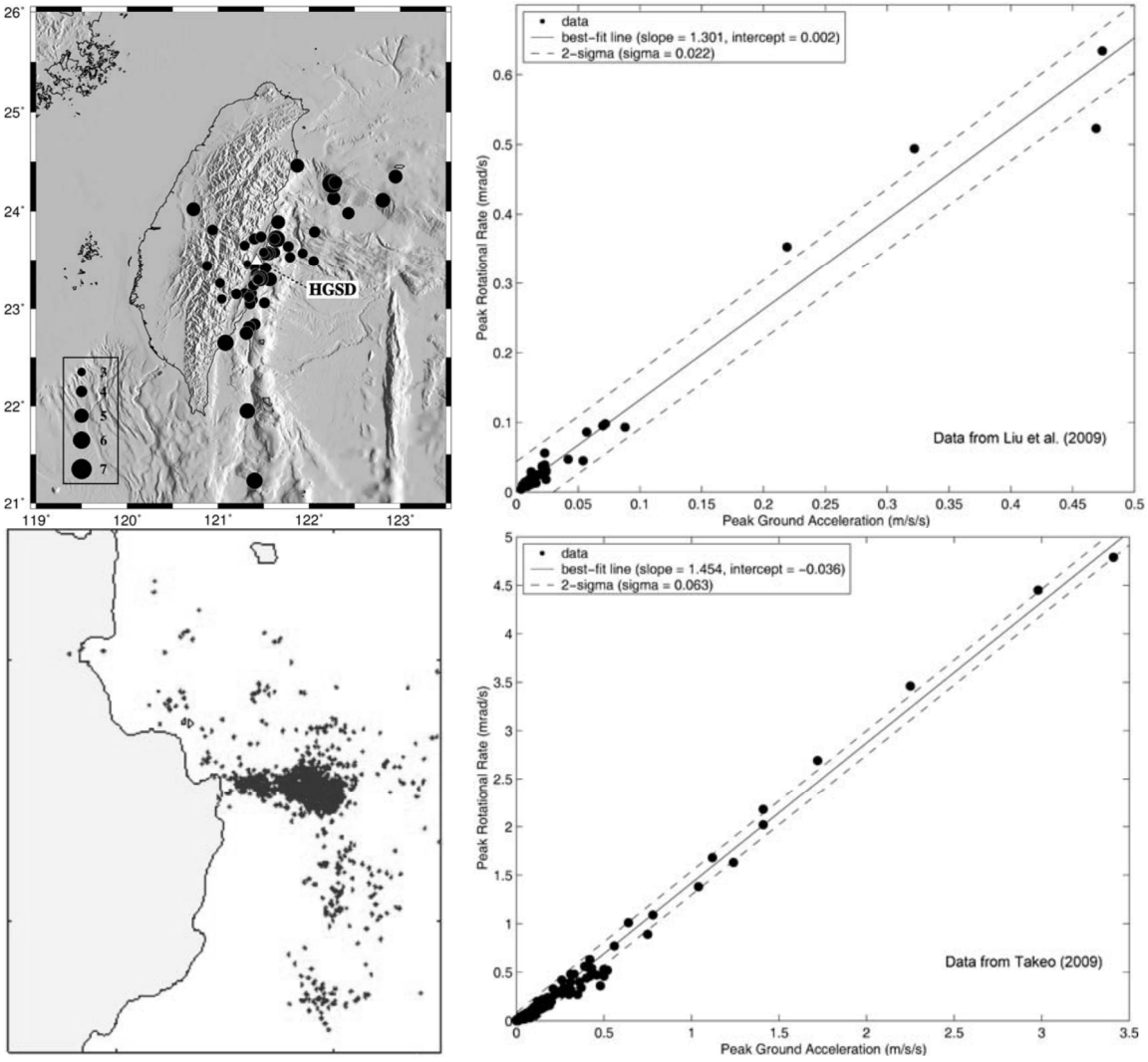

Figure 1.4. Top: Left: Location of earthquakes with good rotational motions recorded at the HGSD station in eastern Taiwan from 8 May 2007 to 17 February 2008. The size of the dot is proportional to the magnitude (From Liu et al. 2009. Right: Peak torsional rate versus peak ground horizontal acceleration for the Taiwan earthquakes data set. (From Lee at al. 2009b). Bottom: Location of the epicentres of the 1998 Ito offshore swarm activity. (From Takeo 2009). Right: Peak torsional rate versus peak ground horizontal acceleration for the Japan earthquakes data set. (From Lee et al. 2009b).

0.63 mrad/s, with much higher amplitudes for the vertical component. This is in agreement with the mathematical evidence that the vertical component of rotational motion is governed by the gradients of the horizontal displacements (equation 1.3c, Cochard et al. 2006).

Takeo (1998 and 2009) observed six components of ground rotational and translational motion in a near-field region during an earthquake swarm in April 1998 offshore from Ito on the Izu Peninsula, Japan, (Figure 1.4c) exploiting a Kinematics FBA-23 triaxial accelerometer, a Systron Donner MotionPak triaxial gyro sensor, a triaxial high-sensitive angular displacement sensor and two six channel digital data loggers. Using these sensors, more than 200 records of ground rotational

motion have been captured ranging from 10^{-7} to 10^{-3} rad at Kape Kawana station. Magnitudes and epicentral distances for the recorded events range from a maximum value of 5.0 to 1.2 and from 1.5 to 10 km, respectively. The maximum measured rotations rate about the vertical axis reach values of 8.1 mrad/s, several times more than the prediction of Bouchon and Aki (1982). This discrepancy, not explainable with a malfunction of the instruments, has been explained by the author in terms of heterogeneity of slip velocity along the fault and local rheology. These factors, therefore, may play a relevant role, especially in the near-field of an earthquake, as pointed out by Huang (2003) and Spudich and Fletcher (2008).

Lee et al. (2009b) performed a data fitting to the data from Liu et al. (2009) and Takeo (2009), suggesting a linear relationship between peak rotational velocity (PRV) and peak ground acceleration (PGA), with results synthesized in Table 1.4 and in Figure 1.4b and 1.4d. In particular the following relations can be obtained for the data set of Liu et al. and Takeo, respectively, a straight line can be fitted:

$$\begin{cases} PRV = 0.002 + 1.301 PGA \\ PRV = -0.0036 + 1.454 PGA \end{cases} \qquad \textit{(1.17 a, b)}$$

Takeo (2009), presenting his data-set of more than 200 earthquakes, shows a linear correlation between peak ground rotations around the vertical axis ($PG\omega_z$) and the peak ground horizontal velocities (PGV_h). A similar relationship has been pointed out by several authors (e.g. Spudich and Fletcher, 2008, Stupazzini et al. 2009b, Wang et al. 2009) and is shown in Figure 1.4. The two plots presented by Lee et al. 2009b and depicted in Figure 1.4 in terms of PRV and PGA are basically equivalent to the relation presented by Takeo, simply avoiding performing the integration for the measured rotational velocities and ground accelerations.

The slope of equations 4a and 4b, with dimension unit of s/km could be interpreted as the inverse of an apparent velocity characterizing the seismic wavefield (Spudich and Fletcher, 2008). Obviously, in order to define a more accurate relationship between rotational velocities and ground accelerations, more data, in a wider range of magnitudes and epicentral distance, are necessary.

1.5 Relevance of rotational strong ground motion for civil engineering structures

Relevance of strong rotational ground motion for civil engineering structures is still under debate by the scientific community. Fostered by a growing interest in performance-based design and structural health monitoring, the recognition that the rotational component of strong motion could contribute significantly to the overall structural response, appeared only recently (e.g. Trifunac and

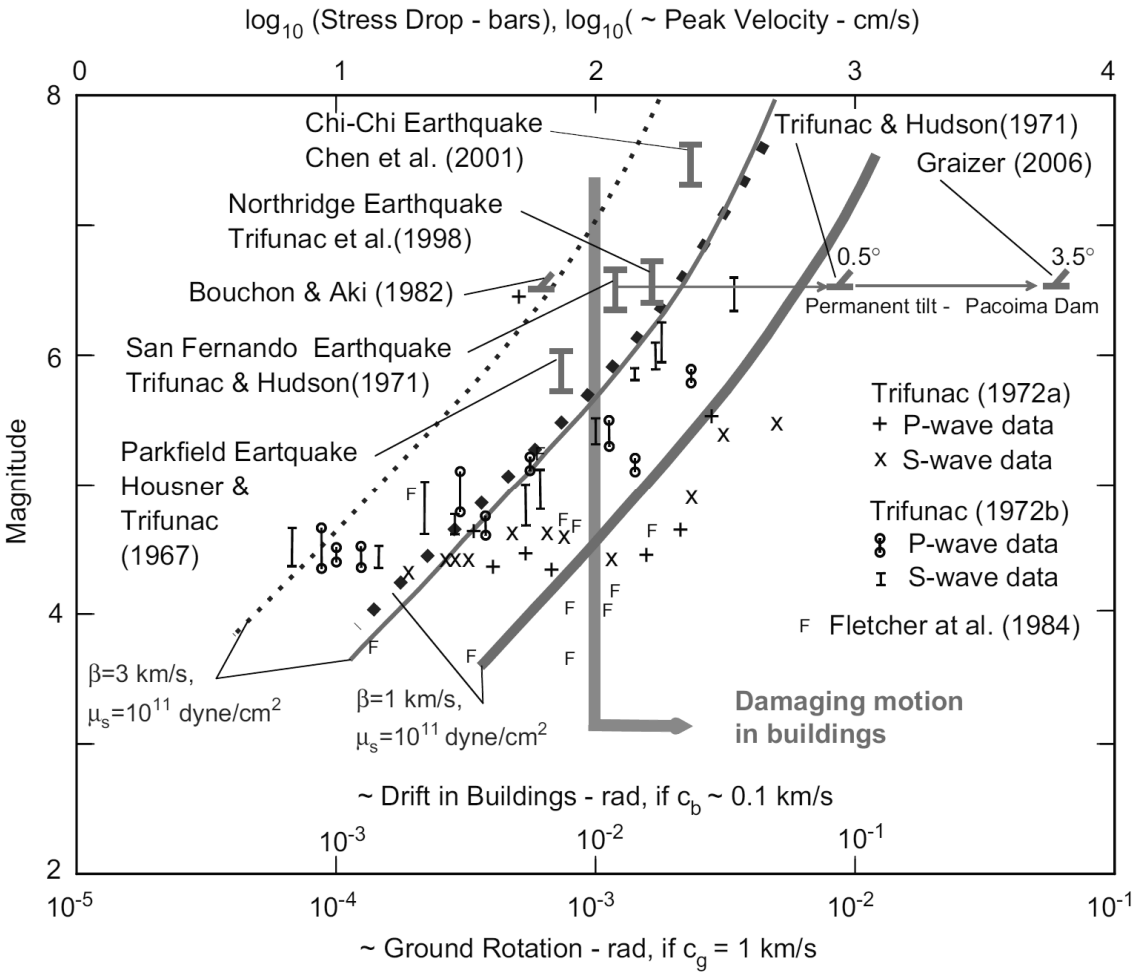

Figure 1.5. Estimation of stress drop from near-field recording of strong motion (different symbols) and from equations 1.8a (solid line) and 1.18b (dotted line). The corresponding order-of-magnitude estimates of peak ground rotation at the fault (with cg = 1 km/s) and the order-of-magnitude of the expected drift in buildings (with cb = 0.1 km/s) are superimposed. (From Trifunac 2009a).

Ivanovic 2003, Ghobarah 2004, Trifunac 2006, Trifunac 2008, Gicev and Trifunac 2008, Trifunac 2009a, Trifunac 2009b). As reviewed by Trifunac 2009b, differential ground motions, ground strains, curvatures, torsional and rocking ground accelerations and their combined action can produce considerable effects on different kinds of civil engineering structures:

i) Damages to pipelines, due to seismic events that are not associated with faulting of landslides but with large differential motions, strains and curvatures of the soil, are consequences of travelling seismic waves and of the corresponding large rotations and twisting of soil blocks, induced by lateral spreads and by early stages of liquefaction (Ariman and Muleski 1981, Trifunac and Todorovska 1997b, 1998).

ii) Large pseudostatic shear and moments in structural members are induced by differential excitation of flexible, extended, multiple and separate foundations. It could be particularly relevant

for high rise buildings or bridges (Trifunac and Todorovska 1997a, Trifunac and Gicev 2006, Jalali and Trifunac 2008). Torsional ground motion determined large torsional responses on tall buildings in Los Angeles (Hart et al. 1975), while the collapse of many bridges during the 1971 San Fernando, 1978 Miyagi-ken-Oki and 1994 Northridge earthquake, could be ascribed to longitudinal differential ground motions (e.g., Bycroft 1980, Trifunac et al. 1996). Furthermore, the so called "wave-passage" effect could generate additional rotation motions in the soil, in the presence of multiple foundations, as typically occurs in densely urbanized area, characterized by closely spaced buildings (Trifunac 2009b).

Analyzing the role of strong motion rotations in the response of structures near earthquake faults, Trifunac (2009a) correlates, in a comprehensive graph, depicted in Figure 1.5, the magnitude of the earthquake, peak ground rotation of strong motion, peak ground velocity, stress drop, and drift in buildings. Strong motion near faults is qualitatively characterized by using displacement and displacement pulses, calibrated against observed fault slip and recorded strong motion (Trifunac 1993). For a strike-slip fault, therefore, two simple displacements are adopted in function of the different earthquake magnitude, to describe the fault-parallel displacement: d_N, toward the permanent static offset, and d_F, perpendicular to the fault. An important physical property of d_N and d_F functions is their initial velocity, expressed at $t = 0$, in the following way:

$$\begin{cases} \dot{d}_F \sim \dfrac{\sigma\beta}{\mu_s} \\ \dot{d}_N \sim 0.5 C_0 \dfrac{\sigma\beta}{\mu_s} \end{cases}, \qquad \textit{(1.18 a, b)}$$

with σ representing the effective stress (stress drop) on the fault surface, β the velocity of the shear waves, μ_s the rigidity of the rocks surrounding the faults and C_0 with typical values of *0.6*, *0.65*, *1.00 1.52* and *1.52* for magnitude M equal to *4*, *5*, *6*, *7* and *8*, respectively (Trifunac 1998). Since there are no strong-motion measurements of peak ground velocity at the fault surface, the peak velocities in eq. 1.18 *a* and *b* can be evaluated indirectly, in terms of the estimated stress drop σ, to check their consistency with other published results, presented in Figure 1.5, for typical values of β and μ_s. It is possible to associate large sudden rotations at the time of wave arrival, adopting the mathematical relations presented in Table 1.3, considering as the horizontal phase velocity in the ground c_g, with, $\beta < c_g < a$, here adopted equal to *1 km/s*. Finally, assuming that a typical value of the phase velocity in the building is *0.1 km/s* (Todorovska and Trifunac 2008), the order of magnitude of the expected drift in buildings can be estimated.

Looking at Figure 1.5, it is possible to observe that for large and intermediate magnitudes, large initial velocities induce damages, in terms of interstory drift, in building locate in the near field of the earthquake. Figure 1.5 suggests that large initial velocity is associated to sudden large rotations that could play a relevant role on the response of structures in the near fault region (Jalali et al. 2007, Jalali and Trifunac, 2008).

In the same Figure, four examples of recorded peak velocities during the 1966 Parkfield (Housner and Trifunac, 1967), 1971 San Fernando (Trifunac and Hudson 1971), 1994 Northridge (Trifunac et al. 1998) and 1999 Chi-Chi earthquakes (Chen et al. 2001) are reported. These examples show the motion recorded close to the moving faults but could have been as much as 20 km away from the fault slip producing the peak velocities. In order to illustrate how much can be large permanent tilts, following non-linear site response, also represented are the permanent rotations of ground (tilt) observed at the strong-motion accelerograph site on gneissic granite-diorite spine, 20 km south of the Pacoima Dam after the 1971 San Fernando (0.5°, Trifunac and Hudson 1971) and 1994 Northridge (3.5°, Graizer 2006) earthquakes.

Results from the literature, therefore, suggest that ignoring the contribution of the rotational components of strong ground motion can result in underestimated drifts in the structures deforming mainly in shear (Trifunac 2009a). This lower bound estimation neglects a series of effects, such as soil-structure interaction, dynamic effects, the contribution from permanent ground tilt, the bending deformations of the structural system, and the nonlinear response of the soil and of the structure. Considering the mutual effect of these contributions, the resulting drift could be considerably larger.

Adding the effect of a propagating excitation, resulting in differential excitation of columns in a building (Trifunac, 1997) or buildings in an urban setting (Trifunac 2009b), the complexity of the response turns out to be considerable.

CHAPTER 2.

FREE-FIELD ROTATIONS DURING EARTHQUAKES: A CLASSICAL SEMI-EMPIRICAL APPROACH

2.1 Introduction

As recalled in the previous chapter, the last few decades have seen several attempts to mathematically describe the propagation pattern of earthquake ground motion. It is generally possible when the source of the shaking is distant from the site and a dominant propagation direction can be assigned.

In the near-field of an earthquake, the distribution of impulsive stress within the source, as well as to the size of the source, leads to an earthquake excitation that varies from point to point along the soil surface (Aki and Tsujiura, 1959). The spatial variability of ground motion is also fostered by local irregularities in topography and soil inhomogeneities that may induce seismic wave scattering (e.g., Bolt et al. 1982, Faccioli and Paolucci 1990). In this region, therefore, it is generally not possible to identify predominant directions of propagation or wave types. Non-linearity and soil anisotropy, indeed, could challenge the reliability of adopting the indefinite equations of equilibrium that hold true for an elastic isotropic material. As a consequence, the rocking and torsional excitations could Moreno longer be represented by the analytical models presented in Chapter 1, and could be more severe in the near-field than in the far-field.

Studies of the wave propagation have been recently revisited with sophisticated mathematical models, capable of representing the spatial distribution of the motion as realistically as possible (e.g., Lavallée and Archuleta 2003, Evans et al. 2006, Lee and Trifunac 2009). Lavallée and Archuleta (2003) have developed a method that includes heterogeneous slip on a finite-fault and

full-wave propagation at high frequencies, as well as site-specific material properties with nonlinear soil response. Wave propagation from source to site is accounted for by using small earthquake recordings as empirical Green's functions. This procedure is capable of accounting for the regional effects of scattering, attenuation, and seismological structure. It yields a broadband (0.5–10 Hz) time history. Zerva and Zhang (1997), implemented a model to estimate a synthetic time history incorporating non-stationarity in the amplitude and frequency of the motions, and depending on earthquake magnitude, source–site distance and local soil conditions.

A similar goal is attempted numerically, with finite element techniques, for the case study of the M_W 6.3 Christchurch earthquake, as will be discussed in Chapter 3. For synthetic simulations of seismic events, over regions of several square kilometres and with models that involve millions of nodal points, to be reliable, a large computational effort, necessarily exploiting high parallelism level, is required.

The semi-empirical method presented in this chapter utilizes the synchronized measurements of translational ground motions, obtained from strong-motion dense-arrays at short distance, to provide a description of the displacement field in near source sites (e.g. Abrahamson et al.1991, Niazi 1990, Haricandran 1991). Thus, the cross-power spectrum of accelerations at nearby stations has been generally utilized to describe the spatial distribution of motion. The chapter recalls the mathematical relation between cross-correlation and the power spectrum of rotations (Castellani and Zembaty, 1996), developing a semi-empirical procedure to evaluate rotational accelerograms starting from measured translational records in closely-spaced array of instruments. Soil rotations around horizontal axes are studied through the set of records collected by closely spaced arrays of instruments at Lotung, Taiwan.

As described in Chapter 1, the direct measurement of point rotations has been recently attempted through "ad hoc" designed devices. Rotational records concerning 52 earthquakes observed at a single station in Taiwan (Liu et al. 2009) and rotations obtained through the procedure introduced herein, show a satisfactory agreement when properly normalized. Direct measurements and the present approach, thus, lead to evaluations of rotation higher than those predicted by mathematical investigations on the basis of the wave-propagation theory discussed in Chapter 1, for comparable circumstances.

2.2 Relevance of free-field rotation for building: role of the coherence and of the vertical input motion

As for the investigation of the effects on buildings, a useful quantity is the average rotation between separate points lying on the surface. This quantity is best obtained through the records of a closely spaced array of instruments. According to Jalali and Trifunac (2009), average and point rotations

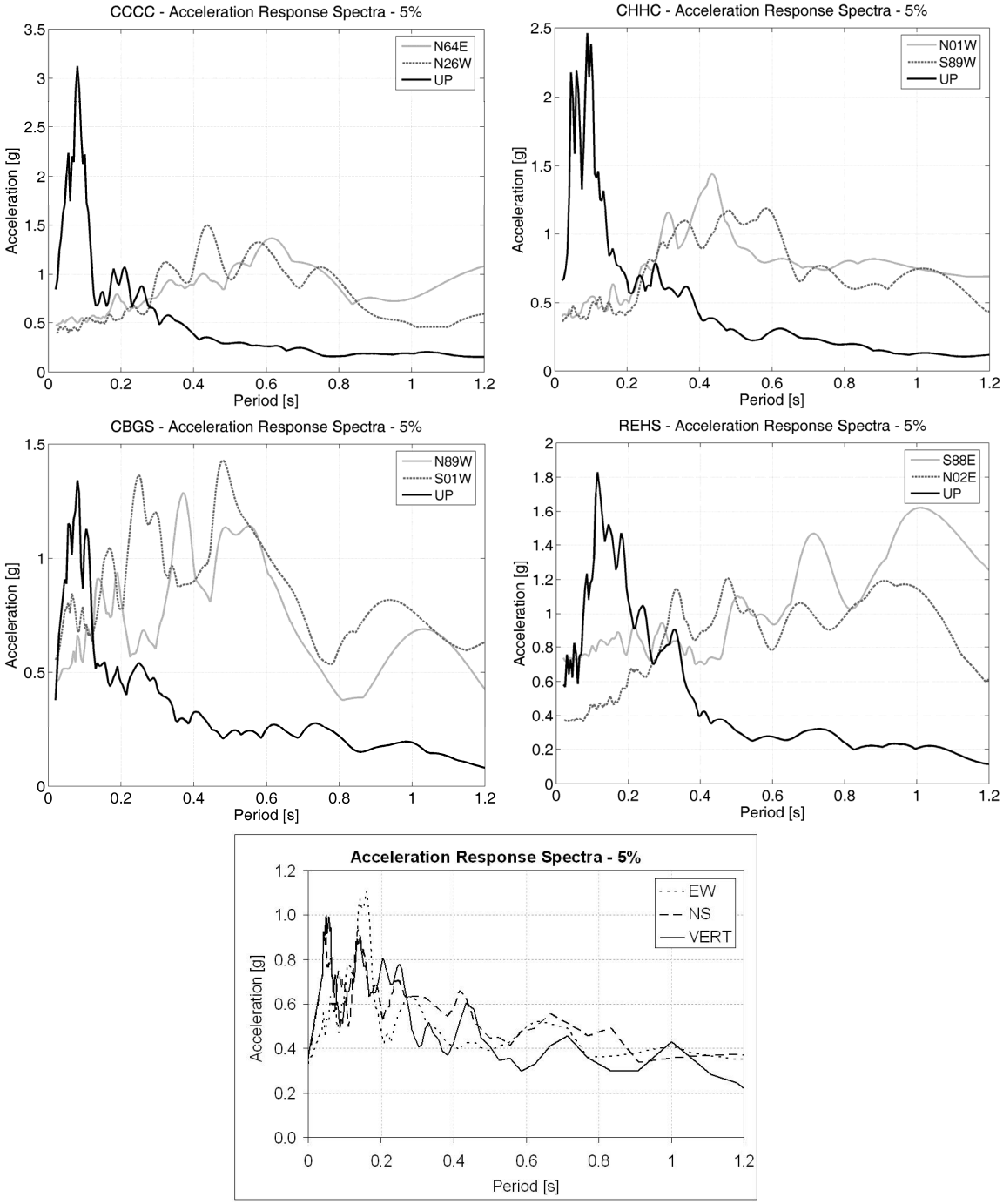

Figure 2.1. Top two rows: Acceleration response spectra for the records of four stations located in the Christchurch CBD during the event of the 22 February 2011. Bottom: Acceleration response spectra for the records collected at Station AQK during the 2009 earthquake event of L'Aquila, Italy.

should be considered at the same time, for proper formulation of dynamic response of some systems.

Considering average rotations between points at distances between 5 and 20 m, rotational acceleration shows a limited energy content at frequencies below 1 Hz, and a meaningful content in

the range of frequencies between 5 and 10 Hz. Local vibration of beams and columns, without important motion of the building centre of mass, is promoted by the high-frequency content of the rotation motion, as shown in Figure II. Overturning motion, involving horizontal displacement of the centre of mass, is provided by the low-frequency content, at frequencies around the first natural frequencies of the building, as shown in Figure II. In the limits of the present study, the second effect seems to be more important in terms of stress in structural elements (Castellani et al. 2012a).
For understanding the relevance for building structures, the procedure has two areas of concern: (i) the coherence, implicit in the cross-power spectra, which depends on the interpolation process of the original records collected by the arrays of instruments; and (ii) the relative importance of the vertical to the horizontal input motion.

As to the first item, three coherency models, taken from the literature, are compared: two of them (Harichandran and Vanmarcke 1984 and Luco and Wong 1986) are based on wave-propagation theory through random media, with parameters estimated from the analysis of experimental data. The two models provide wide differences in rotations, with all other parameters being the same. Opposing conclusions could be drawn in consequence about the relevance of rotations for structures. The third model, employed in the present application, is a coherency model experimentally obtained at the Lotung LSST and SMART-1 array, (Abrahamson 1985, 1991). It leads to results ranging between the previous two.

As for the second item, the rotation component depends on the relative importance of the vertical to the horizontal input motion. Whenever the horizontal and vertical response spectra are comparable, the effects of rotational motions on most engineering structures will be relevant. Regulations in earthquake engineering in general specify vertical soil acceleration lower than the horizontal. However, when records in an area a few kilometres from the epicentre are considered, the response spectrum of vertical motion may be comparable - and in some records even higher - than that of horizontal motion, over a large range of frequencies. This has also been observed for the 2009 earthquake event of L'Aquila, Italy, as shown in Figure 2.1, (Ameri et al. 2009, Paolucci et al 2011). Furthermore, an analysis of the records of the Christchurch, New Zealand, earthquake of 2011 (M_W 6.3) using the present procedure shows a similar trend, for the records collected within 5 to 10 km, e.g. considering the response spectra of four stations located in the Central Business District (CBD), data from http://www.strongmotioncenter.org/ (Figure 2.1). This analysis is presented in Chapter 4. One difficulty is that an apposite coherence function has not been computed as jet, and probably cannot be computed because the instruments are not arranged at distances suitable to calculate the cross correlation. Our evaluation has thus used the coherence evaluated so far by Abrahamson for the records collected by the closely spaced array of instruments at Lotung. The comparison of the coherency functions derived at Lotung are indeed in good

agreement with coherencies computed from the EPRI Parkfield array, suggesting that the Lotung coeherency functions might be applicable to other regions (Abrahamson, 1991).
Some objections have been raised about the present procedure:

i) Only few arrays are sufficiently dense to be suited to reliably obtain the cross power spectrum. A sophisticated regression analysis is employed to records to build up the cross power spectrum. Results depend strongly on the interpolation functions used in the procedure. In particular, it is difficult to infer rotational motions from translational motions using older accelerometer arrays, because they have generally low resolution and are often not conceived with an optimal geometry.

ii) Translation measurements are affected themselves by rotations (Graizer 2006, Trifunac and Todorovska 2001, Kalkan and Graizer 2007).

iii) Acceleration measurement is subject to several spurious effects. This "noise" is amplified in the mathematical elaboration, since rotation is a spatial derivative of translations. This weakness is likely to be present in point rotation instruments as well. The practical application dealt with in the present study has shown that the high frequency content of the rotation motion has little impact. However, this general comment does not apply to the near-field ground motions, where the onset of strong motions displacement is associated with powerful rotational excitations (Trifunac, 2009a).

2.3 Mathematical relation between the Cross-power spectrum and the Power spectrum of rotations

In this section, we recall the mathematical relationship, introduced some years ago, between the rotational power spectrum and the cross-power spectrum of translational accelerations simultaneously recorded in an array (Castellani and Zembaty, 1996). In this procedure, we make use of the "coherency model" to represent the spatial distribution of the ground motion. This approximation leads to manageable theoretical simplifications, although, in a number of cases, it has been equivalent to representing motions in terms of only one (equivalent) phase velocity. A method that does not require use of coherencies is the rotational Fourier spectra, as described in Lee and Trifunac 2009.
Abrahamson and colleagues (1985, 1991), reported that spatial coherency estimates are used to quantify the deterministic (coherent) and stochastic (uncoherent) parts of the strong ground motion. The analytical expression of the Abrahamson (1991) model is the following function:

$$\tanh^{-1}\left|\gamma\left(f,d\right)\right| = \left(a_1 + a_2 d\right)\left[e^{(b_1+b_2 d)f} + \frac{1}{3}f^c\right] + k\,, \qquad (2.1)$$

where f is the frequency, d is the separation distance and the model parameters are estimated a_1 = 2.54, a_2 = -0.012, b_1 = -0.115, b_2 = -0.00084, c = -0.878 and k = 0.35.

Under these premises, a relation derives directly from continuum mechanics to estimate rotation power spectrum from a cross spectrum of data recorded through a dense array. Consider a cartesian system of coordinates with axes x, y, and z, the latter being vertical, according the notation in Figure I. Let u_x, u_y, and u_z be displacements along the same axes. Continuum mechanics defines rotation of the elementary volume around the y axis, ω_y, as:

$$\omega_y = \frac{1}{2}\left(\frac{\partial u_z}{\partial x} - \frac{\partial u_x}{\partial z} \right) \qquad (2.2)$$

and shear strain γ_y as:

$$\gamma_y = \frac{1}{2}\left(\frac{\partial u_z}{\partial x} + \frac{\partial u_x}{\partial z} \right) \qquad (2.3)$$

These quantities for a soil deposit under earthquake excitation are considered. The free surface condition at the top of the deposit implies that the shear strain γ_y is zero:

$$\frac{1}{2}\left(\frac{\partial u_z}{\partial x} + \frac{\partial u_x}{\partial z} \right) = 0 ; \qquad (2.4)$$

therefore the rotation along the free surface is given, equivalently, by:

$$\begin{cases} \omega_y = \dfrac{\partial u_z}{\partial x} \\ \omega_y = -\dfrac{\partial u_x}{\partial z} \end{cases} . \qquad (2.5\ a, b)$$

The rotation component ω_x around the x axis, and the torsion around the vertical axis ω_z are defined in the same way. Let $u_{z,r}(t)$ and $u_{z,s}(t)$ be the vertical components of the free-field translational ground displacement at two points, r and s, and let d be the distance between them. The average rotation between these two points is:

$$\omega_{y,d}(t) = \frac{u_{z,r}(t) - u_{z,s}(t)}{d} . \qquad (2.6)$$

Hereinafter, the index d is implicit. The cross-power spectrum $Su_z(f, d)$ of these two signals is defined as follows:

$$Su_z(f,d) = \lim_{T\to\infty} E\left(\frac{2}{T}\left[U_{z,r}(f)\times U^*_{z,s}(f)\right]\right). \qquad (2.7)$$

where $U_{z,r}(f)$ and $U_{z,s}(f)$ are the Fourier transforms of $u_{z,r}(t)$ and $u_{z,s}(t)$, according to the following expressions:

$$\begin{cases} U_{z,r}(f) = \int_0^T u_{z,r}(t)e^{-ift}dt \\ U_{z,s}(f) = \int_0^T u_{z,s}(t)e^{-ift}dt \end{cases}, \qquad (2.8)$$

where T is the duration of the record, $U_z^*(f)$ is the conjugate of $U_z(f)$, i is the square root of (-1), and $E()$ is the expected value of the quantity in brackets. For a finite duration T, frequency f is defined at discrete values, $f_i = 2\pi i/T$. A common duration should be defined, and thus the symbol $T \to \infty$ means that T should be long enough to cover the longest duration among the records of the ensemble. The averaging procedure is extended over the set of records collected at the stations of the array. The cross-correlation function $Ru_z(\tau,d)$ of the two quantities $u_{z,r}(t)$ and $u_{z,s}(t)$ is:

$$Ru_z(\tau,d) = \int_0^\infty u_{z,r}(t)u_{z,s}(t+\tau)dt\,. \qquad (2.9)$$

Cross-power spectrum and cross-correlation are related to each other by:

$$Su_z(f,d) = \int_0^\infty Ru_z(\tau,d)e^{-if\tau}d\tau\,. \qquad (2.10)$$

The quantity $Su_z(f,d)$ is a complex number. When s tends to r, d tends to 0. $Su_z(f,0)$ is therefore a real, equivalent to the following equation:

$$Su_z(f,0) = \lim_{T\to\infty}\frac{2}{T}\left|U_{z,r}(f)\right|^2 = \lim_{T\to\infty}\frac{2}{T}\left|U_{z,r}(f)^2\right|. \qquad (2.11)$$

From the cross-power spectrum of the translation motion at two points, the "coherency" is defined by a complex number:

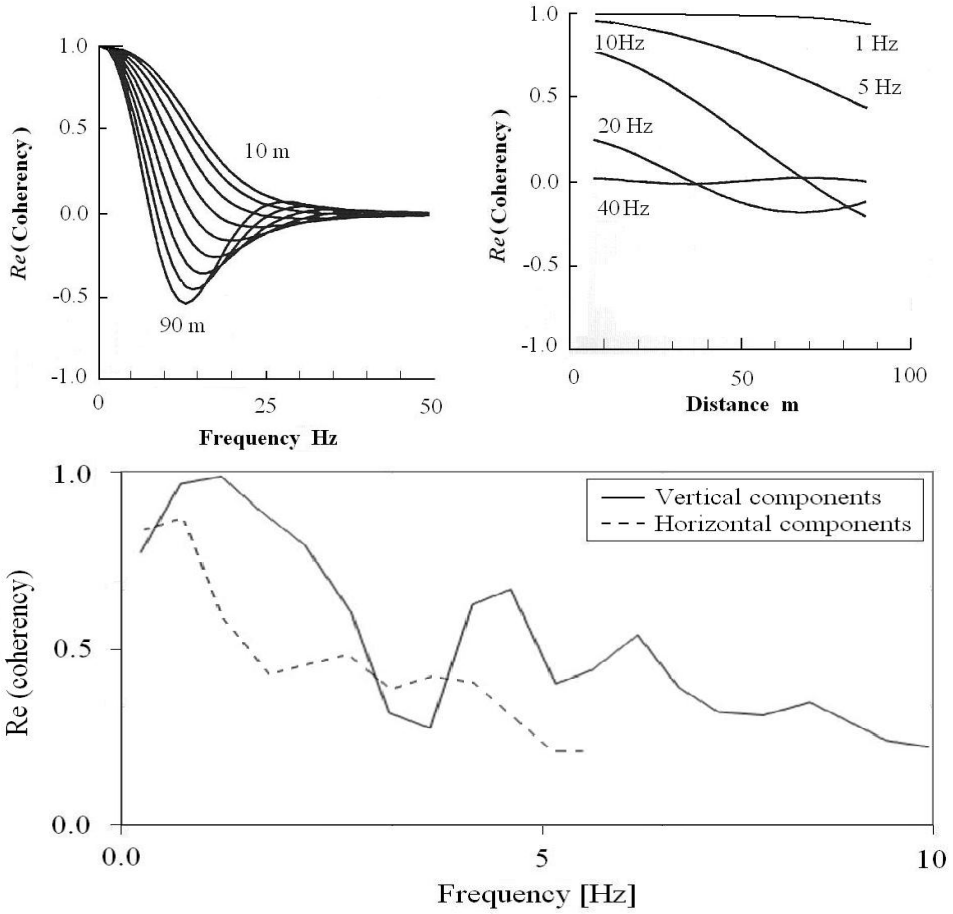

Figure 2.2. Top: Real part of the coherency, Re[γ(f, d)], as a function of frequency (Left hand side) and inter-station distance (Right hand side), for stations aligned in the radial direction. Records of acceleration have been used (from Abrahamson et al. 1991). Bottom: Coherency of vertical components and that of horizontal components, evaluated for a same set of earthquakes records at SMART-1 array, and elaborated in Abrahamson et al. 1991.

$$\gamma_{u_z}(f,d)=\frac{Su_z(f,d)}{Su_z(f,0)} \qquad (2.12)$$

The "coherency", as the cross-power spectrum, is a complex number. Figure 2.2 shows the real part of $\gamma_{uz}(f,d)$; this latter refers to the horizontal components of the ground motion, although a similar trend is expected for the vertical component (see Figure 2.2).

Considering the average rotation between the two points *r* and *s* (Eq. 2.6), the auto-correlation of this quantity is:

$$R\omega_y(\tau,0)=\int_0^{\infty}\left[\frac{u_{z,r}(t)-u_{z,s}(t)}{d}\cdot\frac{u_{z,r}(t+\tau)-u_{z,s}(t+\tau)}{d}\right]dt\,, \qquad (2.13)$$

It is possible to combine Eq. (2.9) and Eq. (2.13) in the following way:

$$R\omega_y(\tau,0)=\frac{1}{d^2}\left[2Ru_z(\tau,0)-Ru_z(\tau,d)-Ru_z(\tau,-d)\right] \qquad (2.14)$$

By applying the Fourier transform to both sides of Eq. (2.14), it is possible to obtain:

$$S\omega_y(f,0)=\frac{1}{d^2}\left[2Su_z(f,0)-Su_z(f,d)-Su_z(f,-d)\right] \qquad (2.15)$$

Introducing the "coherency" function:

$$S\omega_y(f,0)=\frac{1}{d^2}Su_z(f,0)\left[2-\gamma_{u_z}(f,d)-\gamma_{u_z}(f,-d)\right] \qquad (2.16)$$

The phase of the "coherency" is directly proportional to *d*, therefore, being *Re [ ]* the real part of the quantity under brackets:

$$\gamma_{u_z}(f,d)+\gamma_{u_z}(f,-d)=2\,\mathrm{Re}\left[\gamma_{u_z}(f,d)\right] \qquad (2.17)$$

From Eq. (2.16) and (2.17), it is possible to obtain the following relations between cross-power spectrum and power spectrum of rotation:

$$S\omega_y(f,d)=\frac{2Su_z(f,0)}{d^2}\left(1-\mathrm{Re}\left[\gamma_{u_z}(f,d)\right]\right) \qquad (2.18)$$

The power spectrum of rotational motion at a point is the limit for *d* approaching zero:

$$S\omega_y(f,0)=\lim_{d\to 0}S\omega_y(f,d) \qquad (2.19)$$

The power spectrum of rotation, $S\omega_y(f,0)$, is real. Considering the second derivatives with respect to time on both sides in the above equations, it is possible to obtain the rotational accelerations:

$$\begin{cases}\dfrac{\partial^2\omega_y}{\partial t^2}=\dfrac{\partial}{\partial x}\dfrac{\partial^2 u_z}{\partial t^2}\\[2ex] \dfrac{\partial^2\omega_x}{\partial t^2}=\dfrac{\partial}{\partial y}\dfrac{\partial^2 u_z}{\partial t^2}\end{cases}. \qquad (2.20)$$

Equations (2.18) and (2.19) were derived in terms of displacements and rotations. Analogous relations can be derived in terms of translational and rotational accelerations. Hereinafter, translational and rotational components of the ground motion will be written in terms of acceleration, since the original records are presented in the same manner. As a remark, when the function $Re[\gamma(\omega, d)]$ is computed from acceleration records, it tends to one as f tends to zero (see Figure 2.2), while this does not necessarily occur when $Re[\gamma(\omega, d)]$ is derived from displacements. Non-zero residual displacements may be present and vary from point to point. Even artificial time histories can be built with non-zero residual displacements, see Liao and Zerva (2006). In the following, all quantities are related to a coherence function $Re[\gamma(f, d)]$ estimated from acceleration records. An example of this kind of function is presented in Figure 2.2 (see Abrahamson et al. 1991).

It is possible to state that:
i) The power spectrum of rotation at a point, $S\omega(f,0)$, cannot be evaluated with this kind of procedure because the minimum separation between recording stations is some tens of meters. This establishes a distinction between the present approach and that of direct recording of rotation at a point. Nevertheless, the quantity of interest in most engineering applications is the average rotation between points at a distance d, comparable to the horizontal dimensions h of foundations.

ii) For frequencies above ~40 Hz, approaches based on "coherency" show an asymptote, set by noise, and large spectral values appear.

iii) In case of uncorrelated signals, the quantity $\gamma_{uz}(f, d)$ is close to zero, so that:

$$S\omega_y(f,d) = \frac{2Su_z(\omega,0)}{d^2}. \qquad (2.21)$$

2.3.1 Horizontal and vertical components

To explore the quality of coherency data, a major simplification is introduced. The detail of the evaluation procedure of cross-power spectra is available in the literature only for the coherency functions computed on the horizontal components, while for vertical components, similarly detailed studies are not available. Therefore, even if Eq. (2.18) applies to the vertical component of the motion, because our aim is to estimate the rotation around the horizontal axes, we decided to adopt the coherency functions computed for horizontal translational motions. The influence of this assumption can be estimated by comparing coherencies. Figure 2.2 shows a comparison between the coherency of horizontal and vertical components through data recorded with the SMART-1

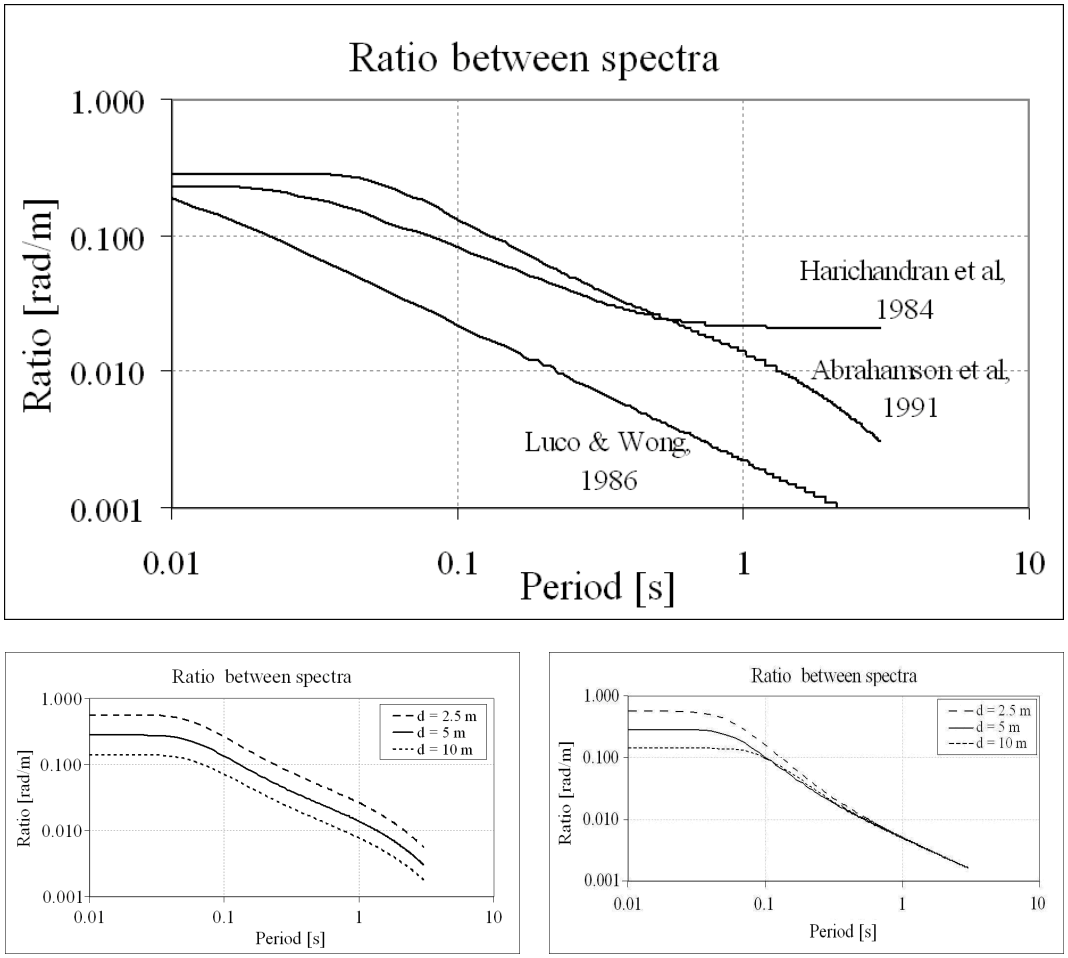

Figure 2.3. Top: Square root of the ratio between rotation and translation power spectrum according three sources of data. Separation between stations d = 5 m. Bottom: (Left hand side) Square root of the ratio between power spectra. The cross-power spectrum established by Abrahamson et al. 1991 is used; (Right hand side) The same ratio, when the power spectrum established by EPRI (1992), focused on short separations d, has been used to evaluate $Su_z(f,0)$.

array: in this case the coherency seems to be marginally higher for the vertical components. On the other hand, Kawakami and Sharma (1999) found in their study that the vertical component correlation is lower than the horizontal one. As will be shown in the next section, more substantial discrepancies might be found in the evaluation of this quantity.

2.3.2 Relevance of the interpolation function in the estimation of cross-power spectra

Figure 2.3 shows the ratio between the power spectrum of average rotation acceleration and that of translational acceleration. The quantity $S\omega(f, d)$ has dimension $[(rad/s^2)^2/(rad/s)]$, $Su_z(f, 0)$ has dimension $[(m/s^2)^2/(rad/s)]$, and consistently the square root of their ratio has dimension $[rad/m]$. We examine three sources of data respectively: (i) Abrahamson et al., 1991; (ii) Harichandran and

Vanmarke, 1984; and (iii) Luco and Wong, 1986. Being reported in logarithmic scale, the differences between these three estimates are quite significant. All of the three coherencies tend to one at low frequencies, and thus $S\omega(f, d)$ tends to zero as f decreases or T increases. Translational velocity and displacement time histories resulting from the model of Harichandran and Vanmarke (1984) exhibit more variability in their waveforms at low frequencies than that of Abrahamson et al. (1991). A lower-coherency $\gamma_{uz}(f,d)$ is the result, and thus also a higher rotation power spectrum. Luco and Wong (1986) presented an analytical cross correlation obtained by a theoretical expression of wave propagation through random media. The model yields perfect correlation at low frequencies, and hence no rotation. The cross-power spectrum between closely spaced stations is somehow affected by the wave-propagation direction according to Paolucci and Smerzini (2008), but it is only marginally affected by this direction according to the data analyzed by Abrahamson et al. (1991). In the following, we will apply the coherence data given by these last authors, and thus we will disregard the propagation direction. Figure 2.3 shows the ratio used in the applications that follow. As noted, the ratio tends to zero for increasing periods because $Re[\gamma(f, d)]$ tends to 1 as f tends to zero (Figure 2.2).

2.3.3 Dependence of the measurements on the separation distance

The report provided by the Electric Power Research Institute (EPRI) 1992 works on the same set of data examined by Abrahamson et al. 1991. Comparing the ratio spectra obtained assuming two interpolation functions, one focused on distance greater than 6 m and the second focused on distance of around 6 m, they conclude that the cross-power spectrum between closely spaced stations depends on the separation distance d between stations, especially for period above 1 s (Figure 2.3). In the present work, the quantities used to represent rotations show an increasing trend with decreasing values of d. This fact agrees with a hint obtained from other sources, that rotations at a point, measured through an apposite instrument, should be larger than average rotations retrieved with an array of translation instruments, any other parameter being the same, (e.g., Suryanto et al. 2006).

2.4 Evaluation of rotational accelerograms on the basis of measured vertical accelerograms

The relationship between rotational and vertical spectra leads to the evaluation of the rotational accelerograms, starting from measured vertical ones. The seismic event used to describe this method is the earthquake recorded in Taiwan through the SMART-1(5) array on 29/01/1981 (namely, station C00), M_L = 6.3, data available from the PEER strong motion database

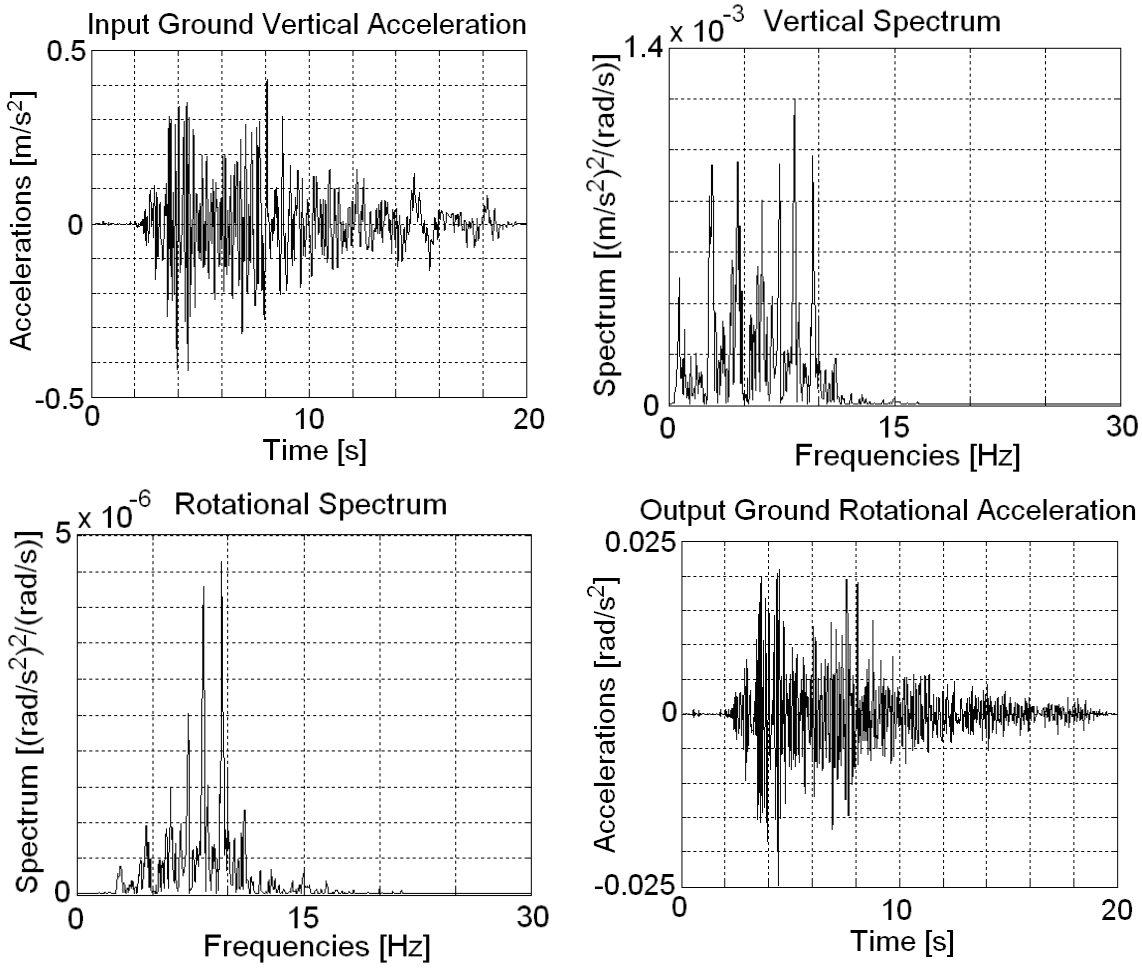

Figure 2.4. a) Vertical ground acceleration: Taiwan SMART-1(5) 29/01/1981 (M_L 6.3) (station C00); b) vertical power spectrum; c) Rotational power spectrum considering a separation distance d equal to 10 m; d) input ground rotational acceleration (d = 10 m).

(http://peer.berkeley.edu/smcat/). Its vertical input accelerogram is shown in Figure 2.4(a). The soil acceleration can be written as a Fourier series, in the conventional way:

$$\ddot{u}_z(t) = \sum_{i=1}^{N} a_i \cos\left(f_i t + \varphi_i\right), \qquad (2.22)$$

where t is time in seconds,

$$f_i = i \cdot f_1 = i \cdot \frac{2\pi}{T}, \qquad (2.23)$$

in rad/s, with T being the duration of the record,

$$a_i = \sqrt{b_i^2 + c_i^2}\ , \tag{2.24}$$

with:

$$\begin{cases} b_i = \dfrac{1}{\pi}\int_0^T \ddot{u}_z(t)\cos(f_i t)\,dt \\ c_i = \dfrac{1}{\pi}\int_0^T \ddot{u}_z(t)\sin(f_i t)\,dt \end{cases} \tag{2.25}$$

and φ_i are the phases, defined as:

$$\varphi_i = \operatorname{atan}\left(\frac{c_i}{b_i}\right) \tag{2.26}$$

The summation consists of N elements, where N is a function of the duration of the record T and of the highest frequency f_N:

$$f_N = \frac{2\pi N}{T} \tag{2.27}$$

The highest-frequency f_N depends on the time sampling rate Δt. According to the Nyquist-Shannon sampling theorem (Bendat and Piersol, 1971), it is possible to establish the relation:

$$N = \frac{T}{2\Delta t} \tag{2.28}$$

Given the input signal as a Fourier series, the vertical power spectrum, Figure 2.4(b), is obtained as:

$$S\ddot{u}_z(f) = \left(\frac{a_i^2}{\Delta f}\right) = \left(\frac{a_i^2}{2\pi / T}\right) \tag{2.29}$$

The coherency $Re[\gamma u_z(f,d)]$ used was evaluated by Abrahamson as unlagged coherence (1991), Figure 2.2. Applying the relationship between rotational and translational power spectrum, of Eq. (2.18), it is possible to write, h being the generic horizontal direction:

$$S\ddot{\omega}_h(f_i, d) = \frac{2S\ddot{u}_z(f_i, 0)}{d^2}\left(1 - \operatorname{Re}\left[\gamma u_z(f_i, d)\right]\right) \tag{2.30}$$

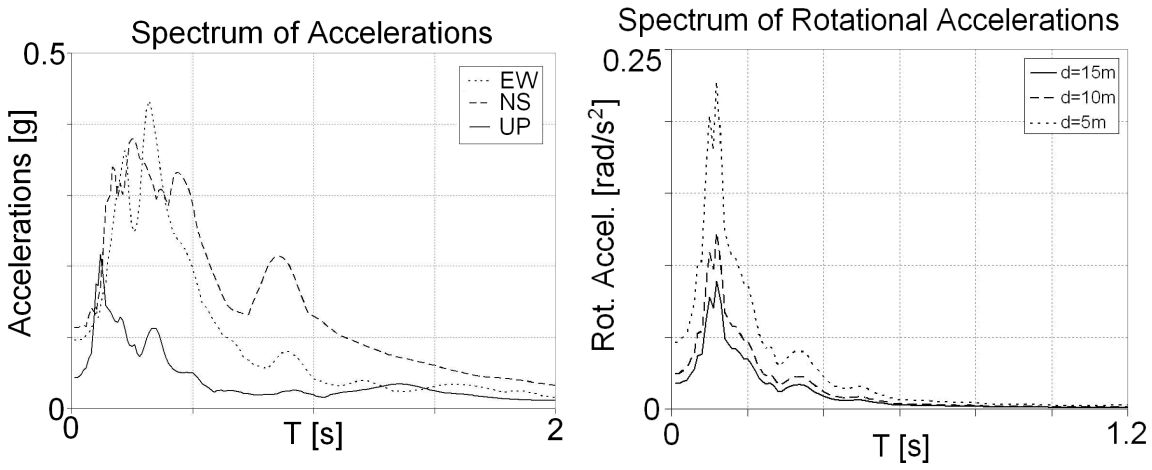

Figure 2.5. a) Response spectra of accelerations of horizontal and vertical directions, for the event TAIWAN SMART-1(5):C00; b) comparison of rotational response spectra for different values of the separation d.

Figure 2.4(c) shows the rotational power spectrum considering a separation d equal to 10 m. Once the rotational power-spectrum is obtained, it is possible to evaluate the rotational accelerogram, as a Fourier series, in the same format of Eq. (2.22).

$$\ddot{\omega}_h(t) = \sum_{i=1}^{N} k_i \cos\left(f_i t + \varphi_i\right), \tag{2.31}$$

where the amplitudes k_i are derived from the equation:

$$k_i = \sqrt{S\ddot{\omega}_h(f_i)\Delta f} = \sqrt{S\ddot{\omega}_h(f_i)\frac{2\pi}{T}}, \tag{2.32}$$

The phases φ_i are those of the original vertical acceleration. Figure 2.4(d) shows the output ground rotational accelerogram, where peak rotational values are localized at the same instants in time as the peaks of the vertical ground acceleration (around 4 and 8 s).

2.4.1 Rotational Response Spectra

Figure 2.5 shows the response spectra of translational accelerations for the same record previously analyzed, presenting the comparison of rotational response spectra for the considered input, varying the separation distance d. The rotational response spectrum is defined analogously to that introduced for the translational response spectrum, as shown in Figure 2.6.

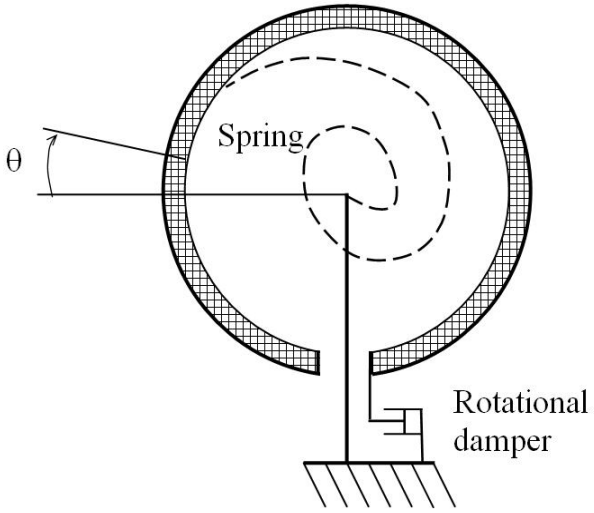

Figure 2.6. Definition of rotation response spectrum. The reference system is excited by a rotational motion. A single-degree-of-freedom rotational oscillator is shown by the crosshatched ring. The rotation response spectrum is the peak rotational acceleration, as a function of the natural period, and a given damping ratio.

For a single-degree-of-freedom oscillator, of fundamental period T, and 5% damping ratio, it represents the peak rotational acceleration of the oscillator during the earthquake's duration.
Notice that the quantities used to represent rotations show an increasing trend with decreasing values of d. This fact agrees with a hint obtained from other sources, that rotations at a point should be larger than average rotations retrieved with an array of translation instruments (Suryanto et al. 2006), as stated in Section 2.3.3.

2.4.2 Results and comparison with available measured data

A number of seismic events used in the analysis, recorded at Taiwan SMART1(5) and Taiwan SMART1(33), are identified in Table 2.1. For each record, the rotation time history of acceleration, and that of velocity, have been computed according to the previously described procedure. Data retrieved with the present approach are comparable and in satisfactory agreement with the direct measurements of Liu et al., 2009. Data presented by Liu and colleagues, concerning 52 earthquake events recorded at a single station in Taiwan, are presented in Figure 2.7 in terms of the ratio between peak ground rotational velocity (PRV) over the peak ground horizontal acceleration (PGA). The peak rotation velocity (PRV) is the maximum among the three components, and the peak ground horizontal acceleration (PGA) is the maximum between the two horizontal components. This ratio is dependent on dimensions, however the peak ground rotation velocity (PRV) is more suited to represent rotations than peak ground rotation acceleration, which may largely depend on noise. This ratio is dependent on the dimensions, however the peak ground rotation velocity (PRV) is more suited to represent rotations than peak ground rotation

Table 2.1. Peak rotation velocity PRV and the peak horizontal acceleration PGA. PRV is the maximum among the three components, assuming d = 10 m. PGA is the maximum between the two horizontal components.

Earthquake	Ep. Dist. [km]	PRV [mrad/s]	PGA [m/s2]	PRV/PGA [(mrad s)/m]
SMART-1(5): C00	30.31	1.265	1.102	1.15
SMART-1(5): O07	28.96	0.946	0.798	1.19
SMART-1(5): O01	31.99	1.296	0.997	1.30
SMART-1(33): C00	44.93	0.913	0.636	1.43
SMART-1(33): O07	44.73	0.634	0.517	1.23
SMART-1(33): O01	45.10	0.691	0.569	1.22
SMART-1(33): M07	44.95	1.054	0.690	1.53
SMART-1(33): I01	44.94	1.563	1.085	1.44

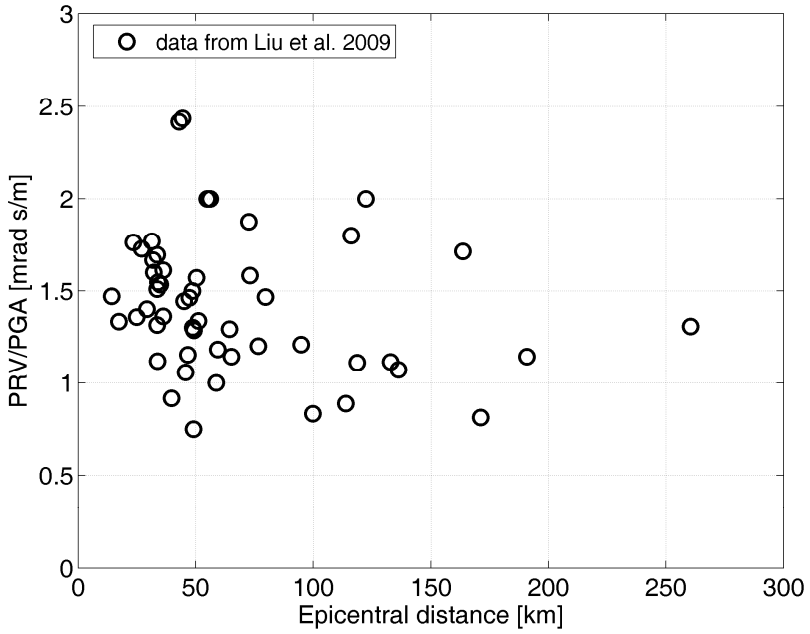

Figure 2.7. Elaboration of data presented by Liu et al. 2009. Ratio between the peak rotation velocity PRV and the peak horizontal acceleration PGA, in [mrad s/m] as a function of the epicentral distance. Average value 1.43.

acceleration, which may largely depend on noise. The ratio is shown as a function of the distance from the epicentre.

According to Figure 2.7 the set of data analysed does not identify a correlation between the PRV/PGA ratio and the distance from epicentre. However, no one record is referring to a distance equal or less to the focal depth, and only 18 refer to a distance less than 1.5 the focal depth. Consistently, in this set of translation data, much higher amplitudes are noticed for the peak horizontal components than that for the vertical component. In consequence, this data, which is the richest available so far, does not provide clear information for the recurrent conjecture that in the near field rotations might be higher, for the same peak ground horizontal acceleration.

The average value of the ratio for the data presented by Liu et al. (2009) is 1.43, while that of Table 2.1 is 1.31. The first group of data are point rotations, while those in Table 2.1 are rotations between points separated by d = 10 m. Bearing in mind the dependence of rotations on the separation, it can be noted that the two sets of data are in satisfactory agreement. In Chapter 4, an analysis of the records of the Christchurch earthquake of 2011 is discussed using the present procedure.

2.5 Concluding remarks

Liu et al. (2009) provide the largest set of experimental data available so far for rotation (Figure 2.7). This chapter presents a computational procedure that predicts rotations starting from measured translations, in good agreement with this available data-set (Table 2.1). The data reported by Liu and colleagues and our predictions are more severe than those resulting from previous studies related to the wave-propagation theory (Todorovska and Trifunac 1992, Castellani and Boffi 1986, 1989). Combining these results we can conclude, even within the limit of the present study:

i) The rotational effects about horizontal axis depend on amplitude of the response spectrum of the vertical component in the long-period range. Figure 2.5 shows the acceleration spectra for one of the events analyzed in our study and Figure 2.1 shows the response spectra of records collected at L'Aquila during the 6 April 2009 event, at a station located a few kilometres from the epicentre, and at four stations located in the Christchurch CBD, during the event of the 22 February 2011. The response spectrum of vertical motion, in the range of periods of interest in the present investigation, is comparable to that of horizontal motion. Important rotational effects can be expected in these circumstances.

ii) In processing the data, this approach points out the necessity of a further discussion of the interpolation function in the elaboration of cross-power spectra of translations, which is linked to the spacing of the instruments within the array.

CHAPTER 3

A CHALLENGING CASE STUDY: THE M_W 6.3 CHRISTCHURCH EARTHQUAKE ON 22 FEBRUARY 2011, NEW ZEALAND

3.1. Introduction

A reliable description of the spatial variability of strong-ground motion, fully taking into account at the same time translational and rotational components, can be obtained through large-scale 3D simulations of seismic-wave propagation, able to include the mutual effects of seismic source, shallow crustal model and near-surface complex geological and topographical irregularities. In this chapter, a meaningful case-study of the Christchurch earthquake is presented, where the exceptionally high vertical accelerations recorded, together with a widespread liquefaction, suggest that rotational motions could have played a crucial role in the overall damage of the city and especially in its densely urbanized Central Business District (CBD). This chapter is therefore devoted to introducing the case study, to the three-dimensional model realized including its dependence on the kinematic source and on the basin geometry, and to validate the model with reference to the available recorded data.

Almost six months after the M_W 7.1 Darfield (Canterbury) earthquake, on 22 February 2011, an earthquake struck the city and the suburbs of Christchurch, the largest city in the South Island of New Zealand, with about 400,000 inhabitants. Several discussions ensued about the effective magnitude of the event, with estimates ranging from M_W 6.1 up to M_W 6.3. For the purposes of this work, the magnitude that was released first, M_W 6.3, is used, even though the scientific community eventually agreed on M_W 6.2 at the end of 2011. In any case, the Christchurch earthquake can be

Table 3.1. Peak ground acceleration (PGA) and peak ground velocity (PGV) values recorded for the stations within a 40 km radius of the epicentre. Stations located on rock are in italics (data from CESMD, Center for Engineering Strong Motion Data: http://www.strongmotioncenter.org/; band-pass filter transition bands are 0.1-0.25 Hz and 24.50-25.50 Hz). R_e denotes the epicentral distance.

Stations Name	Id	R_e	PGA EW	PGA NS	PGA UP	PGV EW	PGV NS	PGV UP
		[km]	[g]	[g]	[g]	[cm/s]	[cm/s]	[cm/s]
Heathcote Valley Primary School	*HVSC*	*1*	*1.230*	*1.261*	*1.466*	*79.96*	*89.12*	*38.51*
Lyttelton Port Company	*LPCC*	*4*	*0.919*	*0.771*	*0.413*	*37.27*	*40.97*	*16.43*
Pages Road Pumping Station	PRPC	6	0.665	0.589	1.629	82.26	74.83	49.48
Christchurch Cathedral College	CCCC	6	0.415	0.375	0.692	64.75	43.58	21.53
Christchurch Cashmere High School	CMHS	6	0.369	0.403	0.796	41.69	46.79	15.17
Christchurch Resthaven	REHS	8	0.719	0.372	0.529	87.30	45.54	21.29
Christchurch Hospital	CHHC	8	0.357	0.337	0.511	65.17	56.58	20.87
Christchurch Botanic Gardens	CBGS	9	0.536	0.432	0.271	63.95	43.12	13.42
Shirley Library	SHLC	9	0.324	0.319	0.500	52.73	51.74	21.73
Hulverstone Drive Pumping Station	HPSC	9	0.232	0.155	0.858	36.21	26.75	33.93
Riccarton High School	RHSC	12	0.297	0.254	0.188	29.95	23.63	12.11
Christchurch Papanui High School	PPHS	12	0.187	0.243	0.195	36.73	28.24	16.82
Styx Mill Transfer Station	SMTC	14	0.182	0.144	0.176	28.55	20.49	12.31
McQueens Valley	*MQZ*	*15*	*0.147*	*0.098*	*0.072*	*7.10*	*5.44*	*4.05*
Christchurch Canterbury Aero Club	CACS	18	0.182	0.180	0.185	15.85	13.88	11.84
Lincoln Crop and Food Research	LINC	19	0.081	0.164	0.084	7.59	16.17	5.41
Templeton School	TPLC	19	0.091	0.099	0.136	10.36	10.09	8.16
Kaiapoi North School	KPOC	23	0.211	0.201	0.057	14.19	19.39	5.71
Rolleston School	ROLC	26	0.164	0.163	0.072	6.30	7.77	4.28
Swannanoa School	SWNC	29	0.251	0.143	0.056	14.69	13.94	4.73
Selwyn Lake Road	SLRC	33	0.086	0.088	0.049	7.25	8.32	2.92
Ashley School	ASHS	35	0.088	0.076	0.037	7.28	5.44	2.30
Cust School	CSTC	39	0.075	0.078	0.042	6.46	6.71	3.09

considered one of the greatest natural disasters recorded in New Zealand. The death toll was over 180 people, with around 2,000 injured, and the civil engineering structures, already weakened by the Darfield event and its aftershocks, badly affected (Cubrinovski and Green 2010; Tonkin & Taylor 2010; Kam et al. 2011). The earthquake was generated by an oblique thrust fault located between the Australian and Pacific Plates, less than 6 km from the city centre. It is worth recalling that prior to the Darfield event there was no surface evidence of the fault that generated the Christchurch earthquake on February 2011, nor of the Greendale Fault, recognized as responsible of the September 2010 earthquake (Quigley et al. 2010). During the past decade a set of seismic surveys across the Canterbury Plains have been carried out (Green et al. 2010), but they did not reveal any convincing evidence of the Greendale Fault, and there was no clear indication that a major earthquake was imminent in this particular region. Beyond the effects and the consequences of the seismic event, attention of the scientific community was drawn to two aspects that had a primary role in the Christchurch earthquake: (i) the extremely severe strong ground-shaking observed, especially on the vertical component, and (ii) the widespread liquefaction phenomena across the city (Cubrinovski and Green 2010, Green et al. 2011).

Between September 2010 and June 2011, the Canterbury area experienced three major earthquakes, all with $M_W \geq 6.0$, and a large number of aftershocks (Gledhill et al. 2011, Bannister et al. 2011) as

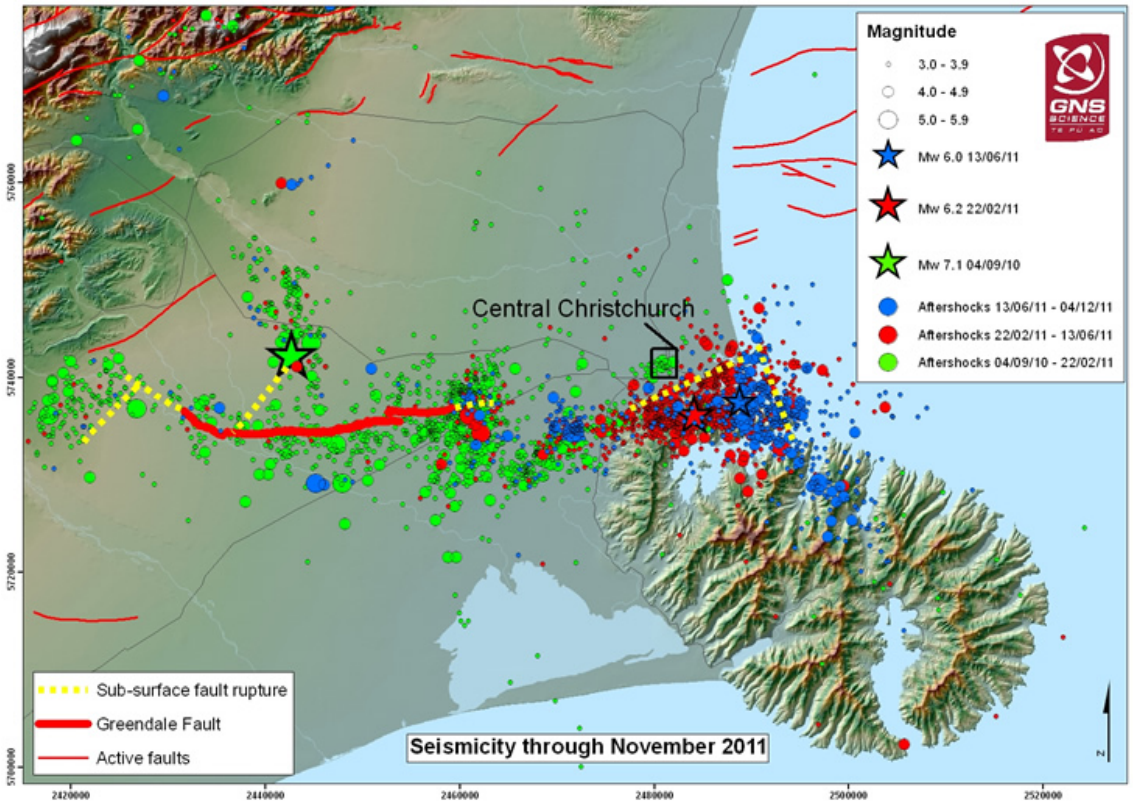

Figure 3.1. Aftershocks map of the Christchurch sequence from GNS website updated November 2011. Stars refer to events with $M_W \geq 6.0$.

depicted in Figure 3.1 by the aftershock map (Institute of Geological and Nuclear Sciences - GNS available at http://www.gns.cri.nz/ Home/ News-and-Events/ Media-Releases/ Most-damaging-quake-since-1931/ Canterbury-quake/ Recent-aftershock-map/). The Christchurch earthquake was recorded by several digital stations of the permanent network operated by the GNS (data available at the GeoNET Data Centre: http://www.geonet.org.nz/). Peak ground motion accelerations in the epicentral region of the earthquake ranged up to 1.261 g, on the horizontal component, and up to 1.629 g, on the vertical component. Table 3.1 shows a list of the accelerometric stations located within a 40 km radius from the epicentre with the corresponding values of Peak Ground Acceleration (PGA) and Peak Ground Velocity (PGV) on both horizontal and vertical components (data from CESMD, Center for Engineering Strong Motion Data: http://www.strongmotioncenter.org/; band-pass filter transition bands are 0.1-0.25 Hz and 24.50-25.50 Hz).

The ground-accelerations recorded within the city of Christchurch are among the largest ever recorded for a New Zealand earthquake, with exceptionally high vertical ground acceleration (Bradley and Cubrinovski, 2011). The unusual severity of the ground-shaking can be explained as a combination of four major effects: i) the proximity of the causative fault to the city, ii) the

directivity of ground motion towards the urban area, iii) the strong amplification effects of the soft alluvial sediments beneath the city, and iv) the hanging wedge effect, causing a significant increase of ground shaking on the hanging wall.

The availability of this unprecedented dataset of near fault strong ground motion, combined with the peculiar geological configuration of the Christchurch area, makes the Christchurch earthquake a relevant benchmark to test the effectiveness of three-dimensional numerical tools for the prediction of the variability of strong ground motion in near fault conditions (Guidotti et al. 2011). To this end, numerical simulation of seismic wave propagation within the Canterbury Plains, extending from the north-western Alps mountain range to the south-eastern Lyttelton-Akaroa volcanic region, was performed through the software package GeoELSE (http://geoelse.stru.polimi.it). Based on the Spectral Element formulation proposed by Faccioli et al. (1997), GeoELSE is designed to perform linear and non-linear dynamic wave propagation analyses in heterogeneous media, exploiting in 3D its implementation in parallel computer architectures. Examples of application of GeoELSE to seismic wave propagation studies in complex geological configurations can be found in Stupazzini et al. (2009a) and Smerzini et al. (2011). Different three-dimensional numerical models were constructed for the Christchurch earthquake, to check the dependence of the results on: i) the kinematic source model, based on the information retrieved from recent seismic source inversion studies and ii) the shape of the alluvial-bedrock interface within the Canterbury Plains. To check the accuracy of the numerical models, the synthetic results are compared against the strong ground motion records. The misfit between simulated and recorded waveforms is evaluated in a quantitative way, in a format suitable for engineering applications, making use of the criteria proposed by Anderson (2004). To give insights into the variability of surface earthquake ground motion, due to the interaction between near fault conditions and strong geological variations, ground shaking maps and snapshots of the velocity wavefield are shown.

3.2. Geology of the Christchurch region

The area under study extends from the north-western Alps mountain range to the south-eastern Lyttelton-Akaroa volcanic region and includes the city of Christchurch, part of the Canterbury Plains and of the Banks Peninsula. Information about the geology of such area comes from the 1:250,000 geological map of Christchurch, produced by the GNS (Forsyth et al. 2008) and sketched in Figure 3.2. Based on the geological map and on the available cross-sections, it was possible to infer a preliminary stratigraphy for the alluvial cover, filling the Canterbury Plains in the area of interest. The basement rock of the whole region is the Torlesse composite terrane, a deformed package of Carboniferous to Cretaceous sedimentary rocks. Late Miocene volcanism forms the two major overlapping volcanoes Lyttelton and Akaroa of Banks peninsula, today largely eroded.

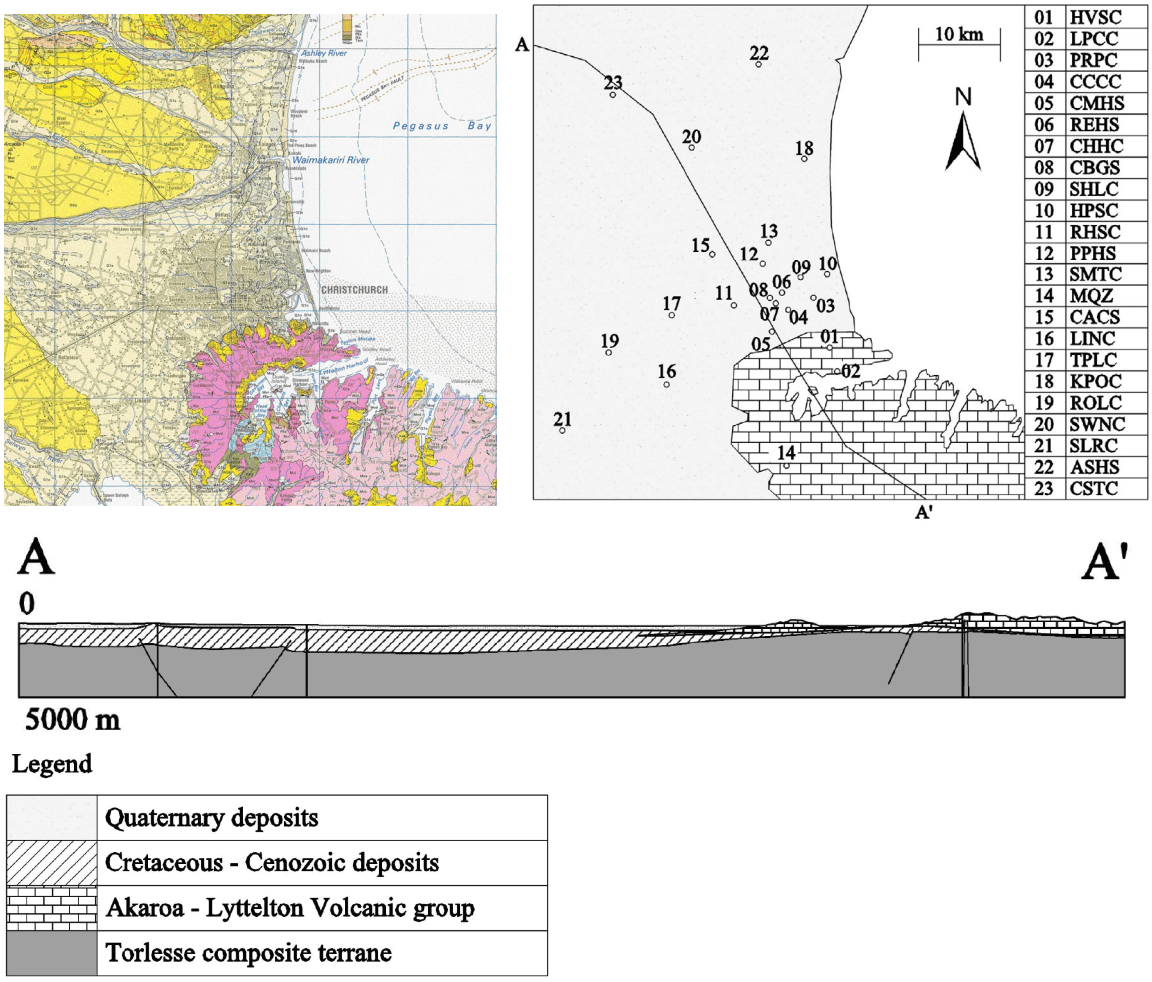

Figure 3.2. Top: (Left hand side) Geological map of parts of the Canterbury Plains and Banks Peninsula from Forsyth et al. 2008. Yellow tones indicate alluvial soil, pink ones outcropping rock; (Right hand side) Corresponding schematization of the area for the model under study, along with the strong ground motion stations. Bottom: geological A-A' cross-section.

Erosion of the shallow landmass and glacial-interglacial climatic fluctuations led to the widespread decomposition of unconsolidated Quaternary sediments that constitute the Canterbury Plains. The alluvial sequence is formed by coal, clay, limestone and sand (Forsyth et al. 2008).

As far as the deep crustal model is concerned, it is possible to consider it as basin sediments overlying a layer of Torlesse graywacke down to around 5 km, overlying, in turn, a layer of Haast Schist down to around 20 km depth. The lower crust is interpreted as mafic (diorite, diabase, and gabbro) Mesozoin ocean crust (Reyners and Cowan 1993; Godfrey et al. 2001; Godfrey et al. 2002, Melhuish et al. 2005). This deep crustal layer subdivision is confirmed by the high-resolution seismic wide-angle data, collected within the framework of the South Island Geophysical Transect (SIGHT) experiment (Kleffmann et al 1998; Mortimer et al. 2002; Long et al. 2003; Scherwath et al. 2003).

3.3 1D Analytical transfer function for the Canterbury Plains

Although the three-dimensional analysis is the better way to properly describe the spatial variability of the seismic response, it is worth to underline the importance of a one dimensional analysis (1D), in particular in the preliminary assessment of the mechanical characteristics of the three-dimensional model. In this section the analytical expression to evaluate the transfer function for a system of N layers over half-space is recalled from Faccioli and Paolucci (2005), describing the theoretical approach to the problem of wave propagation. The specific case of the Canterbury Plains is then taken into account evaluating the one-dimensional analytical Transfer Function considering the system of four layers over bedrock and proper viscous-elastic damping.

3.3.1 Transfer function for a system of N layers over elastic half-space

Let us consider the system of N plain, parallel layers depicted in Figure 3.3, subject to the vertical incidence of a harmonic wave from half-space. The N layers are characterized by different values of shear wave velocity β and density ρ. An infinite depth is assumed for the elastic half-space. Being z_j the local 1D reference system, the horizontal displacement in the j^{th} layers is given by the following expression:

$$v_j\left(z_j,t\right) = A_j \cdot e^{i\omega\left(t+\frac{z_j}{\beta_j}\right)} + B_j \cdot e^{i\omega\left(t-\frac{z_j}{\beta_j}\right)}. \qquad (3.1)$$

The problem has thus $2N+1$ unknowns, that can be evaluated by imposing the continuity conditions of displacement and shear stress at the N interfaces, together with the condition of zero stress on free surface:

$$\begin{cases} v_j\left(z_j = H_j, t\right) = v_{j+1}\left(z_{j+1} = 0, t\right) \\ \rho_j \beta_j^2 \left.\dfrac{\partial v_j}{\partial z_j}\right|_{z_j = H_j} = \rho_{j+1}\beta_{j+1}^2 \left.\dfrac{\partial v_{j+1}}{\partial z_{j+1}}\right|_{z_{j+1}=0} \\ \rho_1 \beta_1^2 \left.\dfrac{\partial v_1}{\partial z_1}\right|_{z_1=0} = 0 \end{cases}. \qquad (3.2\ a, b, c)$$

Introducing the impedance ratio equal to:

$$\eta_j = \frac{\rho_j \beta_j}{\rho_{j+1}\beta_{j+1}}, \qquad (3.3)$$

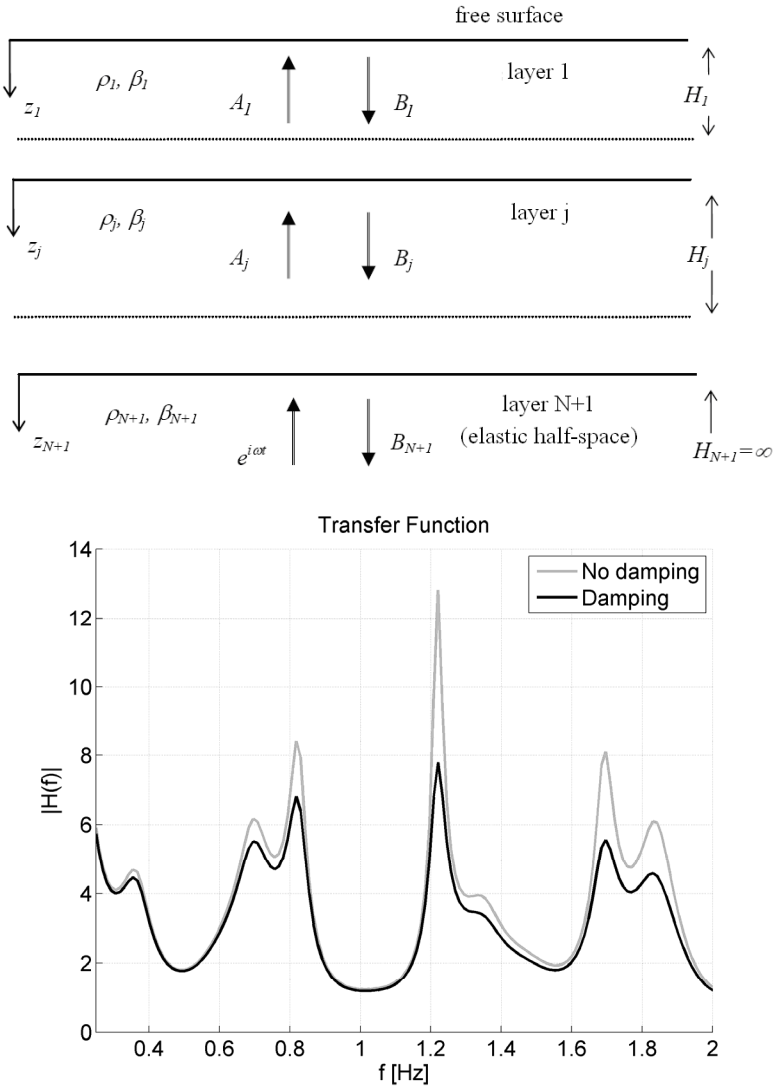

Figure 3.3. Top: Considered model of N plain, parallel layers with different mechanical properties; Bottom: 1D Analytical transfer function for the system of 4 layers of the Canterbury Plains, assuming either viscous-elastic damping or no damping. Mechanical characteristics of each layer are listed in Table 3.2.

it is possible to write the following equations:

$$\begin{cases} A_j \cdot e^{\frac{i\omega H_j}{\beta_j}} + B_j \cdot e^{-\frac{i\omega H_j}{\beta_j}} = A_{j+1} + B_{j+1} \\ \eta_j \left(A_j \cdot e^{\frac{i\omega H_j}{\beta_j}} - B_j \cdot e^{-\frac{i\omega H_j}{\beta_j}} \right) = A_{j+1} - B_{j+1} \\ A_1 = B_1 \end{cases} . \qquad (3.4\ a, b, c)$$

A recursive relation is obtained by solving this system of equations. It establishes a mathematical connection between the displacement amplitude at free surface and in the generic n^{th} layer. By defining the propagation matrix D as:

$$[D]=\begin{pmatrix} d_{11} & d_{12} \\ d_{21} & d_{22} \end{pmatrix}=[D_N]\cdot[D_{N-1}]\cdot\ldots\cdot[D_1]=\prod_{j=1}^{N}[D_j], \qquad (3.5)$$

it is possible to write:

$$\begin{Bmatrix} 1 \\ B_{N+1} \end{Bmatrix}=[D]\begin{Bmatrix} A_1 \\ B_1 \end{Bmatrix}. \qquad (3.6)$$

Applying the condition of zero stress at free surface it is possible to obtain:

$$A_1 = B_1 = \frac{1}{d_{11}+d_{12}}. \qquad (3.7)$$

The displacement at free surface is hence given by:

$$v_1(z_1=0,t)=\frac{2}{d_{11}+d_{12}}\cdot e^{i\omega t}. \qquad (3.8)$$

This represents, without consideration for the harmonic time dependence, the analytical transfer function of the system of N layers over half-space, in respect to the vertical incidence of waves. Under the hypothesis of viscous-elastic damping, it is possible to obtain the same results by substituting the shear wave velocity β with the corresponding value β^*, given by the following expression:

$$\beta^* = \beta(1+i\zeta), \qquad (3.9)$$

where ζ represents the internal damping factor, inversely proportional to the quality factor Q:

$$\zeta = \frac{1}{2Q}. \qquad (3.10)$$

3.3.2 Transfer function for the Canterbury Plains model

Let us consider now the specific case of the Canterbury Plains model. A horizontally layered soil was assumed for the one-dimensional simulation, adopting, when possible, the same mechanical characteristics of the three dimensional model. The soil model consists of four different layers over half-space with shear wave velocity $\beta = V_S$ varying from 300 m/s in the top 300 m, to 1,000 m/s between 300 and 750 m, and to 1,500 m/s at the interface between the alluvial soil and a stiffer material, with V_S equal to 2,890 m/s and the depth up to 5 km. With regard to the elastic half-space, a value of V_S equal to 3,465 m/s was adopted with infinite depth. The mechanical characteristics of the volcanic rock, adopted only in the 3D model, are also listed in Table 3.2, together with the density ϱ and with the quality factor Q of each layer. Exploiting the mathematical relations presented in the previous section it is possible to evaluate analytically the transfer function for the four layers over half-space 1D soil model considered. Its representation, in the range of frequency of interest, is given in Figure 3.3, with or without the hypothesis of viscous-elastic damping. Within the limitations of a 1D representation, the transfer function evaluated in this way allows us to preliminarily assess the resonance frequencies at about 0.35, 0.7, 1.2 and 1.7 Hz, in good agreement with the recorded values, as will be discussed in Section 3.6.

Despite of the limitations intrinsic in a one-dimensional representation, the proposed approach allows us to make a preliminary assessment of the resonance frequencies of the system in a fast and rather simple way and to compare it with available data. In the absence of direct measurements or detailed knowledge of the soil structure, but with a huge amount of data recorded from different earthquakes, as in the specific case of the Canterbury Plains, this assessment turns out to be particularly useful in the assignment of the mechanical properties to each layers, in terms of wave shear velocity, density and depth. In this way it is possible to provide a three-dimensional analysis of a reliable set of mechanical parameters, avoiding, or at least strongly reducing, complex and time-consuming iterations.

3.4. 3D Numerical simulations of the seismic response of the Canterbury Plains

The three-dimensional numerical simulations comprise the following features: (i) kinematic description of the close-by seismic source (ii) horizontally layered deep geological model, (iii) a simplified but realistic description for the Cretaceous-Cenozoic alluvial Canterbury Plains, and (iv) a linear visco-elastic soil behaviour. Note that in these preliminary analyses we considered a relatively rough model for the soil behaviour, by assuming a linear-visco elastic constitutive law, with a quality factor Q proportional to frequency (further details about the implementation of the visco-elastic soil behaviour can be found in Stupazzini et al., 2009a). Different three-dimensional

Table 3.2. Soil profile adopted in the numerical simulations. The top three layers constitute the Canterbury Plains.

Layer	Depth [m]	Thickness [m]	V_p [m/s]	V_s [m/s]	ϱ [kg/m³]	Q
1	0 - 300	300	600	300	1700	70
2	300 - 750	450	1870	1000	2000	100
3	750 - 1500	750	2800	1500	2300	100
4	1500 - 5000	3500	5000	2890	2700	200
5	0 - 5000	5000	5500	3175	2600	200
Half-space	5000 - 20000	15000	6000	3465	2700	250

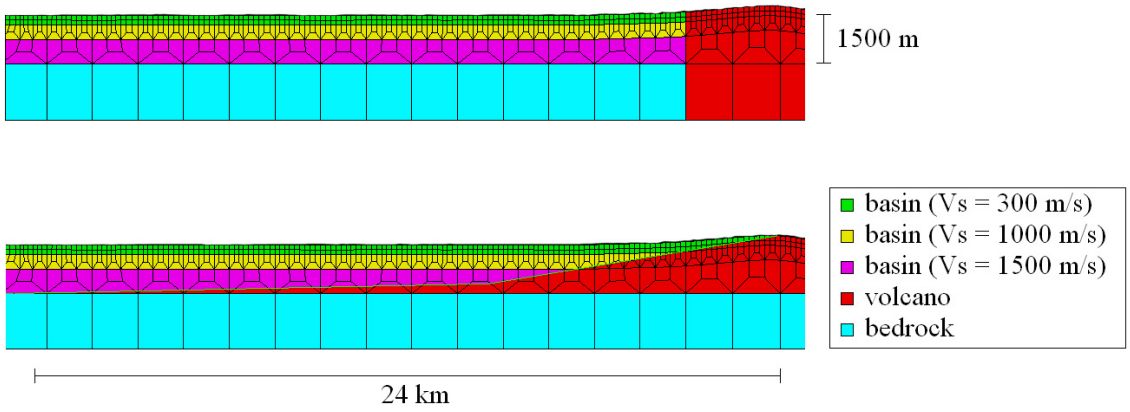

Figure 3.4. Sketch of the "step-like" (top panel) and "smooth" (bottom panel) model, referred to as an approximation of the transition between the soft sediments of the Canterbury Plains and the rigid volcano materials. Note that the alluvial basin has a maximum thickness of 1.5 km and consists of three horizontal layers with V_s ranging from 300 m/s to 1,500 m/s.

numerical models were built for the Christchurch earthquake, in order to achieve the best fit with the ground motion observations, combining: (i) two different kinematic seismic fault solutions, based on recent seismic source inversion studies, and (ii) two simplified models for the shape of the interface between the alluvial soft soil sediments and the rigid volcanic materials. The 3D model of the region of the South Island of New Zealand covers an area of approximately 60x60x20 km around the city of Christchurch, including the information available in the geological map and the 2D cross-sections, shown in Figure 3.2 and described in the Section 3.2.

Two different models were constructed to approximate the complex geological configuration of the Canterbury Plains. The models, referred to as "step-like" and "smooth" hereafter, basically differ in the transition between the alluvial soft sediments and the rigid volcanic materials, as sketched in Figure 3.4. In the "step-like" model (Figure 3.4, top panel), a rough approximation of the alluvial-bedrock shape is adopted. More specifically, the thickness of the alluvial basin is assumed to be 1.5 km and constant across the whole area under study. Instead, in the "smooth" model, the shape of the interface between the soft soil and the volcanic materials is improved, with constraints inferred from the topography of the volcano (Figure 3.4, bottom panel). For both models, the alluvial basin

Table 3.3. Kinematic source parameters adopted for the simulation of the 22 February 2011 Christchurch earthquake. V_R denotes the velocity rupture and τ the rise time.

	Hypocenter [°N, °E, Z]	L x W [km]	Strike [°]	Dip [°]	Rake [°]	Depth of upper points [km]	V_R [km/s]	τ [s]
INGV	-43.58°N, 172.68°E, -10.3 km	14 x 10	45	67	145	1.5	2.4	0.9
GNS	-43.56°N; 172.70°E; -6.47 km	18 x 9	58	68	145	1	2.4	0.9

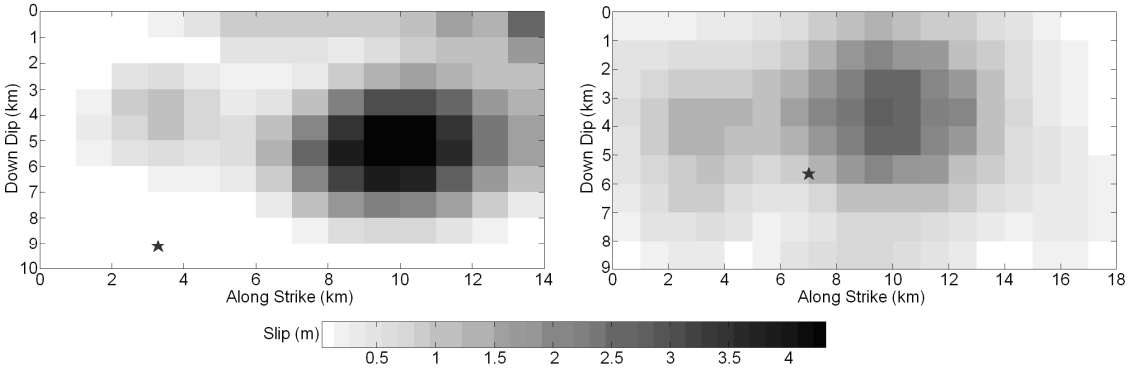

Figure 3.5. Slip distribution according the INGV (left hand side) and the GNS (right hand side) fault solution. The superimposed star denotes the hypocenter location.

consists of three different layers with V_S ranging from 300 m/s in the top 300 m to 1,500 m/s at the interface with the volcanic materials (top three layers of Table 3.2). In absence of direct measurement for the considered area, V_S values adopted are in reasonable agreement with available geotechnical data and engineering geological models, although in a different region of New Zealand (Boon et al. 2011, Semmens et al. 2011). The volcanic region (layer 5 in Table 3.2), with V_S = 3,175 m/s, extends down to a maximum depth of 5 km. Regarding the background geology, a horizontally layered crustal model was assumed, as summarized in Table 3.2 (layers 4 and "half-space"). The frequency proportional quality factor Q values given in Table 3.2 correspond to a frequency f equal to 0.67 Hz, according to the following equation:

$$Q(f) = Q_0 \frac{f}{f_0}, \qquad (3.11)$$

where $Q_0 = \pi f_0/\gamma$, γ is an attenuation parameter and f_0 is a reference value representative of the frequency range to be propagated, herein equal to 2 Hz (Stupazzini et al., 2009a).

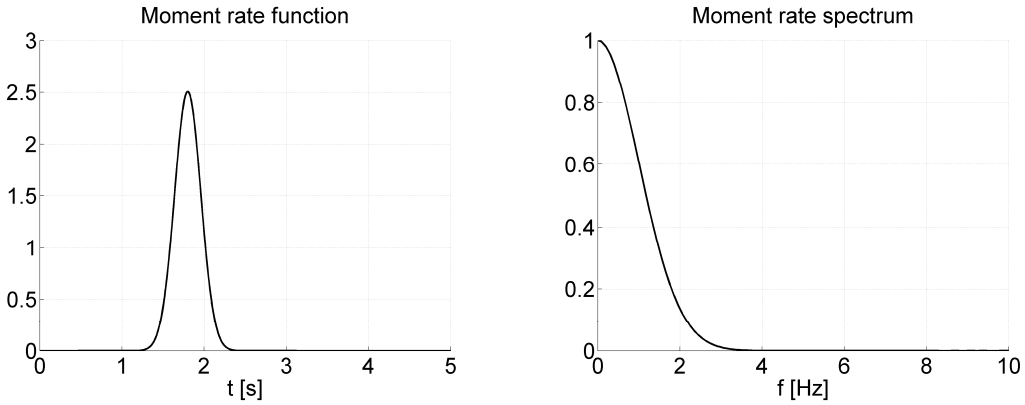

Figure 3.6. Adopted moment rate function (left hand side) and its spectrum (right hand side).

Two different preliminary static fault solutions, proposed by Istituto Nazionale di Geofisica e Vulcanologia – (INGV) (http://www.sigris.it/) and by the New Zealand Institute of Geological and Nuclear Sciences – (GNS) (http://www.gns.cri.nz/ Home/ News-and-Events/ Media-Releases/ Most-damaging-quake-since-1931/ Canterbury-quake/ Hiddenfault), were respectively considered. The source parameters adopted for the two models are summarized in Table 3.3, while the slip distribution across the fault plane, along with the hypocenter location, is presented in Figure 3.5, for both INGV and GNS seismic source inversions. The source model proposed by INGV was identified by the ASI-SIGRIS system, exploiting COSMO-SkyMed images (Atzori and Salvi 2011). The "GNS model", published as a press release, is a static model derived from pre-earthquake and post-earthquake geodetic data using both InSAR and GPS data. An updated version of the model is given by Beavan et al. (2011) and a true kinematic source model based on inversions of strong motion data has been developed by Holden (2011). While the two finite fault solutions have similar size and slip pattern, they differ quite significantly in strike angle, and location of the hypocenter. It is important to emphasize that the models, hereinafter called "kinematic source models", used in this work, have been obtained turning these static models into kinematic models by assuming a rupture velocity, rise time and slip origin and simplifying the "GNS model" shown on the GNS web site by making the rake constant, at 145°. A value V_R equal to 2,400 m/s is assumed as the rupture velocity. The slip source time function is given by an approximate Heaviside function, as follows:

$$M_0(t) = \frac{1}{2}\left[1 + erf\left(2.0\frac{t-2\tau}{\tau/2}\right)\right], \qquad (3.12)$$

where *erf( )* is the error function and τ = 0.9 s is the rise time, assumed to be constant across the fault plane. Figure 3.6 shows a plot of moment rate function and its spectrum.

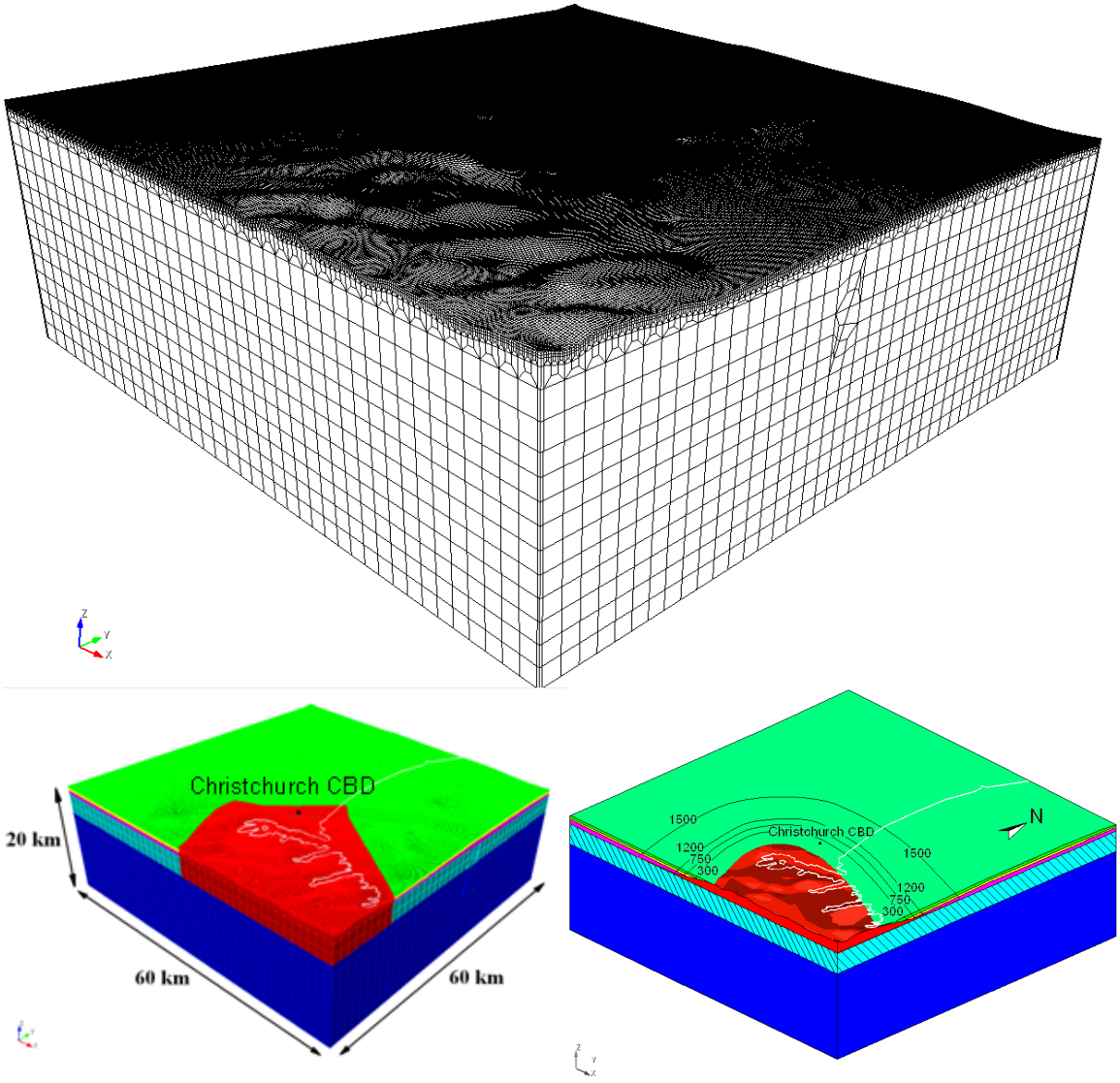

Figure 3.7. Top: 3D mesh of the Canterbury Plains relying on the GNS kinematic seismic source inversion. Bottom: (Left hand side) Corresponding "Step-like" model and (Right hand side) "Smooth" model, with depth contours of the contact between the alluvial soft sediments and the rigid volcanic materials (depth in meters). Position of the CBD is also shown.

The 3D spatial discretization by spectral elements of the area requires the design of a large scale unstructured mesh of hexahedral elements. The computational domain is subdivided into small chunks, each of them is meshed starting from the alluvial basin down to the bedrock. The mesh was constructed making use of the software CUBIT (available at http://cubit.sandia.gov/), according to the technique already described by Casarotti et al. (2007). Note that four different numerical models were constructed to attain the different hypotheses regarding, on one side, the seismic source (INGV vs. GNS) and, on the other side, the alluvial-volcano interface. Both seismic source models, either INGV or GNS, have been tested with the: (i) "step-like" and (ii) "smooth" approximation for the alluvial-volcano interface. In particular the "step-like" model has been

Table 3.4. 3D numerical models size and computational time. Data of CPU time refer to the Lagrange cluster located at CILEA.

Model	SD	Number of Spectral Elements	Number of LGL Nodes	Number of cores	Simulation time (h)
INGV – "Step-like"	4	475,992	~31.6 10^6	64	~75
INGV – "Smooth"	4	475,992	~32 10^6	64	~80
GNS – "Smooth"	4	495,385	~33.3 10^6	128	~107

realized adopting a classical "honoring" meshing strategy, while the "smooth" one has been obtained with a "not-honoring" strategy (for a proper understanding of methods and procedures at the basis of the two different meshing approaches see Appendix B).

The 3D hexahedral spectral element mesh, adopted for the numerical simulations by GeoELSE, consists of about 476,000 and 496,000 elements for the INGV and GNS model, respectively. The size of the elements ranges, in both cases, from a minimum of about 150 m (at the top of the alluvial basin) up to 1,500 m at bedrock. The mesh is, hence, designed to propagate up to about 2 Hz, for spectral degree equal to 4. The three-dimensional mesh of the Canterbury Plains relying on the GNS kinematic seismic source inversion, with corresponding "step-like" model and "smooth" model, with depth contours of the contact between the alluvial soft sediments and the rigid volcanic materials is depicted in Figure 3.7. The numerical simulations were performed on the Lagrange cluster located at CILEA. The main characteristics and the performances of the analyses are summarized in Table 3.4.

3.5 Role of the basin geometry and of the kinematic seismic source in the spatial variability of strong ground motion: Numerical results in the near source region

This section aims to show the main results obtained through the numerical simulations by GeoELSE. The 3D synthetic seismograms are compared with the observed waveforms at a set of stations located in the near source region of the earthquake. In order to point out the role of the 3D geometry of the Canterbury Plains and of the kinematic seismic source, we proceeded in the following way. At first, we addressed the issue regarding the effect of the model assumed for the alluvial-bedrock transition, "step-like" vs. "smooth", considering the fault solution proposed by INGV. Afterwards, we evaluated the dependence of the results on the fault model, INGV vs. GNS, considering only the "smooth" alluvial-bedrock transition.

Figures 3.8 and 3.9 compare the three-dimensional numerical simulations with strong ground motion observations in terms of velocity time histories and corresponding Fourier amplitude spectra. The comparison is presented for four representative stations: HVSC, laying on outcropping rock, REHS; located on alluvial soil in the CBD; SHLC, situated on alluvial soil at epicentral distance R_e = 9 km, close to the CBD; and SLRC, laying on alluvial soil at R_e = 33 km, south-west

of the epicentre. Both observed and simulated waveforms have been processed with a band-pass acausal Butterworth filter between 0.1 and 2 Hz.

A quantitative estimation of the overall quality of the numerical analyses can be inferred evaluating the misfit parameters proposed by Anderson (2004). Stating that a single parameter is inadequate to assess the correspondence between simulated and observed time-histories, Anderson (2004) introduced a set of ten parameters, each one evaluated for a specific frequency band of interest: Arias duration (AD), energy duration (ED), Arias intensity (AI), energy integral (EI), peak acceleration (PA), peak velocity (PV), peak displacement (PD), response spectra (RS), Fourier spectra (FS) and cross-correlation (CC). A score between 0 and 10, with 0 signifying no agreement and 10 perfect agreement, is calculated for each of these parameters, yielding an overall goodness of fit. Figure 3.10 depicts the goodness of fit parameters computed in the frequency band 0.25-0.50 Hz for the 3 models under study, "step-like" INGV, "smooth" INGV and "smooth" GNS, and for three components of motion (EW, NS and UD). The scores of the aforementioned parameters are shown for the 23 stations summarized in Table 3.1.

3.5.1 Dependence of results on the geometry of the Canterbury Plains

In this Section we address the issue regarding the role of the 3D geometry of the Canterbury Plains, i.e. the "step-like" vs. "smooth" model, on the simulated waveforms. Referring to Figures 3.8 and 3.9, it is noted that, in spite of the rough approximations behind the "step-like" model, the overall agreement is fairly satisfactory. For most of the considered stations, the "step-like" model reproduces the first arrivals and the PGVs with reasonable accuracy. The agreement between synthetics and observations is satisfactory for the stations located in the central-western portion of Canterbury Plains, while it deteriorates for the station located on the southern volcanic region. Nonetheless, such models tend to overestimate PGV values measured in the eastern area of Christchurch, where major liquefaction effects were observed. This effect may be due to the rough representation of the interface between the volcanic material and the soft soil of the basin, leading to a very large concentration of energy towards the city of Christchurch as a consequence of the high impedance contrast between the volcano region and the surrounding soft sediments.

The introduction of the "smooth" model yields significant improvements of the simulated waveforms, in particular for the reproduction of the coda-waves inside the alluvial plain. The smooth interface between volcanic rock and alluvial soil leads to a better agreement in terms of PGV, nonetheless, the model still tends to overestimate the peak values measured in the CBD and in the eastern-coastal area of Christchurch and underestimate the peak values recorded far from the epicentre, especially in the south-western region of the model.

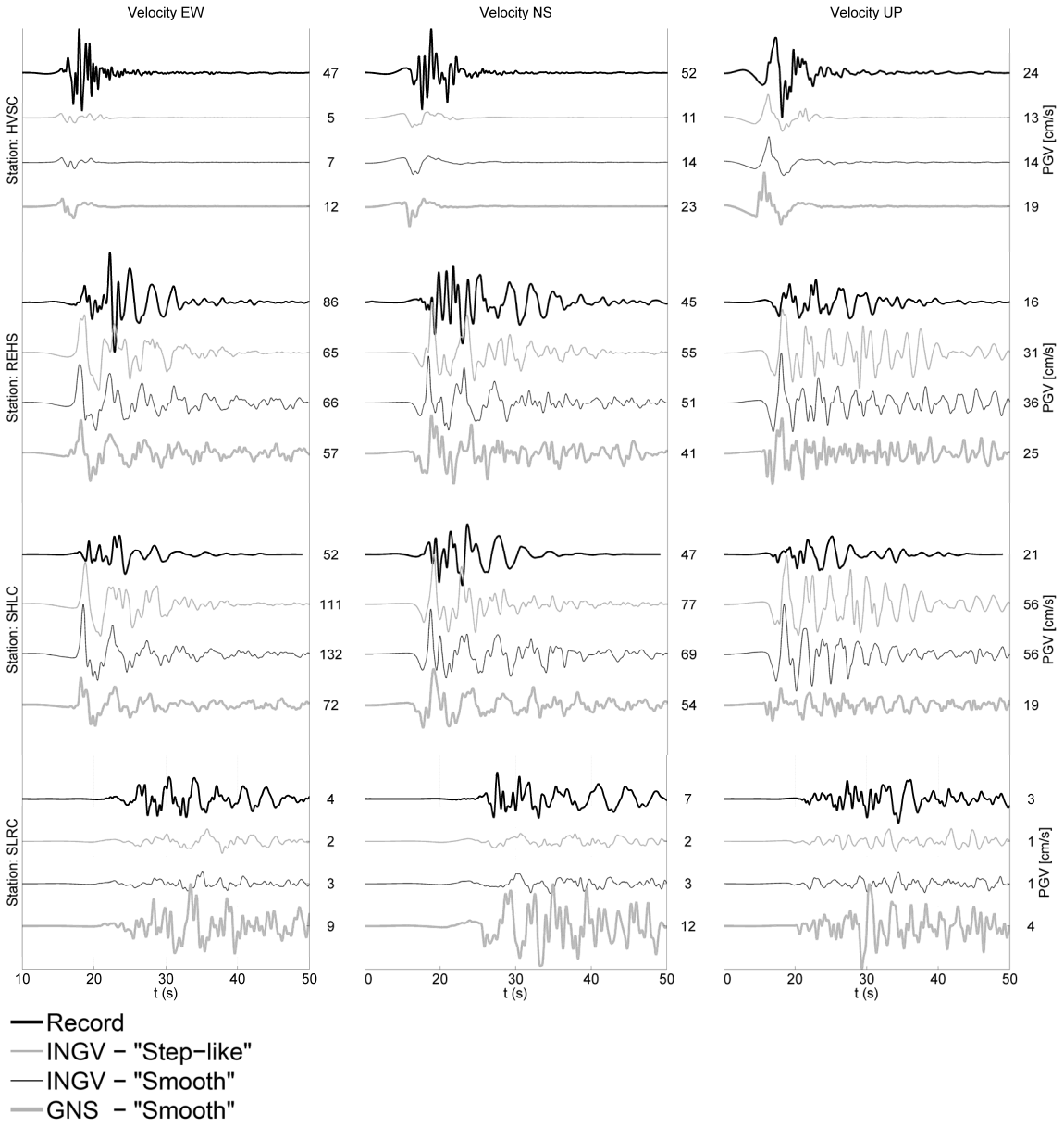

Figure 3.8. Comparison of 3D numerical simulations by GeoELSE with strong ground motion observations, in terms of three components velocity time histories, obtained at stations: a) HVSC, at outcrop rock, b) REHS, on soft sediments in the CBD, c) SHLC, on soft sediments at R_e = 9 km, d) SLRC, on soft sediments at R_e = 33 km, in the south-western portion of the model. Observed and simulated data are band-pass filtered between 0.1 and 2.0 Hz.

Figure 3.10 allows us to a have a quantitative criterion for assessing the performance of the different numerical simulations. While the "step-like" model shows at least six stations with good scores for the whole set of parameters (Figure 3.10a), the INGV "smooth" model, with at least nine station with good average scores (Figure 3.10b), yields actual improvement of the numerical analyses. As a general remark, for both simulations, integral measures of Arias and energy duration (AD and ED) and peak ground acceleration, velocity and displacement values (PA, PV and PD)

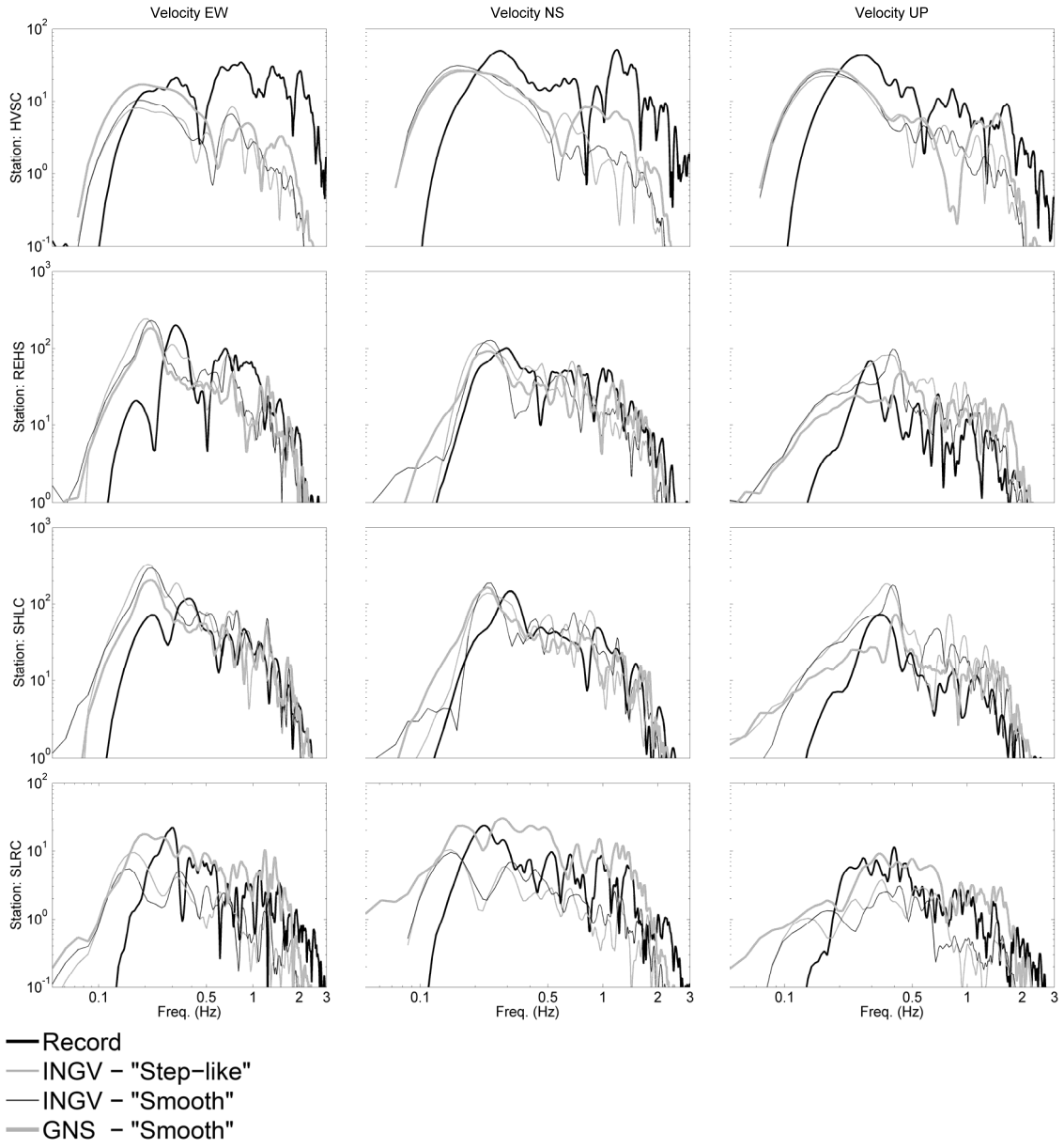

Figure 3.9. As in Figure 3.8 but in terms of velocity amplitude Fourier spectra.

present a good fit for all the considered stations, while the score is poor for intensity measurements (AI and EI), spectral amplitudes, and cross-correlation (RS, FS, and CC).

3.5.2 Effect of the kinematic seismic source

After having illustrated the results obtained for the "step-like" and "smooth" model, we look in this section at evaluating the effect of different kinematic seismic sources. To this end, we will show a comparison of the numerical results obtained for the INGV and GNS fault solutions (see

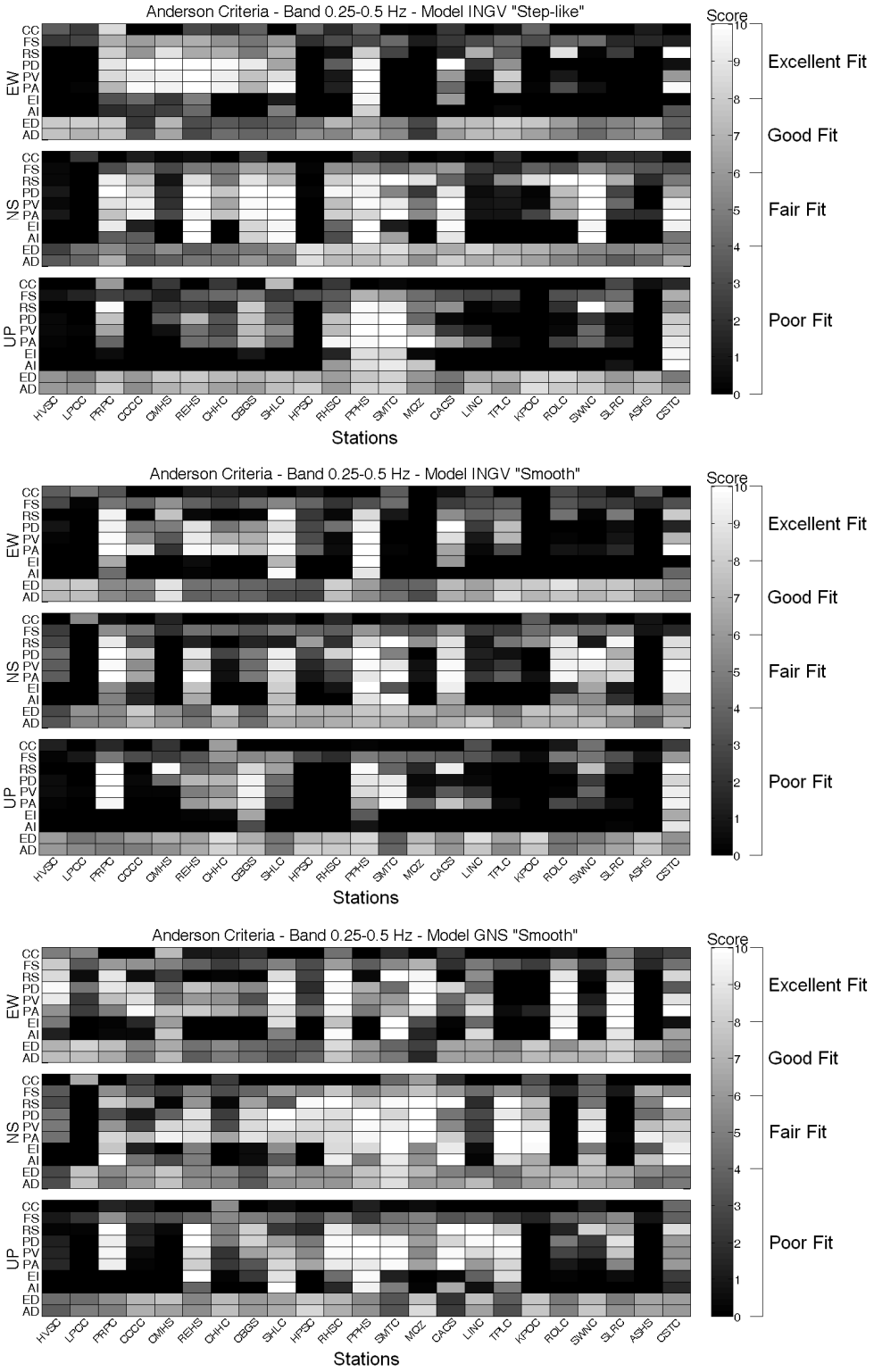

Figure 3.10. Misfit parameters (Anderson, 2004) of simulated ground motion for the three components of motion, evaluated at the 23 stations under consideration (see Table 3.1 and Figure 3.2) in the frequency band between 0.25 and 0.50 Hz. The results are shown for the INGV "step-like"(top panel), INGV "smooth" (centre panel) and GNS "smooth" model (bottom panel).

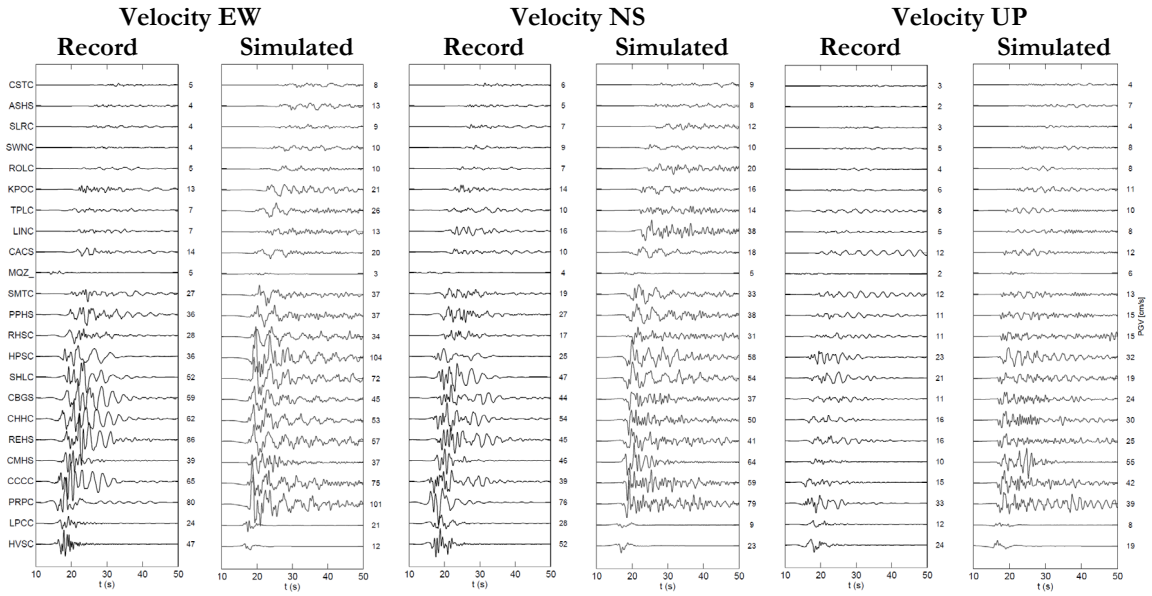

Figure 3.11. Comparison between recorded and simulated (GNS "smooth") velocity time histories (in cm/s), on the EW, NS and the UD component for the whole set of stations at R_e < 40 km. The label on the left vertical axis reports the peak value of the corresponding time history.

Figure 3.5), relying on the "smooth" model, which produces satisfactory results, as discussed in the previous section.

The comparisons in Figures 3.8 and 3.9 show that the GNS fault model leads to a better agreement between recorded and simulated ground motion velocities at the four stations under consideration. For this kinematic source model, a good agreement is found both at stations located on alluvial soil a few kilometers from the epicentre and at those stations located several kilometers further away in the south-western portion of the model. In spite of the rough assumptions behind the GNS "smooth" model, numerical simulations are able to reproduce with reasonable accuracy the PGVs within the Canterbury plains. Nonetheless, the agreement between synthetics and observed values is still quite poor for the station located on the volcanic region. This is most likely due to the simplified model assumed for the topography of the Banks Peninsula, that is approximated as a smooth surface and does not capture the complex geometry of bays and coves, that may play an important role in seismic wave propagation phenomena. Furthermore, a homogeneous soil profile is assumed for the volcanic region, so that erosion and weathering phenomena of the surface rock layers are not taken into account.

The analysis of the Anderson misfit criteria (Figure 3.10c), confirms the quality of the numerical simulations, showing good average scores for almost all the stations under consideration. As mentioned previously, there is good agreement in terms of PGVs (parameter PV), for many stations inside the computational domain. Figure 3.11 shows a comprehensive comparison between recorded and simulated (GNS "smooth" model) velocity time histories for the whole set of

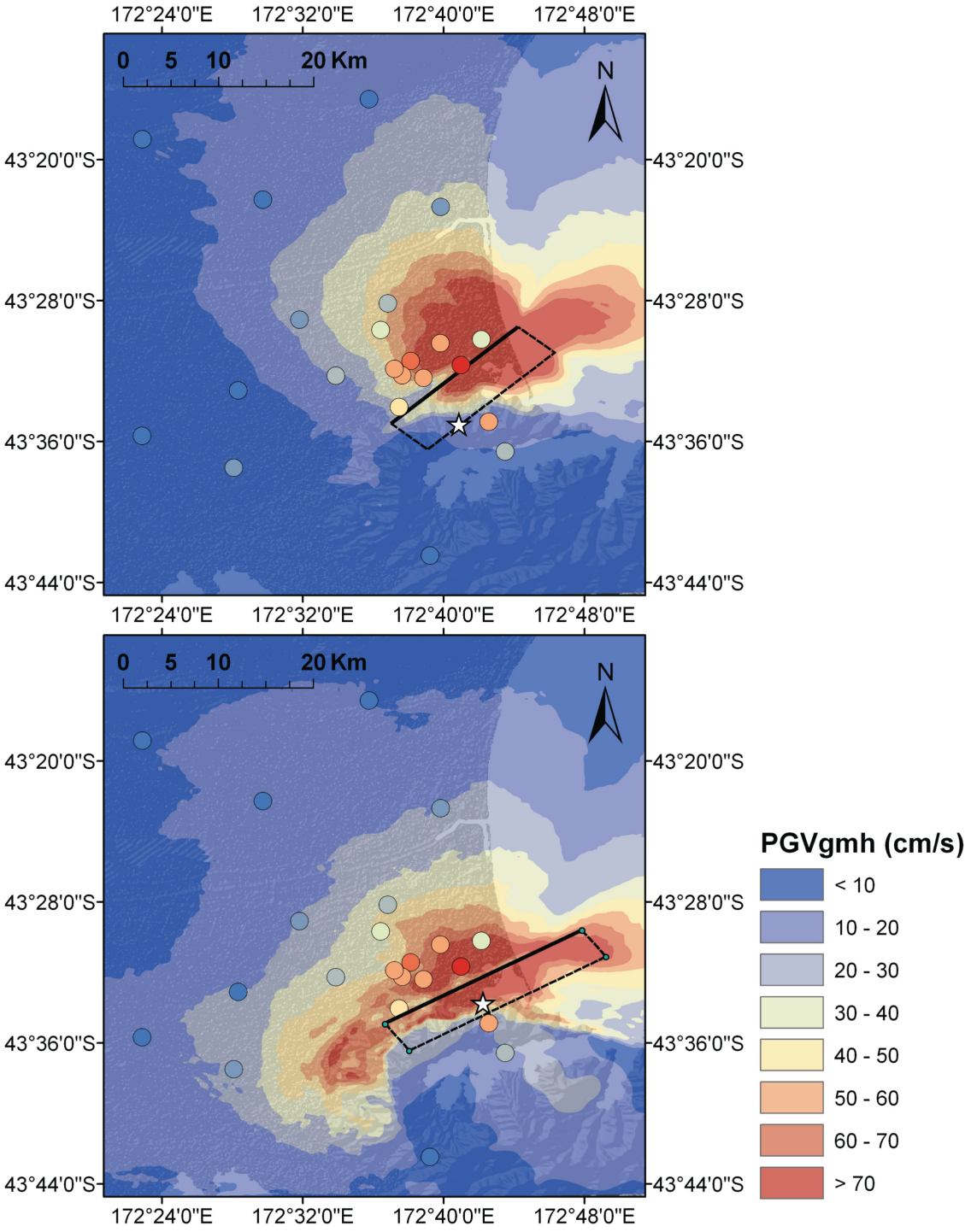

Figure 3.12. Spatial variability of Peak Ground Velocity (geometric mean of horizontal components) as estimated by 3D numerical simulations with the INGV "smooth" model (top panel) and GNS "smooth" model (bottom panel). The recorded PGV values (filled dots) are superimposed for comparison purposes.

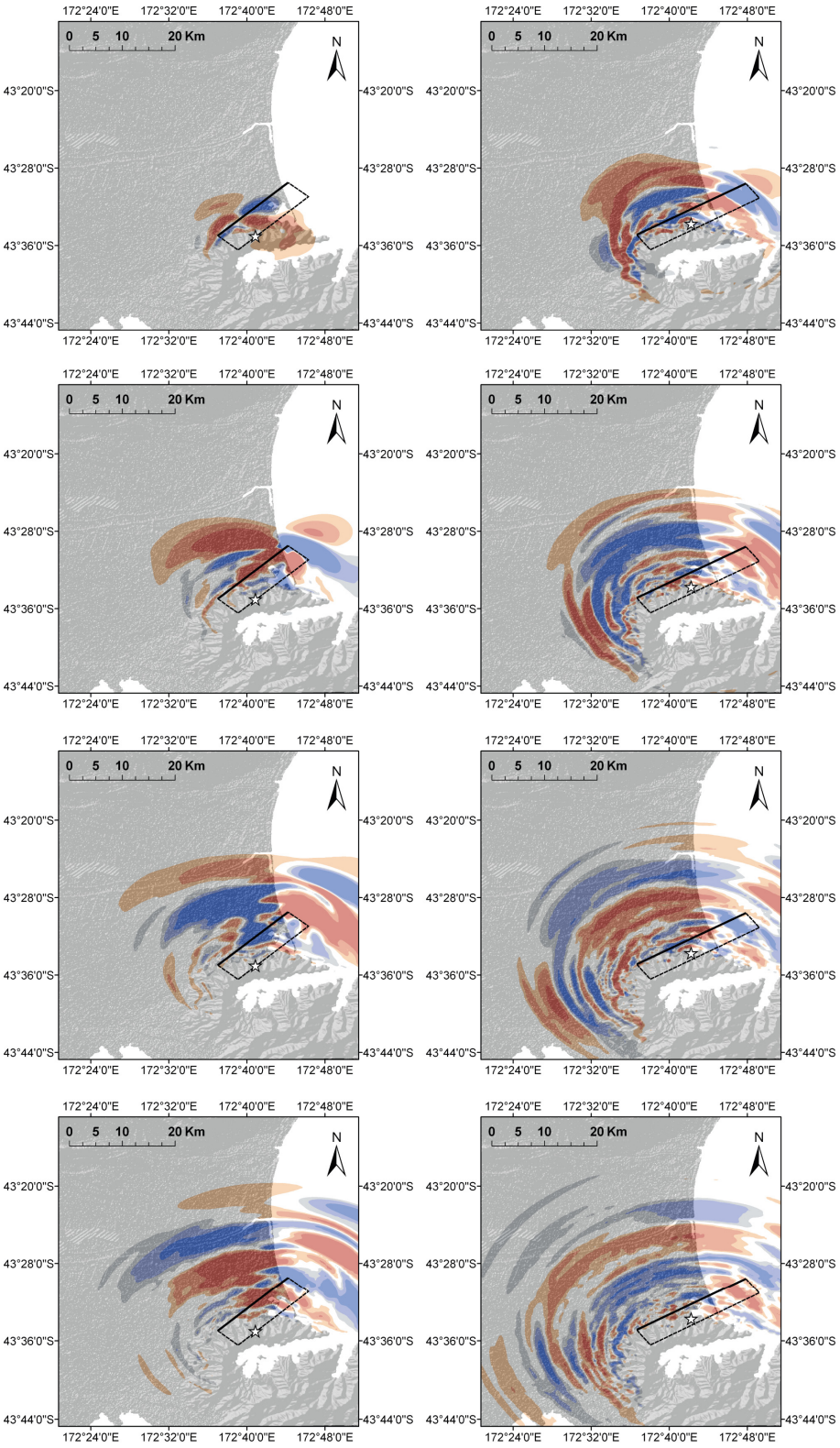

Figure 3.13. Snapshots (t = 7, 9, 11 and 13 s, from top to bottom) of the simulated fault normal velocity wavefield with the INGV "smooth" model (left hand side) and GNS "smooth" model (right hand side).

accelerometric stations inside the computational model, ordered by epicentral distance. Good agreement is found in terms of arrival times, peak ground values and attenuation with distance, despite the rough assumptions concerning the characterization of soil mechanical properties. To have a broad picture of seismic wave propagation effects and of the spatial variability of strong ground motion, Figure 3.12 depicts the spatial distribution of PGV values obtained through GeoELSE along with the observed values (superimposed filled dots), for both the INGV and GNS "smooth" models. Furthermore, Figure 3.13 shows some representative snapshots of the simulated fault normal velocity wavefield, in which it is clearly distinguishable the seismic wave propagation field with the high contrast between rock and alluvial soil and the directivity toward the city of Christchurch. In particular, looking at Figure 3.12 it is possible to notice that the GNS fault model better reproduces the variability of PGV values for the whole modeled area. From Figures 3.12 and 3.13 it is apparent that the INGV source model produces strong "up-dip" directivity effects in the central-eastern part of Christchurch, in agreement with the spatial distribution of observed damage and liquefaction phenomena. The wave propagation pattern obtained with the GNS fault model produces noticeable directivity off the sides of the fault due to the relatively shallow hypocenter (around 6.5 km) and since the rake is oblique (145°). This leads to larger ground motion amplitudes in the south-western portion of the city.

3.6 Comparison with observed Standard Spectral Ratios

As a concluding check of the quality of three-dimensional numerical simulations, in this section we examine the comparison between simulations and observations in terms of Standard Spectral Ratios (SSR). Most of the 23 stations included in the numerical model are located on alluvial soil, while 3 of them lie on outcropping volcanic rock, namely HVSC, LPCC, and MQZ. For this purpose, we considered the four stations located in the Christchurch CBD, on soft alluvial sediments, namely CCCC, REHS, CHHC and CBGS. Station LPCC, located on rock around 15 km south-east from the CBD, is considered a reference rock station.

The SSRs computed as the ratio of the Fourier spectrum of the recordings at CCCC, REHS, CHHC and CBGS (geometric mean of the horizontal components), over that at LPCC reference station are shown in Figure 3.14, for 3 September 2010 Darfield earthquake, with epicentre located around 40 km west of the considered set of stations. We referred to the Darfield earthquake, viewing this event as more reliable than the Christchurch event for evaluating the SSR, because of the strong non-linear soil behaviour verified in the latter and the short distance (less than 10 km) between the epicentre and the considered stations. It is worth noting that stable resonance peaks are found at around 0.3, 0.6, 1.3 and, more consistently, at around 1.7 Hz. The recorded SSRs are compared, on one side, with the one dimensional analytical transfer function obtained for a system

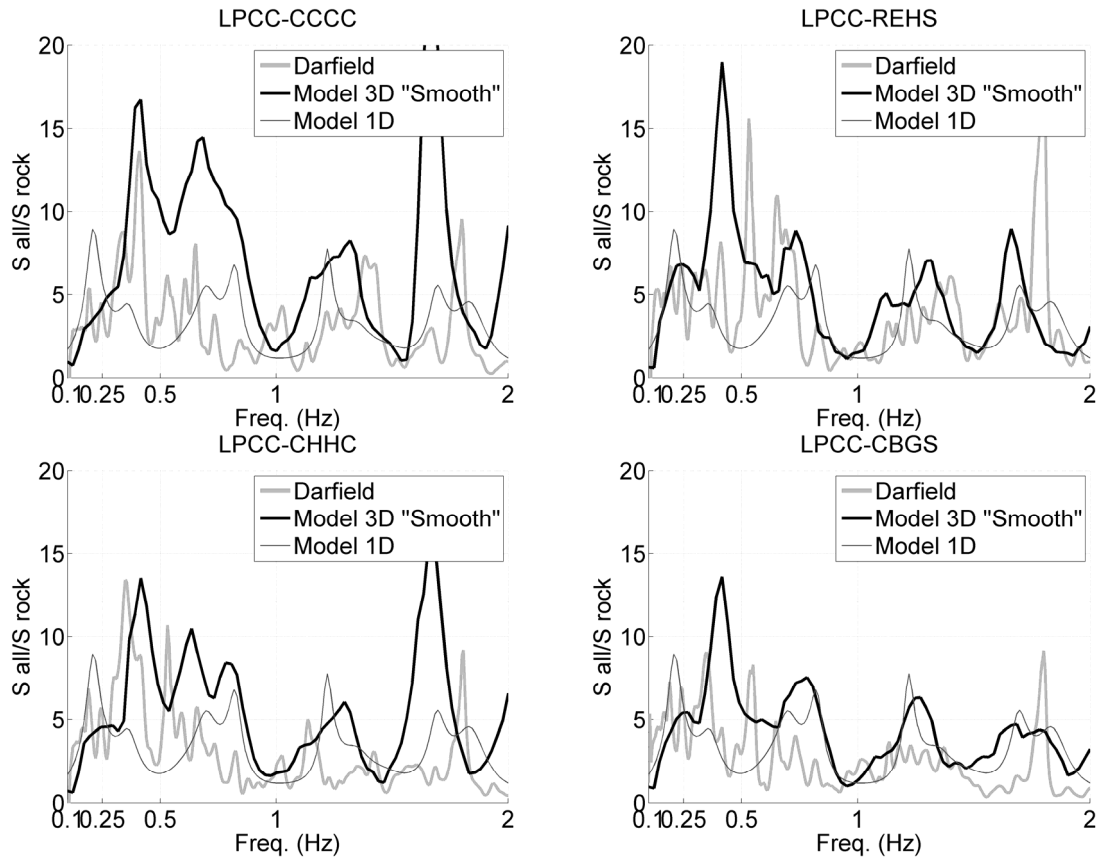

Figure 3.14. Standard Spectral Ratios (SSRs) of the four stations of CBD: CCCC (top-left panel), REHS (top-right panel), CHHC (bottom-left panel), and CBGS (bottom-right panel) located on soft alluvial sediments, over the rock reference station LPCC. The SSRs obtained from strong ground motion recordings during Darfield earthquake are compared with the 1D analytical transfer function and with the SSRs computed with the 3D numerical simulations (GNS "smooth" model).

of 4 layers over a half-space discussed in Section 3.3, and, on the other side, with the SSRs obtained through three-dimensional numerical simulation (GNS "smooth" model). Compared with the one dimensional amplification function, the 3D SSRs show a better agreement with the records, in terms of peak amplitude and frequency, pointing out resonance frequencies at about 0.4, 0.7, 1.3 and 1.7 Hz.

3.7 Concluding remarks

The main aim of this Chapter is to perform three-dimensional numerical simulation of the M_W 6.3 Christchurch earthquake on 22 February 2011, the most devastating and deadliest event of the seismic sequence that struck the Canterbury Plains and particularly the city of Christchurch, since September 2010, and to compare the numerical results with strong ground motion observations,

in order to have a reliable tool to represent transversal as well rotational component of the strong ground motion

The numerical simulations of seismic wave propagation within the Canterbury Plains, where widespread damage was recognized during the post-earthquake reconnaissance surveys, were performed by means of the Spectral Element code GeoELSE. Based on the available geological and seismological data, three-dimensional numerical simulations of the Christchurch earthquake were carried out, combining the following features: (i) two different kinematic finite fault models, provided by INGV and GNS seismic source inversion studies; and (ii) two simplified models for the description of the interface between the stiff volcanic rock of the Bank Peninsula and the soft materials within the Canterbury Plains, referred to as "step-like" and "smooth" models, respectively. As a preliminary assumption, linear visco-elastic soil behaviour was assumed. The comparison of the results obtained through three-dimensional numerical simulations with the strong ground motion records in the epicentral area of the earthquake ($R_e < 40$ km) shows a good agreement both in time and frequency domains, especially for the "smooth" model with the GNS kinematic extended fault model. It is worth remarking that the simplified assumption of linear visco-elastic soil behaviour cannot adequately describe the amplification phenomena and the shift in fundamental frequency, clearly recorded in many stations located on the alluvial soil of the Canterbury Plains. Although the GNS "smooth" model is found to produce the best agreement with the observed waveforms, it should be noted that accounting for a more complex constitutive model could significantly improve the results with the INGV smooth model.

Three-dimensional numerical simulations allow us to reproduce the most significant features of surface earthquake ground motion in the near-fault region. Ground motion shaking maps, in terms of PGV, and snapshots of simulated velocity wavefield are discussed, giving insights into seismic wave propagation effects in realistic geological structures and under near fault conditions. In spite of the simplified assumptions behind the numerical model, three-dimensional numerical simulations represent a relevant tool that may play a major role in seismic hazard assessment studies for predicting realistic earthquake translational and rotational ground motion in complex tectonic and geological environments, for different seismic source scenarios.

CHAPTER 4

ROTATIONAL GROUND MOTION DURING THE M_W 6.3 CHRISTCHURCH EARTHQUAKE: SYNTHETICS vs. SEMI-EMPIRICAL RESULTS IN THE NEAR-FIELD REGION

4.1 Introduction

Rotational ground motions have been obtained from corresponding translational ground motions through a semi-empirical procedure, described in Chapter 2, exploiting the mathematical relationship between cross-power spectra and power spectra of rotations (Castellani and Zembaty, 1996). In Chapter 3, three-dimensional models of the Canterbury Plains were presented and validated. The one that provided the best results in the validation phase, hereinafter the so called "GNS-smooth" model, is adopted. Through this numerical simulation it is possible to retrieve a full set of information concerning the wave propagation, including the rotational component of strong ground motion and its spatial variability.

In this chapter, semi-empirical and synthetic data are analyzed in terms of peak ground values, aiming at a further understanding of the correlation between rotational and translational wave field. By comparing semi-empirically retrieved and synthetic rotational strong motions with past studies on rotations, it is possible to infer an overall good agreement, even though semi-empirical values suggest an higher value of peak ground rotations in the near-field of an earthquake with respect both to array-derived measurements and to numerical models. This could be explained mainly by considering that the adopted numerical model is able to propagate frequency up to 2 Hz, while the semi-empirical values has been obtained from recorded translational accelerations with

band-pass filter transition bands of 0.1-0.25 Hz and 24.50-25.50 Hz (from Center for Engineering Strong Motion Data - CESMD: http://www.strongmotioncenter.org/).

Despite of this intrinsic limit, the three-dimensional model allows a comprehensive description of the wave field and in particular of its spatial variability. Maps of the spatial distribution of the peak ground values of velocity and of the ratio between peak ground velocity and peak ground rotation in the near-field of the earthquake are precious tools to assess the dependence of the spatial variability of motion on the local site conditions, topographical features, epicentral distance, and source directivity.

4.2 Correlation between rotational and translational ground motions

As described in Chapter 1 (Eq. 1.15 a, b), it is possible to correlate rotational and translational ground motions. Considering the maximum values of velocity (PGV_z and PGV_h) and knowing, from direct or indirect sources, the peak rotational values ($PG\omega_h$ and $PG\omega_z$), it is possible to write:

$$\begin{cases} \dfrac{PGV_z}{PG\omega_h} \approx C \\ \dfrac{PGV_h}{PG\omega_z} \approx 2C \end{cases}, \qquad (4.1\ a, b)$$

where C can be considered a scaling factor between translational and rotational peak ground motion. Considering plane waves of arbitrary amplitudes, harmonically propagating through parallel layers, it is possible to interpret the ratio between peak velocity and peak rotation in time as an average or equivalent estimation of the horizontal apparent velocity of propagation (e.g. Spudich and Fletcher, 2008, Stupazzini et al., 2009b, Wang et al. 2009, Fichtner and Igel 2009).

The rotational motion, as shown in Chapter 1 (Table 1.2), can be divided in a torsional component, about the vertical axis, associated to pure shear and involving the contribution of SH and Love waves (Lee and Trifunac, 1985) and in a rocking component, about the horizontal axis, associated with P, S, and Rayleigh waves (Lee and Trifunac, 1987). The aforementioned division implies the knowledge of the polarization of the incident wave field - which is, despite recent findings, (Langston et al. 2009), not trivial to recover.

Without direct measurements of strong rotational motions, study of the spatial variability of the ratios in Eq. 4.1 allows us to investigate the correlation between translational and rotational ground motion, highlighting the physical implications, e.g., the local site conditions, the topographical features, the epicentral distance, and the source directivity.

Table 4.1. Values of semi-empirical peak rotational velocity and recorded peak ground accelerations for the 23 stations within a radius of 40 km from the epicentre of the 22 February Christchurch earthquake. Band-pass filter transition bands are 0.10-0.25 Hz and 24.50-25.50 Hz (data of PGA from www.strongmotioncenter.org). PRV is the maximum among the three components, assuming d = 10 m. PGA is the maximum between the two horizontal components. In italic are typed stations located on outcropping rock.

Station	Code	R_e [km]	PGA [m/s²]	PRV [mrad/s]	PRV/PGA [mrad s/m]
Heathcote Valley Primary School	*HVSC*	*1*	*12.361*	*18.794*	***1.520***
Lyttelton Port Company	*LPCC*	*4*	*9.011*	*12.736*	***1.413***
Pages Road Pumping Station	PRPC	6	6.518	17.319	**2.657**
Christchurch Cathedral College	CCCC	6	4.070	7.039	**1.730**
Christchurch Cashmere High School	CMHS	6	3.955	7.283	**1.842**
Christchurch Resthaven	REHS	8	7.051	5.395	**0.765**
Christchurch Hospital	CHHC	8	3.505	6.779	**1.934**
Christchurch Botanic Gardens	CBGS	9	5.252	5.436	**1.035**
Shirley Library	SHLC	9	3.177	4.531	**1.426**
Hulverstone Drive Pumping Station	HPSC	9	2.280	9.372	**4.111**
Riccarton High School	RHSC	12	2.914	3.059	**1.050**
Christchurch Papanui High School	PPHS	12	2.381	2.854	**1.199**
Styx Mill Transfer Station	SMTC	14	1.783	2.571	**1.442**
McQueens Valley	*MQZ*	*15*	*1.445*	*1.822*	***1.261***
Christchurch Canterbury Aero Club	CACS	18	1.783	2.035	**1.141**
Lincoln Crop and Food Research	LINC	19	1.611	1.153	**0.716**
Templeton School	TPLC	19	0.967	1.564	**1.617**
Kaiapoi North School	KPOC	23	2.064	2.458	**1.191**
Rolleston School	ROLC	26	1.605	2.119	**1.321**
Swannanoa School	SWNC	29	2.464	3.226	**1.309**
Selwyn Lake Road	SLRC	33	0.865	0.968	**1.119**
Ashley School	ASHS	35	0.858	1.093	**1.273**
Cust School	CSTC	39	0.763	0.842	**1.104**

4.3 Semi-empiric and synthetic rotational wave field for the M_W 6.3 Christchurch earthquake

In the present section the mathematical procedure introduced and discussed in Chapter 2 is applied to translational measurements, recorded by a set of strong motion stations located within a 40 km radius of the epicentre of the 22 February Christchurch earthquake. The results are presented in a format suitable for a comparison with the available directly measured data, from Liu et al. 2009 and Takeo 2009 (Chapter 1, Figure 1.4, Chapter 2 Figure 2.7).

As stated in Chapter 2, it is worthwhile to emphasize that an apposite coherence function has not been computed as yet for the Canterbury Plains, and probably cannot be computed because the instruments are not arranged at distances suitable for calculation of the cross correlation. Our evaluation has thus used the coherence so far evaluated by Abrahamson for the records collected by the closely spaced array of instruments at Lotung, in any case suitable to be applicable to other regions (Abrahamson 1991).

Table 4.1 lists the values of semi-empirical peak rotational velocity (PRV) together with the recorded peak ground accelerations, with band-pass filter transition bands of 0.10-0.25 Hz and

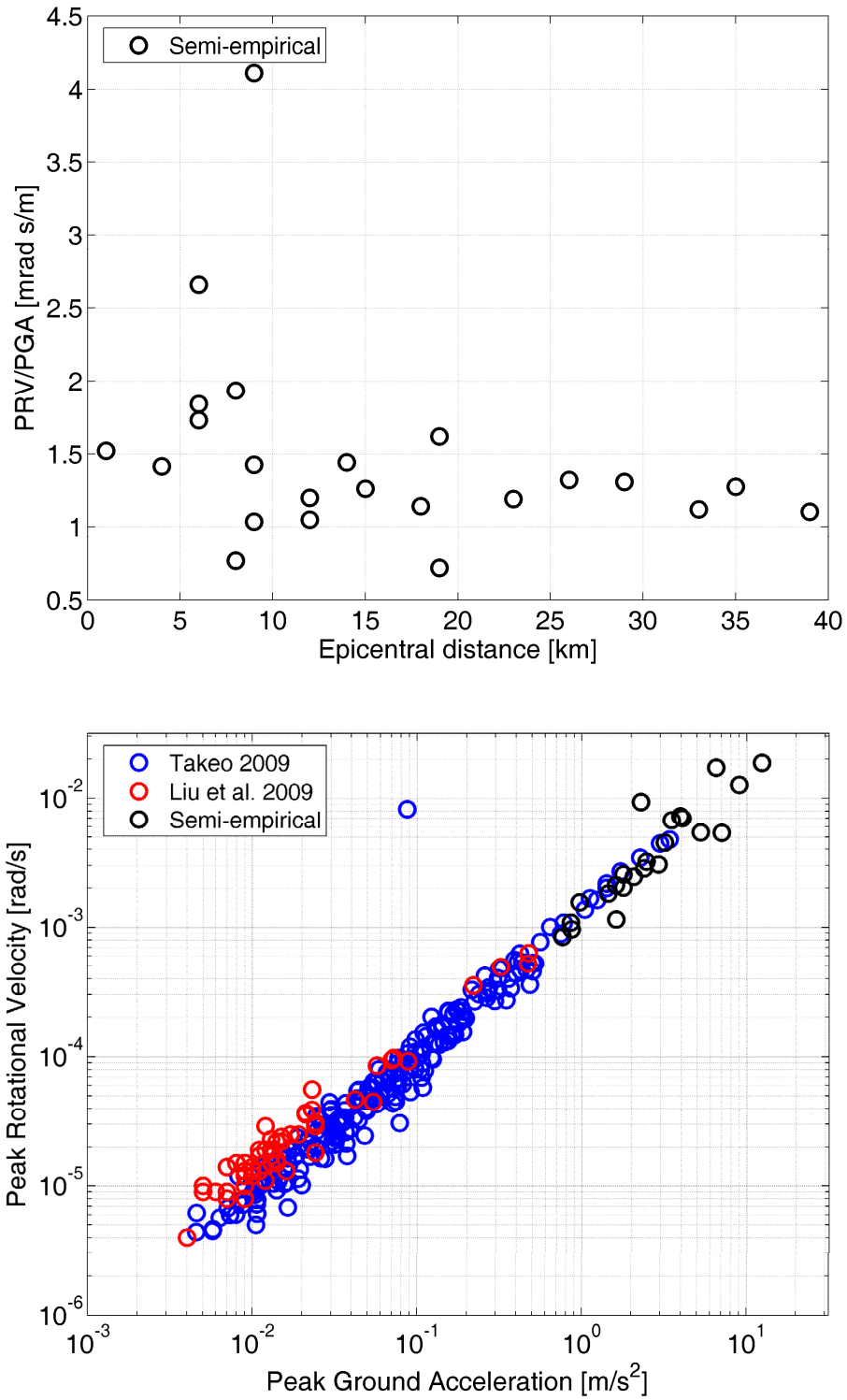

Figure 4.1. Top: Ratio between the semi-empirical peak rotation velocity PRV and the peak horizontal acceleration PGA, in [mrad s/m], evaluated for the 23 stations considered for the Christchurch earthquake, with separation d = 10 m in function of the epicentral distance. Average value is 1.486. Bottom: Semi-empirical peak rotational velocity vs. peak ground acceleration (black) in logarithmic scale, superimposed to available measured values from Liu et al. 2009 (red) and Takeo 2009 (blue).

Table 4.2. Values of semi-empirically retrieved peak rotation and peak rotational velocity for a set of stations within a radius of 40 km from the epicentre of the 22 February Christchurch earthquake. Data filtered between 0.1 and 2.0 Hz. In italic are typed stations located on outcropping rock.

Station Code	R_e [km]	PGω [mrad]			PRV [mrad/s]		
		ω_{z1}	ω_{z2}	ω_h	ω_{z1}	ω_{z2}	ω_h
HVSC	*1*	0.563	0.492	0.239	4.548	3.734	1.344
LPCC	*4*	0.222	0.355	0.140	1.575	1.450	0.682
PRPC	6	0.752	0.665	0.257	3.376	2.691	1.863
CCCC	6	0.889	0.494	0.172	3.761	2.237	0.688
CMHS	6	0.501	0.573	0.106	2.920	2.932	0.718
REHS	8	1.131	0.456	0.158	5.258	3.109	0.775
CHHC	8	0.762	0.509	0.163	3.690	2.621	0.708
CBGS	9	0.727	0.405	0.111	3.670	2.199	0.666
SHLC	9	0.647	0.628	0.194	2.868	2.679	0.939
HPSC	9	0.436	0.247	0.357	1.515	1.012	1.736
RHSC	12	0.222	0.198	0.128	1.582	1.220	0.371
PPHS	12	0.396	0.316	0.133	1.608	1.886	0.693
SMTC	14	0.263	0.232	0.105	1.387	0.941	0.405
MQZ	*15*	0.057	0.032	0.030	0.407	0.191	0.166
CACS	18	0.176	0.102	0.090	0.709	0.544	0.299
LINC	19	0.084	0.212	0.062	0.454	0.955	0.252
KPOC	23	0.179	0.174	0.055	1.081	0.961	0.220
ROLC	26	0.045	0.066	0.035	0.231	0.404	0.126
SWNC	29	0.044	0.082	0.042	0.357	0.501	0.152
ASHS	35	0.050	0.046	0.023	0.351	0.310	0.124
CSTC	39	0.057	0.071	0.037	0.298	0.442	0.176

24.50-25.50 Hz (data from www.strongmotioncenter.org). For a comparison with data from Liu et al. and Takeo, in Table 4.1: PRV is the maximum among the three components, assuming a separation distance d = 10 m; and PGA is the maximum between the two horizontal components. The ratio between the semi-empirical peak rotation velocity (PRV) and the recorded peak horizontal acceleration (PGA), in *[mrad s/m]*, evaluated in Table 4.1 for the considered set of stations for the Christchurch earthquake, has an average value of 1.486, in agreement with the value retrieved by Liu et al. 2009.

In Figure 4.1 the ratio PRV/PGA is shown as function of the epicentral distance for a comparison with the data from Liu et al. (Figure 2.7). Results present an overall agreement, even if for the records collected within 5 to 10 km, mainly in the CBD, results show a value of the ratio between two and three times larger than the average value reported by Liu et al.

In Figure 4.1, semi-empirical peak rotational velocity versus measured peak ground acceleration are superimposed in a logarithmic scale to the available measured values from Liu et al. 2009 and Takeo 2009, showing a satisfactory agreement. It should also be noted that these data are average rotations between points separated by a given distance. Point rotations, consistent with these data are higher. As already suggested in Chapter 2, direct measurements and the semi-empirical approach, for comparable circumstances, lead to rotations higher than those predicted by mathematical investigations presented in Chapter 1.

Table 4.3. Values of synthetic peak rotation and peak rotational velocity for a set of stations within a radius of 40 km from the epicentre of the 22 February Christchurch earthquake. Data filtered between 0.1 and 2.0 Hz. In italic are typed stations located on outcropping rock.

Station Code	R_e [km]	PGω [mrad]			PRV [mrad/s]		
		ω_x	ω_y	ω_z	ω_x	ω_y	ω_z
HVSC	*1*	*0.023*	*0.022*	*0.020*	*0.111*	*0.066*	*0.055*
LPCC	*4*	*0.021*	*0.018*	*0.021*	*0.124*	*0.058*	*0.164*
PRPC	6	0.768	0.364	0.389	5.173	1.727	2.709
CCCC	6	0.559	0.183	0.262	3.545	1.403	0.741
CMHS	6	1.284	1.511	0.603	8.975	9.844	3.345
REHS	8	0.358	0.172	0.237	1.753	0.721	0.951
CHHC	8	0.459	0.185	0.103	1.972	1.388	0.796
CBGS	9	0.302	0.152	0.091	1.604	1.056	0.571
SHLC	9	0.313	0.137	0.169	2.602	1.076	1.142
HPSC	9	0.301	0.120	0.195	1.350	1.125	0.855
RHSC	12	0.304	0.386	0.315	2.347	2.682	1.347
PPHS	12	0.130	0.065	0.063	0.917	0.546	0.415
SMTC	14	0.072	0.060	0.055	0.732	0.515	0.314
MQZ	*15*	*0.020*	*0.006*	*0.005*	*0.114*	*0.034*	*0.025*
CACS	18	0.046	0.044	0.029	0.342	0.311	0.185
LINC	19	0.042	0.060	0.104	0.337	0.535	0.534
KPOC	23	0.048	0.027	0.050	0.336	0.234	0.180
ROLC	26	0.030	0.040	0.041	0.218	0.369	0.261
SWNC	29	0.027	0.021	0.023	0.214	0.163	0.132
ASHS	35	0.027	0.021	0.027	0.124	0.204	0.110
CSTC	39	0.018	0.015	0.013	0.126	0.124	0.068

It is important to remark that while Lee and colleagues and Takeo refers to a set of different earthquakes recorded at a single station, herein, both in the semi-empirical and in the synthetic approach is considered a set of different stations that recorded the same earthquake. In this way, without loss of generality, it is possible to infer some important hints on the physical nature of the rotational wave field and of its spatial variability, taking into account source directivity and topographical features.

4.3.1 Semi-empirical vs. synthetic rotational wave field

By comparing semi-empirically retrieved and synthetic rotational wavefields, it is possible to infer higher values for the semi-empirical estimates with respect both to array-derived measurements and this or past numerical models. This could be explained considering the following reasons: i) the numerical model herein adopted is able to propagate frequency up to 2 Hz, while the semi-empirical values have been obtained from recorded translational accelerations with band-pass filter transition bands 0.1-0.25 Hz and 24.50-25.50 Hz; ii) As discussed in Chapter 3 the numerical model is able to represent in a good way the spatial variability of strong ground motion, even if it tends to underestimate peak ground values, especially in the vertical direction and on outcrop rock, consequently also the corresponding rotational variables may result underestimated; iii) the model

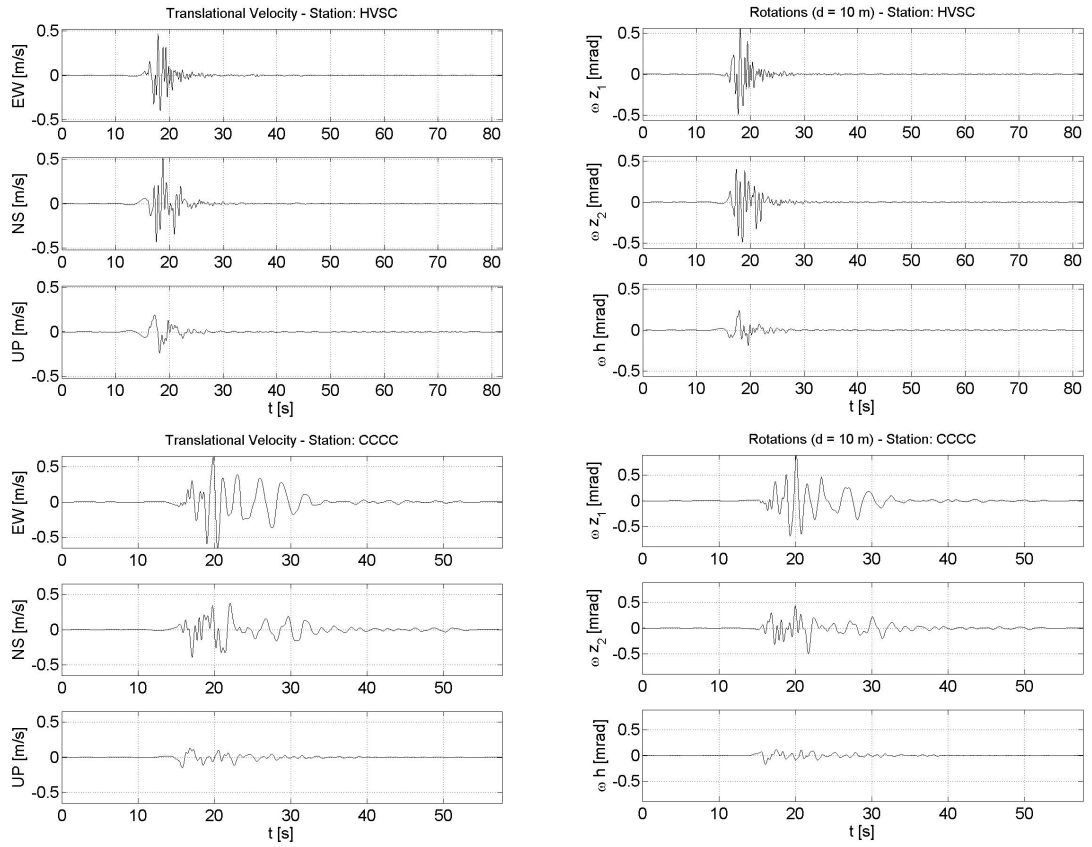

Figure 4.2. Recorded velocity time history and semi-empirically retrieved rotational waveforms at stations: a) HVSC, on outcrop volcanic rock and b) CCCC on soft soil in the CBD. Rotation about horizontal axis (ω_h) are associated to vertical component of ground motion (UP), while to the two horizontal components EW and NS correspond rotational motions about the vertical axis (ω_{z1}, ω_{z2}). Data are band-pass filtered between 0.1 and 2.0 Hz.

presented relies on a visco-elastic soil behaviour, which could be too simplistic, especially in areas that experienced strong liquefaction, and may result in underestimated rotational ground motions.

Tables 4.2 and 4.3 list, respectively, the values of semi-empirically retrieved and synthetic peak rotation and peak rotational velocity for a set of stations within a radius of 40 km from the epicentre. Time histories of translational velocity, rotations and rotational velocity evaluated through the semi-empiric approach at a given recording station, and by the corresponding six-component synthetic seismometer, are presented in Figures 4.2 and 4.3, respectively. Time-histories refer to two reference stations, namely HVSC, on outcropping rock, and CCCC, on soft soil in the CBD (see Figure 3.2). In Figure 4.2, rotations about horizontal axis (ω_h) are associated with vertical components of ground motion (UP), while to the two horizontal components EW and NS correspond to rotational motions about the vertical axis (ω_{z1}, ω_{z2}). For a proper comparison between the two approaches data are band-pass filtered between 0.1 and 2.0 Hz.

While the semi-empirical approach is related to the measured values of translational strong ground motion, and therefore its applicability is necessarily limited to the number of available records,

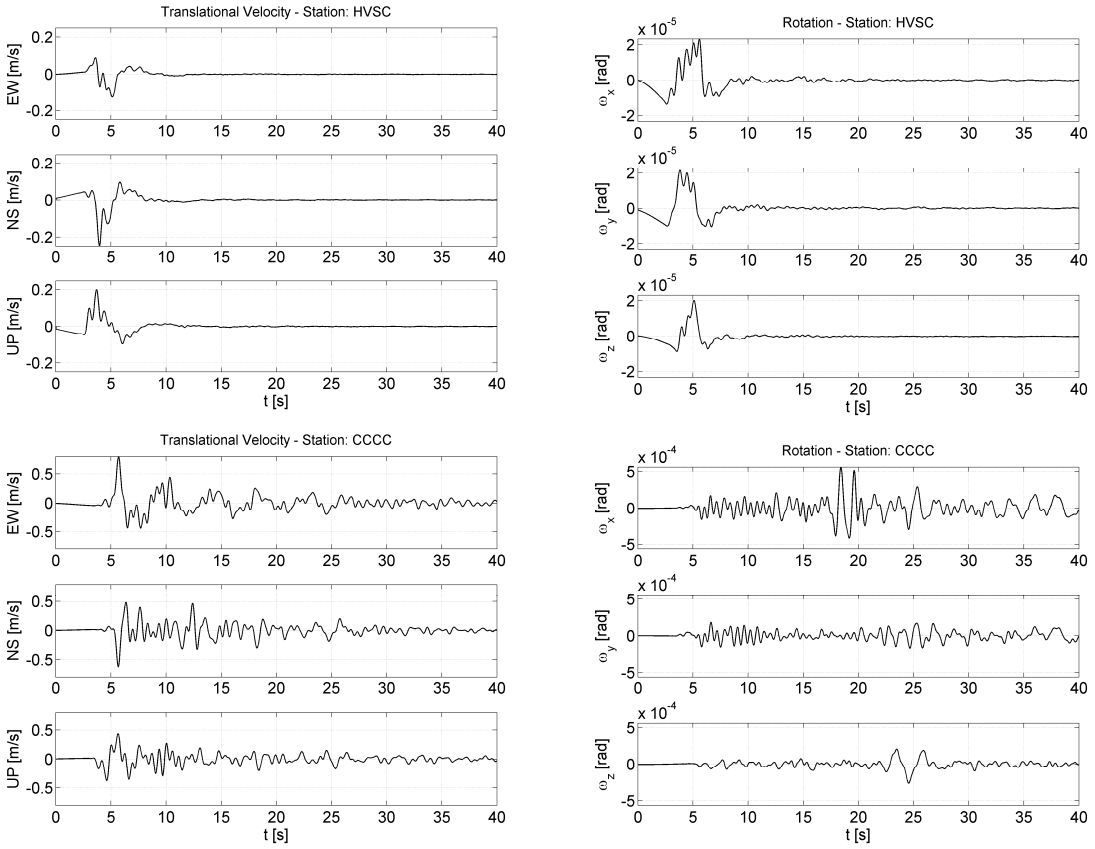

Figure 4.3. Velocity and rotational waveforms obtained from the six-component synthetic seismograms located at stations: a) HVSC, on outcrop volcanic rock and b) CCCC on soft soil in the CBD. Data are band-pass filtered between 0.1 and 2.0 Hz.

the numerical model allows the adoption of a huge number, namely 25,488 in the considered case, of synthetic six-component seismograms located on the top surface (Figure 4.4). For each one of these synthetic seismograms it is possible to compute the peak ground rotation and to plot it as a function of the corresponding peak ground velocity. Peak ground torsion ($PG\omega_z$) and peak ground rocking ($PG\omega_h$), respectively computed as a function of peak horizontal and vertical velocity. Results are presented in Figure 4.5 and it is possible to observe, in the logarithmic scale, the following features i) Results show a linear trend, as already pointed out by Takeo 2009, presenting his data set of more than 200 earthquakes. A similar relationship has been discussed in Chapter 1 and it is equivalent to the representation in terms of PRV vs. PGA. Hereinafter the representation in terms of peak ground velocity will be preferred to the representation in terms of peak ground acceleration, as the latter is more sensitive to noise. ii) Both peak torsional and rocking ground motions present a pronounced dependence on site effects, with seismometers on alluvial soil recording higher values of peak ground rotations. iii) Results, even suggesting a linear average trend

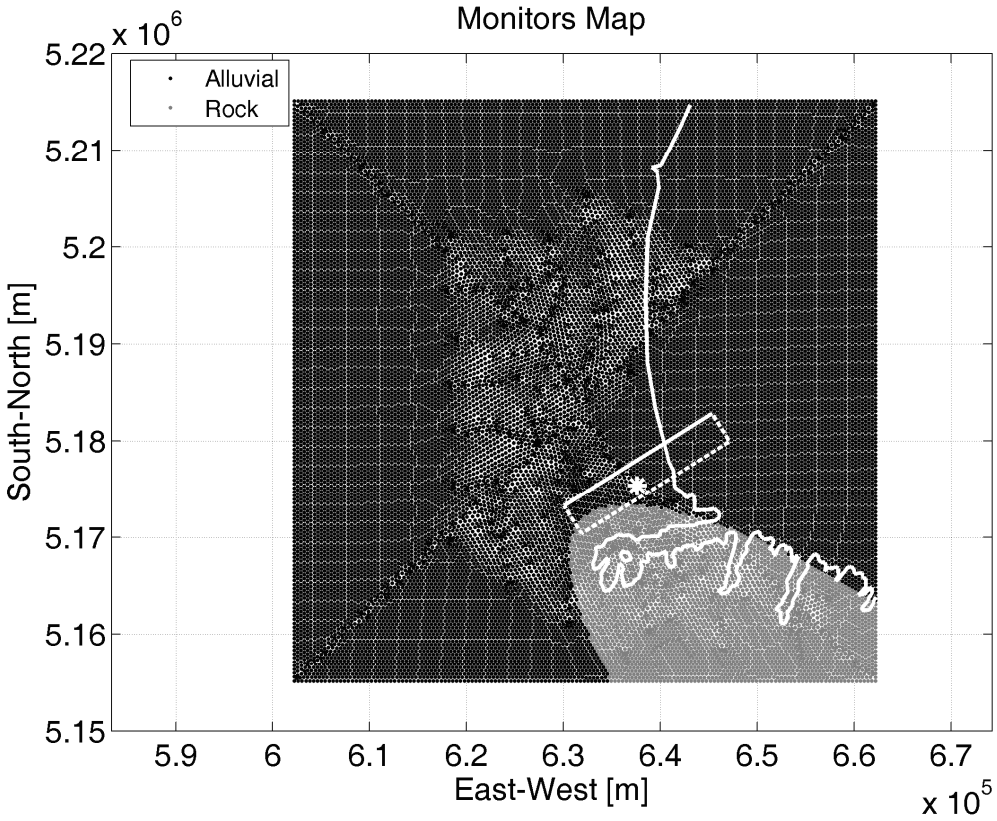

Figure 4.4. Map of the 25,488 six-component synthetic seismograms located on the top surface of the numerical model. Grey dots refer to monitors placed on outcropping volcanic rock, black dots refer to monitors located on the alluvial soil. Superimposed in white are the coastline of the region and the projection of the fault. Star denotes the epicentre of the earthquake.

in both the directions, have a large peak ground rotation variability, of around one order of magnitude, considering the same peak ground velocity.

When not directly estimated, the values of peak torsional and rocking motion are defined as the geometric mean of the corresponding components, as already done in Chapter 3 in describing the spatial variability of peak ground velocity (Figure 3.12):

$$\begin{cases} PG\omega_h = \sqrt{\left|PG\omega_x \cdot PG\omega_y\right|} \\ PG\omega_z = \sqrt{\left|PG\omega_{z_1} \cdot PG\omega_{z_2}\right|} \end{cases}, \qquad (4.2\ a, b)$$

In Figure 4.6 the synthetic data obtained, using the whole set of numerical data and the reference set of stations, are compared with the semi-empirically retrieved data. With both the semi-empirical peak torsional and rocking ground motion values confined to the same range of variability as the synthetic ones, we observe average higher values for the torsional component, with differences of a factor of 4, while the semi-empiric rocking components has differences of a factor of 2.

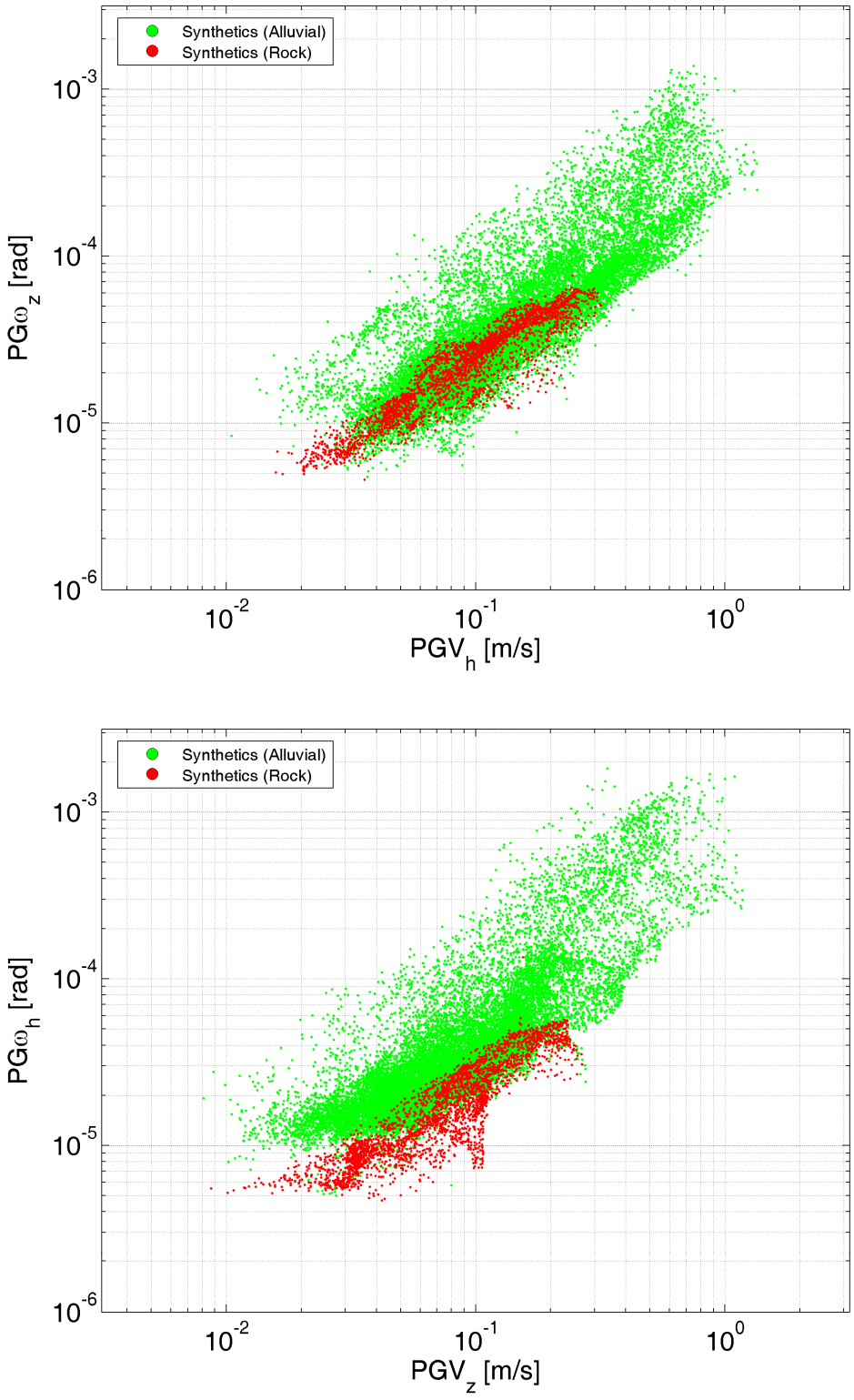

Figure 4.5. Top: Synthetic values of peak ground horizontal velocity (PGV_h) versus peak ground rotation around vertical axis ($PG\omega_z$) in logarithmic scale obtained for the M_W 6.3 Christchurch earthquake. Bottom: Synthetic values of peak ground vertical velocity (PGV_z) versus peak ground rotation around horizontal axis ($PG\omega_h$).

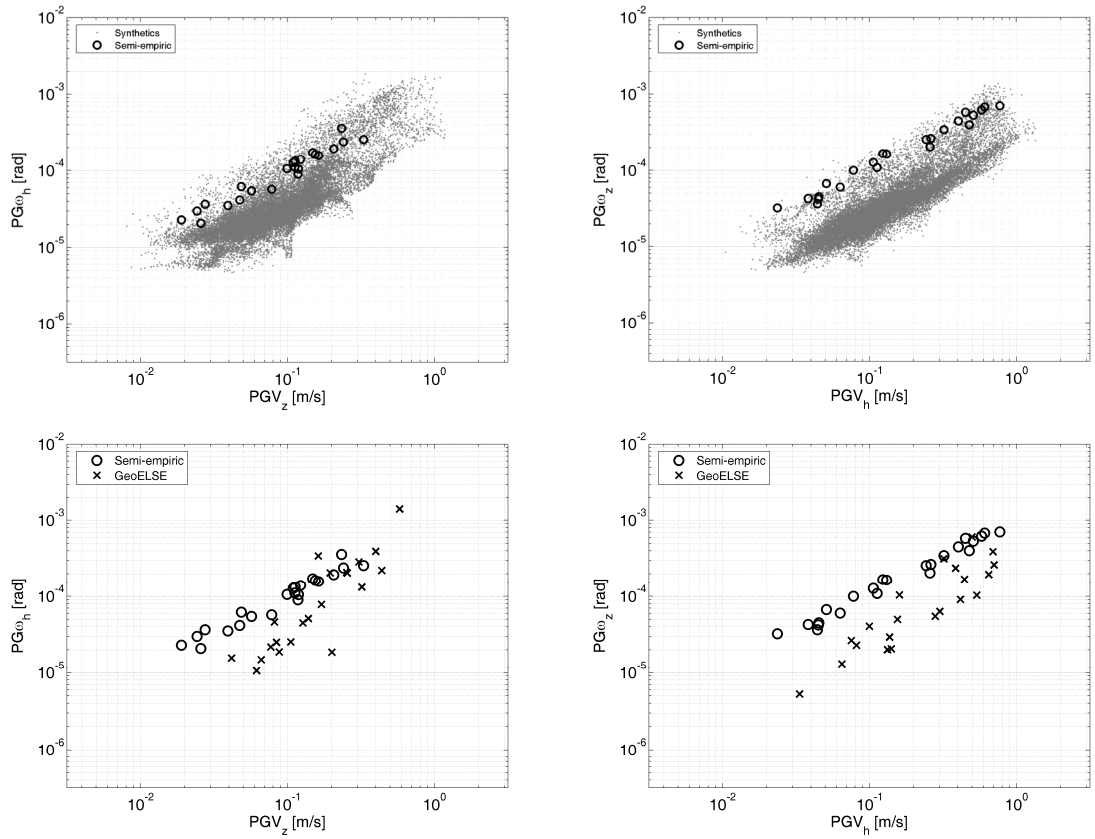

Figure 4.6. Peak ground vertical velocity (PGV_z) versus peak ground rocking ($PG\omega_z$) and peak ground horizontal velocity (PGV_h) versus peak ground torsion ($PG\omega_z$) in logarithmic scale. Semi-empiric values, obtained from translational records, are superimposed to synthetics values, as results of the 3D numerical model, considering both the whole set of 25,488 monitors (Top) and the 21 monitors located on the reference stations (Bottom). Values filtered between 0.1 and 2.0 Hz.

These misleading average values are largely due to the high differences in stations laying on rock that the numerical model tends to strongly underestimate, as explained in Chapter 3. By considering only the stations laying on soft soil the differences are reduced to factors of 2.5 and 1.3, respectively for the torsional and rocking components.

4.3.2 Current vs. Past studies data of rotational ground motions

In this section we recall and update the bibliographic work from Stupazzini et al. 2009b and presented in Chapter 1, in Table 1.3 and in Figure 1.3. The complete dataset is illustrated in Figure 4.7 and refers to the peak ground horizontal velocity (PGVh) versus peak ground torsion (PGωz). In this figure the current dataset of semi-empirically retrieved and numerically obtained peak rotational ground motion is superimposed on a dataset coming from past studies and on available measured data.

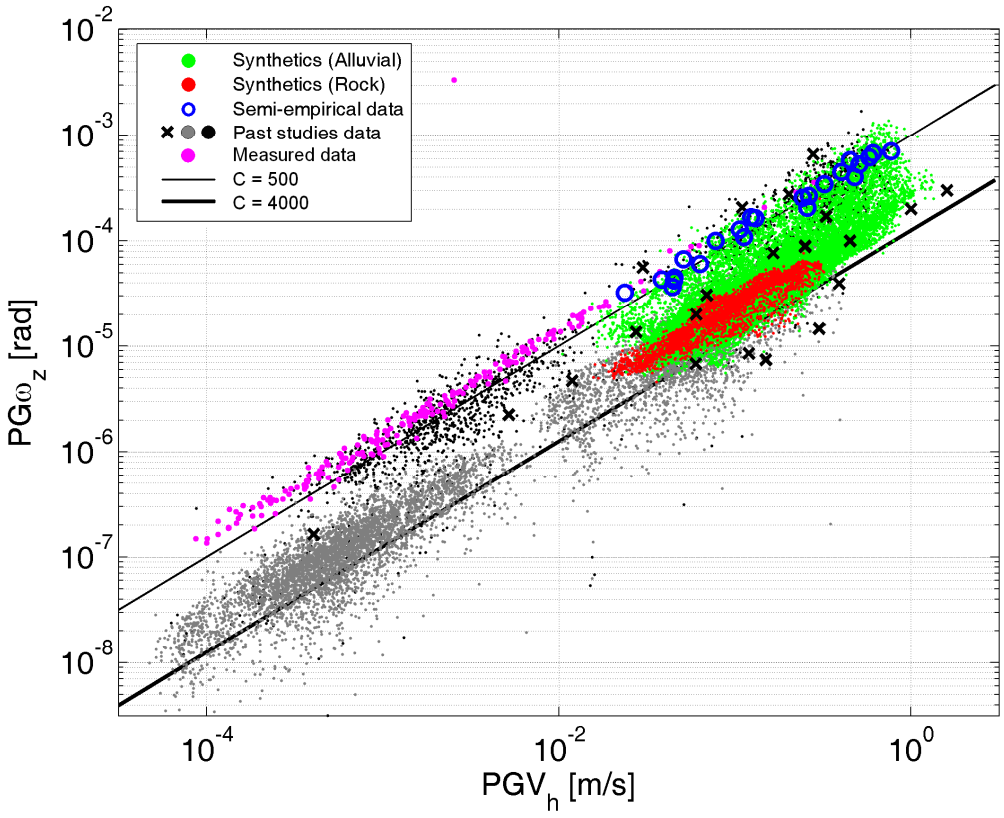

Figure 4.7. Superposition of peak ground horizontal velocity (PGV_h) versus peak ground rotation ($PG\omega_z$) in logarithmic scale of synthetic data on alluvial soil (green) and rock (red), semi-empirical data (blue) and data retrieved from literature, listed in Table 3.1 and described in Figure 1.3; in particular black and gray dots refer to synthetics (alluvial and rock, respectively) obtained for a 3D model of Grenoble valley, France (Stupazzini et al. 2009b). Magenta dots refer to the measured data from an earthquake swarm in 1998, offshore the city of Ito, Japan, from Takeo (2009).

As far as the datasets of past studies are concerned, they include a large variety of data, presented in Table 1.3, consisting of numerical, array-derived, and direct measurement of explosions. In particular, data labelled from 16 to 24 refer to array-derived estimations obtained by Paolucci and Smerzini (2008) and Spudich and Fletcher (2008) and are plotted in Figure 1.3, with their minimum and maximum values denoted by bars. In Figure 4.7, for simplicity, the whole dataset of Table 1.3 is represented by the same symbol (black x), referring to Figure 1.3 and Table 1.3 for a detailed description and characterization of the past studies data. In the same dataset, with a different symbol, the numerical study on the Grenoble Valley is represented (see Appendix B) for M_W 6.0 and M_W 4.5 scenarios, along with distinguishing records on the outcropping rock and inside the alluvial basin (respectively gray and black dots). Finally, the dataset of more than 200 directly measured near-field data from Takeo 2009 is superimposed (magenta dots). It was not possible to use the contribution from Liu et al. 2009 because only the rotation rate is available.

The comprehensive comparison of the current dataset with data retrieved from literature, despite the large variability in the quality and origin of data, indicates an excellent fit. In particular, over a larger scale of peak ground values, the linear trend is more clear, suggesting a linear relation between peak ground horizontal velocity and peak ground torsion, as showed in Eq. 4.1a. Furthermore, the semi-empirically retrieved data are in good agreement with the measured data from Takeo 2009, which turn out to be larger than the other estimates by factors of 5 to 60, as pointed out by Spudich and Fletcher (2008). The author explains these discrepancies in term of heterogeneity of slip velocity along the fault or local rheology. This is in general agreement with the argument that higher values of rotational ground motions characterize the near-field of an earthquake.

4.4 Spatial variability of peak ground rotation in the Canterbury Plains

Despite the aforementioned intrinsic limits of the numerical model, it allows a comprehensive description of the wave field and in particular of the spatial variability of strong ground motions, as already described in Chapter 3, relating to the spatial variability of Peak Ground Velocity described in Figure 3.12.

In Figure 4.8 the decay with distance of the peak ground rotation is evaluated and compared with the decay with distance of the peak ground velocity. It is noted that rotation decreases with epicentral distance, just as velocity does. A similar correlation was noticed by Wang et al. 2009 in terms of peak ground horizontal acceleration and peak ground rotational velocity about the vertical axis. This turns out to be particularly useful in seismic engineering, suggesting that the attenuation relationship of the rotational components could be adopted much as has been done for the translational component of motion.

Applying the ratio between peak ground translational velocities and peak ground rotations (Eq. 4.1 a, b) to the whole set of about 25,000 monitors of the three dimensional model, it is possible to infer some hints about its spatial variability. The simplified models, presented in Chapter 1, assuming an incident wave plane, associate a constant value of C to this ratio, that could be considered as a representative phase velocity. This argument, that implicitly assumes that velocity and rotation are in phase, is generally trustworthy in the far-field, whenever the epicentral distance is large compared to the considered wavelength and source dimensions. This is the case for a great number of ground motion observations, but, as discussed in Chapter 2, in the near-field region this assumption seems to be too simplistic, and, therefore, a large variability of the ratio is expected.

Figure 4.9 investigates this variability among the Canterbury Plains, applying Eq. 4.1 a, b to the whole set of synthetic seismograms. In this figure are depicted the spatial variability of velocity, of rotations, and of their ratio. The spatial variability of the peak ground translational velocity, already

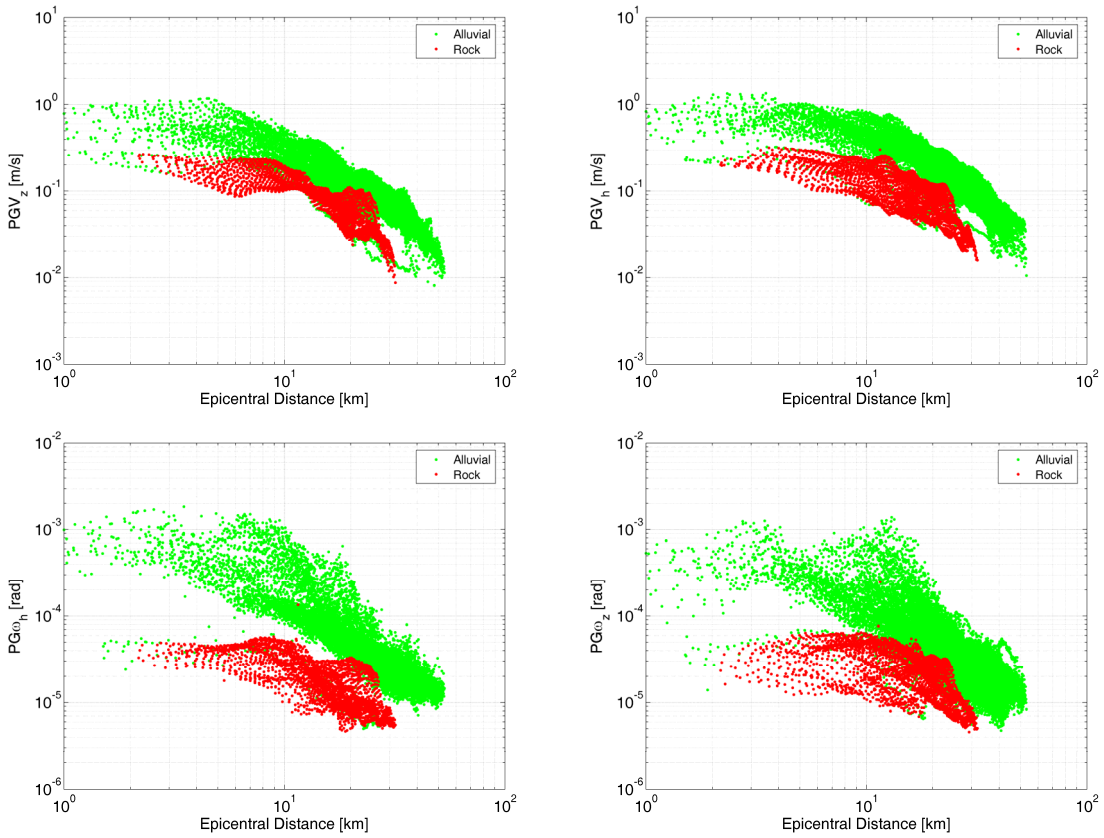

Figure 4.8. Comparison of the decay with distance from the epicentral location of the horizontal and vertical component of peak ground velocities (Top; left hand side: PGV_z, right hand side: PGV_h) and corresponding peak ground rotations (Bottom; left hand side: $PG\omega_h$, right hand side: $PG\omega_z$).

studied in Chapter 3 is presented considering both its horizontal (PGV_h) and its vertical (PGV_z) component, while the spatial variability of peak ground rotations is evaluated presenting the maps of peak ground torsion ($PG\omega_z$) and peak ground rocking ($PG\omega_h$).

The wave propagation pattern inferred by values of PGV both for the translational and vertical direction, shows noticeable directivity off the sides of the fault due to the relatively shallow hypocenter (around 6.5 km) and the obliqueness of the rake (145°). This led to large ground motion amplitudes in the south-western portion of the city. The translational direction of the velocity also shows a directivity "up-dip" toward the city of Christchurch. The spatial variability of strong ground velocity is in reasonable agreement with the spatial distribution of observed damage and liquefaction phenomena. The maps of the corresponding rotational ground motion - namely peak ground torsion ($PG\omega_z$) for the peak ground horizontal velocity (PGV_h) and peak ground rocking ($PG\omega_h$) for the peak ground vertical velocity (PGV_z) - highlight similar characteristics of spatial variability. The effect, that the complex topography of the stiff volcanic rock has in the spatial distribution of peak rotations, that reach higher values on the region of soft soil surrounding

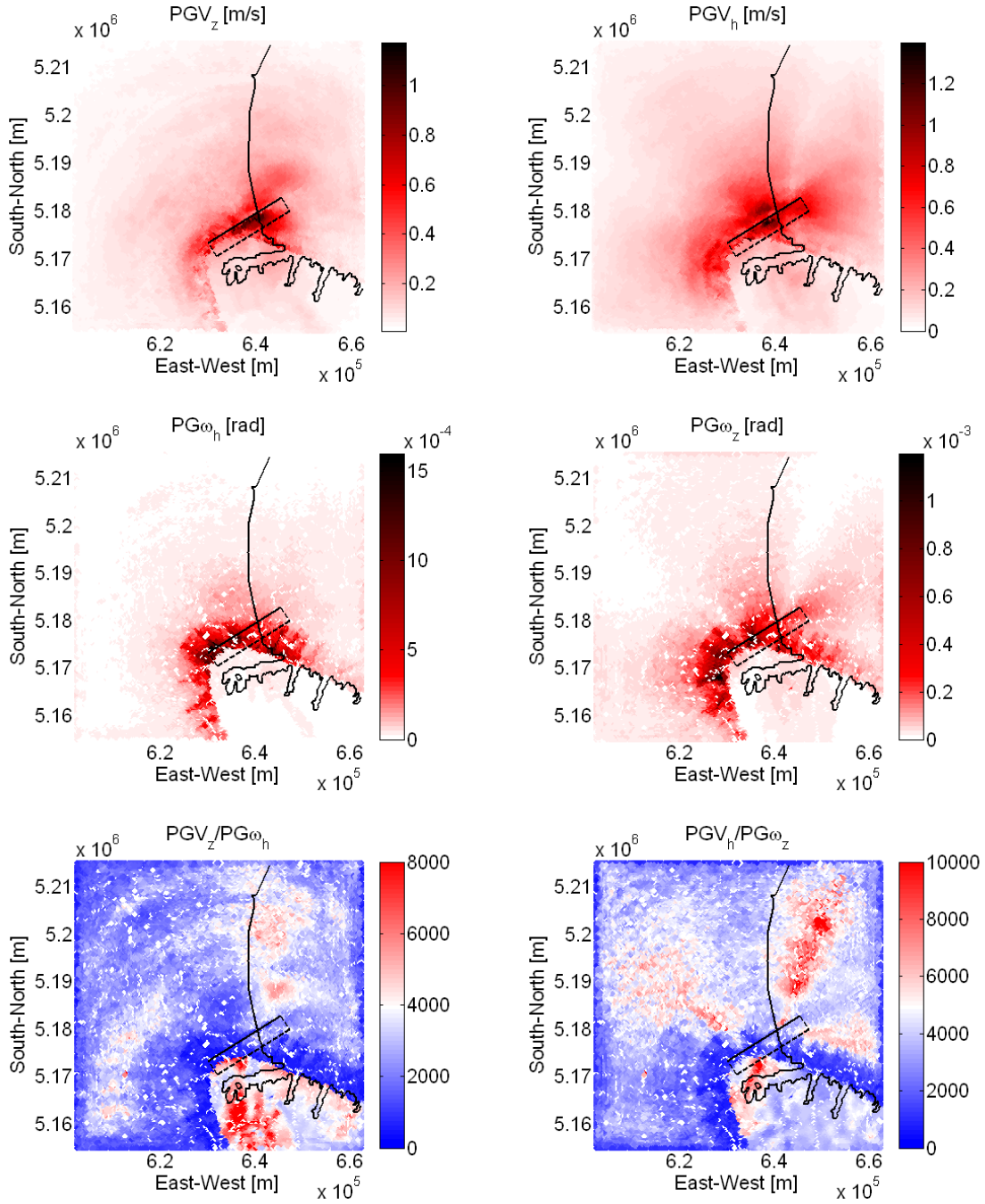

Figure 4.9. Top: Left: Spatial variability of peak ground vertical velocity (PGV_z) as estimated by 3D numerical simulation; Right: Spatial variability of peak ground horizontal velocity (PGV_h, geometric mean of horizontal components). Middle: Left: Spatial variability of peak ground rotation around horizontal axis ($PG\omega_h$, geometric mean of horizontal components); Right: Spatial variability of peak ground rotation around vertical axis ($PG\omega_z$). Bottom: Left: Spatial variability of the ratio between PGV_z and $PG\omega_h$; Right: Spatial variability of the ratio between PGV_h and $PG\omega_z$.

the volcanic rock, characterized by a sharp change of propagation velocity, is particularly evident. The effect of the topographic amplification has been widely investigated in the literature (e.g., Géli et al. 1988, Paolucci et al. 1999). The smooth contact between the soft soil of the basin and the volcanic rock provides a proper representation of the peak rotational values also in the south-western portion of the model. As the map of the peak horizontal velocity, also the $PG\omega_z$ map shows, in addition to the directivity off the side of the fault, an "up-dip" directivity, in the direction normal to the fault.

The similar characteristics of the spatial variability showed by the peak ground values of velocity and rotation is in agreement with the assumption retrieved both by empirical and numerical data that describe a direct correlation between these values, as described in Eq. 4.1 a and b, C being their scaling factor (Wang et al. 2009).

The spatial variability of this scale factor C is addressed in figure 4.9 by its map. Looking at the map, it is possible to clearly distinguish the lower values located in the soft alluvial soil, surrounding the volcanic region: to this sharp change of impedance and, thus, of wave propagation velocity, corresponds a sharp change in the values of the factor C, that assumes higher values outside the basin, on outcropping rock. Higher than expected values of the ratio are also distinguishable, especially looking at the map of the ratio $PGV_h/PG\omega_z$, in the alluvial basin, toward the North and the East. Having the fault system directivity off the side of the fault (direction North-East) and up-dip toward the city, (direction North-West) it is possible to recognize that the regions of the Canterbury Plains characterized by the higher values of the ratio *C* have an angular shift of 45° from this directions, therefore being the less interested by the directivity effects of the fault, in a sort of "cone-of-shadow". On the basis of these considerations the interpretation of *C* as the representative phase velocity could be misleading, especially in the near-field of an earthquake, as pointed out by several authors (e.g., Spudich and Fletcher, 2008, Stupazzini et al. 2009b). *C* could be reasonably considered as a scaling factor between peak rotations and translations, keeping in mind that a large variability of this factor is expected in the near-field region, as showed in Figure 4.9, due to the local site conditions, topographical features and source directivity.

4.5 Concluding remarks

In this chapter semi-empirical and synthetics data has been analyzed in terms of peak ground values, compared with each other and with data from past studies. On the basis of these comparisons it is possible to conclude that:

i) Semi-empirically retrieved data show higher values of synthetics peak rotational ground motions, mainly due to the intrinsic limit of the model to propagate up to frequency higher than 2 Hz and to a linear visco-elastic description of the soil behaviour not able to capture phenomena, such as liquefaction, that could produce sensibly higher values of peak rotations.

ii) Semi-empirically retrieved data and the few available measurements of peak ground rotational motion (Liu et al. 2009, Takeo 2009) are in satisfactory agreement, especially considering the dependence of rotations on distance and that point measurements should be consistently higher.

iii) In the logarithmic plane PGV_h-$PG\omega_z$ synthetics and semi-empirical estimations of rotational motion, superimposed to a wide dataset of past studies of rotations retrieved from literature show a substantial agreement.

iv) Plotted in a logarithmic scale, the ratio between peak ground values of velocity and rotation shows a linear trend, that could be interpreted, at least in far-field region as an equivalent apparent velocity of the system, allowing a quick estimate of the average rotational peak values on the basis of the corresponding values of peak ground velocity.

v) Despite the linear trend inferred by the ratio $PGV_h/PG\omega_z$, a large variability of this ratio is notable, from 1 up to 2 orders of magnitude around the average trend, especially in the near-field of an earthquake.

vi) Looking at the map of the spatial variability of the strong ground motion, peak ground torsion and rocking maps show a significant similarity in their characteristics (topographic effects, source effect, directivity, etc.) with corresponding maps of strong ground horizontal and vertical velocity.

vii) In order to visualize the spatial variability of the correlation factor *C* between PGV_h and $PG\omega_z$, maps of their ratio have been plotted. In the near-field region of an earthquake this ratio has a large variability. This implies that to consider this factor as an equivalent apparent velocity is too simplistic and that average values only are not enough to represent the complex behaviour of rotations at the surface.

In conclusion, in order to define a more accurate relationship between rotational and translational ground motion, more data, in a wider range of magnitudes and epicentral distances, is necessary. It is important to underline the significance of developing direct measurements of the rotational components in the near-field of an earthquake, together with the three translational components of motion. In this way, with a richer set of measured data, it will be possible to have a deeper

understanding of the complex correlation between rotations and translations, explaining the large variability of their ratio, especially in region few kilometres from an earthquake.

CHAPTER 5

FREE FIELD ROTATIONS DURING EARTHQUAKES: RELEVANCE ON CIVIL ENGINEERING STRUCTURES

5.1 Introduction: rotations in structural response

The goal of this chapter is to investigate the relevance of the rotational strong ground motions obtained from the semi-empirical procedure in Chapter 2 and from the three-dimensional numerical model described in Chapter 3 for a series of civil engineering structures. We pursued the goal by obtaining time histories of rotations and their expected maximum values, i) theoretically, recalling the mathematical relationship between the rotational power spectrum and the cross-power spectrum of translational accelerations simultaneously recorded in a closed spaced array of accelerometers; and ii) numerically, using a spectral element technique applied to a three-dimensional simulation of the Christchurch earthquake.

In the previous chapter, a direct comparison of the results obtained with the two approaches, between each other and with data from past studies was presented, in terms of peak ground values and their ratios. This chapter is thus devoted to the evaluation of the relevance of rotational ground motion for different kinds of civil engineering: i) buried pipelines, ii) wind turbines and antennas; iii) high rise versus. squat buildings; and iv) pounding-prone compounds of buildings with different height, at a site-city scale. The present case-study of Christchurch encompasses all these different kind of structures.

In the following section, the wave passage effect is studied for a buried pipeline network in terms of peak ground rotational velocity and acceleration. The crucial role of pipelines and lifelines during

the emergency management and in the recovery phase after an earthquake, has been highlighted by disastrous seismic events, as the 22 February Christchurch earthquake, drawing the attention of the scientific community and of stakeholders. In the next section, a numerical study on a wind tower, located at Gebbie Pass, New Zealand, is presented. This kind of structure, as well as broadcasting antennas, plays a strategic role, especially soon after a seismic event, when the energy and communication demand is of crucial importance. In the fourth section, an example of a high rise building that experienced heavy damages is taken into account, analyzing the possible role of a rotational input motion superimposed to a translational one on its seismic behaviour. Finally, in the fifth section, the complexity of the seismic input is fully considered at a site-city scale, where the Christchurch Central Business District (CBD) is fully modelled numerically, therefore naturally including all the six components of motion, with the aim of evaluating, at the same time, the seismic response of a pounding-prone compounds of buildings and the effect of a densely urbanized area in the spatial variability of strong ground motion.

5.2 Wave passage effect in buried pipelines: the Bazzano, L'Aquila, case.

The strategic role of pipelines and lifelines during emergency management and in the recovery phase has been highlighted by recent disastrous seismic events, as e.g. the 2011 Christchurch or the 2009 L'Aquila earthquakes, drawing the attention of the scientific community (Pitikalis et al. 2006, Castellani and Bonfanti 2007, Dolce et al. 2009).
This section provides experimental evidence on the structural planning of a buried unreinforced concrete pipeline network, under the action of a seismic motion, with reference to the Eurocode 8 (EC8) and to the Italian Code (NTC). The present application is based on the following.

i) The observation of the seismic effects on an important buried pipeline in Bazzano, L'Aquila, surveyed few months after the 2009 earthquake. According to the design procedure described in literature (e.g. Castellani and Bonfanti, 2007) minor damages were expected, and the survey confirms this prediction for a wide portion of the pipeline network. However, some sections experienced more considerable damage, likely due to a slip of the nearby fault of Bazzano or because the so called wave passage effect.

ii) The collection of evidence during the recent Christchurch earthquake, about the curvature and elongations imposed by the earthquake to the ground, retrieved by the semi-empirical study presented in Chapter 2 and by the numerical model described in Chapter 3. This provides experimental data of interest, because the section of EC8 concerning the topic of buried pipelines(Part 1.4 Tanks and Silos Pipelines) does not adopt experimental data, and refers to a simplified theoretically retrieved model of the soil behaviour.

The choice of the buried pipelines of Bazzano, L'Aquila, for consideration was driven by the quantity of experimental evidence in our possession, and because it allows a direct comparison with the case of Christchurch, New Zealand. Both the events (L'Aquila 2009 and Christchurch 2011) indeed show similar features, having same magnitude, M_W 6.3, similar fault dimension and depth of the hypocenter. In addition, as discussed in Chapter 2, the L'Aquila earthquake was also characterized by high values of strong ground motion in the vertical direction (Figure 2.1). Furthermore a huge amount of damage to buried pipelines and lifelines has been observed in Christchurch after the February 2011 earthquake by many authors (e.g., Cubrinovski et al. 2011, Orense et al. 2011).

5.2.1 Seismic effects on buried pipelines

Observing the seismic effects on the buried pipeline network in Bazzano, it is assumed that the pipelines are subjected to the load combination that includes permanent actions and accidental actions due to road traffic, properly factorized. Depending on these factors, the seismic load condition may have a significant effect, on pipeline design. The seismic load conditions listed in the Eurocode for a buried pipeline are the following:

i) Without soil rupture, an horizontal and vertical acceleration field that is superimposed to the gravitational field, acting on the soil and on the load due to the road traffic on the free surface. This combination produces effects generally not significant on pipelines having load conditions including the permanent gravity action and the accidental action due to the road traffic, properly factorized.

ii) In presence of a ground rupture, the "landslide" of a clod increases the horizontal and vertical pressures. This is the load condition that drives the design of the pipeline in the transversal plane and it is usually significant for pipelines in high seismicity areas (zone 1 and 2) and with burying deeper than 3 m.

iii) A different ground motion from point to point induces deformations in a plane that includes the longitudinal axis. This is the design condition for the angle of rotation that has to be tolerated by the gasket between elements. Depending on the distance between the wells, it also defines the maximum elongation that can undergo the gasket between the joints of near elements.

iv) The worst condition is produced by a slip between fault surfaces that propagates up to the surface. An active fault, known as the "fault of Bazzano", is in the place, as depicted in Figure 5.1. Its movement has been monitored, as well as the movement of the more important Paganica fault, having an "antithetical" configuration respect to the Fault of Bazzano.

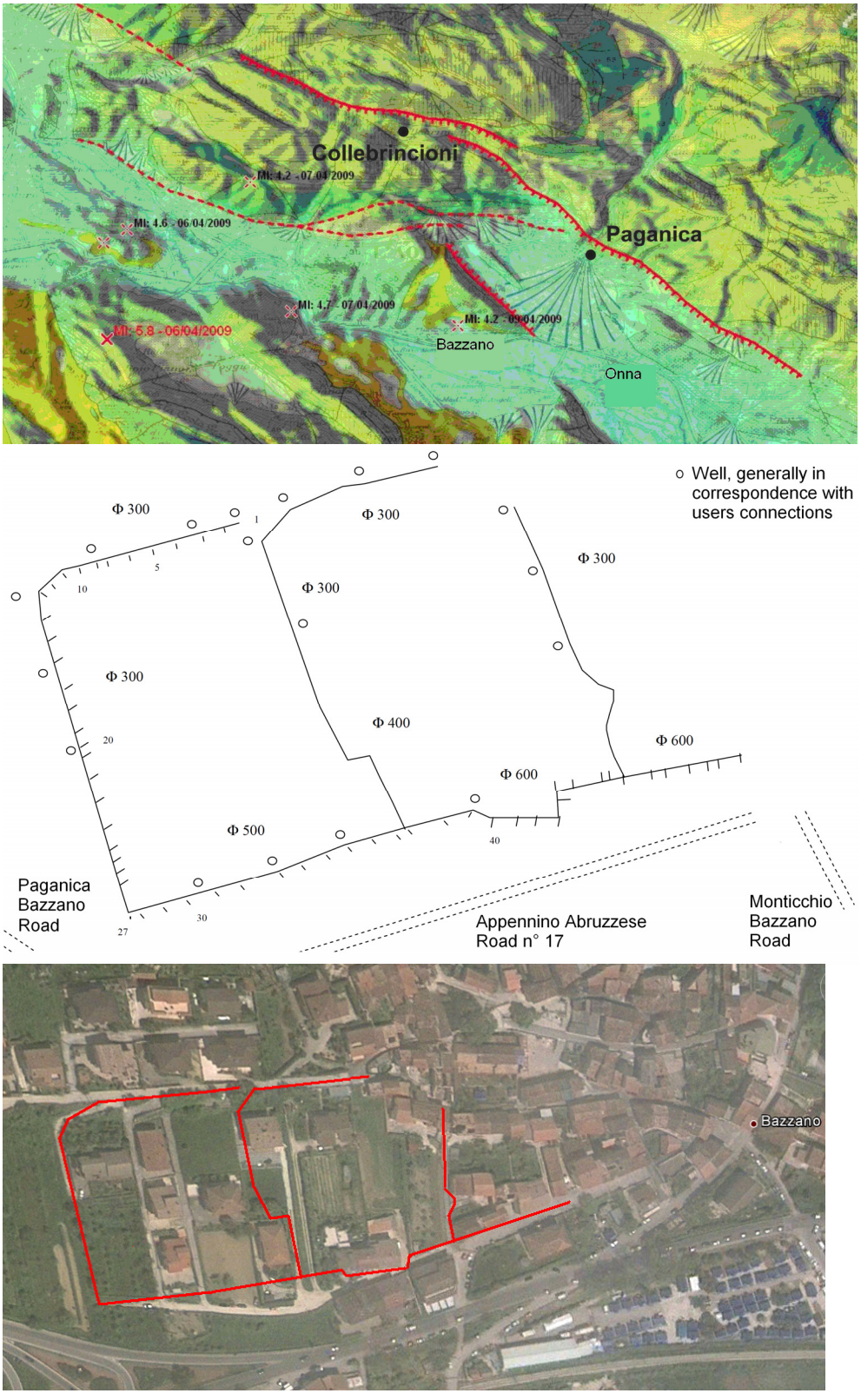

Figure 5.1. Top: Fault of Bazzano and the anthitetical fault of Paganica. Middle: sketch the buried pipeline network of Bazzano, object of the visual inspection through remote-controlled camera; Bottom: pipeline network scheme superimposed to the aerial view of the urbanized area of Bazzano.

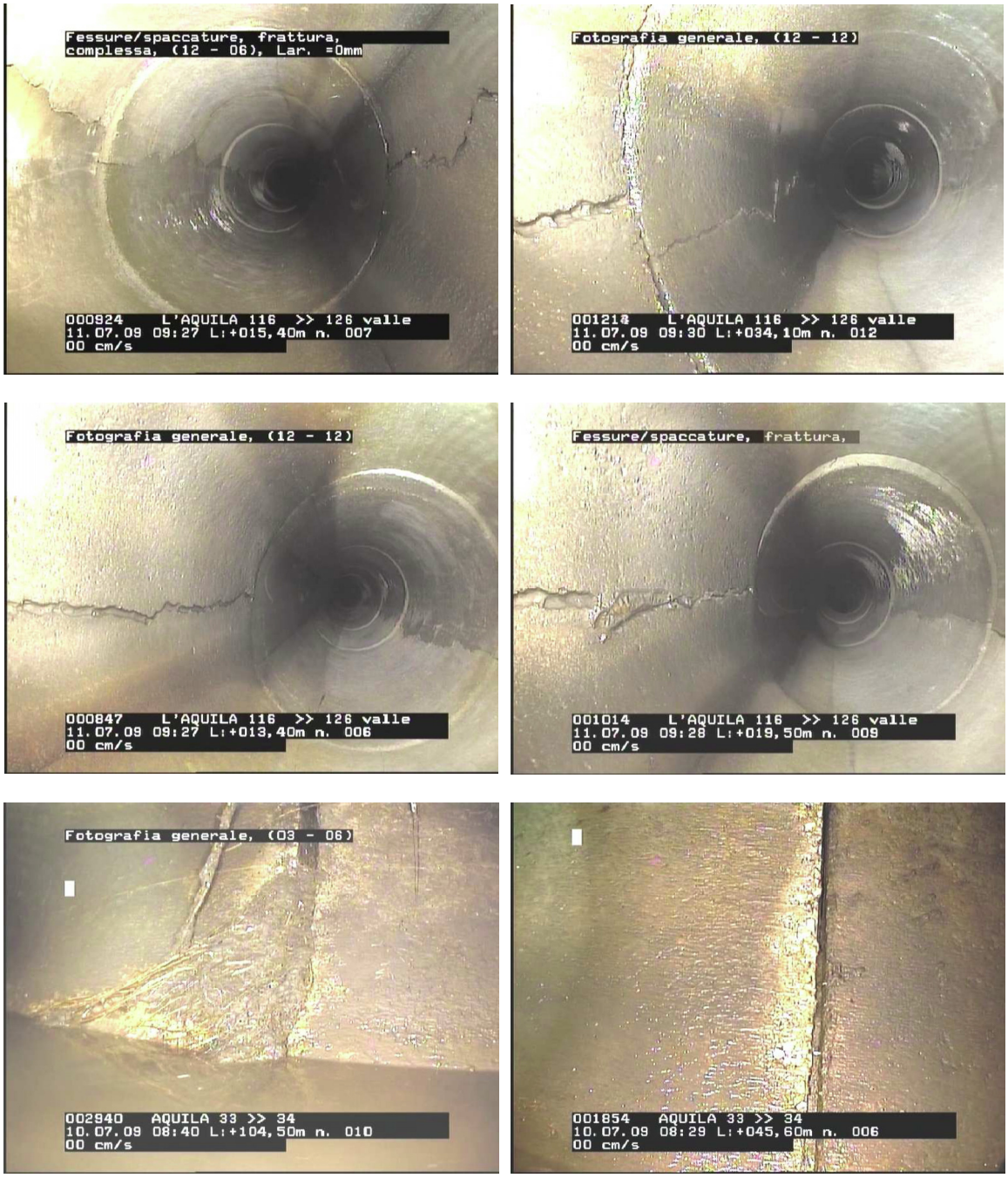

Figure 5.2. Pictures from the visual inspection through a moving remote-controlled camera of the buried pipeline network of Bazzano, L'Aquila. Pictures in Top and Middle row present an horizontal crack that could be explained with the increase of the pressure due to a landslide of a soil clod, while pictures in the Bottom row could be due to a different ground motion from point to point (wave passage effect) or to a fault movement.

It could be possible to ascribe the main damages experienced by the pipeline network to the fault of Bazzano movement, during the M_W 6.3 L'Aquila earthquake of April 2009, even though a certain measure of the fault movement should be retrieved, in order to better explain the major damages observed. In the present application we will analyze on the basis of the procedure presented in Chapter 2 the third point of the aforementioned list, namely the seismic effect induced in a buried pipelines by a ground motion different from point to point.

5.2.2 Seismic behaviour of the buried pipeline network of Bazzano during the 2009 L'Aquila earthquake: direct observation of damages

A few kilometres from the city of L'Aquila, in the city of Bazzano, a survey using a moving remote-controlled camera, examined an important buried pipeline network, depicted in Figure 5.1 (Assobeton, 2009). It is composed of un-reinforced concrete circular pipes having diameters varying from 300 to 600 mm, with average burying of around 3 m.

The seismic effect due to the landslide of a clod increasing the horizontal and vertical pressures (point ii of the list in section 5.1.1) has been recently addressed by Castellani et al. (2012b), concluding that, respecting the load conditions of the permanent gravitational action and of the accidental action of the road traffic, properly factorized, the pipelines should carry the seismic action (characterized by PGA = 0.15g), without any damage, or with only minor damages. It is important to underline two possible sources of uncertainty: i) the buried pipelines, built between pre-existent roads (Figure 5.1), could not have taken into account the possibility of having a road traffic load; ii) the soil is assumed to be of type B, according the Eurocode classification. A less stiff soil, e.g., type C or D, accentuates the differences between static and seismic conditions.

The whole set of direct observations of the buried pipeline consists of several hundred pictures and the most significant are showed in Figure 5.2. It is possible to notice cracks parallel to the longitudinal direction of the pipe, with an inclination of around $\pm 20°$ from the horizontal, and noticeable joint deformation.

5.2.3 Wave passage effect according to Eurocode 8

Listed as third effect in section 5.1.1 a different ground motion from point to point maximizes the bending action in the longitudinal plane, due to a different seismic motion along the longitudinal axis. This is referred as wave effect in Eurocode 8, par. 4 and it is sketched in Figure 5.3. This motion, differing from point to point, bends the pipe imposing a curvature and a relative displacement. Maximum values of curvature and displacement, in function of the seismicity and of the mechanical characteristics of the soil, determines the conditions for testing the joints between contiguous elements.

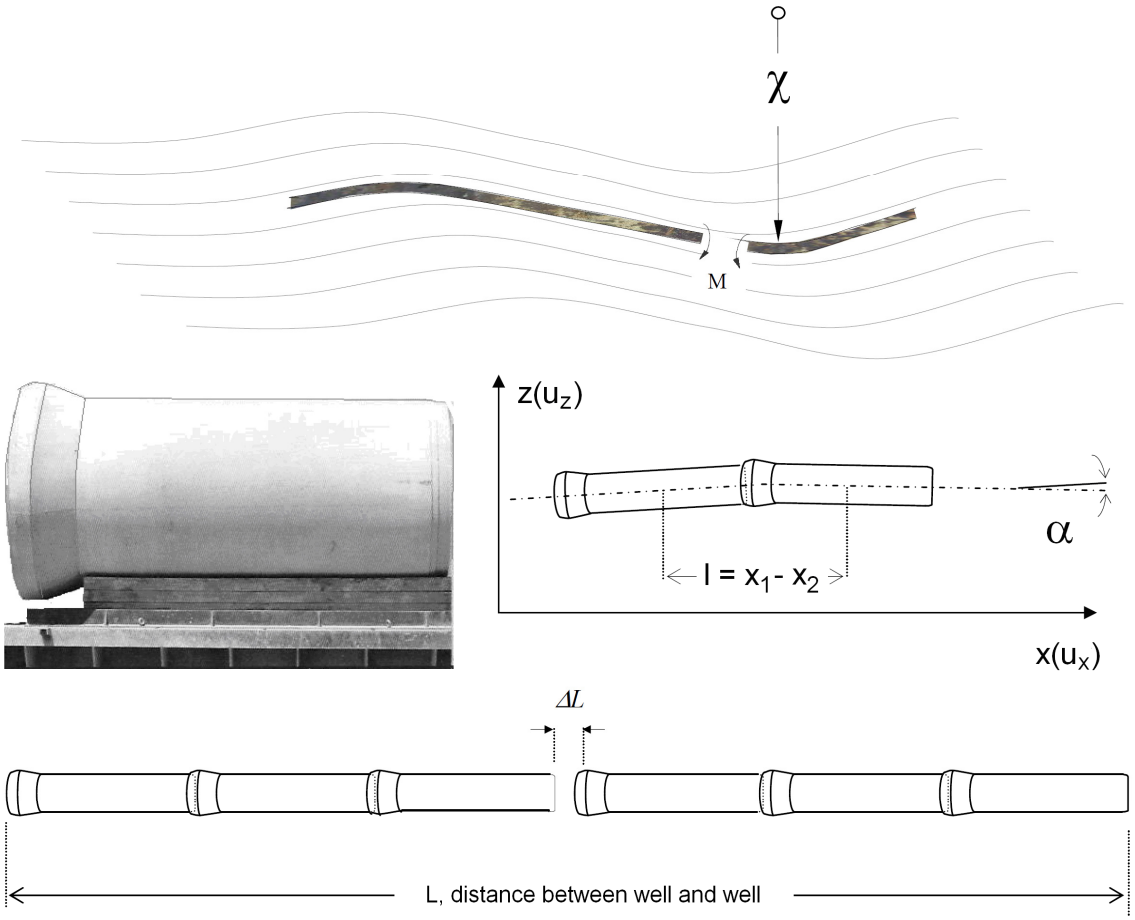

Figure 5.3. Description of the wave passage effect. Top: A different ground motion from point to point maximizes the bending action in the longitudinal plane, imposing curvature and longitudinal action to the pipeline. Middle: Picture of a pipe and sketch of the curvature effect, producing an angle a between consequent elements. Bottom: sketch of the elongation effect with detachment of the gasket.

5.2.3.1 Longitudinal action

The value of the relative displacement ΔL between two points in the longitudinal direction (Figure 5.3) can be evaluated in the following way:

$$\Delta L = \varepsilon_r L, \qquad (5.1)$$

where L is the distance between the two points and r is the unit strain, given by:

$$\varepsilon_r = d_g \frac{\sqrt{2}}{L_g}, \qquad (5.2)$$

Table 5.1. Soil maximum displacement, in meters, as a function of the local seismicity and the soil mechanical characteristics. In bold the value that refers to Bazzano.

Soil Type	$d_g = 0.025\ a_g\ S\ T_C\ T_D$			
	Zone 1	Zone 2	Zone 3	Zone 4
A	0.0858	0.0613	0.0368	0.0123
B	0.1030	0.0736	**0.0442**	0.0147
C	0.1184	0.0846	0.0508	0.0169
D	0.1854	0.1324	0.0795	0.0265
E	0.1202	0.0859	0.0515	0.0172

Table 5.2. Strain ε_r as a function of the local seismicity and of the mechanical characteristics of the soil. In bold the value that refers to Bazzano.

Soil Type	L_g [m]	$\varepsilon_r = 2^{0.5}\ d_g/L_g$			
		Zone 1	Zone 2	Zone 3	Zone 4
A	*600*	2.02E-04	1.44E-04	8.67E-05	2.89E-05
B	*500*	2.91E-04	2.08E-04	**1.25E-04**	4.16E-05
C	*400*	4.19E-04	2.99E-04	1.79E-04	5.98E-05
D	*300*	8.74E-04	6.24E-04	3.75E-04	1.25E-04
E	*500*	3.40E-04	2.43E-04	1.46E-04	4.86E-05

where d_g is the maximum ground displacement (Table 5.1) and L_g is the distance beyond which the ground motion can be considered uncorrelated. If the distance between the two points is lower than L_g, ΔL is proportional to the absolute displacement d_g; otherwise if L is greater than L_g, ΔL is given by:

$$\Delta L = \varepsilon_r L_g = d_g \sqrt{2}\ . \qquad (5.3)$$

Values of L_g, for the different soil type are listed in Table 5.2 together with the values of ε_r as a function of the seismicity and of the soil characteristics, obtained from Eq. 5.2. The stresses corresponding to the longitudinal strains are given by:

$$\sigma_{long} = E \cdot \varepsilon_r \qquad (5.4)$$

Since the elastic modulus E of the concrete equal to 30,000 MPa, from data collected in Table 5.2, we obtain stress values for the pipelines network of Bazzano, assuming soil type B, equal to 1.25 MPa and 3.75 MPa, in zones 4 and 3, respectively. These values are greater than the available resistance, but, the presence of a joints, where the deformation can be released, tends to nullify the stresses. Considering a straight pipe of length L, the strain can be concentrated only on one joint, computing a value ΔL (Eq. 5.3). In the case under study, the distance between wells is around 50 m, we obtain ΔL = 6 mm.

Table 5.3. Curvature, in m^{-1}, as a function of the local seismicity and of the mechanical characteristics of the soil, considering values of apparent velocity C from the literature (Castellani and Boffi, 1989). In bold the value that refers to Bazzano.

Soil Type	C [m/s]	$\chi = d_g/C^2$ Zone 1	Zone 2	Zone 3	Zone 4
A	*1000*	8.58E-08	6.13E-08	3.68E-08	1.23E-08
B	*825*	1.51E-07	1.08E-07	**6.49E-08**	2.16E-08
C	*650*	2.80E-07	2.00E-07	1.20E-07	4.00E-08
D	*475*	8.22E-07	5.87E-07	3.52E-07	1.17E-07
E	*300*	1.34E-06	9.54E-07	5.72E-07	1.91E-07

5.2.3.2 Curvature

In order to retrieve the curvature value, an estimate of the apparent velocity C is required. An infinite value for the apparent velocity C implies simultaneously identical motion at any point of the surface. The lower the value of this velocity, the stronger the strain on the joints. As a function of the different seismicity and soil condition, Table 5.3 lists maximum values of curvature, assuming the apparent velocity *C* values retrieved from the literature and generally considered as conservative (Castellani and Boffi, 1989). The angle between element and element (Figure 5.3) is equal to:

$$\alpha = \chi \cdot l\,, \qquad (5.5)$$

where *l* is the length of the pipe. Varying *l* generally between 2 and 8 m, the curvature listed in Table 5.3 determine values of α always lower than 1°, even in high seismicity areas.

5.2.4 Variability of the apparent velocity and limit of the Eurocode approach

In the previous section the model provided by Eurocode 8 for the estimation of the wave passage effect has been presented. Both curvature and maximum elongation evaluated in this way provide values that can easily carried by the gaskets. However, after a seismic event it is common to observe malfunctioning, detachment and failure of pipelines, as in the cases of Bazzano and Christchurch. This evidence suggests that model proposed by the Eurocode could be too simplistic. The approach of the Eurocode is based on the representation of the ground motion *u(t,x)* as an harmonic wave having frequency *f*, amplitude *d* and propagating at surface with apparent velocity *C*:

$$u(x,t) = d\sin\left[f\left(t - \frac{x}{C}\right)\right]. \qquad (5.6)$$

Deriving respect to the spatial coordinate *x*, along the direction of the pipeline, it is possible to obtain the slope (tilt) of the ground:

$$\frac{\partial u}{\partial x} = \frac{fd}{C}\cos\left[f\left(t - \frac{x}{C}\right)\right]. \tag{5.7}$$

Deriving respect to time *t* it is possible to obtain the velocity of such slope:

$$\frac{\partial}{\partial t}\left(\frac{\partial u}{\partial x}\right) = -\frac{f^2 d}{C}\sin\left[f\left(t - \frac{x}{C}\right)\right], \tag{5.8}$$

having maximum value equal to:

$$\left.\frac{\partial^2 u}{\partial t \partial x}\right|_{\max} = \frac{f^2 d}{C}. \tag{5.9}$$

The product $f^2 d$ represents the peak ground acceleration (PGA). The quantity at the left hand side of Eq. 5.9 is the peak ground rotational velocity (PRV), extensively studied in Chapter 4. It is thus possible to rewrite equation Eq. 5.9 as:

$$PRV = \frac{PGA}{C}, \tag{5.10}$$

in a format analogue to Eq. 1.15 a, b and Eq. 4.1 a, b. In this way it is possible to compare, in terms of *C*, prescription of the Norms with our experimentally (semi-empirically or synthetically) retrieved data, as extensively discussed in Chapter 4.

5.2.5 3D numerical study of the Bazzano pipeline network

A numerical simulation of the M_W 6.3 L'Aquila earthquake on 6 April 2009 has been performed, relying on the three-dimensional numerical model described in Smerzini (2010) and Smerzini and Villani (2012), including the description of the Aterno Valley and the causative Paganica fault. A set of 20 monitors has been located in correspondence of the pipeline network of Bazzano with spacing of around 50 m (Figure 5.4). Table 5.4 lists synthetics peak values of longitudinal strain, velocity (geometric mean of the horizontal components) and rotation around the vertical axis. Synthetics values of strain are in overall agreement with the values presented in Table 5.3,

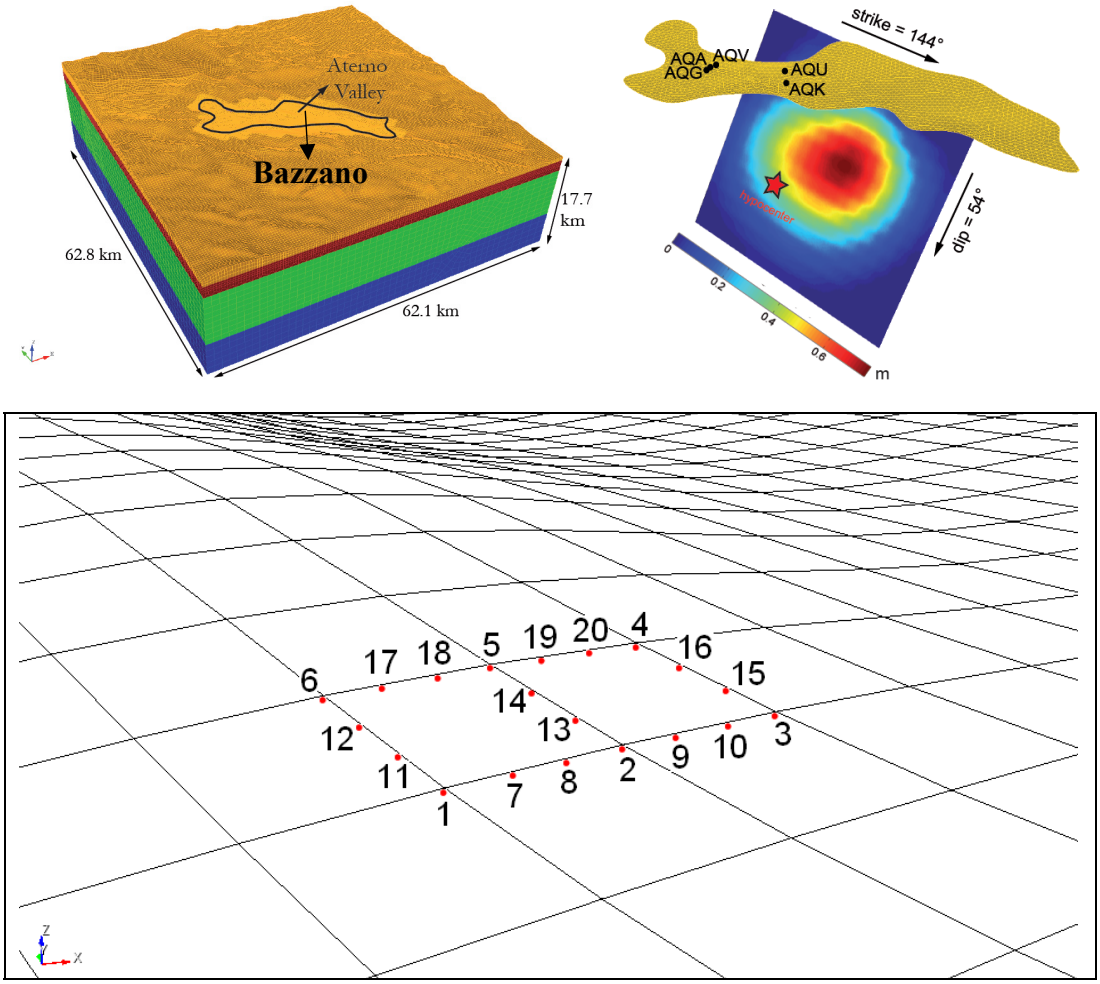

Figure 5.4. Top: 3D numerical model introduced, validated and described in Smerzini (2011) and Smerzini and Villani (2012), including the Aterno Valley and the causative Paganica fault. Bottom: set of 20 receivers located in correspondence of the Bazzano pipeline network (Figure 5.1).

considering soil type B and zone 3, with a maximum value equal to 1.38 10^{-4}: it corresponds to a value of stress equal to 4.13 MPa and a value of ΔL equal to 7 mm.

In Table 5.4 the values of C in m/s, resulting from equation 4.1b, have been evaluated for the 20 monitors considered. Values of C estimated in this way are much greater than the value assumed in Table 5.3, equal to 850 for soil type B, and a large variability of these values between 3,500 and 7,000 is registered in a relatively small area.

The evaluation of peak ground velocity (PGV) values allows us to quantitatively assess the earthquake impact on the pipeline network of Bazzano. It is commonly measured in terms of the Repair Rate (RR), the number of pipelines repairs in an area divided by the length of the pipelines in the same area. Several fragility relations proposed in the literature are listed in Table 5.5 as a function of the peak ground velocity. PGV is indeed correlated with the ground strain that can be transferred to the pipeline and a good correlation between PGV and damage is expected

Table 5.4. Peak Ground Velocity (geometric mean of the horizontal components) and strain ε_r in correspondence of the 20 sections of the pipeline network depicted in Figure 5.1, retrieved from the 3D numerical model of L'Aquila (data filtered between 0.1 and 2.0 Hz).

Section	ε_r	PGV_h [m/s]	$PG\omega_z$ [rad]	C [m/s]
1	1.38E-04	1.84E-01	2.12E-05	4324
2	1.01E-04	2.06E-01	1.73E-05	5936
3	1.04E-04	2.27E-01	1.57E-05	7237
4	9.83E-05	2.39E-01	2.88E-05	4151
5	9.99E-05	2.18E-01	3.12E-05	3489
6	1.02E-04	1.93E-01	2.68E-05	3610
7	1.14E-04	1.92E-01	2.05E-05	4673
8	1.02E-04	1.98E-01	1.71E-05	5798
9	1.03E-04	2.13E-01	1.72E-05	6199
10	1.05E-04	2.20E-01	1.66E-05	6622
11	9.02E-05	1.88E-01	1.93E-05	4862
12	6.60E-05	1.91E-01	2.28E-05	4192
13	7.04E-05	2.11E-01	2.07E-05	5096
14	5.88E-05	2.15E-01	2.52E-05	4280
15	5.95E-05	2.32E-01	1.89E-05	6143
16	5.46E-05	2.36E-01	2.28E-05	5180
17	1.03E-04	2.01E-01	2.86E-05	3521
18	1.02E-04	2.09E-01	3.01E-05	3477
19	1.00E-04	2.25E-01	3.04E-05	3700
20	9.93E-05	2.32E-01	2.97E-05	3903

Table 5.5. Repair Rate - Peak Ground Velocity pipelines fragility relations proposed in the literature, together with the estimated Repair-Rate range of values for the Bazzano pipeline network, corresponding to the synthetically retrieved PGV range of values, between 18.35 and 23.9 cm/s.

Authors	Fragility relation	RR-range [per km]
Eidinger et al., 1998	$0.0001658 \cdot PGV^{1.98}$	0.053-0.089
M. O'Rourke and Ayala, 1993	$0.0001 \cdot PGV^{2.25}$	0.070-0.126
T. O'Rourke and Jeon, 1999	$0.0011 \cdot PGV^{1.22}$	0.038-0.053
Isoyama et al., 2000	$0.00311 \cdot (PGV - 15)^{1.3}$	0.015-0.053
T. O'Rourke et al., 2001	$e^{1.55 \ln PGV - 8.15}$	0.026-0.040
Am. Lifeline Alliance, 2001	$0.002416 \cdot PGV$	0.044-0.058

(Esposito et al, 2011). In Table 5.5 the range of RR corresponding to the range of PGV evaluated by the numerical simulation is presented, giving a quantitative estimation of damage, with a peak value of Repair Rate equal to 0.126 (12.6%), in agreement with the observed level of damage (Castellani et al. 2012b).

5.2.6 Concluding remarks

In this section the wave passage effect has been studied for a buried pipeline network located in the city of Bazzano, a few kilometres from the city of L'Aquila. The comparison between the Eurocode prescription with experimental and numerical data is apparently good. Thus, the Eurocode

assumption is generally trustworthy for a large number of cases, as long as it is limited to the far-field region, where the assumption of harmonic wave propagation could be reasonable. Experimental evidence, such as the case of the visual survey of the pipeline network of Bazzano and the semi-empirical and numerical studies of the Christchurch event discussed in the present work as well the three-dimensional numerical study of the pipeline network, suggest that in the near-field region of an earthquake, the Eurocode assumption turns to be too simplistic, since a large variability of the ratio can be expected, due to the local site conditions, topographical features and source directivity.

This strong variability of the ratio between rotational and translational ground motion could help to explain the failures observed at the joints of the pipeline network of Bazzano, and more generally the malfunctioning, detachment and failure of the gaskets of buried pipelines, typically observed after an earthquake. It could be assessed with further studies and more direct measurements of the rotational ground motion, especially in near-field region.

5.3 The Gebbie Pass Wind Tower, Christchurch: relevance of rotational ground motion for simple oscillator structural models

Around 15 km south west of the epicentre of the 22 February Christchurch earthquake, in the Lyttelton-Akaroa volcanic region of the Banks Peninsula, at Gebbie Pass, a 30 m tall wind tower is situated. From pictures presented in Figure 5.5. showing the tower some days before and after the earthquake, it is possible to observe the good seismic response of this structure.

In order to model the earthquake response of this kind of structures, which could be considered as simple oscillators, to translational and rotational motion, we adopted a simplified four degree of freedom model and a Finite Element simulation, considering and comparing in both cases the response of the structure to simple translational motion and to the rotational motion superimposed to the translational one.

Since a recorded station was located on outcropping rock, at Mc Queen Valley (MQZ), a few hundreds of metres from the Gebbie Pass, the translational seismic input on the tower is assumed to be known.

5.3.1 Four degrees of freedom oscillator: the Chopin model

The mathematical model introduced by Paolucci in 1997 and developed by Figini et al. (2011) for dynamic soil-structure interaction analyses has been adopted and modified ad hoc, introducing the possibility of considering, in the input definition, a rotational acceleration in addition to the translational ones.

Figure 5.5. Before (09/03/2010, left-hand side) and after (23/02/2011, right-hand side) earthquake satellite pictures of the 500 kilowatt wind turbine located at Gebbies Pass, around 15 km south west of the epicentre of the 22 February Christchurch earthquake. The two pictures show the good seismic response of the structure.

The superstructure is modelled with one degree-of-freedom (DOF) while the isolated shallow foundation with three DOF (horizontal and vertical motion and rocking around its centre of mass): the resulting simplified model acts as a four DOF oscillator.

Linear behaviour is assumed for the superstructure, and, within the limits of the present application, the foundation behaviour is modelled as visco-linear, with springs and dashpots, with values of stiffness and damping retrieved from the literature as a function of the foundation dimension and of the mechanical characteristics of the soil (Gazetas 1991, Nova and Montrasio 1991). In particular, in the case in which the wind tower is located on outcropping rock a fixed base model could be adopted and the 4-DOF system could be simplified to a single degree of freedom (SDOF). In Figure 5.6 the 4-DOF model is sketched, together with its simplified version for a SDOF with a fixed base.

5.3.1.1 Theoretical outline of the method

The total horizontal displacement x^{tot} of the mass m_1 in the 4-DOF model in Figure 5.6 is made up of three parts: a rigid-body component associated with the displacement of the ground x_g and with its rotation $h\theta_g$, where h is the height of the mass above the base, the rigid-body component associated with the displacement x_0 and with the rocking motion $h\varphi$ of the basement and the relative motion x^{def} between the mass m_1 and the base with mass m_0 associated with structural deformation. The latter two parts constitute the displacement of the structure x_1 relative to the foundation soil.

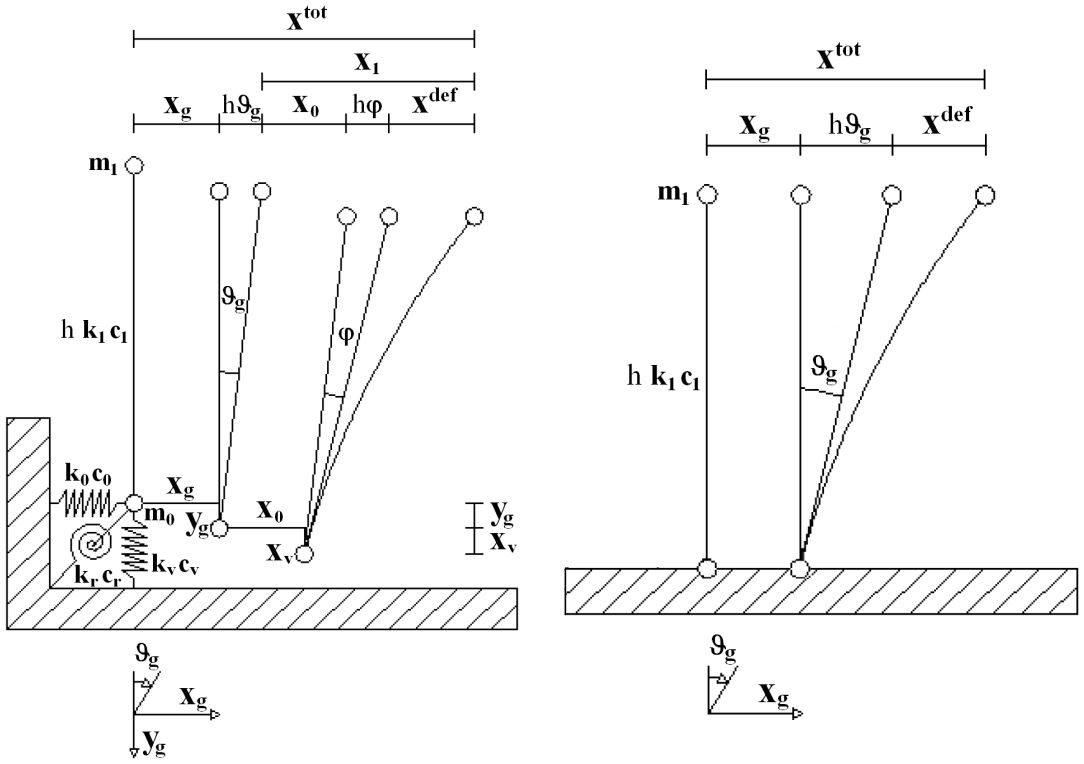

Figure 5.6. 4-DOF model for dynamic soil-structure interaction analyses taking into account rotational ground motion (left hand side) and its simplified version for SDOF with fixed base (right hand side).

The dynamic equilibrium of the 4-DOF system in Figure 5.6 is described by the following set of equations:

$$\mathbf{M}\ddot{\mathbf{x}} + \mathbf{C}\dot{\mathbf{x}} + \mathbf{K}^{S}\mathbf{x} + \mathbf{F} = \mathbf{p}\,, \tag{5.11}$$

where:

$$\mathbf{x} = \begin{bmatrix} x_1 & x_0 & \varphi & x_v \end{bmatrix}^T; \tag{5.12}$$

$$\mathbf{F} = \begin{bmatrix} 0 & H & M & V \end{bmatrix}^T; \tag{5.13}$$

$$\mathbf{p} = \begin{bmatrix} -m_1\left(\ddot{x}_g + h\ddot{\vartheta}_g\right) & -m_0\ddot{x}_g & -J\ddot{\vartheta}_g & -\left(m_1 + m_0\right)\ddot{y}_g \end{bmatrix}^T; \tag{5.14}$$

$$\mathbf{M} = \begin{bmatrix} m_1 & 0 & 0 & 0 \\ 0 & m_0 & 0 & 0 \\ 0 & 0 & J & 0 \\ 0 & 0 & 0 & m_1 + m_0 \end{bmatrix}; \tag{5.15}$$

$$\mathbf{C}=\begin{bmatrix} c_1 & -c_1 & -c_1\tilde{h} & 0 \\ -c_1 & c_1+c_0 & c_1\tilde{h} & 0 \\ -c_1\tilde{h} & c_1\tilde{h} & c_1\tilde{h}^2+c_r & 0 \\ 0 & 0 & 0 & c_v \end{bmatrix}; \qquad (5.16)$$

$$\mathbf{K}^S=\begin{bmatrix} k_1 & -k_1 & -k_1\tilde{h} & 0 \\ -k_1 & k_1 & k_1\tilde{h} & 0 \\ -k_1\tilde{h} & k_1\tilde{h} & k_1\tilde{h}^2 & 0 \\ 0 & 0 & 0 & 0 \end{bmatrix}. \qquad (5.17)$$

The vector of structural elastic forces is separated from *F*, containing the soil restoring forces; in the assumption of linear visco-elastic behaviour of the soil-foundation system the vector of soil reactions can be obtained by the following relation:

$$\mathbf{F}_{n+1}=\mathbf{F}_n+\mathbf{K}^i\left(\mathbf{x}_{n+1}-\mathbf{x}_n\right), \qquad (5.18)$$

where

$$\mathbf{K}^i=\begin{bmatrix} 0 & 0 & 0 & 0 \\ 0 & k_0 & 0 & 0 \\ 0 & 0 & k_r & 0 \\ 0 & 0 & 0 & k_v \end{bmatrix}, \qquad (5.19)$$

with k_0, k_r and k_v representing equivalent elastic spring coefficients of the soil-foundation system, respectively associated with translational, rocking and vertical modes of vibration. Under the hypothesis of shallow foundations, no coupling terms have been introduced.

As previously stated, in the case of the tower located on outcropping rock, a fixed base model is adopted and the 4-DOF system could be simplified in an SDOF model, as presented in Figure 5.6. In this case the dynamic equilibrium of the system is given, with the same meaning of symbols, by the following equation:

$$m_1\ddot{\mathbf{x}}+c_1\dot{\mathbf{x}}+k_1\mathbf{x}=-m_1\left(\ddot{x}_g+h\ddot{\vartheta}_g\right). \qquad (5.20)$$

Table 5.6. Main characteristic values of the three different wind towers lumped mass models adopted in the parametric analysis, together with the values adopted for the mass, stiffness and damping matrix.

			Wind Tower 1	Wind Tower 2	Wind Tower 3
Height	**H**	**[m]**	30.00	45.00	60.00
Diameter	**D**	**[m]**	2.00	3.00	4.00
Foundation width	**B**	**[m]**	4.00	7.00	10.00
Fundamental Period	**T**	**[sec]**	0.999	0.988	1.037
Equivalent spring coefficients	k_h	**[kN/m]**	1.923E+06	2.696E+06	3.439E+06
	k_v	**[kN/m]**	1.499E+06	2.374E+06	3.238E+06
	k_r	**[kNm]**	9.240E+06	3.306E+07	8.114E+07
Equivalent dashpot coefficients	c_h	**[Ns/m]**	1.706E+07	3.741E+07	6.425E+07
	c_v	**[Ns/m]**	1.794E+07	4.361E+07	7.975E+07
	c_r	**[Nsm]**	4.392E+07	2.547E+08	8.658E+08

5.3.1.2 Parametric study

In order to have a wider view of the relevance of rotational input for the wind tower a parametric analysis has been conducted, considering three different models having different values of height, diameter and foundation width. For each of these models, a set of nineteen locations is considered, in correspondence with the different recording stations. The first model is the closer in size to the Gebbie Pass wind tower, having height of 30 m, diameter of to 2 m and foundation width of 4 m, with a resultant fundamental period of around 1 s. The main characteristic values of the three different wind tower models, together with the values adopted for the mass, stiffness and damping matrix, are synthesized in Table 5.6.

For a lumped mass model, the top displacement of the model is adopted as a characteristic parameter for evaluating the incidence of the rotational ground motion input in addition to the translational one. Furthermore, since the model is naturally though as two-dimensional, the East-West (EW) and North-South (NS) component of motion are considered separately, and consistent with the respective vertical motion and the rocking motion.

Top displacements obtained with semi-empirically retrieved rotational accelerations are compared with top displacements obtained using synthetic rotational acceleration inputs. The results are listed in Table 5.7 for the first model. Top displacement obtained at two of the twenty different locations are presented in Figures 5.7 and 5.8 in terms of time history, in order to visualize the effect of the rocking component in the two translational dimensions and with an odometric scheme, in order to highlight the differences in the EW-NS plane. The two sites considered in Figures 5.7 and 5.8, are at Mc Queen Valley (MQZ) station on outcropping rock, close to the effective location of the Gebbie Pass wind tower, and at PRPC, on alluvial soil.

Table 5.7. Top displacement obtained with synthetically and semi-empirically retrieved rotational accelerations, considering the two horizontal direction of motion and a translational (T) and a roto-translational (R-T) input, for the Wind Tower 1 model (see Table 5.6).

Top Displacement		GeoELSE						Semi-empirical					
		EW			NS			EW			NS		
Stations	Re [km]	T [cm]	R-T [cm]	Δ [%]	T [cm]	R-T [cm]	Δ [%]	T [cm]	R-T [cm]	Δ [%]	T [cm]	R-T [cm]	Δ [%]
HVSC	*1*	*3.09*	*3.10*	*0.09*	*7.05*	*7.07*	*0.21*	*19.36*	*19.72*	*1.86*	*21.33*	*21.34*	*0.04*
LPCC	*4*	*8.84*	*8.89*	*0.56*	*3.92*	*3.92*	*0.11*	*12.23*	*12.28*	*0.44*	*5.49*	*5.70*	*3.69*
PRPC	6	23.13	23.44	1.37	29.39	30.32	3.17	15.09	16.70	10.70	16.37	17.41	6.36
CCCC	6	16.62	16.81	1.19	25.86	26.34	1.86	20.92	22.17	5.97	20.17	21.11	4.69
REHS	8	11.35	11.67	2.83	13.44	13.80	2.68	54.77	55.41	1.17	37.10	38.49	3.76
CHHC	8	15.45	15.60	0.99	15.52	15.70	1.17	22.38	22.40	0.09	27.04	27.18	0.51
CBGS	9	10.33	10.35	0.23	9.34	9.53	1.96	22.00	22.99	4.47	24.83	25.72	3.56
SHLC	9	20.41	20.87	2.25	14.05	14.28	1.68	28.82	29.31	1.72	34.02	34.31	0.85
HPSC	9	24.95	25.42	1.86	20.04	21.13	5.42	17.09	18.21	6.60	8.73	8.82	1.03
PPHS	12	9.37	9.47	1.15	12.18	12.28	0.78	12.06	12.45	3.23	14.06	14.17	0.77
SMTC	14	10.02	10.09	0.69	11.01	11.28	2.49	15.13	15.68	3.67	12.49	12.98	3.85
MQZ	*15*	*0.95*	*0.97*	*2.26*	*1.71*	*1.75*	*2.65*	*2.89*	*2.90*	*0.41*	*0.92*	*1.01*	*10.05*
CACS	18	3.46	3.49	0.85	6.47	6.59	1.92	6.46	6.91	6.99	4.54	5.09	12.19
LINC	19	9.95	9.98	0.36	17.51	17.60	0.52	2.86	2.97	3.70	9.68	10.13	4.68
KPOC	23	7.63	7.76	1.79	6.46	6.52	0.93	6.18	6.19	0.15	3.69	3.81	3.23
ROLC	26	4.06	4.06	0.07	11.53	11.77	2.11	1.66	1.67	1.02	3.32	3.36	1.26
SWNC	29	3.45	3.47	0.42	3.89	3.89	0.08	2.48	2.57	3.86	2.89	3.00	3.54
ASHS	35	4.44	4.47	0.65	3.17	3.22	1.53	1.82	1.84	1.11	1.34	1.54	15.55
CSTC	39	2.78	2.79	0.56	1.82	1.87	3.04	1.81	2.11	16.43	3.15	3.51	11.34

From the analysis of data presented in Table 5.7 and from the diagrams in Figures 5.7 and 5.8 it is possible to note that the percentage differences between the top displacement evaluated considering the rotational component of motion in addition to the translational component, range up to around 15% in some locations, suggesting that in some cases, the rotational component could play an important role in the seismic response of these structures; in particular, considering the reference station MQZ, on outcropping rock, a maximum difference of around 10% is estimated along the NS direction. Furthermore, an overview of the results suggests that the relative importance of considering the rotational component of motion is not attenuated by the distance from the epicentre, but also models located further (up to 40 km) from the epicentre present high values of percentage differences.

Results presented in Table 5.7, however, show an average incidence of the rotational component less than 3% for the results obtained with GeoELSE and around 5% for the Semi-empirical ones. These differences could be due to the limited range of frequency that the numerical simulation is able to describe, especially considering in input the values of acceleration, that could be the most affected by noise. Furthermore, the table shows a large response variability; this could be explained with the strong non linear soil behaviour that some areas of the Christchurch Plains experienced during the earthquake that neither the three-dimensional numerical model obtained with GeoELSE, nor the adopted 4-DOF wind tower 2D model adopted are able to fully represent. This constitutes a natural development of the present approach in order to assess the role of non-linearity in the relevance of rotational ground motion for civil engineering structures.

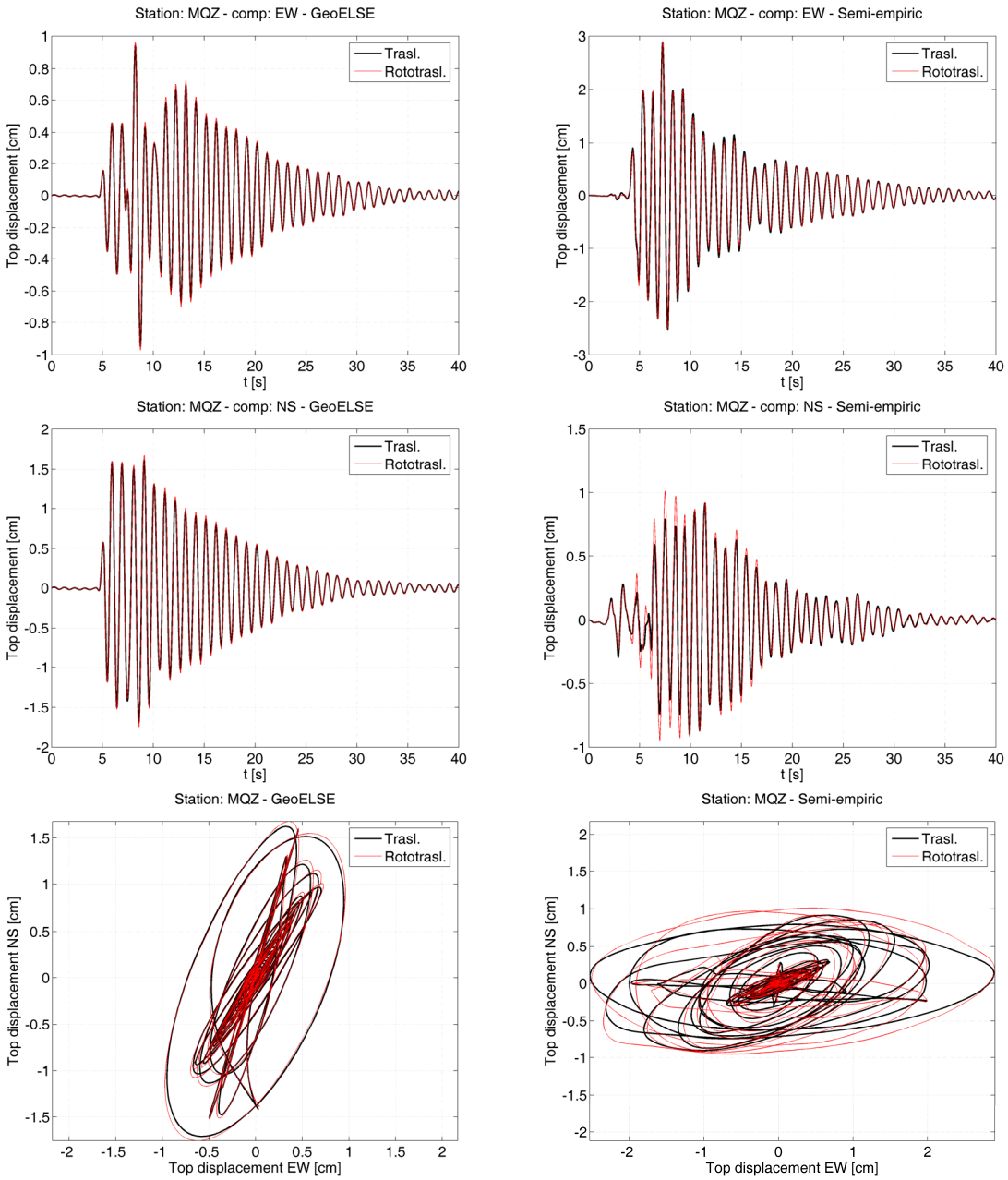

Figure 5.7. Displacement of the mass at top of the wind tower located at station MQZ, on outcropping rock, considering the effect of the rotational component of motion, using as input numerical data (left column) and semi-empirical data (right column). First row refers to displacement along East-West direction, second row is along the North-South direction. In the third row, an odometric representation of displacement in the two direction is presented.

Tables 5.8 and Table 5.9 present results with a format similar to Table 5.7, referring to the parametric analysis, adopted to evaluate the size effect of the structure Two further models are thus considered, with height of the tower equal to 45 m and 60 m, respectively. In order to have a similar fundamental period T equal to around 1 s, a diameter of the tower equal to 3 m and 4 m, respectively, has been adopted. Consequently the foundation width of the two towers is respectively

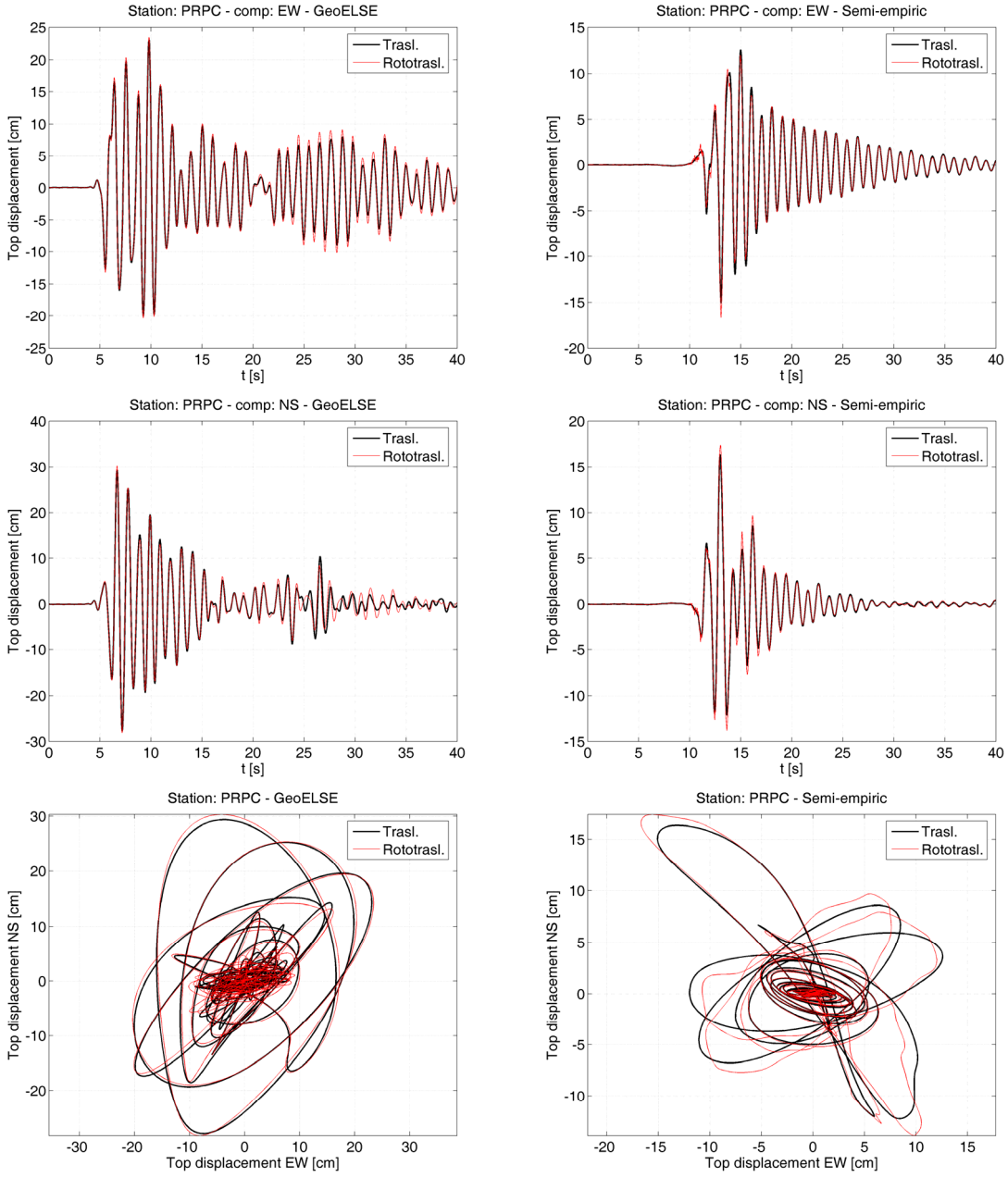

Figure 5.8. Displacement of the mass at top of the wind tower supposed located at station PRPC, on alluvial soil, considering the effect of the rotational component of motion, using as input numerical data (left column) and semi-empirical data (right column). First row refers to displacement along East-West direction, second row is along the North-South direction. In the third row, an odometric representation of displacement in the two direction is presented.

equal to 7 m and 10 m. Looking at data collected in Tables 5.8 and 5.9, it is noteworthy that the average values of the percentage difference of top displacement show an increasing trends from the first model to the third one. In particular, the average values of the differences obtained starting from semi-empirical data range up to around 10% in the last case, while mean results obtained from synthetic data are still confined to around 3%. This effect, related to the increased height

Table 5.8. Top displacement obtained with synthetically and semi-empirically retrieved rotational accelerations, considering the two horizontal direction of motion and a translational (T) and a roto-translational (R-T) input, for the Wind Tower 2 model (see Table 5.6).

Top Displacement		GeoELSE						Semi-empirical					
		EW			NS			EW			NS		
Stations	Re [km]	T [cm]	R-T [cm]	Δ [%]	T [cm]	R-T [cm]	Δ [%]	T [cm]	R-T [cm]	Δ [%]	T [cm]	R-T [cm]	Δ [%]
HVSC	*1*	*2.94*	*2.95*	*0.46*	*7.06*	*7.08*	*0.28*	*19.32*	*19.74*	*2.20*	*22.18*	*22.23*	*0.22*
LPCC	*4*	*8.92*	*8.99*	*0.74*	*3.83*	*3.84*	*0.15*	*11.75*	*12.29*	*4.59*	*5.39*	*5.70*	*5.87*
PRPC	6	20.03	20.44	2.06	28.03	29.17	4.07	14.33	16.42	14.63	15.26	16.37	7.26
CCCC	6	15.83	16.17	2.16	24.50	25.04	2.20	19.30	20.93	8.48	17.48	18.78	7.44
REHS	8	11.50	11.96	4.04	13.51	13.91	2.96	53.29	54.38	2.03	37.48	39.17	4.50
CHHC	8	13.62	13.71	0.70	14.78	15.08	2.04	21.68	21.82	0.67	26.13	26.16	0.11
CBGS	9	10.73	10.84	0.98	9.06	9.66	6.69	22.62	23.84	5.38	23.66	24.82	4.92
SHLC	9	20.73	21.33	2.88	14.21	14.48	1.91	25.31	26.05	2.95	32.61	33.10	1.51
HPSC	9	25.34	26.14	3.16	18.77	19.96	6.37	16.84	18.08	7.36	8.30	8.61	3.79
PPHS	12	9.75	9.90	1.52	11.23	11.63	3.54	12.36	13.12	6.14	11.15	11.76	5.41
SMTC	14	9.51	9.70	2.07	10.56	10.88	3.02	15.00	15.66	4.42	12.61	13.17	4.49
MQZ	*15*	*0.90*	*0.93*	*3.11*	*1.59*	*1.61*	*0.89*	*2.95*	*2.98*	*0.92*	*0.95*	*1.07*	*13.25*
CACS	18	4.11	4.13	0.41	6.46	6.61	2.28	7.06	7.39	4.60	4.51	5.25	16.53
LINC	19	9.72	9.75	0.23	17.88	18.01	0.74	2.55	2.59	1.76	8.50	9.03	6.27
KPOC	23	7.72	7.80	1.09	6.44	6.54	1.58	6.26	6.28	0.32	3.98	4.08	2.46
ROLC	26	4.13	4.21	1.98	10.87	11.19	2.93	1.94	1.97	1.71	2.77	2.80	1.17
SWNC	29	3.11	3.13	0.71	3.68	3.70	0.59	2.23	2.26	1.04	2.99	3.08	3.03
ASHS	35	3.86	3.93	1.94	2.59	2.64	1.99	1.82	1.83	0.79	1.47	1.61	10.15
CSTC	39	2.90	2.97	2.41	1.83	1.86	1.52	1.73	2.15	23.85	2.46	2.73	11.04

Table 5.9: Top displacement obtained with synthetically and semi-empirically retrieved rotational accelerations, considering the two horizontal direction of motion and a translational (T) and a roto-translational (R-T) input, for the Wind Tower 3 model (see Table 5.6).

Top Displacement		GeoELSE						Semi-empirical					
		EW			NS			EW			NS		
Stations	Re [km]	T [cm]	R-T [cm]	Δ [%]	T [cm]	R-T [cm]	Δ [%]	T [cm]	R-T [cm]	Δ [%]	T [cm]	R-T [cm]	Δ [%]
HVSC	*1*	*3.48*	*3.49*	*0.24*	*6.91*	*6.94*	*0.38*	*19.71*	*20.43*	*3.66*	*17.87*	*18.66*	*4.42*
LPCC	*4*	*8.55*	*8.61*	*0.81*	*4.13*	*4.15*	*0.52*	*13.60*	*13.66*	*0.41*	*5.38*	*5.59*	*4.02*
PRPC	6	25.59	26.07	1.89	30.59	32.01	4.66	15.86	18.33	15.57	17.35	19.24	10.90
CCCC	6	17.32	17.54	1.27	26.93	27.72	2.93	23.33	24.98	7.11	22.39	23.71	5.90
REHS	8	11.02	11.46	3.98	13.52	14.05	3.94	55.39	56.24	1.54	35.93	37.72	5.00
CHHC	8	17.13	17.44	1.81	15.94	16.15	1.29	23.09	23.18	0.41	26.96	27.14	0.64
CBGS	9	9.92	9.95	0.24	9.70	10.05	3.57	21.53	22.95	6.60	24.44	25.73	5.26
SHLC	9	20.04	20.70	3.30	14.94	15.10	1.05	30.90	31.58	2.18	33.08	33.49	1.24
HPSC	9	29.21	29.76	1.88	20.80	22.44	7.88	16.71	18.50	10.69	9.06	9.46	4.40
PPHS	12	9.06	9.21	1.70	12.51	12.59	0.63	12.14	12.59	3.66	16.25	16.30	0.31
SMTC	14	11.35	11.44	0.76	11.36	11.77	3.65	14.40	15.28	6.13	11.40	12.15	6.63
MQZ	*15*	*1.14*	*1.17*	*3.02*	*2.23*	*2.34*	*5.00*	*2.48*	*2.53*	*1.95*	*0.80*	*1.14*	*41.96*
CACS	18	3.60	3.65	1.26	6.51	6.66	2.31	6.20	6.76	9.10	4.47	5.11	14.39
LINC	19	9.44	9.58	1.39	18.29	18.42	0.72	3.07	3.27	6.56	10.20	10.81	5.91
KPOC	23	7.27	7.49	3.09	6.43	6.50	1.06	5.79	5.83	0.70	3.55	3.77	6.26
ROLC	26	3.10	3.33	7.48	12.07	12.41	2.82	1.38	1.44	3.70	3.28	3.36	2.51
SWNC	29	4.19	4.20	0.23	3.97	4.00	0.78	2.51	2.72	8.15	3.01	3.21	6.72
ASHS	35	4.89	4.93	0.90	3.58	3.65	2.07	1.57	1.63	3.81	1.36	1.59	16.71
CSTC	39	3.16	3.19	1.19	2.49	2.56	2.58	1.94	2.20	13.49	3.67	4.23	15.32

of the structure, is particularly evident in the latter case for the MQZ station, where a percentage difference greater than 40% is reached.

Table 5.10. Main structural technical specifications of the 500 kilowatt wind turbine located at Gebbies Pass.

Windflow 500		
Blade	Material:	Laminated wood/epoxy
	Weight:	900 kg
Rotor	Number of Blades:	2
	Diameter:	33.2 m
	Hub height:	30 m
	Weight:	4,000 kg
Tower	Type:	Tubolar
	Height:	29 m
	Weight:	15,400 kg
Total Weight	Nacelle and Rotor:	13,700 kg
	Total:	29,100 kg

Table 5.11. Modal properties of the wind tower model, considering the first 8 modes of vibration. z denotes the vertical axis and Ux, Uy, Uz, Rx, Ry and Rz represent the cumulative of the participation factor of the mode to the respective component of motion.

Mode	Description	Period [s]	Frequency [cyc/s]	Ux	Uy	Uz	Rx	Ry	Rz
1	bending x direction	1.008	0.99242	0	0.78	0	0.98	0	0.16
2	bending y direction	1.006	0.99363	0.78	0.78	0	0.98	0.98	0.16
3	Torsion around z axis	0.122	8.1967	0.78	0.79	0	0.99	0.98	0.86
4	bending y direction	0.099	10.081	0.89	0.79	0	0.99	1	0.86
5	bending x direction	0.096	10.413	0.89	0.89	0	1	1	0.89
6	bending y direction	0.036	27.533	0.93	0.89	0	1	1	0.89
7	bending x direction	0.035	28.855	0.93	0.93	0	1	1	0.89
8	axial translation z direction	0.025	40.408	0.93	0.93	0.77	1	1	0.89

5.3.2 The Gebbie Pass wind tower: a Finite Element model

On the basis of the available information, from the technical specifications listed in Table 5.10, a Finite Element model of the Gebbie Pass wind tower has been realized with the software SAP2000 (Brunetta et al. 2006), showed in Figure 5.9, together with a picture of the wind turbine. The maximum height of the structure is 30 m, with diameter of the steel tower varying linearly from 2.5 m at the basis to 1.5 m at the top, where the nacelle and the 2 blades are located. Table 5.11 shows the modal properties of the wind tower model for the first 8 modes of vibration.

The station located at Mc Queen Valley has been chosen as reference. A seismic analysis has been performed, taking the rotational input from synthetics and semi-empirical data, along with the translational input. Results are presented as a function of the top displacement in Figure 5.10, in the same format as Figure 5.7. The 3D model shows good agreement with the 2D model described in the previous section, with similar values for the percentage differences of the top displacement, and it is able to better represent its variability in the horizontal plane, as presented in the odometric graphs in Figure 5.10.

Figure 5.9. Picture of the Wind tower installed at Gebbie Pass (left hand side) and its numerical representation with FE code (right hand side).

In order to assess the differences between simulations with and without the rotational seismic input, the distribution of the envelope of longitudinal (top) and circumferential (bottom) stresses along the tower's height are presented in Figure 5.11. Longitudinal stress reaches a maximum value at the base of the tower of 20.46 MPa considering the effect of pure translational input, when the rotational motion is introduced, the maximum stress reaches a 22.68 MPa, a percentage increase of around 11%. A similar trend is observed for the circumferential stresses, with maximums of 6.15 MPa and 6.82 MPa, respectively.

5.3.3 Concluding remarks

A numerical study on a wind tower, located at Gebbie Pass is presented in order to assess the relevance of a rotational seismic input superimposed for a translational one for these kinds of structures that present a large inertial mass on the top and a marked rotating component around horizontal axis.

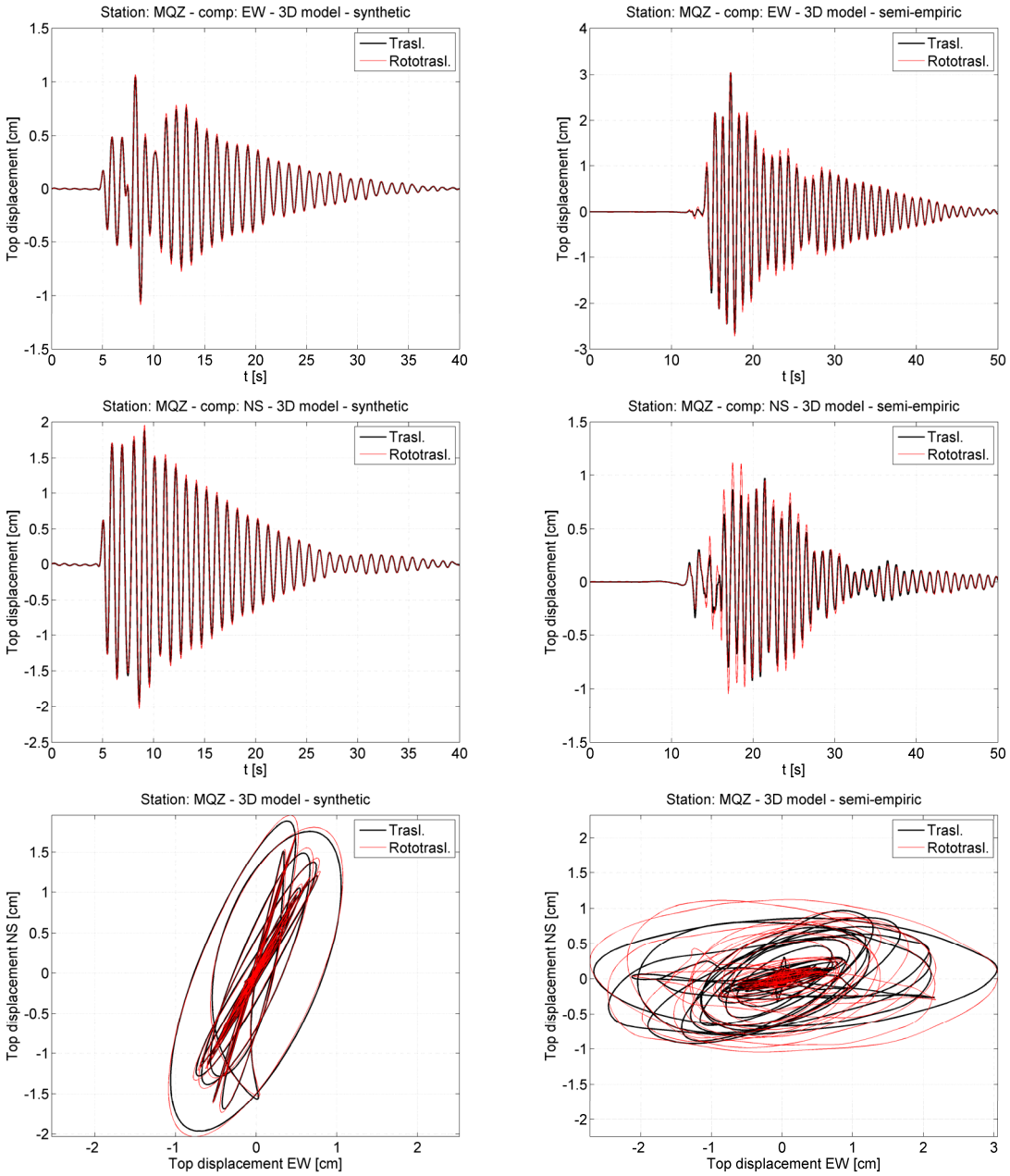

Figure 5.10. Displacement of the mass at top of the wind tower located at station MQZ, on outcropping rock, obtained with the 3D model, considering the effect of the rotational component of motion, using as input numerical data (left column) and semi-empirical data (right column). First row refers to displacement along East-West direction, second row is along the North-South direction. In the third row an odometric representation of displacement in the two direction is presented.

A 2D lumped mass model has been considered for a parametric analysis of the seismic response of wind towers, varying the height of the tower, its diameter, and the foundation width, as well as the location of the tower in proximity to the nineteen recording stations, on alluvial soil, among the Canterbury Plains, and on outcropping volcanic rock. Synthetically and Semi-empirically retrieved

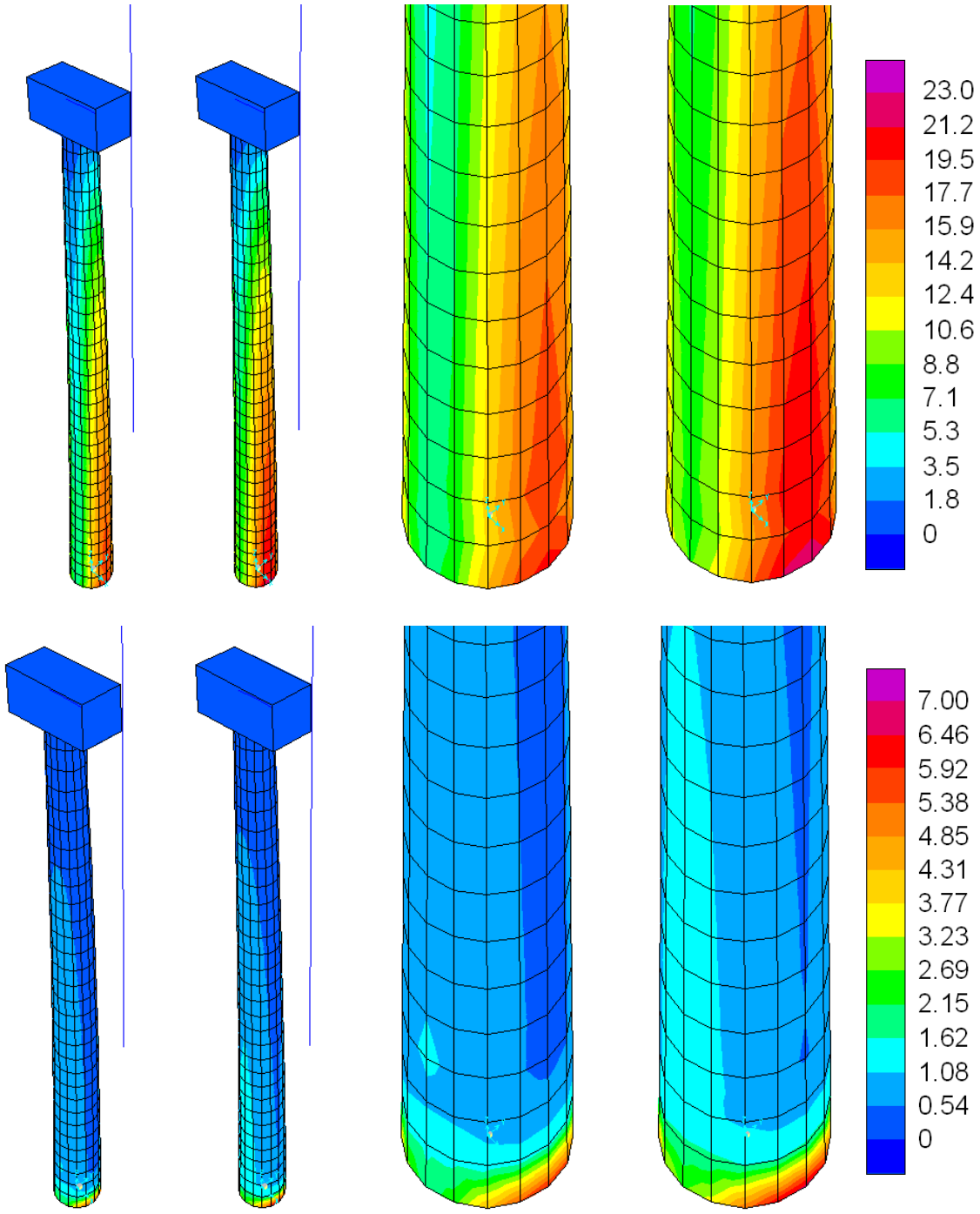

Figure 5.11. Distribution of the envelope of longitudinal (top) and circumferential (bottom) stresses along the tower's height, and zoom on the tower's basis, where they reach their maximum values. Values are in MPa.

rotation inputs have been adopted and the top displacement of the model has been evaluated as characterizing the structural response of the wind tower. A 3D simple finite element model provided insight into the variability of the stress field along the height of the tower.

Results obtained in the present study confirm the evidence of a good seismic response of this kind of structures, suggesting at the same time that rotational motion could play an important role in the seismic analysis of wind turbines, with increases in stress and top displacement, especially for high rise structures. In any case, the large response variability obtained suggests a need for confirmation with further analysis, primarily taking into account the non-linearity in the soil-structure interaction.

5.4 Grand Chancellor, Christchurch, Canterbury Business District. Relevance of rotational ground motion for a tall building

A large number of studies describe the effects likely to occur during an earthquake, when the ground motion is not uniform along the free surface; typically, these works focus on the behaviour of bridges subjected to motions at piers. Results depend on the way this non-uniformity is modelled, and on its quantitative assessment The following application aims to illustrate the relevance of an input motion represented by the rotational ground motion evaluated in the previous chapters, with respect to the effects of a horizontal excitation consistent with the motion.
There is one procedure, valid in the general case, for dealing with a ground motion that differs from point to point. It requires imposing a different time history at the building's base. In the present case, a simplified, approximate procedure is applied, which works under the following assumptions:

i) A unique, rigid foundation slab is laid at the base of the building. The free-field rotation is thus applied to this foundation, without modification from reaction forces, e.g., disregarding the soil compliance.

ii) An average rotation related to a separation distance d =10 is considered.

These assumptions distinguish the present approach and that of direct recording of rotation at a point. Nevertheless, the most interesting value for most engineering applications is the average rotation between points at a distance d, compared to the horizontal dimensions h of the foundation.
The value taken into account as representative of the level of damage in the structure is the interstory drift, being specified by many codes as the allowable drifts for the design of structures under dynamic loads. The interstorey drift can be evaluated as the chord rotation between two levels, namely dividing the differences of the displacement of the centre of mass of two contiguous stories by the height of the level. In particular, referring to Ghobarah 2004, and Figure 1.5 (Trifunac 2009a), for a ductile moment resistant frame irreparable damages being to occurs for drift higher than 0.01 rad (1%), and severe damage with partial collapse and threat to life (Life-safe), occurs for drift higher than 1.8%.

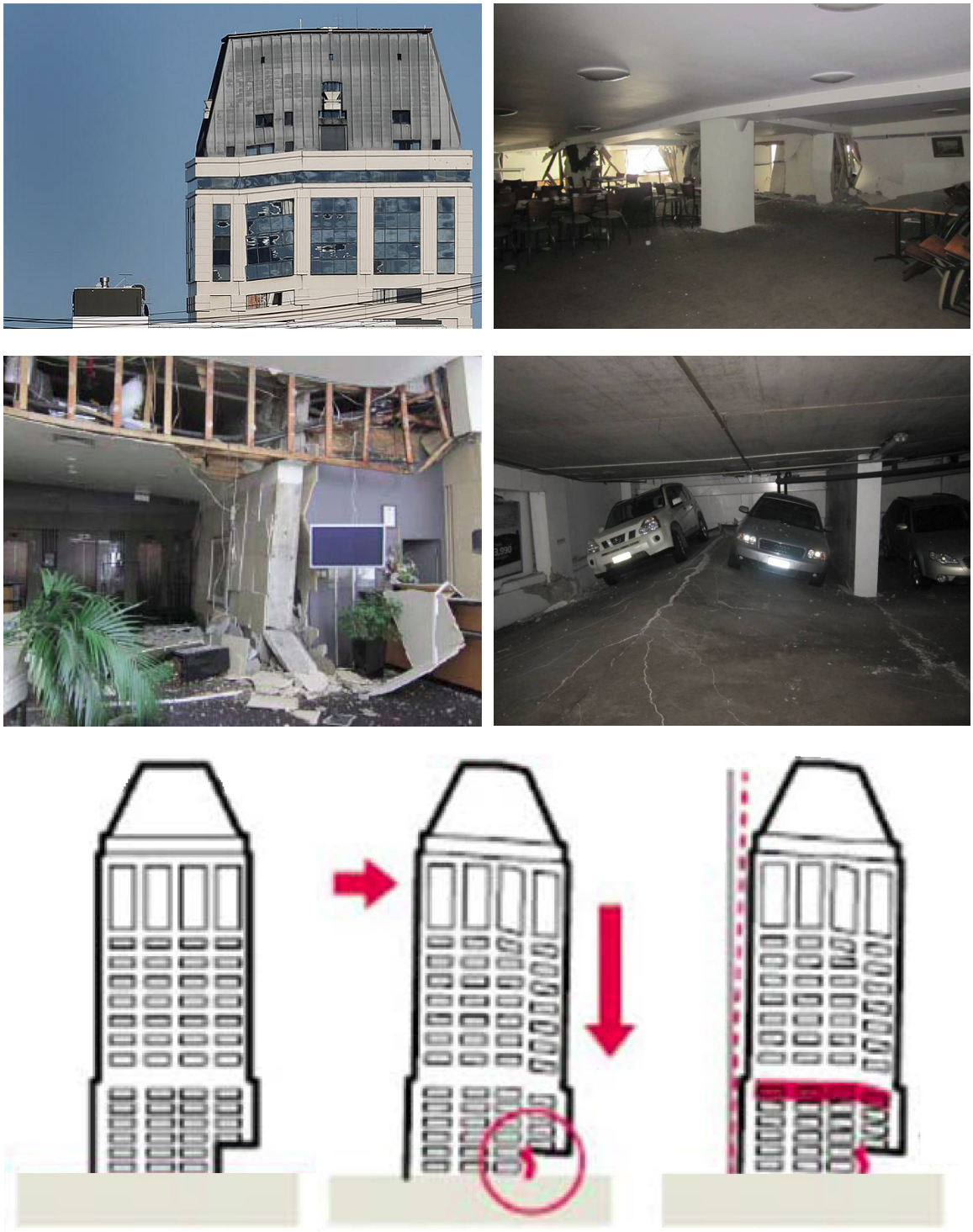

Figure 5.12. Top and middle row: Pictures of the damages occurred at the Grand Chancellor Hotel. It is particularly evident the wall failure on the south-eastern side, causing the building to slump in the corner. Bottom: graphical reconstruction of the inferred collapse sequence (source: Critical Buckling Group, NZ Herald).

5.4.1 Observed damages in the Grand Chancellor Hotel

In order to evaluate the relevance for buildings for a rotational input superimposed on a translational one in the present application, the attention is focused on a high rise building in the Christchurch CBD, namely the Grand Chancellor Hotel.
With its 28 levels and a total height of 85 m, the Grand Chancellor Hotel is the tallest building in Christchurch, with dimension in plan equal to 24 m x 32 m. It is a reinforced-concrete structure with a peculiar eastern cantilevered wall, that during the seismic event experienced heavy levels of damage. Looking at the pictures of the Grand Chancellor Hotel taken after the earthquake it is possible to infer the damage sequence (Figure 5.12). In particular it received severe damages to its south-eastern side, with the cantilevered wall failing and producing a slump at the corner of the building.

5.4.2 Three-dimensional model of the Grand Chancellor Hotel

In the present application we aim to evaluate the interstory drifts experienced during the Christchurch earthquake by the Grand Chancellor, and in particular to assess how is the percentage relevance of a rotational input motion. For this, we rely on a liner elastic behaviour of the material; the introduction of the non-linearity of materials may lead to results closer to the real level of drift experienced by the building.
The three-dimensional model of the building, realized with the software SAP2000 (Brunetta et al. 2006), is showed in Figure 5.13 together with a general view of the structure. The modal properties of the model are characterized by a period T of the first mode of vibration of around 2 s. A series of time-history analyses have been performed, taking a pure translational ground motion as input, retrieved from recorded data and a superposition of translational and rotational ground motion, using the procedure presented in Chapter 2, that provided the highest values of peak rotational ground motion, as described in Chapter 4.
Results in terms of interstory drift along the height of the Grand Chancellor Hotel are listed in Table 5.12 and are shown in Figure 5.14, using four recording stations of reference, namely stations CCCC, REHS, CBGS and CHHC, located in the CBD. Looking at the results it is possible to highlight the following features:

i) In all the stations considered, the superposition of a rotational input to the translational one induce higher values of interstory drift, of the order of 15%, with higher values at the top of the building.

Figure 5.13. Top: Picture of the Grand Chancellor Hotel in the Christchurch CBD, after the earthquake (left hand side) and its numerical model with FE code (right hand side). Bottom: Technical drawing of a typical building story, from level 1 to 14 (left hand side) and from level 15 to 28 (right hand side).

ii) The interstory drift reaches a values higher than 1% (irreparable damages) in all the case considered, with values for the REHS and CCCC stations passing the 1.8% threshold (damage with partial collapse).

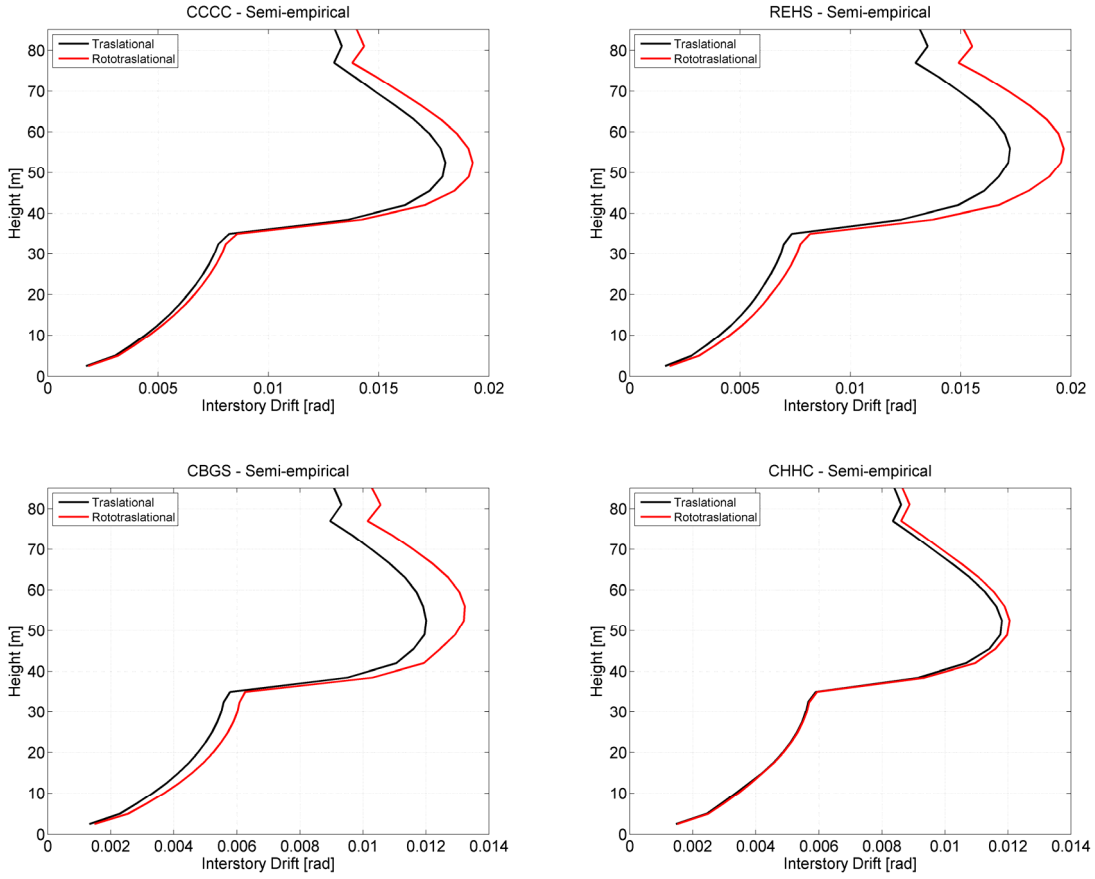

Figure 5.14. Interstory drift along the height of the Grand Chancellor Hotel, evaluated considering a pure translational input (black line) and a rotational input superimposed to the translational one (red line), considering the four stations of reference, namely CCCC, REHS, CBGS and CHHC, located in the neighbourhood of the CBD.

iii) It is possible to clearly identify, for all the performed simulations, a sharp change in the drift value at approximately the 14th level of the Grand Chancellor, at a height of around 35 m. This is due to a sharp change of the geometrical configuration of the building, as depicted in the technical drawing presented in Figure 5.13 and it is in agreement with the observed damages for this floor (Figure 5.12).

5.4.3 Concluding remarks

A numerical model of Christchurch's tallest building, the Grand Chancellor Hotel, that experienced severe damages during the earthquake, has been presented, to evaluate the relevance of a rotational ground motion, superimposed to a consistent translational motion, for buildings. The interstory drift has been adopted as index of the damage level experienced by the structure and results are in agreement with the direct observation of damages, presented in Figure 5.12.

Table 5.12: Interstory drift obtained by the numerical model of the 28 story Grand Chancellor Hotel, considering a translational (T) and a roto-translational (R-T) input motion, considering the set of four strong motion seismometers located in the neighbourhood of the CBD. Percentage difference between interstory drifts is provided.

	CCCC			REHS			CBGS			CHHC		
Level	T [mrad]	R-T [mrad]	Δ [%]	T [mrad]	R-T [mrad]	Δ [%]	T [mrad]	R-T [mrad]	Δ [%]	T [mrad]	R-T [mrad]	Δ [%]
28	13.01	14.00	7.59	13.15	15.13	15.04	9.08	10.29	13.27	8.39	8.65	3.07
27	13.32	14.34	7.60	13.50	15.53	15.03	9.32	10.56	13.35	8.61	8.88	3.13
26	12.97	13.80	6.36	12.95	14.90	15.05	8.95	10.14	13.27	8.35	8.60	3.11
25	13.92	14.90	7.06	14.00	16.10	14.99	9.65	10.92	13.13	8.99	9.26	3.09
24	14.81	15.91	7.43	14.92	17.15	14.92	10.26	11.58	12.90	9.60	9.88	2.98
23	15.74	16.92	7.47	15.79	18.12	14.76	10.84	12.20	12.53	10.22	10.51	2.87
22	16.61	17.83	7.33	16.50	18.91	14.60	11.34	12.70	12.08	10.79	11.08	2.67
21	17.31	18.56	7.21	17.00	19.44	14.36	11.70	13.06	11.65	11.28	11.56	2.50
20	17.81	19.06	7.02	17.23	19.67	14.15	11.91	13.24	11.16	11.63	11.89	2.29
19	18.02	19.26	6.87	17.16	19.55	13.92	12.01	13.20	9.96	11.81	12.05	2.08
18	17.89	19.09	6.68	16.72	19.01	13.71	11.95	12.93	8.19	11.76	11.98	1.86
17	17.31	18.43	6.47	16.06	18.08	12.58	11.61	12.45	7.29	11.41	11.60	1.68
16	16.19	17.09	5.55	14.88	16.73	12.39	11.06	11.93	7.87	10.67	10.96	2.77
15	13.64	14.26	4.59	12.32	13.77	11.80	9.51	10.31	8.40	9.18	9.36	2.01
14	8.22	8.58	4.39	7.34	8.17	11.29	5.78	6.26	8.27	5.90	5.94	0.78
13	7.73	8.07	4.37	6.98	7.73	10.76	5.58	6.08	9.08	5.66	5.69	0.66
12	7.55	7.88	4.44	6.84	7.56	10.57	5.50	6.01	9.32	5.58	5.62	0.67
11	7.31	7.64	4.49	6.64	7.34	10.57	5.38	5.89	9.52	5.46	5.49	0.49
10	7.03	7.35	4.52	6.39	7.06	10.58	5.21	5.72	9.68	5.30	5.33	0.50
9	6.71	7.02	4.63	6.10	6.74	10.60	5.01	5.50	9.80	5.10	5.12	0.41
8	6.34	6.64	4.77	5.80	6.38	10.05	4.76	5.24	10.13	4.85	4.87	0.39
7	5.94	6.21	4.55	5.45	6.01	10.41	4.47	4.93	10.19	4.55	4.57	0.42
6	5.49	5.72	4.27	5.04	5.58	10.65	4.14	4.57	10.47	4.19	4.21	0.36
5	4.98	5.18	4.03	4.58	5.09	11.03	3.75	4.15	10.55	3.77	3.84	1.66
4	4.40	4.58	4.07	4.06	4.52	11.38	3.32	3.68	11.01	3.35	3.43	2.50
3	3.75	3.91	4.25	3.46	3.87	11.90	2.82	3.14	11.27	2.90	2.98	2.72
2	3.04	3.18	4.56	2.79	3.13	12.22	2.28	2.55	11.65	2.43	2.49	2.46
1	1.73	1.83	5.66	1.60	1.80	12.89	1.32	1.48	12.49	1.46	1.51	2.86

Comparing the results, it is possible to assess that that in the near-field region of an earthquake, for relatively tall buildings having a ratio of height to plan dimensions around 3 or more on soft soil, as the case-study of the Grand Chancellor, rotations deserve a deeper investigation. To disregard the rotational component of motion, indeed, results in underestimated drifts as claimed by Trifunac 2009a. It is important to underline, however, that values greater than 1.8% have been observed, considering the translational component of motion alone. There are no reasonable doubts that the severe damages that the structure experienced are mainly due to the impressively high peak values of translational (horizontal and vertical) ground motions that the building experienced, and due to the cantilevered eastern side of the structure that was not able to carry the seismic load induced by the quake.

5.5. The Christchurch Canterbury Business District. Relevance of site-city interaction effect in the spatial variability of motion

In this section, the variability of the strong motion is studied at a site-city scale, a scale studied by relatively few, compared to the large, regional scale of alluvial basins and to the small scale of a single structure. First, this scale has a major role in seismic wave propagation and amplification and, second, it is the most suitable for a proper assessment of structural damages. A densely urbanized area located in an alluvial basin could influence the seismic wave field, both in a passive way, as the buildings and their foundations are obstacles to the seismic wave front, and actively, acting as an extended surface source area consisting of a large number of closely spaced sources of translational and rotational motions (Trifunac 2009a).

In the present application, the CBD, social and economic heart of the city of Christchurch, characterized by a high density of tall buildings, has been modelled and set into the regional model of the Canterbury Plains, described in Chapter 3. The three-dimensional model of the densely urbanized area of Christchurch allow us, naturally including translational and rotational ground motion, to evaluate the wave effect discussed in section 5.2 on a pounding-prone compounds of buildings and, at the same time, the effect of a densely urbanized area in the spatial variability of strong ground motion, trying to explain the observed damage variability in apparently homogeneous areas.

5.5.1 Site-City Interaction

Site-effect, the phenomenon of amplification of seismic waves in a free field in an alluvial basins, has been widely studied in recent years, distinguishing stratigraphic effects due to the impedance difference between soil layers, and topographic effects, that could scatter or focus the wave field (e.g. Bouchon 1973, Bard and Bouchon 1985, Bielak et al. 1999, Paolucci 2002, Semblat 2002). The issue of the potential influence of a city on the seismic response of an alluvial basin has only been seriously considered after the 1985 Michoacan earthquake in Mexico, where extremely high strong motion amplification were recorded in a densely urbanized area, suggesting that a cluster of buildings could modify the ground motion during an earthquake.

Early studies and applications of the so called site-city interaction are presented by Semblat et al. 2008 and mainly rely on one- or two-dimensional models. This, on one hand, simplified the understanding of this phenomenon, but, on the other hand, strongly limited the description of the mutual and simultaneous action of a cluster of buildings in the strong motion variability.

It could be assessed by three-dimensional modelling of this multi-scale problem. A proper model of the city and of the basin, indeed, requires a remarkable computational burden that has long limited its wide applicability. Studies of Taborda (2010) and Taborda and Bielak, (2011), on full three-dimensional integration of site-city interaction effects in earthquake simulations, relying on an

artificial inventory of buildings, indicate that the presence of the urbanized area considerably changes the ground motion in the city and in its neighbourhood, observing significant changes in the spatial variability of the ground motion.

5.5.2 Three-dimensional numerical model of the CBD

In this application we integrate the numerical model of the Canterbury Plains presented in Chapter 3 with a real inventory of buildings, namely the full set of around 150 buildings that compose the Christchurch CBD, heavily damaged by the 2011 earthquake.

That would have been not possible without the adoption of a new software, namely SPEED (SPectral Elements in Elastodynamics with Discontinuous Galerkin), in the development phase at Politecnico di Milano with a joint-venture between the Department of Structural Engineering and the Laboratory for Modelling and Scientific Computing (MOX) in the Department of Mathematics. Relying on "non-conforming" techniques (Antonietti et al, 2012), like Discontinuous Galerkin Spectral Element Method, SPEED allows us to use meshes as independently generated and different spectral approximation degrees in different subdomains. For a detailed description of the non-conforming approach and its main differences with a standard approach we refer to Appendix B.

In Figure 5.15, the meshing process is described. As a starting point, the real configuration of the CBD has been considered, taking information on height and floorplan dimensions of the cluster of around 150 buildings, in an area having a dimension of about1 km x 1 km. Also the foundations for an average depth of 10 m and for the soil around foundations, a depth of 50 m has been taken into account. The mesh size of around 5 m leads to around 500,000 hexahedral elements. This mesh has been successively set into the numerical model described in Chapter 3, allowing the contact between elements having size of around 5 m on one side (CBD model) and 50 m on the other side (Canterbury Plains model).

The resulting model reaches a global number of hexahedral elements of more than one million, requiring a huge level of parallelization, performed on the Lagrange cluster located at CILEA. Having the hexahedral of the CBD model size of around 5 m, a spectral approximation degree equal to 1, has been adopted in this domain. Therefore, despite adopting twice as many elements, the overall number of LGL nodes is only slightly higher than the numerical model proposed in Chapter 3. The main characteristics of the model and the performances of the analysis are summarized in Table 5.13.

As far as the characteristics of the material are concerned, no change has been made to the Canterbury Plains model described in Chapter 3, with the soil around the foundations having the same characteristics of the top layer of the previous model, but with a different spectral approximation degree, equal to 1.

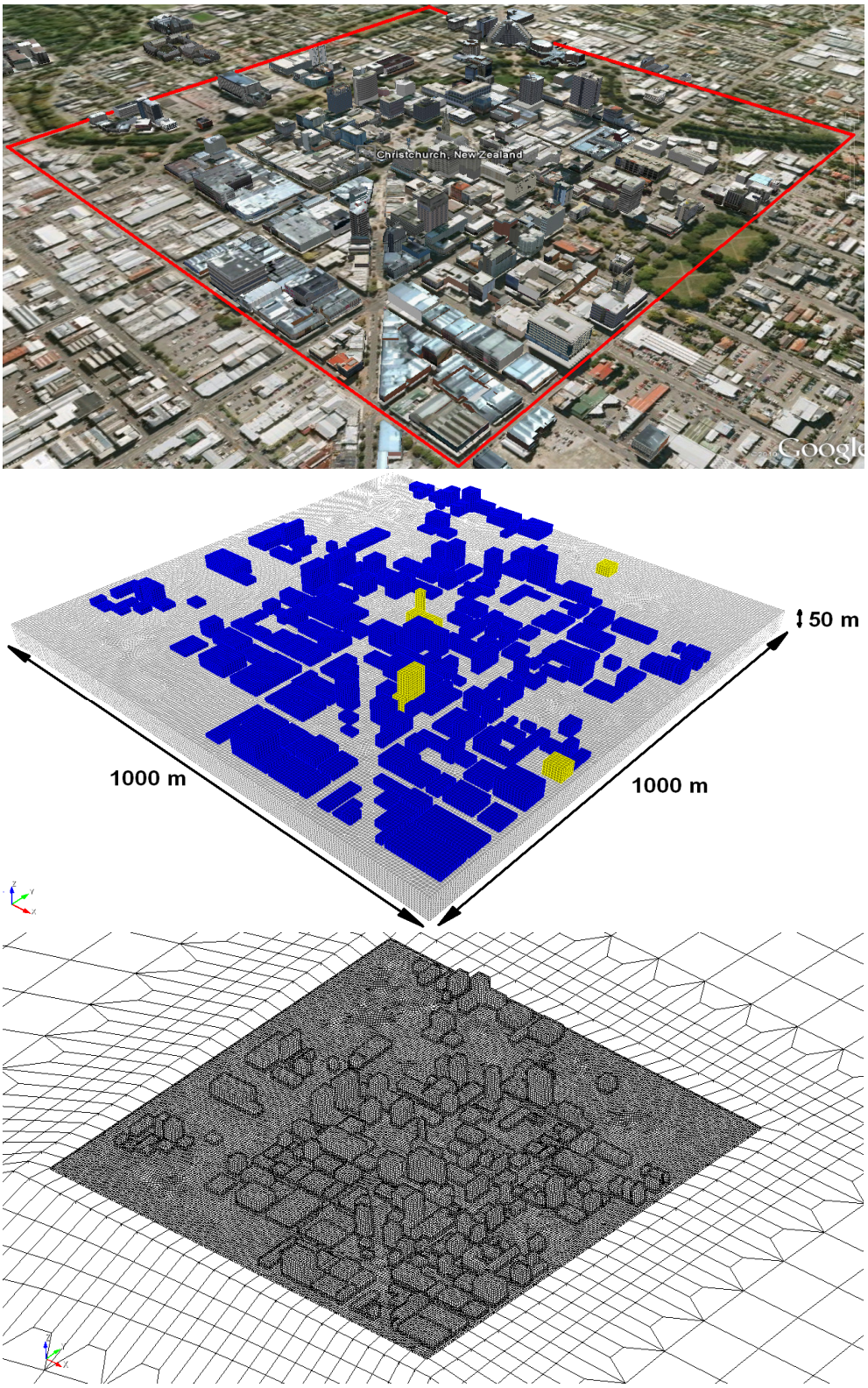

Figure 5.15. Top: Aerial view of the Christchurch CBD. The red contour defines the modelled area. Middle: Corresponding three-dimensional model, independently meshed with element size around 5 m. Also foundations and soil around foundations are meshed. In yellow significant building are highlighted. Bottom: Model of the CBD set into the model of the Canterbury Plains described in Chapter 3.

Table 5.13. Size and Computational time of the 3D aggregated numerical model of the CBD and Canterbury Plains in comparison with the parameters of the model described in Chapter3. Data of CPU time refer to the Lagrange cluster located at CILEA.

Model	SD	Number of Spectral Elements	Number of LGL Nodes	Number of cores	Simulation time (h)
GNS "Smooth"	4	495,385	~33.3 10^6	128	~107
GNS "Smooth"+CBD	4 + 1	1,043,364	~37.5 10^6	180	~450

The buildings, modelled as homogeneous blocks, could be considered as shear beams, as recalled by different authors (Trifunac 2009a, Taborda and Bielak 2011). Their period of vibration could be approximated in two way, as:

$$\begin{cases} T = \dfrac{4h}{V_S} \\ T = \dfrac{N}{10} \end{cases} . \qquad (5.21\ a, b)$$

In 5.21 a, h and V_S are the thickness and the shear velocity of the stratum, and, in 5.21 b, N is the number of stories of the building. Combining this relations, and being the effective height of the first mode of vibration equal to the 70% of the total height of the building ($h = 0.7H$), equal to N times the interstory height h_s ($H=Nh_s$), it is possible to obtain (Taborda and Bielak, 2011):

$$V_S = 28 \cdot h_S . \qquad (5.22)$$

Varying typical interstory height to around 4 m, in the numerical model a value of V_S equal 100 m/s was adopted. A stiffer values was adopted for the foundations, equal to 400 m/s, while $V_P = 2.5\ V_S$ has been considered. The density of the buildings material has been considered equal to 300 kg/m^3, while a quality factor Q, equal to 10, corresponds to a critical damping ratio of 5%. These values are in agreement with values adopted by Taborda and Bielak in their 3D model and with other 2D studies (e.g. Wirgin and Bard 1996, Tsogka and Wirgin 2003).

5.5.3 Results: Peak ground values, strong motion variability and wave passage effect

In order to evaluate the role of the densely urbanized area of the CBD in the wave propagation, we compare in Figure 5.16 the time histories of velocity recorded for the three translational components of motion at the four reference stations located in the neighbourhood of the Christchurch CBD, considering both the presence and the absence of the cluster of buildings.

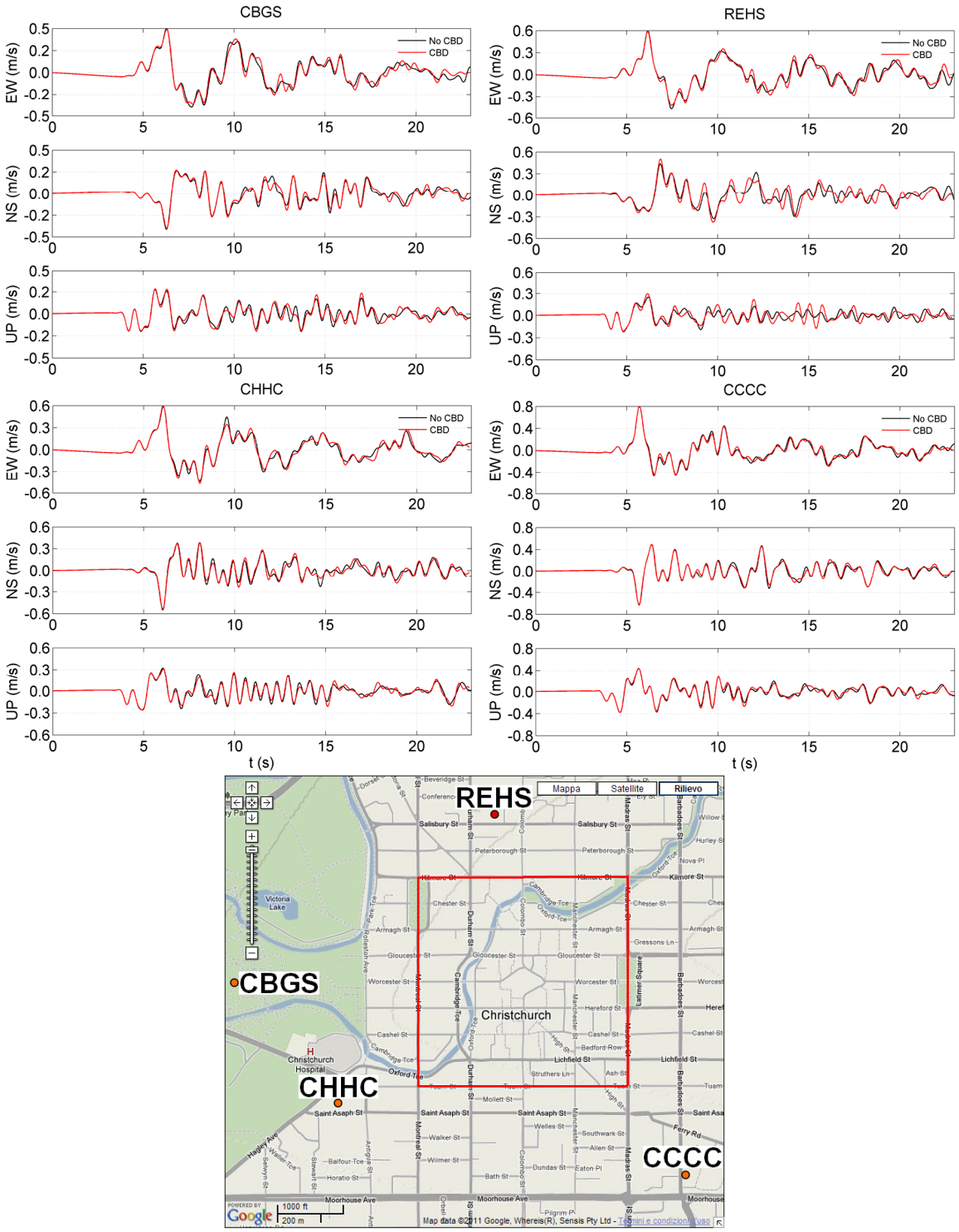

Figure 5.16. Time histories of velocity recorded for the three translational components of motion at the four reference stations located in the neighbouring of the Christchurch CBD, considering (red line) or not (black line) the presence of the densely urbanized cluster of buildings. Bottom: Location of the four monitors on the map, the red contour delimits the numerical model of the CBD.

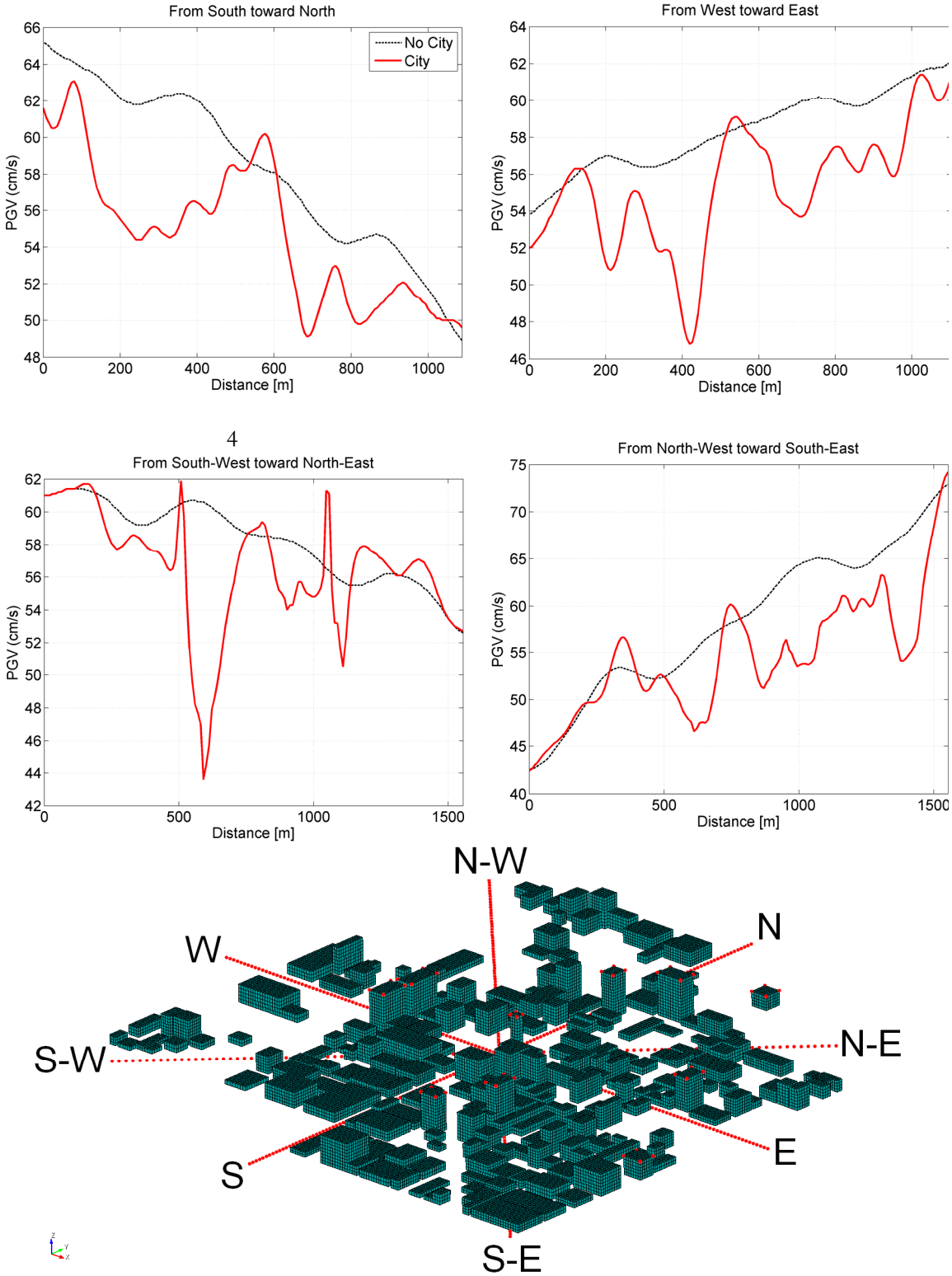

Figure 5.17. Peak ground velocity taken along the four directions across the CBD, namely South-North (S-N), East-West (E-W), South West-North East (SW-NE) and South-East-North-West (SE-NW), considering (red line) or not (black line) the presence of the densely urbanized cluster of buildings. Bottom: Set of monitors located along the four aforementioned directions (red dots). Distance between monitors varies between 7.5 and 10 m.

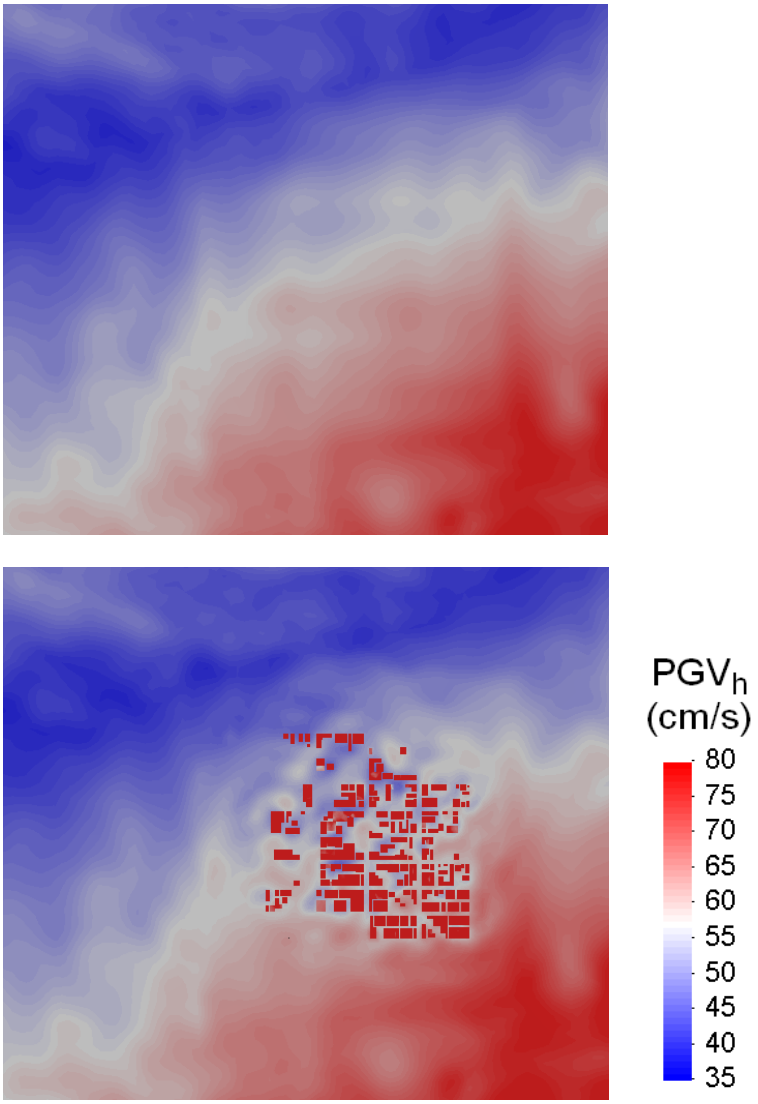

Figure 5.18. Spatial variability of Peak Ground Velocity (geometric mean of horizontal components) as estimated by 3D numerical simulations without (top panel) and with the city (bottom panel).

It is possible to notice that the major effects are concentrated on the coda of the REHS station, with the directivity of the wave-field toward the northwest. Consequently the other three stations are not or only slightly affected by the site-city interaction.

In order to highlight this effect, Figure 5.17 shows the peak ground velocity values, retrieved along the four directions across the CBD, namely South-North (S-N), East-West (E-W), South West-North East (SW-NE)and South-East-North-West (SE-NW), with and without the presence of the buildings, while in Figure 5.18 a comparison between the case without city and city is presented in a comprehensive way using the map of the peak ground velocity (geometric mean of the horizontal components).

It is possible to observe that the interactions and the interferences of the buildings and their foundations reduce or amplify the ground motion, considerably increasing the spatial variability of the surface response within the CBD.

Looking at the variability of surface earthquake ground motion, also through snapshots of the velocity wavefield presented in Figure 5.19, it is possible to observe the active role played by the buildings cluster, in substantial agreement with the words of Trifunac (2009a): this urban setting of buildings indeed is not merely an obstacle to the wave propagation field, but plays an active role, acting as an extended surface source area consisting of a large number of closely spaced sources of translational and rotational motions.

Some important hints about the wave passage effect on a pounding-prone compound of buildings, could be inferred looking at the snapshot of the simulated displacement of the buildings and of the wave-field, plotted in Figure 5.20. The wave passage effect is characterized by a strong ground motion differing from point to point that produces rotational motions at the bases of the buildings that could be in counter phase. It is possible to observe, through the snapshots, the movement of the buildings, that, after few seconds, according to their different height and excitation, are effectively characterized by different movements in counter phase that could determine, in a compound of buildings, noticeable pounding effects.

5.5.4 Concluding remarks

In this section, the CBD, characterized by a high density of tall buildings has been modelled and set into the regional model of the Canterbury Plains described in Chapter 3, exploiting the recently developed software, SPEED. The observation of the results obtained by the three-dimensional model of the densely urbanized area of Christchurch, naturally including translational and rotational ground motion, allow us to draw the following conclusions:

i) The ground motion inside the city of Christchurch is considerably changed by the presence of the city, this effect is recognized in a station located Northward of the city, along the directivity of the wave field and with a set of monitors located through the city, along different directions.

ii) Looking at the spatial variability of the peak ground motion, it is evident that the cluster of buildings plays not only a passive role, but, actively as source area, consisting of a large number of closely spaced sources of translational and rotational motions.

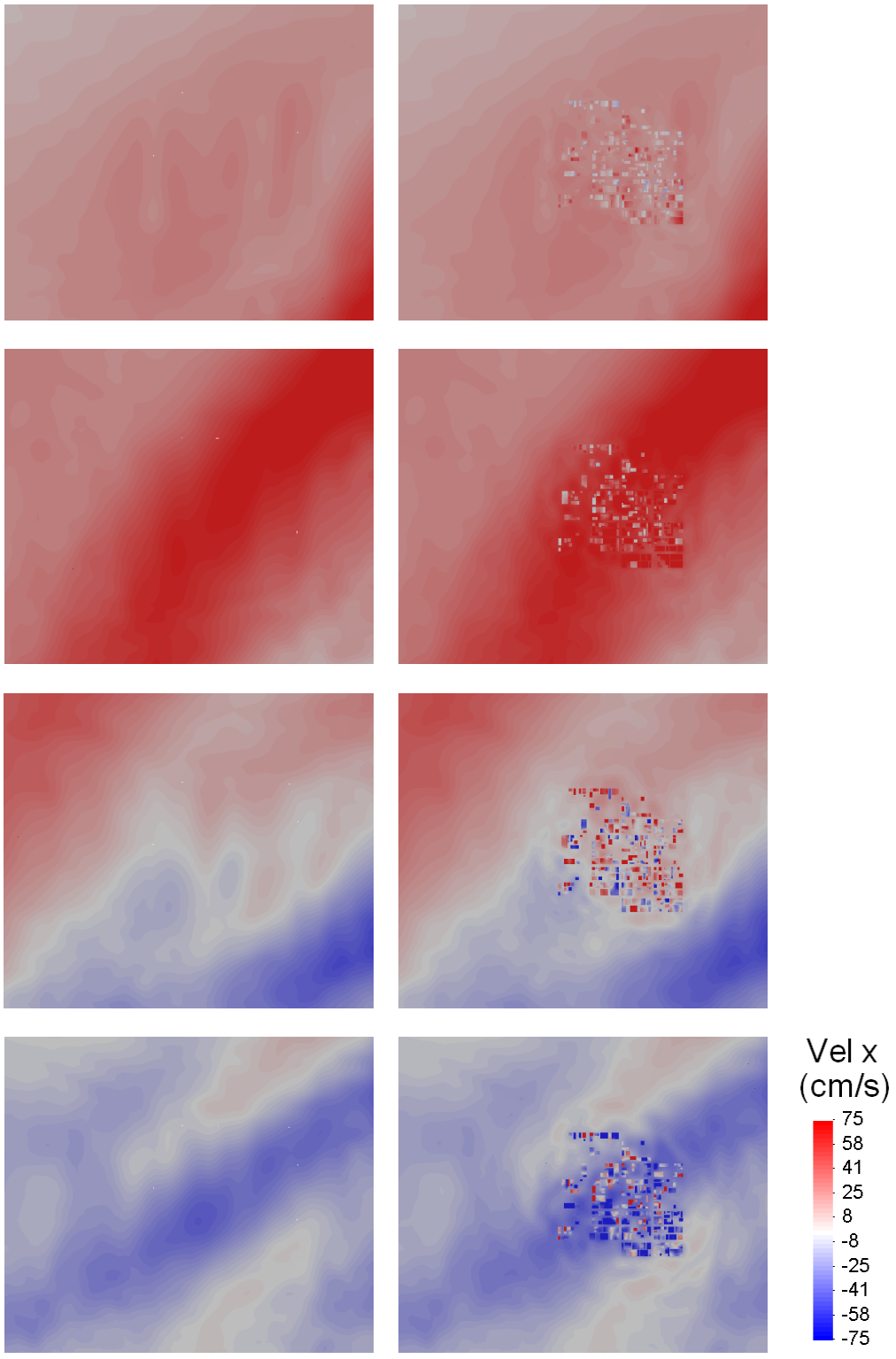

Figure 5.19. Snapshots (t = 5.5, 6, 6.5 and 7 s, from top to bottom) of the simulated velocity wavefield without the city (left hand side) and with the city (right hand side).

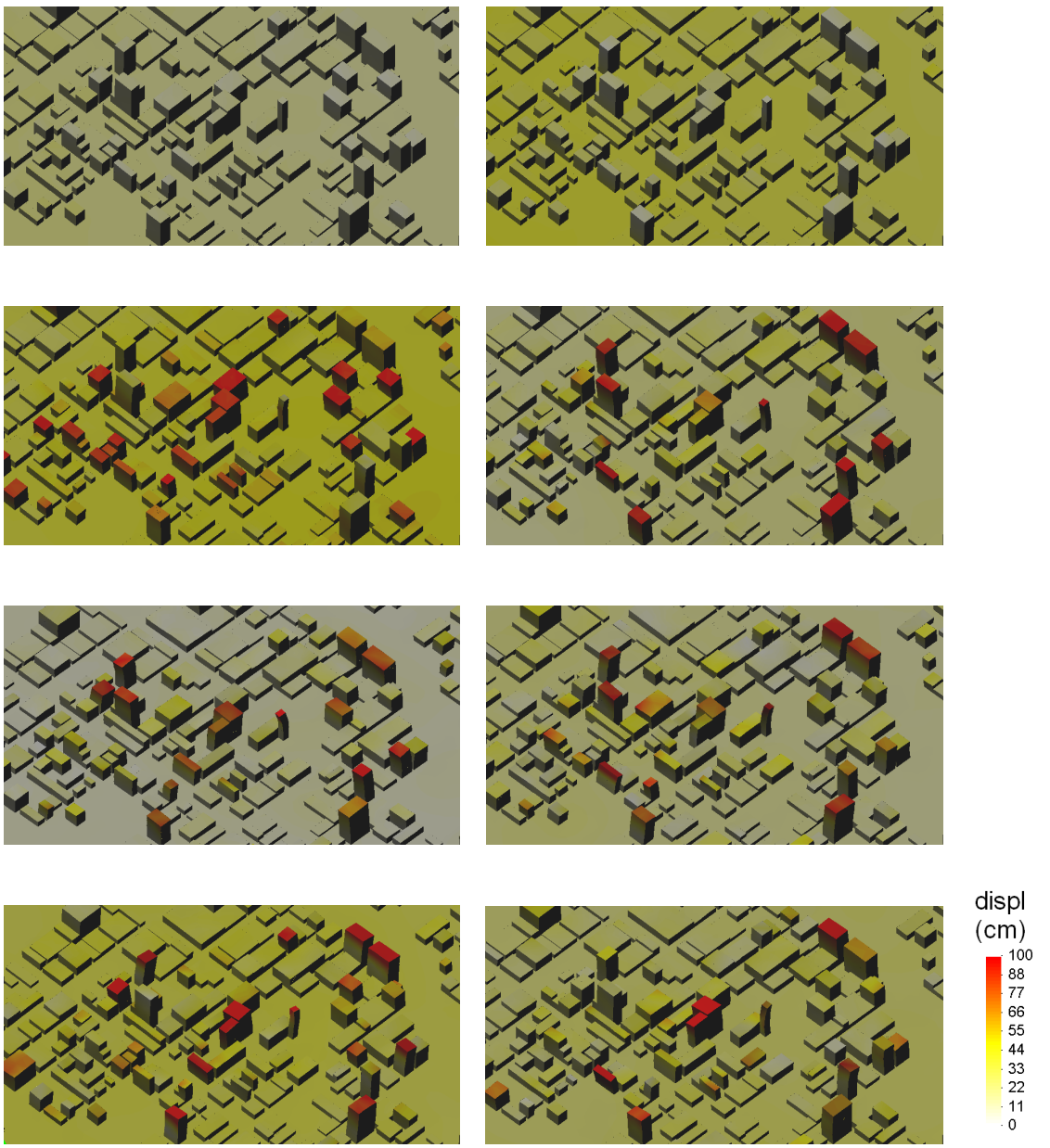

Figure 5.20. Snapshots (t = 5, 6, 7, 8, 9, 10, 11 and 12 s, from top to bottom) of the simulated displacement of the buildings of the CBD. Displacements are considered in their absolute values. On the ground, between buildings, is visible the displacement wave-field.

iii) The wave passage effect, characterized by a strong ground motion differing from point to point, produce rotational motions at the bases that could be in counter phase and produce high level of damage in pounding-prone compounds of buildings. This can be observed through the snapshot of the displacement of building.

This model, with an element size equal to 5 inside the city, is naturally suitable to further development, particularly considering a non-linear soil behaviour. The implementation of a model that can reliably represent the complex phenomena of liquefaction, would be of great interest to the city of Christchurch, and could significantly improve the presented results and help to explain, together with the spatial variability of the strong motion, the observed damage variability in apparently homogeneous areas.

CHAPTER 6

CONCLUDING REMARKS

The goal of this work is to make a contribution to the study of rotational ground motion in near-field region. Direct measurements of rotational strong ground motion are limited to a few examples and, consequently, the knowledge of the rotational wave field is still insufficient. On the basis of the present work it is possible to draw the following concluding remarks:

i) Strong ground motions measurements should no longer be limited to only the three components of translational motion, but should simultaneously include the three components of rotational motion, especially in the near field of earthquakes, where soil response influences ground motions in a complex way. Furthermore, acceleration recorded by translational sensors may be affected by rotations and this effect should be reliably quantified and corrected. To collect translational and rotational information together can yield a more complete description of the wave field, allowing a substantial improvement in studies of velocity heterogeneity, source complexity, and media nonlinearity in strong ground motions.

ii) The lack of direct measurements fostered the development of different methods to assess the magnitude of the rotational ground motion, and its dependence from the magnitude of earthquake or fault distance, as commonly assessed for the translational ground motion. The classical elastic theory turns out to be too simplistic, since the approximation of the seismic wave field with a monochromatic harmonic wave does not take into account the complex phenomena that characterize the scattering and focusing of the wave, especially in the near-field region. Two of

these methods, aiming at the estimation of the rotational wave-field, namely a semi-empirical approach based on the mathematical relation between cross spectra and power spectrum of rotation, and a complex three-dimensional spectral elements model, have been elaborated and compared, pointing out the main characteristics of each one.

iv) The comparison of current results with data from past studies allows us to conclude that, superimposing in a logarithmic plane PGV_h-$PG\omega_z$, synthetics, semi-empirical, and an available dataset of past studies on rotations, shows a substantial agreement. In particular a linear trend can be inferred; it could be interpreted, at least in far-field region as an equivalent apparent velocity of the system, allowing a quick estimate of the average rotational peak values on the basis of the corresponding values of peak ground velocity. However, the large variability of this ratio is remarkable, from 1 up to 2 orders of magnitude around the average trend, especially in the near-field, suggesting that to consider this ratio as an equivalent apparent velocity is too simplistic and that average values only are not enough to represent the complex behaviour of rotations at the surface. In order to define a more accurate relationship between rotational and translational ground motion, especially in region few kilometres from an earthquake, more data are necessary.

v) From a civil engineering point of view, the relevance for civil engineering structures is still under debate by the scientific community. Only recently has recognition that the rotational component of strong motion could contribute significantly to the overall structural response appeared and drawn the attention of the scientific community. As pointed out by the studied applications, rotations could play an active role in the damage of several categories of civil engineering structures, e.g. pipelines, high-rise structures, or pounding prone compounds of buildings, especially when soil-structure interaction effects are taken into account. In particular, in buildings, considering a vertical motion differing from point to point, the wave passage effect provides an overall rotation of the base of the structure, with an overturning motion, involving horizontal displacement of the centre of mass. To disregard this effect could result in underestimated interstory drift and, consequently, higher levels of damage than expected.

vi) Referring to a realistic earthquake scenario, the M_W 6.3 Christchurch earthquake of 22 February 2011, where exceptionally high vertical accelerations were experienced, it has been possible to assess the relevance of the rotational ground motion, superimposed to the translational motion, considering both the semi-empirical approach and the three-dimensional numerical model, on a wide range of civil engineering structures. In particular the relevance of rotational ground motion has been studied for buried pipelines, wind towers, high-rise buildings, considered alone or in densely urbanized area. In particular some hints on the seismic-wave effect are given at the Site-City

scale. The combination of the wave passage effect, with the site-city interaction could help to explain the observed variability of damage in apparently homogeneous areas.

The methods and the procedures introduced and adopted, together with the main results obtained, constitute a basis for future developments and further studies. As far as the evaluation of the parameter C, proportional to the ratio between peak ground velocity and rotation, is concerned, results retrieved from the three-dimensional numerical model show values higher than those inferred by available measured data. It could be possible to refine the estimation of this parameter, e.g., i) introducing a non-linear soil behaviour and ii) combining the broadband spatial coherence information of the semi-empirical approach with the synthetics results, limited up to 2 Hz. In particular, the innovative non-conforming meshing approach, introduced in the modelling phase of the Christchurch CBD, allowing the contact between elements of different sizes in different sub-domains, lays the basis for a noticeable development of the numerical simulations i) reducing the overall number of elements and therefore the computational burden of the problem and ii) allowing the study of the typically multi-scale wave propagation problem from far-field to near-field regions, up to the evaluation of local Site-City interaction effect.

In this way, it could be possible to numerically model and compare earthquakes that interest regions of several thousand square kilometres., as the recent events of Maule, Chile (M_W 8.8 27/02/2010) or Tohoku, Japan (M_W 9.0 06/04/2011), without increasing dramatically the computational burden of the problem. Notwithstanding their low probability, "Christchurch-like" seismic events are not isolated cases. They deserve special attention and constitute an important element in overall risk management approach, proving that, even if earthquake engineering, and all the related research fields, tackle efficiently the challenge of earthquake catastrophes, nonetheless the fragility of modern society is still quite high. How to work toward building an earthquake resilient society seems to be the next defiance. Furthermore, the major events of the last two years dramatically reminded us that the reliable assessment of earthquake-induced damages and losses is a problem of paramount importance, leading us to further reflect on the way risk is presently addressed and about the role of numerical simulations in seismic hazard assessment studies.

APPENDIX A

THE GRAN SASSO LABORATORY AS A POSSIBLE LOCATION FOR A RING-LASER GYROSCOPE: STUDY ON THE NOISE LEVEL

A.1 Introduction

In classical seismology, the general motion of the particles in a solid body can be divided into three kinds: translation, rotation, and deformation. Modern observational seismology is based mainly on measuring translational motions due to the difficulties involved in measuring rotational motions and strains, and because of a widespread belief that rotational motions are insignificant, basically because there were no instruments sensitive enough to measure rotation motions at the level of microradians per second (μrad/sec) in past decades. The lack of instrumental sensitivity has been to be the main obstacle to observing rotational motions. Modern direct measurements of rotational ground motion began only about a decade ago when affordable angular sensors became sensitive enough (capable of measuring an angle of less than ten thousandth of a degree) to detect rotations from small earthquakes, while large ring laser gyros (intended for studying the Earth's rotation) became capable of detecting even smaller rotations from distant earthquakes at the nano-radian level (e.g., McLeod et al. 1998, Igel et al. 2005, Schreiber et al. 2005, Cochard et al. 2006, Schreiber et al. 2009a).

Recently, ring laser technology has provided the means to develop instruments (Ring-laser system or Geosensor) that allow, in principle, the observation of rotational motions in a wide frequency band and epicentral distance range. This system's purpose is the detection of space-time

perturbations predicted by general relativity in connection with Earth's rotation. Ring-laser gyroscopes have long been used in aircraft navigation. This system is intended to permit precision measurement of irregularities in the Earth's velocity of rotation. These data can help correlate stationary reference systems, in the form of extraterrestrial objects such as quasars or stars, with Earth reference systems. Such measurements are essential for satellite-based navigation systems, including global positioning systems (e.g. Schreiber et al. 2003, 2004a, 2004b).

These precise rotational measurements can also help geophysicists gain a better insight into Earth's interior structure, including displacements inside the Earth, the continental drift, and earthquakes. This technology, originally designed for geodesy, is indeed also capable of providing accurate and useful observations for seismology, like the estimation of wavefield properties (e.g. phase velocities, propagation directions), otherwise only accessible through seismic array measurements, polarization analysis, or additional strain measurements (e.g., Pancha et al. 2000, Schreiber et al. 2006, 2009b). Collocated measurements of translations and rotations are of relevant importance, indeed they may: i) allow transformation of translational seismograms to the complete ground motion of an observation point; ii) help to further constrain rupture processes; and iii) provide additional hazard-relevant information to earthquake engineers.

A.2 Ring laser Gyro: Principles of operation

The principles of operation are depicted in Figure A.1: Ring lasers are inertial rotation sensors using the Sagnac effect, which is the frequency splitting of two counter-rotating laser beams due to rotation (Sagnac 1913). A minimum of three mirrors form a closed light path in a ring resonator. The resonator cavity is filled with the laser medium, a helium/neon gas mixture. The plasma is excited at one location by an alternating electrical field generating two counter-propagating laser beams. When this assembly is rotating, the (also rotating) observer sees a frequency difference between the co-rotating and the counter-rotating beam being proportional to the rotation rate (Schreiber et al. 2004b). This beat frequency or Sagnac frequency delta_f is described by the Sagnac formula for active resonators:

$$\delta f = \frac{4A}{\lambda P}\mathbf{n}\cdot\boldsymbol{\Omega} \qquad (A.1)$$

Where A is the enclosed area, P the perimeter (beam path length), λ the optical wavelength, $\boldsymbol{n}$ the normal vector to A and $\boldsymbol{\Omega}$ is the rotation vector. The task is to measure the frequency of the optical interference pattern, which is roughly 12 order of magnitude below the optical frequency, with a relative precision of 10^{-9}. A horizontally installed ring laser, rigidly attached to the Earth,

measures the projection of the Earth rotation vector onto the laser plane normal vector. Considering the orientation, the inner product between the rotation and the normal vector can be expressed as:

$$\mathbf{n} \cdot \boldsymbol{\Omega} = \Omega \sin(\varphi + \delta_N) \cos(\delta_E) \qquad (A.2)$$

where φ is the geographic latitude and δ_N and δ_E are small angular variations towards North and East, respectively. When using one ring laser alone, variations of the rotation rate and angular variations between the ring laser and the rotation axis cannot be distinguished

A.3 Ring Laser technology: the meaningful example of Wettzell, Germany

The world's largest (4 x 4 m) ring-laser gyroscope for Earth rotational measurements is in an underground laboratory at the Wettzell Fundamental Research Station, a geodetic laboratory near Kötzting in the Bavarian Forest mountains of Germany (Figure A.1). The project was commissioned by the German Federal Cartography and Geodesy Office (Frankfurt, Germany).
The centrepiece of the large ring-laser G is a disk of thermally stable Zerodur ceramic glass, 4.25 m in diameter and 25 cm thick. This slab has been placed on a 60-cm-thick granite slab with a weight approaching 10 tons, which is embedded in a monumental concrete table in the laboratory. Four bars are rigidly attached to a base plate forming the edges of a square with 4 m side length. The coefficient of thermal expansion is less than 1×10^{-8} K^{-1}. The four mirrors and their mirror holders are attached at the face sides of the bars by molecular adhesion. This technique ensures a stable vacuum seal. Once surveyed and attached, the mirrors can never be readjusted. The only possibility to slightly affect the beam path is to adjust the gain tube. The mirrors are of extreme quality, only losses of few ppm are allowed to reduce backscattering to an uncritical level. They are slightly concave with a radius of 4 m to keep the laser beam in line. The laser medium, a Helium/Neon gas mixture with a pressure of few hPa, is excited in a Pyrex gain tube by an alternating electrical field to maintain the lasing process. The optical beam power is continuously monitored and kept constant by a feedback loop steering the excitation power. At one mirror the transmitted fraction of each of the laser beams is separated and interfered at the beam combiner, where the interference signal is converted to an electrical frequency by a photomultiplier or a PIN diode.
The "G" ring laser is resting on a polished granite table embedded in a 90 t concrete monument. The monument is attached to a massive 2.7 m diameter concrete pillar, which is founded on crystalline bedrock 10 m below the former surface. A system of concrete rings and isolation

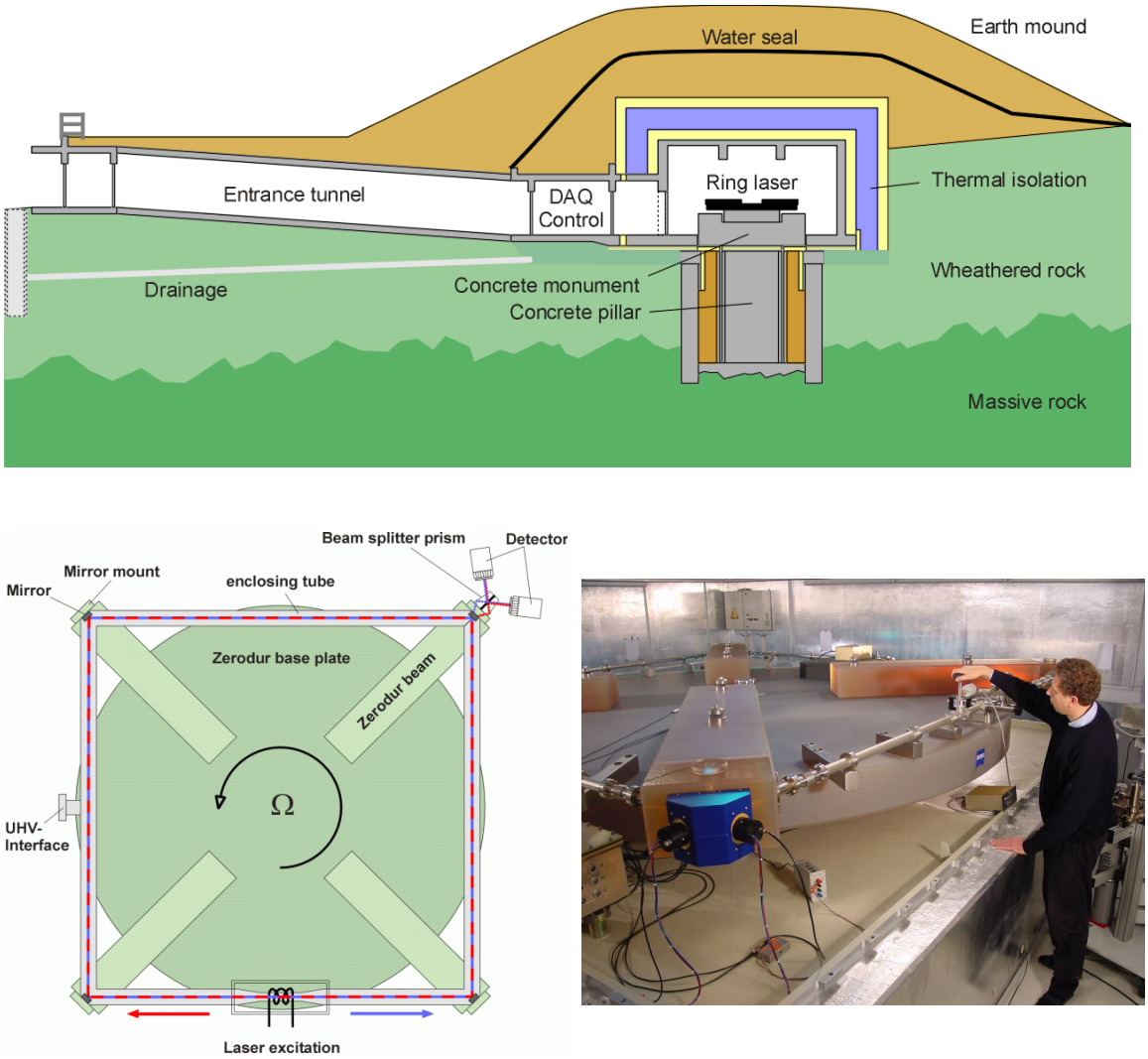

Figure A.1. Top: Schematic section through the "G" underground lab located in Wettzell, Germany. Bottom: (Left hand side): Principle of operation of the ring Laser "G"; (Right hand side): Picture of the ring laser "G".

material shield the monument and pillar from lateral deformations and heat flow. The instrument is protected against external influences in a subsurface installation, where a passive thermal stability is reached by a 2 m alternating layer of styrofoam and wet clay, and a 4 m earth mound. A lateral entrance tunnel with 5 isolating doors and a separate control room minimize thermal perturbations. Because variations in air pressure and temperature could still have some influence on the volume of the Zerodur disk, it is enclosed in a steel tank for thermal protection of the ring laser and to ensure constant air pressure. After 2 years of thermal adaptation, the average temperature reached 12.2 °C with seasonal variations of less than 0.6 °C.

A.4 Study of the noise level of the Gran Sasso Laboratory, Italy

Ring laser gyro observations at Wettzell and the ones measured by a smaller system located at Piñon Flat, California, have demonstrated consistent measurements of rotational ground motion in the far field, but the cost of this high-precision instruments (US$1 million or more) makes widespread deployment unlikely and of crucial important the assessment of the level of noise of the place where it should be located (Schreiber et al. 2008).

The main goal of the presented study is to understand the feasibility of measuring low-amplitude ground motions at the Gran Sasso Laboratory in central Italy. This involves in particular the measurement of rotational ground motions in connection with a possible future installation of one multi-component Ring Laser Gyro in these underground laboratories. The structural engineering aspects of the projects consist in the evaluation of the noise characteristics of the underground laboratory, trying to estimate the effects of the cavity on measurements of rotations (Smerzini et al. 2009b).

Thanks to the collaboration with the INGV of Pisa, five months of broadband data (from January to May 2008) for a KS2000 (120-s Geotech) seismometer located inside the tunnel have been analyzed. A time-frequency analysis allows the quantitative description of the translational noise characteristics.

In order to evaluate the long-term seismic noise levels for the available broadband seismic data a probability density function (PDF) to display the distribution of seismic power spectral density (PSD) has been adopted. PDF noise plots are useful for characterizing the current and past performance of existing broadband sensors, for detecting operational problems within the recording system, and for evaluating the overall quality of data for a particular station. The advantages of this approach include: i) an analytical view representing the true ambient noise levels rather than a simple absolute minimum; ii) an assessment of the overall health of the instrument/station; and iii) an assessment of the health of recording and telemetry systems (McNamara and Buland 2004).

A.4.1 Cultural noise

The most common source of seismic noise is from the actions of human beings at or near the surface of the Earth. This is often referred to as "cultural noise" and originates primarily from the coupling of traffic and machinery energy into the earth. Cultural noise propagates mainly as high-frequency surface waves (>1-10Hz, 1-0.1s) that attenuate within several kilometres of distance and depth. For this reason cultural noise will generally be significantly reduced in boreholes, deep caves and tunnels. Cultural noise shows very strong diurnal variations and has characteristic frequencies depending on the source of the disturbance.

A.4.2 Microseisms

There are two dominant peaks in the seismic noise spectrum that are both widespread and easily recognizable. The lower amplitude, longer period peak (T = 10-16 s), known as the single-frequency peak. It is generated in shallow coastal waters where ocean wave energy is converted directly into seismic energy either through vertical pressure variations or from the crashing of surf on shore. The higher amplitude, shorter period peak (T = 4-8 s), known as the double frequency peak, is generated by the superposition of ocean waves of equal period travelling in opposite directions, thus generating standing gravity waves of half the period of a standard water wave. The standing gravity waves cause perturbations in the water column that propagate to the ocean floor and increase significantly during large oceanic storms.

A.4.3 Earthquakes

In this approach there is no attempt to screen the continuous waveforms to eliminate body and surface waves from naturally occurring earthquakes. Earthquake signals are included in processing because they are generally low probability occurrences even at low power levels (small magnitude events). Being interested in the true noise that a given station will experience, thus all signals are included. For example, including these events tells us something about the probability of teleseismic signals being obscured by small local events as well as various noise sources. Large teleseismic earthquakes can produce powers above ambient noise levels across the entire spectrum and are dominated by surface waves >10s, while small events dominate the short period, <1s. Earthquakes are observed in the PDFs as low probability smeared signal at short and long periods.

A.4.4 Power Spectral Density and Probability Density Function

For each one of the transversal components of the broadband seismometer located in the Gran Sasso Laboratory, the Power Spectral Density of acceleration is evaluated, considering 1-day long windows, overlapping 50% (Figure A.2, left column). Blank stripes means missing or unreadable data. For each PSD is then constructed a Probability Density Function (PDF) (Figure A.2, right hand column). The probability of occurrence of a given power at a particular period is plotted for direct comparison to the Peterson (1993) high and low noise models (HNM, LNM).
In the diagrams of the three components, a peak in the cultural noise is easily distinguishable between periods of 0.08-0.1 s, due to the human activities, originates primarily from the coupling into the earth of traffic due to the near highway and energy due to the machinery in the laboratory. Clearly perceptible, at least for the N and Z component are the microseism peaks at around 4 and 10 s, respectively. As for the E component, only the first is visible.

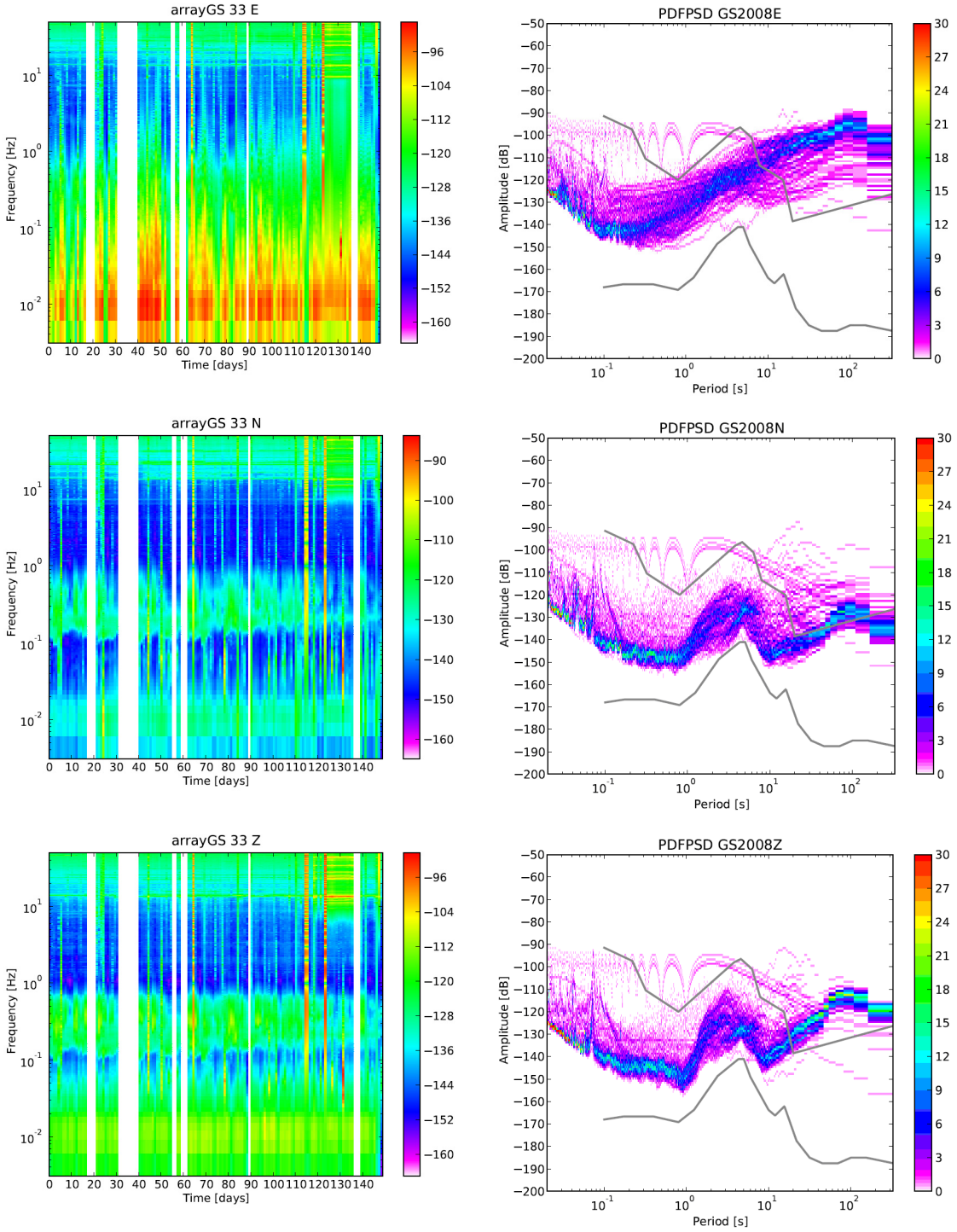

Figure A.2. Power spectral density (PSD) (Left hand column) and its corresponding probability density function (PDFPSD) (Right hand column) of the three component of acceleration (East-West, North-South, Up-Down from top to bottom) recorded between January and May 2008, by a broadband seismometer located in the Gran Sasso Laboratory.

All the three components show an excellent behaviour at short period, being not far from the low noise model curve, whereas they have an unexpected behaviour at long period, approaching or even overtaking the high noise model curve, starting from period of around 10 s. This could be mostly explainable by lack of instrumental resolution. Since the Ring laser gyroscope is supposed to work in the range of frequency between 3 mHz and 10 Hz (Schreiber et al. 2004b), further analysis and measurement are necessary, before there is more debate about the ring laser installation and the possible effects of the cavity on measurements of rotations.

A.5 Concluding remarks

In this appendix the complex technology at the basis of the ring laser systems has been presented. The high complexity and costs of this instrument make its diffusion extremely difficult, and particularly important to assess the level of noise a prospective location.
With the prospect of a future installation of a ring laser system inside the Gran Sasso Laboratory, a study of the noise level has been completed, plotting the probability density function of the power spectral density of the accelerations recorded for five months, between January and May 2008, by a broadband seismometer located in the underground laboratory.
All the three components show an excellent behaviour at short period, whereas they have an unexpected behaviour at long period, approaching or even overtaking the high noise model curve. This is mostly explainable by lack of instrumental resolution, requiring further measurements before there is more debate about the ring laser installation

A.6 Acknowledgements

The author deeply thanks Prof. Gilberto Saccorotti of Istituto Nazionale di Geofisica e Vulcanologia (INGV), Sezione di Pisa, for kindly providing the data of the KS2000 seismometer located inside the Gran Sasso Laboratory. Prof. Heiner Igel, Prof. Joachim Wassermann and Dr. Martin Käser of Ludwig Maximilians Universitaet (LMU), Department of Earth and Environmental Sciences, Section Geophysics, Munich, Germany, are deeply acknowledged for their supervision and useful suggestions.

APPENDIX B

HONORING vs. NOT-HONORING vs. NON-CONFORMING: THREE MESHING APPROACHES FOR 3D COMPLEX SEISMIC SCENARIOS

B.1 Introduction

The spectral element method (SEM) is a powerful, well-established, numerical technique naturally suited for three-dimensional seismic wave propagation analyses. A class of SEM has been widely used in the seismological field thanks to its capability of providing fast and highly accurate solution, allowing the implementation of optimized parallel algorithms and decomposing the three-dimensional computational domain into a family of non-overlapping hexahedra. The purpose of the study is to tackle the meshing problem by comparing the standard approach, herein called "honoring" (H), with different strategies, herein referred as "not honoring" (NH) and "non-conforming" (NC). In the NH approach the Lagrange polynomial interpolation between the Gauss-Legendre-Lobatto (GLL) nodes, with their own values of mechanical properties, accomplishes the task of reproducing sharp interfaces. NC techniques, allowing different mesh sizes between neighbouring sub-domains, provide considerable geometrical flexibility, with the double consequence of an improvement in the level of quality metric of the mesh and a reduced computational burden of the problem. A description of the three criteria is presented here, focusing on the response of alluvial valleys. The comparison of the obtained solutions using with the different strategies suggests that a proper combination of NH and NC strategy could be an

appealing and fast way to solve the mesh creation problem whenever a reasonable compromise between accuracy and computational time is required.

B.2 The meshing problem

The advantages of hexahedral elements meshes over tetrahedral ones are manifold (Komatitsch et and Vilotte 1998, Komatitsch et al. 2001, Igel et al. 2011, Peter et al., 2011) and can be summarized in the lower computational burden of the wave propagation solutions, with diagonal mass matrix and optimized tensor products, particularly suitable in a parallel computing strategy (Komatitsch et al. 2003, Carrington et al. 2008) and in the typically smaller number of elements (Hesthaven and Teng 2000, Vos et al. 2010). On the other side, while three-dimensional unstructured tetrahedral meshes can be achieved quite easily with commercial or non commercial software (George and Borouchaki 1998), the creation of a three-dimensional non-structured hexahedral mesh is more complex and it is still recognized as a challenging problem. Furthermore, a general, robust and automatic procedure able to subdivide any given geometry into hexahedral elements does not exist in the literature (Blacker, 1994). Moving from regularly horizontally layered models to more complex and realistic cases, with the presence of alluvial basins, the task to honor complex geometrical interfaces and tuning the elements size according to the variation of mechanical properties, implies a long and tedious pre-processing, linked with the specific case under study, with little chance to be implemented in a recursive manner. Through the years, various authors have presented different examples of three dimensional hexahedral meshes suitable to study seismological problems, like the seismic response of an alluvial valley, fully taking into account and modelling the contact between soft sediments and the bedrock (Komatitsch et al. 2004, Chaljub et al. 2007, Lee et al. 2008, Stupazzini et al. 2009a).

In this chapter the meshing problem already introduced in Chapter 3, in the creation of the three-dimensional hexahedral spectral element meshes for the Canterbury Plains model is discussed. Different meshing strategies, herein called "honoring" (H), "not honoring" (NH) and "non-conforming" (NC), are compared. The former, H strategy, is the standard meshing approach: the domain under study is subdivided into non overlapping portions (characterized by polynomial variation of the mechanical properties) and each of them is modelled with hexahedral elements that have to strictly respect, through a 3D unstructured conforming mesh, the constraints related with the (i) sampling of the incoming wave and the (ii) shape of the interfaces. The "step-like" model of the Canterbury Plains described in Chapter 3 is realized with this classical technique. The NH strategy, allow us to soften the requirement to honour the shape of the interface, that is also the most demanding during the generation of the mesh, only respecting the constraints related with the sampling. The task of reproducing sharp interfaces is accomplished thanks to the Lagrange

polynomial interpolation between the GLL nodes, characterized by their own values of mechanical properties. In this way the complex interface between the alluvial soil of the Canterbury Plains and the volcanic rock of the Banks Peninsula has been described in the "smooth" three-dimensional model presented in Chapter 3. NC technique has been adopted in the modelling phase of the densely urbanized area of the Christchurch CBD, described in Chapter 5. Allowing the contact between faces different in shape and size, non conforming techniques turn out to be particularly useful in seismic engineering modelling of wave propagation, whenever a sharp change of soil mechanical properties is encountered. Non-conforming high order strategies for the approximation of elastic wave problems in heterogeneous media have been recently extensively analyzed by Antonietti et al. (2012).

B.3 The study case: Valley of Grenoble

A comparison of the three meshing approach is here presented, focusing on the modelling of alluvial valleys. The set-up proposed by ESG2006 committee in the frame of the numerical benchmark of a three-dimensional ground motion simulation in the valley of Grenoble, French Alps (Chaljub et al. 2007, Dumbser et al. 2007) has been adopted. Particularly, the set-up includes a series of information that should be taken into account during the generation of a three-dimensional model for the considered region: (i) the topography of the area (DEM with 250 m spacing), (ii) the shape of the alluvial basin (DEM with 250 m spacing) and (iii) the mechanical properties of the area, varying inside the alluvial basin accordingly to the depth from the surface and layered stratified into the bedrock. No theoretical solutions are available for such a complex problem and, therefore, it is not possible to measure errors by comparison with a reference solution. Nevertheless, a peculiar features of the Grenoble valley, that makes it a valuable benchmark to test different meshing strategies, is, in addition to the good quality of the provided information, the availability of other numerical techniques that have presented results for the same three-dimensional area and the same source (Stupazzini et al. 2009a, Igel et al. 2011).
In order to accurately and efficiently provide the seismic wave propagation analyses, exploiting the available information, it is necessary to decompose the domain into an unstructured mesh of non-overlapping hexahedral elements. The creation of the mesh, for the presented models, is performed thanks to the commercial mesher CUBIT (http://cubit.sandia.gov/), state of the art software in the field of three-dimensional unstructured hexahedral decomposition, incorporating an extensive library of powerful and advanced meshing schemes. Nevertheless, it is worth pointing out that the meshing of a large domain (compared to the minimum required element size), like the valley of Grenoble, with unstructured three-dimensional hexahedral elements it is not feasible with an automatic procedure, due to the complex three-dimensional shape of the basin and to the wide

Table B.1. 3D numerical models produced with the different meshing strategies.

Model Name	N. of elem.	Spectral Degree	N. of nodes	Δt_simulation [sec.]	ΔtCFL [sec.]	% of ΔtCFL
H	202,477	4	13,300,892	1.8742x10-4	7.700x10-04	24.34%
NH	272,416	4	17,765,697	2.6416x10-4	1.321x10-3	20.00%
NH-NC	230,900	4	15,273,550	2.5007x10-4	1.824x10-3	13.71%

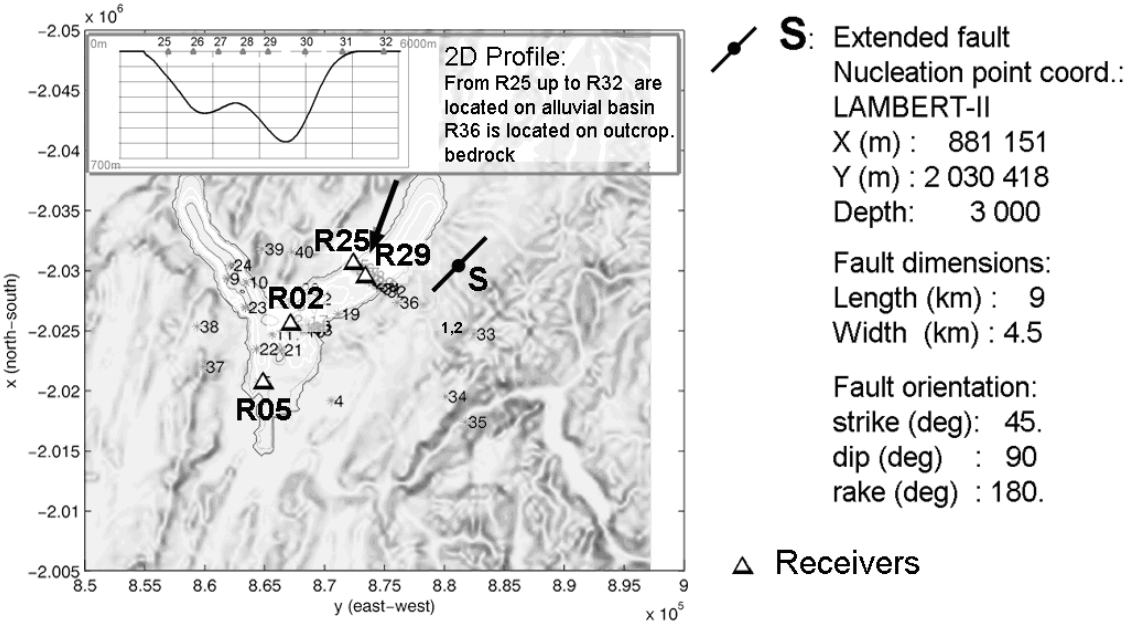

Figure B.1. Receivers location along the valley, contour line of the outcropping bedrock and topography adopted during the ESG06 "Grenoble Benchmark". Dimensions and orientations of the extended fault S are listed above, together with the position of the receiver from R25 to R32 located along the 2D profile.

range of the size of the elements, ranging from 100 m at the top of the model, inside the basin, up to 1 km or even more at the bottom of the model. In the following sections we extensively present procedure and meshes, obtained with the H, NH and NC strategy (Table B.1), and then we compare the resulting time histories, obtained exciting the model with an extended fault (Figure B.1), herein called S.

B.4 Honoring (H) meshing strategy

The H strategy is the standard meshing approach: the domain under study is subdivided into non-overlapping portions, modelled with hexahedral elements that have to strictly honor the constraints related with the sampling of the incoming wave and the shape of the geometrical interfaces (e.g.: alluvial deposits and bedrock). In the specific case of the Grenoble valley, the decomposition of the area adopts the contour of the alluvial basin as a physical separation interface and the elements are meant to follow it

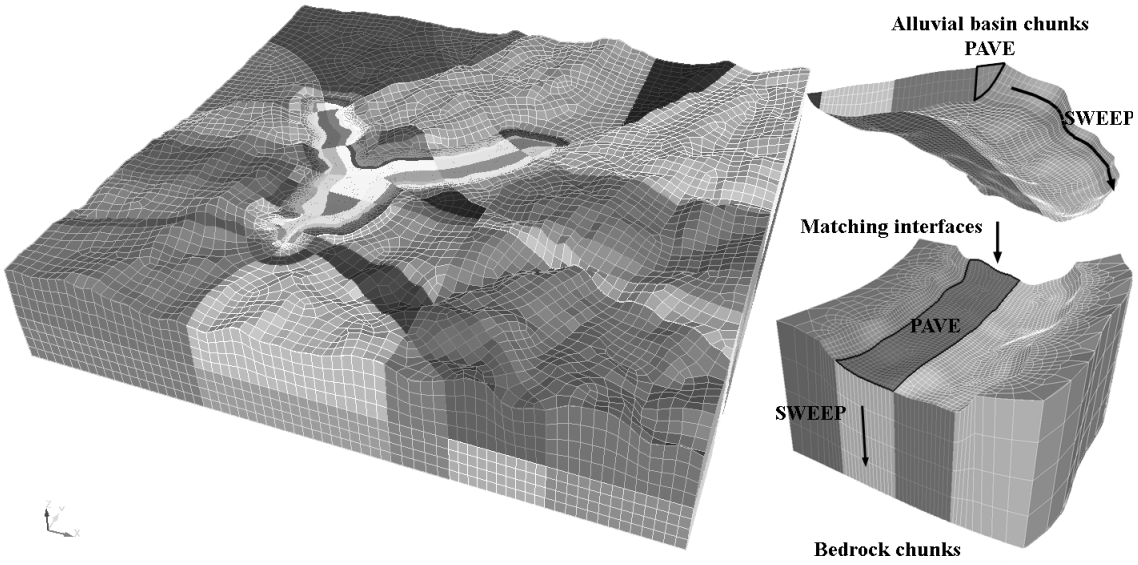

Figure B.2. 3D numerical model obtained with the H strategy and used for the simulations of ESG06 "Grenoble Benchmark". The computational domain is subdivided into small chunks and each is sequentially meshed starting from the alluvial basin down to the bedrock (a sketch of the meshing procedure is here presented). For simplicity, the spectral elements are shown without the GLL nodes.

To accomplish this task the whole domain is subdivided in small (a few kilometres) hexahedral chunks (Figure B.2). Each one of these chunks is meshed with a standard scheme (e.g.: the "pave" mesh scheme is applied on one of the surface and then a sweeping is performed along the other direction). This technique for the splitting the area under examination into hexahedral , strictly respects the geometrical constraint, but implies a worsening of the overall level of the quality metric of the resulting mesh (Taylor and Flanagan 1989, Knupp 2000) and an increase in the total number of elements. Furthermore it is important to point out that the mesh creation is performed in a not-automatic way. It means that and the task of honoring complex geometrical interfaces implies a long and tedious pre-processing, specific and different case by case, and, moreover, if new information becomes available afterwards (e.g.: through geophysical perspections or borehole drilling), increasing the level of knowledge of the investigated area and changing significantly the alluvial basin shape, the whole procedure would need to be repeated from scratch. Moreover, the H strategy, following carefully the edge of the alluvial deposit, has other major drawbacks: (i) the element size decreases significantly whenever the basin is very complex (steep gradient of the dip or high curvature of the contour) and (ii) some element results to be strongly deformed (elongated or stretched) in order to provide an efficient unstructured mesh.

The final mesh, obtained through the H strategy, is depicted in Figure B.2. It consists of 202,477 elements ranging from a minimum size of 21 m, in the alluvial deposit, up to 1,000 m, in the deep bedrock, at the bottom of the model. The mesh is hence designed to propagate correctly up to 3 Hz with SD equal to 4.

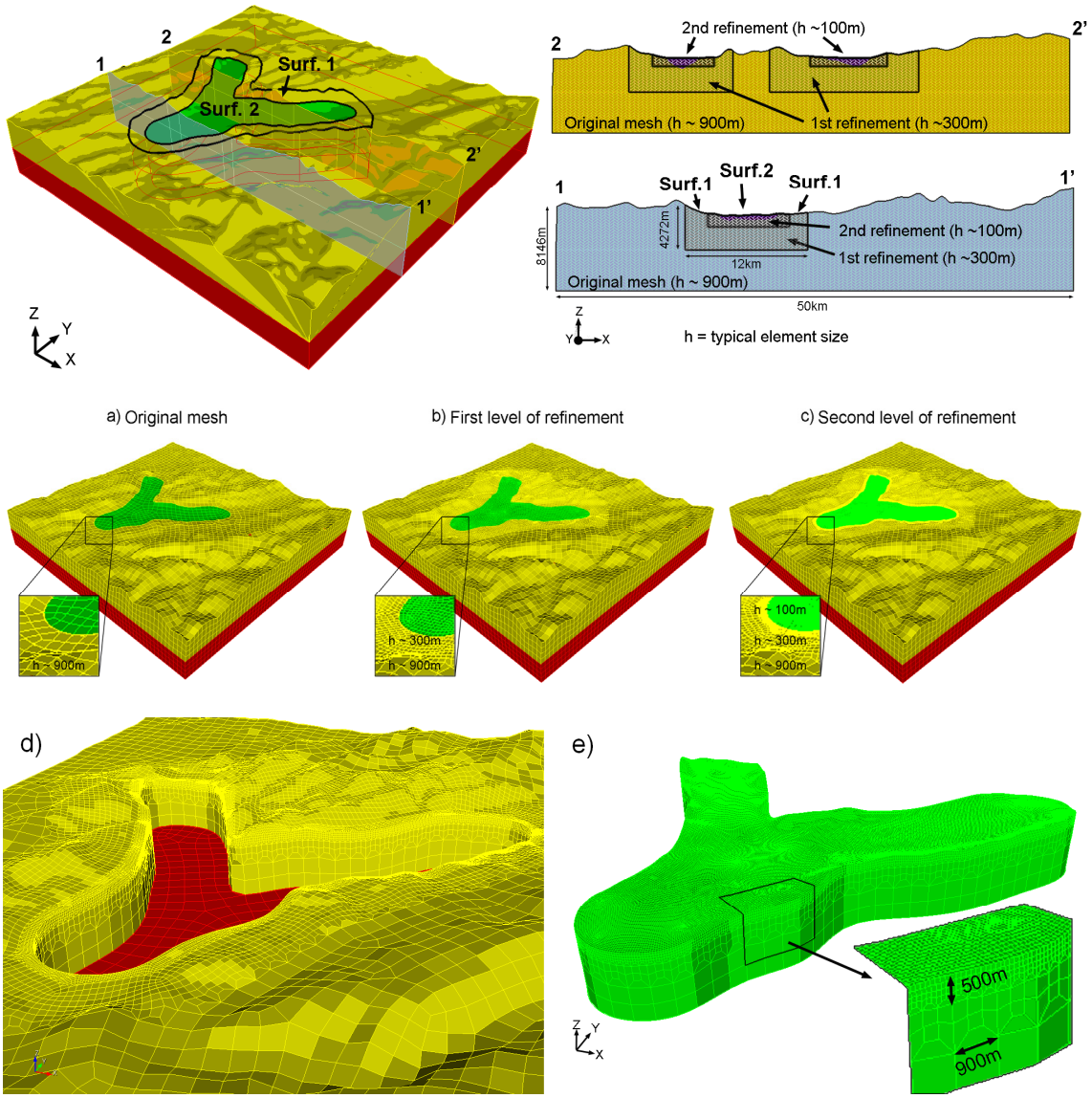

Figure B.3. Three-steps, Not Honoring meshing strategy. (Top) Topography of the Grenoble area with highlighted the two surfaces adopted in the meshing strategy: a) The computational domain is subdivided into big regular chunks and each one is meshed with a "pave" scheme on the top and then swept down to the bottom. b) First refinement, provided automatically by CUBIT; element size goes from 900 m down to 300 m. c) Second refinement with an imposed depth; elements in the surroundings of the alluvial deposit have a typical size of 100 m. d) and e) Final NH mesh of Grenoble: the domain is fully unstructured. The dark volume in a), b) and c) is here extracted from the inner core of the mesh to better highlight the interior design of the mesh with its refinements. For simplicity only the spectral elements are shown without GLL nodes

B.5 Not Honoring (NH) meshing strategy

The NH meshing strategy allows us to soften the demanding requirement of respect of the complex shape of the interfaces, only respecting the constraints related with the sampling. The task

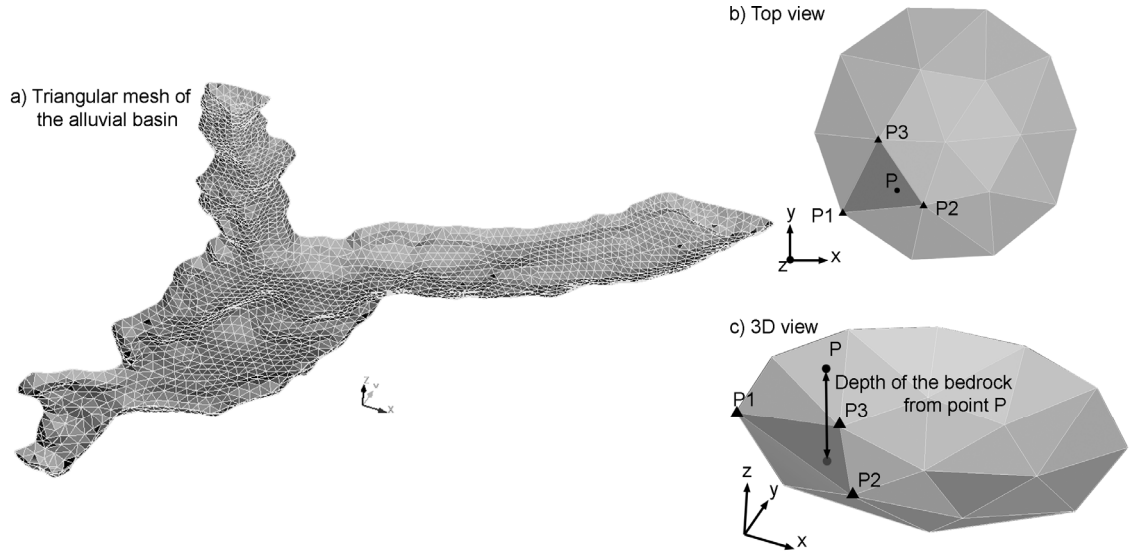

Figure B.4. a) DEM of the alluvial basin, meshed with a triangle with a typical edge size of 300 m. Zoom of the triangular mesh: top view b) the generic point P is inside the projected 2D triangle with vertex P1-P2-P3. c) the depth of the bedrock from point P is computed as the distance between P and the plane passing through the points P1-P2-P3, along the z axis.

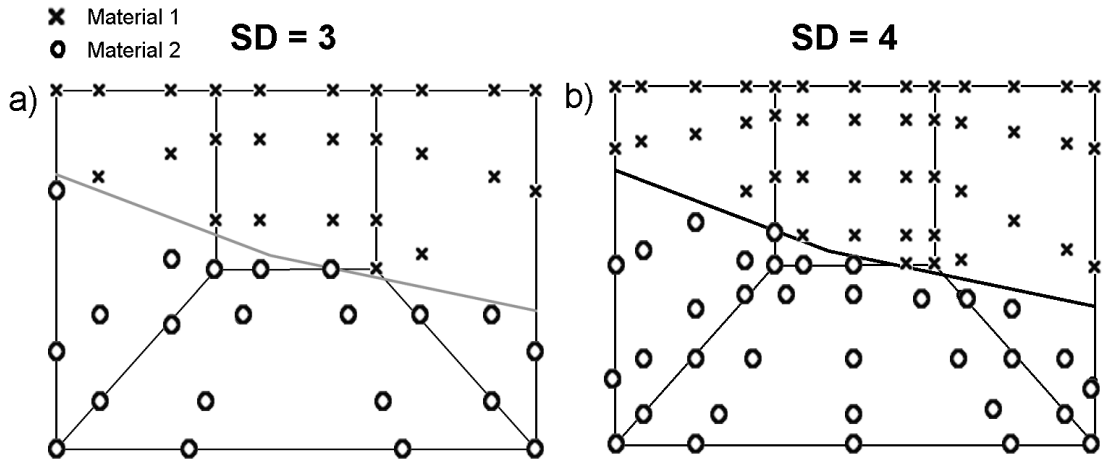

Figure B.5. Not Honoring meshing strategy: the mechanical properties are distributed node by node according to the depth of the bedrock previously computed, as shown in Figure B.4.

of reproducing sharp interfaces is accomplished thanks to the Lagrange polynomial interpolation between the GLL nodes, characterized by their own values of mechanical properties. The NH meshing strategy can be described as a "three step" procedure, illustrated in Figure B.3.

The first step consists in the generation of a coarse mesh (size of 1,000 m) with element honoring the topographical constrain and the interfaces of the layered bedrock. The deep geometry of the alluvial basin is given as a soft constrain in the sense that the inner volume (dark colour) in Figure B.3 includes the alluvial basin and has a simplified geometrical shape compared to its real shape. It is noteworthy that 1,000 m is a size of the element compatible with a correct sampling of

f_{max} = 3Hz propagating inside the outcropping bedrock (characterized by shear velocity VS = 3200 m/s). The second step refines surface 1 and 2 up to a certain depth. The transition algorithm adopted is the so called "three_to_one" scheme and can be applied even to unstructured paved mesh with no particular worries concerning the resulting quality of the generated hexahedral. The third step refines only surface 1, up to an imposed depth. The whole strategy basically drives the element size from 1,000 m down to 100 m, and this size is compatible with a correct sampling up to 3 Hz of the upper part of the alluvial deposit (characterized by shear velocity VS = 300 m/s) with SD equal to 4. It is worthwhile to underline that the procedure described in Figure B.3 can be programmed and parallelized. Furthermore, improvements and generalizations are feasible and some major geometrical constrains could become part of the model description (e.g.: bottom of the alluvial basin, neglecting the edges) and handled by the automatic procedure implemented on the basis of the CUBIT software, called GeoCUBIT (Casarotti et al. 2007).

In the final mesh depicted in Figure B.3, the domain is fully unstructured and for simplicity only the spectral elements are shown without GLL nodes. At this stage the mechanical properties can be efficiently assigned but we still need to introduce in the model a description of the geometrical interface between alluvial soil and bedrock. An efficient way to provide such information is to realize a triangular decomposition of the surface delimiting the alluvial deposits and the bedrock, as shown in Figure B.4. An algorithm for the search of the relative position of the node with respect to this interface assign at run time the mechanical properties, simply providing, in the input phase, the triangular mesh of the soft deposit and the values of SD. Each GLL node of the element is automatically associated with the mechanical properties of the material in which it is included, basically distinguishing if the node is over or under the alluvial interface, even when it cross the considered element (Figure B.5).

B.6 Non-Conforming (NC) meshing strategy

As presented and analyzed in Antonietti et al. (2012), non-conforming techniques, like Discontinuous Galerkin Spectral Element Method (DGSEM) or Mortar Spectral Element Method (MSEM), are numerical strategies for the solution of partial differential equations, herein applied to the field of the elastodynamics. These techniques employ high-order finite element discretization on a non-overlapping subdomain partition of the computational domain, allowing the adoption of independently generated meshes and different spectral degrees in different sub-domains.

Removing the constraint that element faces should have the same shape and size in the contact regions, non-conforming techniques avoid the generation of a huge number of transition elements between areas characterized by different mechanical properties. This is particularly useful in seismic engineering modelling of wave propagation, whenever the passage between the soft soil of the

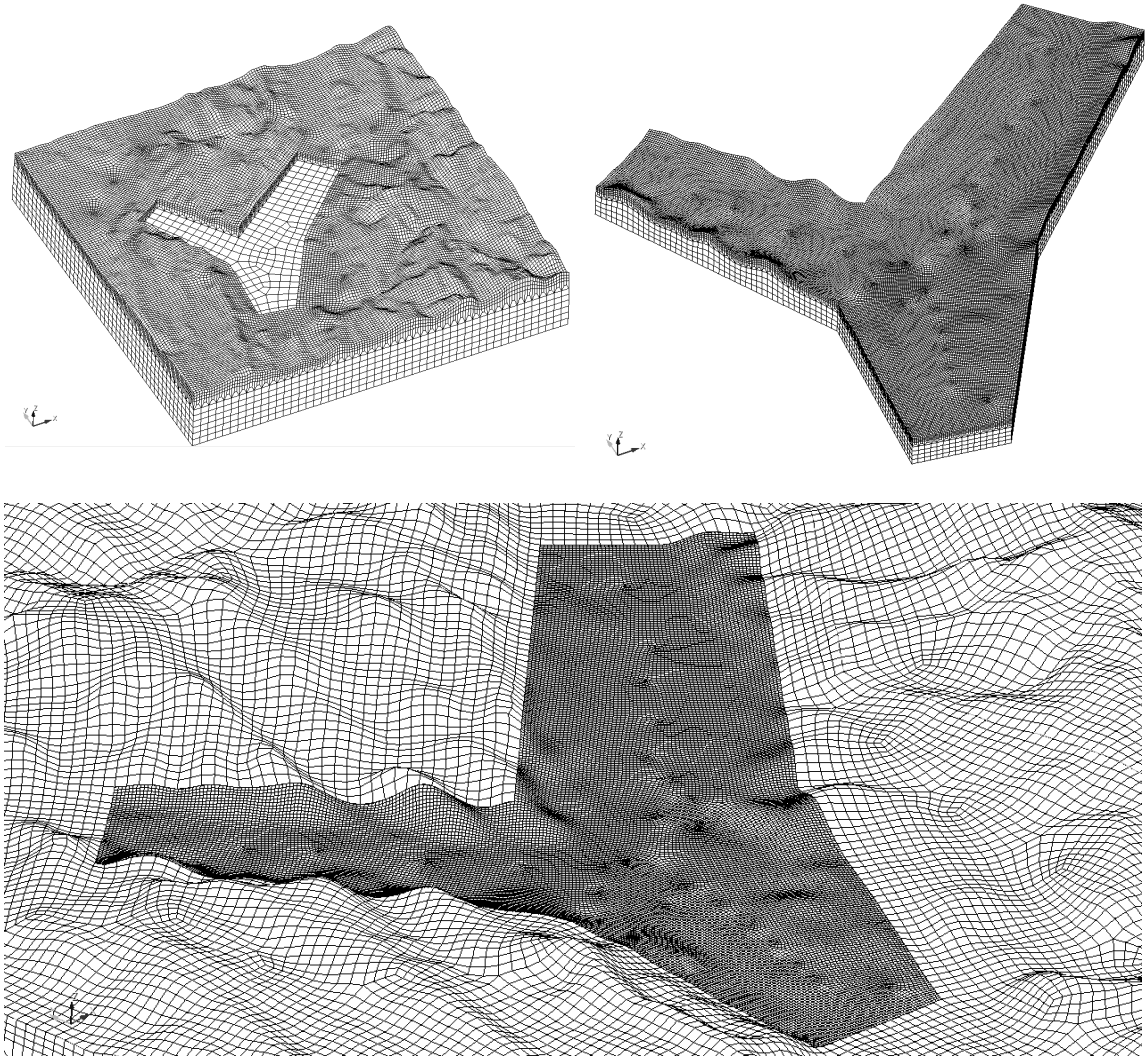

Figure B.6. Non-conforming mesh approach. Volumes with different mechanical properties are meshed independently (top) and subsequently re-aggregate (bottom). Non-conforming techniques allow the contact between faces different in shape and size. With the resulting mesh the NH strategy can be adopted, describing the shape of the alluvial basin through the DEM depicted in Figure B.4.

alluvial basin and the stiff material of the bedrock requires a sharp change of soil mechanical properties (in terms of shear wave velocity and density) and therefore a sharp change in the size of the elements of the mesh. The possibility to nimbly vary the mesh element size, with the only constraint being a proper wave propagation, offers thus the possibility to numerically tackle the wave propagation problem from different scales, from far-field to near-field, from near-field to the site-city interaction, as discussed in Chapter 5.

The non-conforming meshing strategy, then, is particularly suited to be coupled with a Not-Honoring strategy, as has been done in the case of the Grenoble Valley and depicted in Figure B.6. The non-conforming techniques accomplish the task of roughly separate volumes that are

supposed to have different mechanical properties, while the proper definition of the complex geometry of the alluvial basin is performed through a Not-Honoring strategy. In this way it is possible to adopt a refined mesh only in the portion of the model where it should be necessary, obtaining a reduced number of elements, or, alternatively, as depicted in Figure B.6, it is possible to adopted a finer and deeper refinement in the specified areas, with approximately the same total number of elements, furthermore characterized by a better level of the quality metric, with a considerable reduction of the time needed to perform the mesh. As depicted in Figure B.6 in realizing the NH-NC model two volumes have been separated and independently meshed, with a size of the external volume varying from 1,000 m at the bedrock to around 300 m at surface, whereas the inner volume has size of elements varying from 300 m and 100 m at surface. The non-conforming technique allows the re-composition of these subdomains and the NH strategy can be adopted with the resulting mesh.

B.7 Numerical simulation: Extended fault input

In this section we compare the models obtained with H and NC-NH strategy, in the case of an Extended Fault input (source S in Figure B.1). The moment magnitude M_W of the synthetic earthquake is 6.0 and the mechanism of the event is a right-lateral strike-slip occurring on the eastern side of the alluvial basin, along the Belledonne fault. This fault has a rectangular shape (9 km x 4.5 km) with a circular crack propagating from the centre of the rectangle with a rupture velocity of 2,800 m/s. The source time function adopted is an approximate Heaviside function:

$$M_0(t) = \frac{1}{2}\left[1 + erf\left(2.0\frac{t-2\tau}{\tau/2}\right)\right], \qquad (B.1)$$

where the rise time τ = 1.116 s. These values are chosen to define a slip velocity of approximately 1 m/s. It is important to underline that the source in the H and in the NC-NH meshes is not exactly the same, due to the changes in the surroundings of the fault area, introduced by the different mesh designs. Nevertheless the kinematic implementation of the rupture, as a distribution of seismic moment tensor density, allows to minimize these differences.

The results obtained with the different meshing approach are presented in Figure B.7, in terms of velocity along the three translational directions for the eight receivers located along the two-dimensional profile, from receivers R25 to R32. The results reveal an excellent agreement both in amplitude and phase between the H, conforming approach and NH, NC model, even if some major differences arise in the evaluation of the peak ground velocity values. That could be due to the fact that the maximum value of one component in a time history is a local parameter, highly

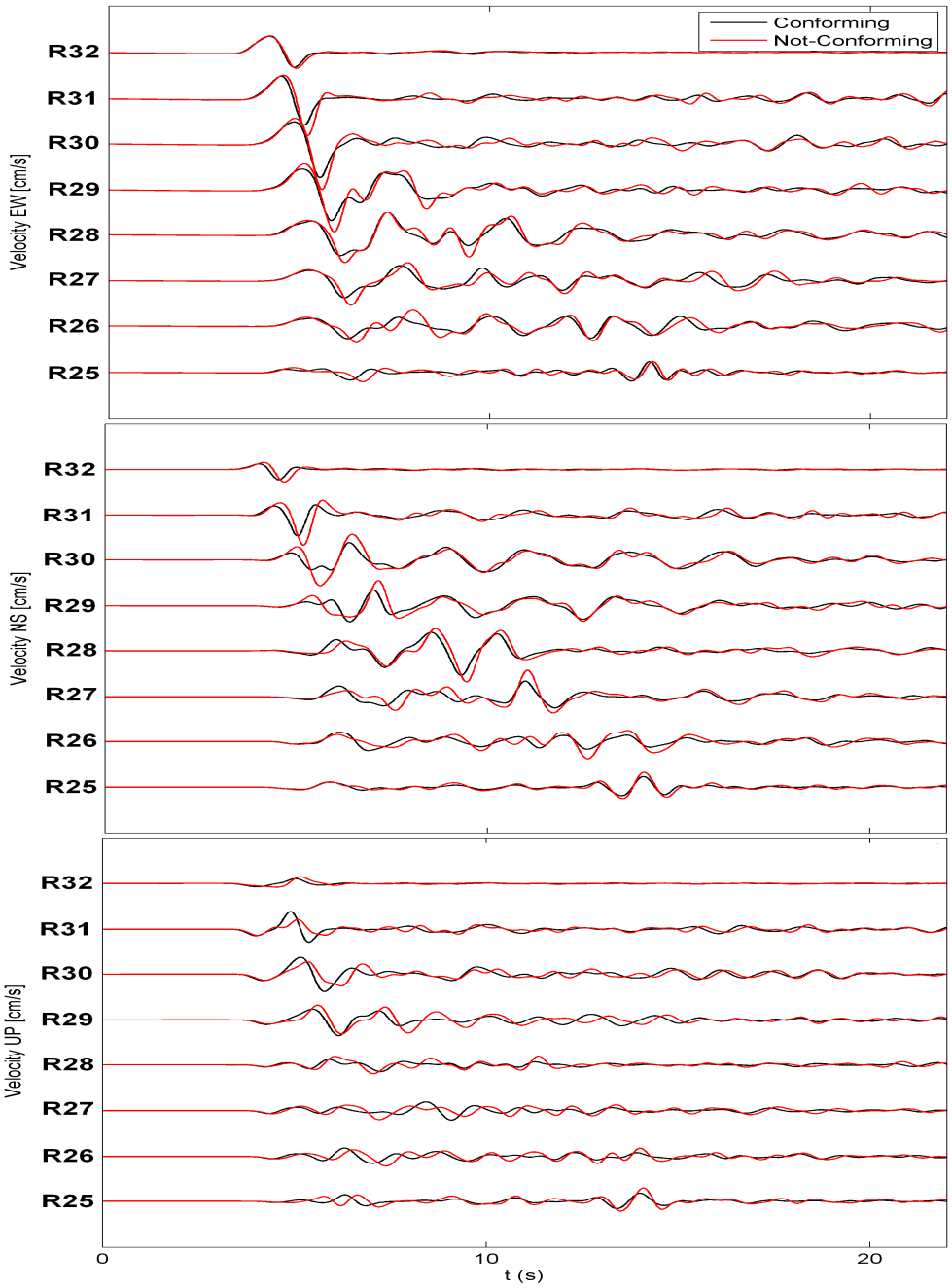

Figure B.7.Superimposed synthetics of EW, NS and UD velocity component excited by source S, obtained for the Honoring, conforming model (black line) and for the Not-Honoring-Non-Conforming model (red line) Receivers R25, R26, R27, R28, R29, R30, R31, R32 are recorded along the 2D profile (Figure B.1).

susceptible of sudden changes. Nevertheless, from an engineering point of view the importance of comparing the PGV values, and their misfit, is evident, especially for the central role of this parameter in assessing hazard and drawing seismic scenario map. A deeper analysis of the comparison between the different time-histories could be quantitatively assessed, evaluating the misfit parameters according to Anderson 2004 and Kristekova et al. 2006.

B.8 Concluding remarks

The purpose of this work is to tackle the meshing generation problem, presenting three different strategies (H, NH and NC), focusing on the response of alluvial valleys, and particularly on the valley of Grenoble, in the French Alps, because of the recognized importance of this geological structures in the assessment and accurate estimation of seismic hazards in specific area (i.e.: Los Angeles, Taipei, Christchurch, Santiago, Gubbio Basin). Nevertheless, the same strategy can be generalized and extensively adopted for all the strong variation of mechanical properties (e.g.: faults, layered media or any kind of complex stratification). By comparing the results for the specific case under study, it is possible to assess a good agreement between the time histories evaluated with the different meshing strategies presented.

The coupling of the NC and NH strategies presents at least two major advantages over the H strategy: (i) it can be implemented into an automated parallel procedure (Casarotti et al., 2007) and (ii) the three-dimensional mesh obtained is more efficiently unstructured (small elements are adopted in the area where it is strictly necessary) and the resulting elements are characterized by a better level of quality. Nevertheless a major drawback of the NH technique is the tendency to smear the discontinuities and as a result to increase the potential risk of changing the resonance frequency of the system and the amplification response.

Particular attention should be given to the trade off between the time dedicated to providing the final results, comprehending the pre-processing and meshing phase, and the accuracy of the obtained results, also considering the sensitivity of fundamental seismic design parameters to different meshing strategies. The chance to automatically provide an high quality mesh able to take into account all the geological, geo-mechanical and tectonic information collected regarding the area considered, avoiding simplistic approximation often forced by the poor development of the CAD or the meshing tools adopted, strongly encourages the adoption of Non-conforming and Not-Honoring meshing strategies. A series of good results has been achieved in reproducing the variability of surface earthquake ground motion, exploiting the Not-Honoring strategy for the description of complex alluvial-bedrock interfaces and of accurate geometrical configurations, among different regions worldwide (Stupazzini et al. 2009a, Smerzini et al. 2011, Pilz et al. 2011), including the case study of New Zealand, presented in this work. Fostered by the extreme versatility of the NC technique, early applications presented in this work suggest that NC and NH strategies could be an appealing way to solve the mesh creation problem whenever a reasonable compromise between accuracy and computational time is required

REFERENCES

Abrahamson, N. A. (1985). "Estimation of seismic wave coherency and rupture velocity using the SMART 1 Strong - motion Array Recordings", Report no. UBC/EERC 85/02. **[p. 30, 31**]

Abrahamson, N. A., J.F. Schneider and J. C. Stepp (1991), "Empirical spatial coherency functions for application to soil-structure interaction analyses", Earthquake Spectra, vol. 7, pp.1-27. **[p. 28, 30, 31, 34, 36, 37, 38, 40, 71]**

Aki, K and M. Tsujiura (1959). "Correlation study of near earthquake waves". Bull. Earthquake Res. Inst. Univ. Tokyo, vol. 37, pp.207-231. **[p. 27]**

Aki, K. and P. G. Richards (1980). "Quantitative Seismology", First Edition, W. H. Freeman, San Francisco, California. **[p. 17]**

Aki, K. and P. G. Richards (2002). "Quantitative Seismology", Second Edition, University Science Books, Sausalito, California. **[p. 17]**

Ameri G., M. Massa, D. Bindi, E. D'Alema, A. Gorini, L. Luzi, S. Marzorati, F. Pacor, R. Paolucci, R. Puglia, C. Smerzini (2009). "The 6 April 2009 M_W 6.3 L'Aquila (Central Italy) Earthquake: Strong-motion Observations". Seismological Research Letters, vol. 80, no. 6; p. 951-966. **[p. 30]**

American Lifelines Alliance - ALA (2001). "Seismic Fragility Formulations for Water Systems. Part 1 – Guideline". Technical report prepared by a public-private partnership between FEMA and ASCE, 104 pp. http://www.americanlifelinealliance.org. **[p. 98]**

Anderson, J. G. (2004). "Quantitative Measure of the goodness of fit of synthetic seismograms". 13th World Conference on Earthquake Engineering, Vancouver, B.C., Canada, Paper No. 243. **[p. 5, 48, 59, 62, 151]**

Antonietti, P., I. Mazzieri, A. Quarteroni and F. Rapetti (2012). "Non-conforming high order approximations of the elastodynamics equation". Comput. Methods Appl. Mech. Engrg., vol. 209-212, pp. 212–238. **[p. 119, 143]**

Ariman, T. and G. E. Muleski (1981). "A review of the response of buried pipelines under seismic excitation". Earthquake Engineering and Structural Dynamics, vol. 9, pp. 133-151. **[p. 23]**

Assobeton (2009). "Sistemi fognari SCARL a Bazano (L'Aquila)". Visual investigation on July 2009. **[p. 92]**

Atzori, S., and S. Salvi (2011). "Preliminary source inversion of the destructive Christchurch earthquake identified by the SIGRIS system", SIGRIS activities for the Christchurch (New Zealand) earthquake. http://www.sigris.it/. **[p. 56]**

Bannister, S., B. Fry, M. Reyners, J. Ristau, H. Zhang (2011). "Fine-scale relocation of aftershocks of the 22 February M_W 6.2 Christchurch earthquake, using double-difference tomography". Seismological Research Letters, vol. 82, pp. 839-845. **[p. 46]**

Bard, P. Y,. and M. Bouchon (1985). "The two-dimensional resonance of sediment-filled valleys". Bulletin of the Seismological Society of America, vol. 75 no. 2, pp. 519-541. **[p. 118]**

Bath, M. (1979). "Introduction to Seismology". Birkhauser Verlag, Basel. **[p. 9]**

Beavan, J., E. Fielding, M. Motagh, S. Samsonov, N. Donnelly (2011). "Fault location and slip distribution of 22 February 2011 M_W 6.2 Christchurch, New Zealand, earthquake from geodetic data". Seismological Research Letters, vol. 82, pp. 789-799. **[p. 56]**

Bendat, J.S. and A. G. Piersol (1971). "Random Data: analysis and measurement procedures". John Wiley and Sons, New York, 407p. **[p. 40]**

Bielak, J., J. Xu and O. Ghattas (1999). "Earthquake ground motion and structural response in alluvial valleys". J. Geotech. Geoenviron. Eng., vol. 125, pp. 413-423. **[p. 118]**

Blacker, T. (1994). "CUBIT Mesh generation environment users manual", Vol. 1, Sandia National Laboratories, Albuquerque, NM. **[p. 142]**

Bodin, P., J. Gomberg, S. K. Singh and M.Santoyo (1997). "Dynamic deformations of shallow sediments in the valley of Mexico, part I: Three dimensional strains and rotations recorded on a seismic array". Bulletin of the Seismological Society of America, Vol. 87, pp. 528-539. **[p. 10, 18, 20]**

Bolt, B.A., Y. B. Tsai, K. Yech and M. K. Hsu (1982). "Earthquake strong motions recorded by a large near-source array of digital seismographs". Earthquake Engineering and Structural Dynamics, vol.10, pp. 561-573. **[p. 27]**

Boon, D., N. D. Perrin, G.D. Dellow, R. Van Dissen, and B. Lukovic (2011). "NZS 1170.5:2004 Site Subsoil Classification of Lower Hutt", in Proceedings of the Ninth Pacific Conference on Earthquake Engineering, Building an Earthquake-Resilient Society, 14-16 April, 2011, Auckland, New Zealand, paper n. 13. **[p. 55]**

Bouchon, M. (1973). "Effects of topography on surface motion". Bulletin of the Seismological Society of America, Vol. 63, pp. 615-622. **[p. 118]**

Bouchon, M. and K. Aki (1982). "Strain, tilt, and rotation associated with strong ground motion in the vicinity of earthquake faults". Bulletin of the Seismological Society of America, Vol. 87, pp. 528-539. **[p. 10, 18, 20, 22, 23]**

Bradley, B. A., and M. Cubrinovski (2011). "Near-source strong ground motions observed in the 22 February 2011 Christchurch Earthquake". Seismological Research Letters, vol. 82, pp. 853-865. **[p. 5, 47]**

Brunetta, M., L. Bandini and M. De Lorenzi (2006). "SAP2000 analisi lineare/non lineare integrata con verifiche per strutture tridimensionali", Brunetta e Brunetta Engineering Srl, Vicolo Chiuso 4, 33170 Pordenone, Settembre 2006. **[p. 108, 114]**

Bycroft, G. N. (1980). "Soil-foundation interaction and differential ground motions", Earthquake Engineering and Structural Dynamics, vol. 8, pp. 397-404. **[p. 24]**

Carrington, L., D. Komatitsch, M. Laurenzano, M. Tikir, D. Michéa, N. Le Goff, A. Snavely and J. Tromp (2008). "High frequency simulations of global seismic wave propagation using SPECFEM3D_GLOBE on 62 thousand processor cores", in Proceedings of the ACM/IEEE Supercomputing SC'2008 Conference, Austin, TX, pp.1-11, Article no. 60. **[p. 142]**

Casarotti E., M. Stupazzini, S. Lee, D. Komatitsch, A. Piersanti and J. Tromp (2007), "CUBIT and seismic wave propagation based upon the Spectral-Element Method: An advanced unstructured mesher for complex 3D geological media", in Proceedings of the 16th Int. Meshing Roundtable, editors M.L. Brewer and D. Marcum, Springer, New York, NY. **[p. 57, 148, 152]**

Castellani, A. and G. Boffi (1986). "Rotational components of the surface ground motion during an earthquake", Earthquake Engineering and Structural Dynamics, vol. 14, pp. 751-767. **[p. 10, 18, 20, 44]**

Castellani, A. and G. Boffi (1989). "Rotational components of seismic motion", Earthquake Engineering and Structural Dynamics, vol. 18, pp. 785-797. **[p. 13, 44, 95]**

Castellani, A. and Z. Zembaty (1996). "Comparison between earthquake rotation spectra obtained through different experimental source". Eng. Struct., vol. 18, pp. 597-603. **[p. 4, 12, 28, 31, 69]**

Castellani, A. and C. Bonfanti (2007). "Tubazioni interrate in zona sismica". Ingegneria sismica, Anno XXIV, no. 4, pp. 35- 47. **[p. 88]**

Castellani A., M. Stupazzini and R. Guidotti (2012a). "Free field rotations during earthquakes: Relevance on buildings". Earthquake Engineering and Structural Dynamics. Published online in Wiley Online Library (wileyonlinelibrary.com). DOI: 10.1002/eqe.1163. **[p. 2, 30]**

Castellani, A., C. Bonfanti and R. Guidotti (2012b). "Evidenze sperimentali sul comportamento di tubazioni interrate durante un sisma". Submitted for publication at Assobeton. **[p. 92, 98]**

Cecchi, P. F. (1876). "Sismografo elettrico a carte affumicate scorrevoli". Atti Acad. Pontiff. Nuovi Lincei 29, 421-428. **[p. 11]**

Chaljub E., D. Komatitsch, J.-P. Vilotte, Y. Capdeville, B. Valette and G. Festa (2007), "Spectral element analysis in seismology", in Advances in wave propagation in heterogeneous media, edited by Ru-Shan Wu and Valérie Maupin, Advances in Geophysics, Elsevier, vol. 48, pp. 365-419. **[p. 142, 143]**

Chen, K. C., B. S. Huang, J. H. Wang, W. G. Huang, T. M. Chang, R. D. Hwang, H. C. Chiu and C. C. Tsai (2001). "An observation of rupture pulses of the 20 September 1999 Chi-Chi, Taiwan, earthquake from near-field seismograms". Bulletin of the Seismological Society of America, Vol. 91, no. 5, pp. 1247-1254. **[p. 23, 25]**

Cochard, A., H. Igel, B. Schuberth, W. Suryanto, A. Velikoseltsev, U. Schreiber, J. Wassermann, F. Scherbaum and D. Vollmer (2006). "Rotational motions in seismology: theory, observation, simulation". In Earthquake Source Asymmetry, Structural Media and Rotations Effects. R. Teisseyre, M. Takeo, and E. Majewski (Editors). Springer Verlag, Berlin-Heidelberg. **[p. 9, 17, 21, 133]**

Cosserat, E. and F. Cosserat (1909). "Theorie des Corps Deformables". Hermann, Paris (available from the Cornell University Library digital). **[p. 11]**

Cubrinovski, M., and R. A. Green, eds. (2010). "Geotechnical reconnaissance of the 2010 Darfield (Canterbury) earthquake". Bulletin of the New Zealand Society for Earthquake Engineering, vol. 43, pp. 243–320. **[p. 5, 46]**

Cubrinovski, M., J. D. Bray, M. Taylor, S. Giorgini, B. Bradley, L. Wotherspoon, and J. Zupan (2011). "Soil Liquefaction Effects in the Central Business District during the February 2011 Christchurch Earthquake". Seismological Research Letters, vol. 82, pp. 893-904. **[p. 89]**

Day, S. M., R. Graves, J. Bielak, D. Dreger, S. Larsen, K. B. Olsen, A. Pitarka and L. Ramirez-Guzman (2008). "Model for basin effects on long-period response spectra in southern California". Earthquake Spectra, vol. 24, pp. 257-277. **[p. 10]**

Dolce, M., S. Giovinazzi, I. Iervolino, E. Nigro and A. Tang (2009). "Emergency management for lifelines and rapid response after L'Aquila earthquake". Progettazione Sismica. Seismic Design Journal. Vol 3. November 2009. IUSS PRESS Editor. ISSN 1973-7432. **[p. 88]**

Dumbser M., M. Käser and F. T. Eleuterio (2007). "An arbitrary high-order Discontinuous Galerkin method for elastic waves on unstructured meshes - V. Local time stepping and p-adaptivity". Geophys. J. Int.,vol. 171, pp. 695-717. **[p. 143]**

Eidinger, J. (1998). "Water distribution system," in: Ashel J. Schiff (ed.) The Loma Prieta California Earthquake of October 17, 1989 – Lifelines. USGS Professional Paper No. 1552-A, US Government Printing Office, Washington, A63-A78. **[p. 98]**

Electric Power Research Institute, EPRI (1992). "Spatial variation of earthquake ground motion for application to soil-structure interaction". Report EPRI TR-100463. **[p. 37, 38]**

Esposito, S., L. Elefante, I. Iervolino and S. Giovinazzi (2011). "Addressing ground-shaking-induced damage of the gas distribution network in the 2009 L`Aquila earthquake", atti di XIV Convegno Nazionale "L'Ingegneria Sismica in Italia", Bari, paper n. 1014. **[p. 98]**

Evans J. R., V. Graizer, B. S. Huang, K. W. Hudnut, C. R. Hutt., W. H. K. Lee, C. C. Liu, R. Nigbor, E. Safak, W. U. Savage, M. Trifunac and C. F. Wu (2006). "Workshop on Rotational Ground Motion", Menlo Park, 16 February 2006. **[p. 27]**

Evans, J. R. and International Working Group on Rotational Seismology (IWGoRS) (2009). "Suggested notation conventions for rotational seismology". Bulletin of the Seismological Society of America, Vol. 99, no. 2B, pp. 1073-1075. **[p. 1, 2]**

Faccioli, E. and R. Paolucci (1990). "Engineering seismology studies for the design and analysis of bridge structures". Eur. Earthquake Engineering, vol.3, pp. 17-28. **[p. 27]**

Faccioli, E., F. Maggio, R. Paolucci, A. Quarteroni (1997). "2D and 3D elastic wave propagation by a pseudospectral domain decomposition method". Journal of Seismology 1(3):237–251. **[p. 48]**

Faccioli, E. and R. Paolucci (2005). "Elementi di sismologia applicata all'ingegneria". Pitagora Editrice, Bologna, ISBN 88-371-1500-8. **[p. 50]**

Ferrari, G. (2006). "Note on the historical rotation seismographs", in Earthquake Source Asymetry, Structural Media and Rotation Effects, R. Teisseyre, M. Takeo, and E. Majewski (Editors), Springer-Verlag, Heidelberg, pp. 367-376. **[p. 11]**

Fichtner, A. and H. Igel (2009). "Sensitivity densities for rotational ground-motion measurements". Bulletin of the Seismological Society of America, Vol. 99, no. 2B, pp. 1302-1314. **[p. 17, 70]**

Figini, R., R. Paolucci and C. T. Chatzigogos (2011). "A macro-element model for non-linear soil-shallow foundation-structure interaction under seismic loads: theoretical development and experimental validation on large scale tests". Earthquake Engineering and Structural Dynamics. DOI: 10.1002/eqe.1140. **[p. 99]**

Fletcher, J., J. Boatwright, L. Haar, T. Hanks, A. McGarr (1984). "Source parameters for aftershocks of the Oroville, California, earthquake". Bulletin of the Seismological Society of America, Vol. 74, no. 4, pp. 1101-1123. **[p. 23]**

Forsyth, P. J., D. J. A. Barrell, and R. Jongens (2008). "Geology of the Christchurch Area". Institute of Geological and Nuclear Sciences 1:250 000 geological map 16, 1 sheet + 67 pp. Lower Hutt, NZ: GNS Science. **[p. 48, 49]**

Furumura, T. and Hayakawa (2007). "Anomalous propagation of long-period ground motions recorded in Tokyo during the 23 October 2004, M_W 6.6 Niigata-ken Chuetsu, Japan, earthquake". Bulletin of the Seismological Society of America, Vol. 97, pp. 863-880. **[p. 10]**

Gazetas, G. (1991). "Foundation vibrations", in Foundation Engineering Handbook, 2nd Edition. Ed. H. Y. Fang, Van Nostrand Reinhold, New York. **[p. 100]**

Géli, L., P. Y. Bard and B. Jullien (1988). "The effect of topography on earthquake ground motion: A review and new results". Bulletin of the Seismological Society of America, Vol. 78, pp. 42-63. **[p. 84]**

George, P. L.and H. Borouchaki (1998). "Delaunay triangulation and meshing: application to Finite Elements", Editions HERMES, Paris, 1998. **[p. 142]**

Ghayamghamian, M. R. and G. R. Nouri (2007). "On the characteristics of ground motion rotational components using Chiba dense array data". Earthquake Engineering and Structural Dynamics, vol. 36, no. 10, 1407-1429. **[p. 10]**

Ghobarah, A. (2004). "On drift limits associated with different damage levels". Proceedings of the International Workshop on Performance-Based Seismic Design, Bled, Slovenia, 321-3332. **[p. 3, 23, 112]**

Gicev, V. and M. D. Trifunac (2008). "Rotations in a shear-beam model of seven story building caused by nonlinear waves during earthquake excitation". Structural control and health Monitoring. **[p. 3, 23]**

Gledhill, K., J. Ristau, M. Reyners, B. Fry, and C. Holden (2011). "The Darfield (Canterbury, New Zealand) M_W 7.1 Earthquake of September 2010: A Preliminary Seismological Report". Seismological Research Letters 82, pp. 379-386. **[p. 46]**

Godfrey, N. J., F. Davey, T. A. Stern, and D. Okaya (2001). "Crustal structure and thermal anomalies of the Dunedin Region, South Island, New Zealand", Journal of Geophysical Research, vol. 106, no. B12, pp. 30,835-30,848. **[p. 49]**

Godfrey, N. J., N. I. Christensen, and D. Okaya (2002). "The effect of crustal anisotropy on reflector depth and velocity determination from wide-angle seismic data: a synthetic example based on South Island, New Zealand". Tectonophysics, vol.355, pp. 145-161. **[p. 49]**

Graizer, V. M. (1991). "Inertial seismometry methods". Izv. USSR Acad. Sci., Phys. Solid Earth 27, no 1, 51-61. **[p. 17]**

Graizer, V. M. (2005). "Effect of tilt on strong motion data processing". Soil Dynamics and Earthquake Engineering, 25, 197-204. **[p. 2]**

Graizer, V. M. (2006). "Tilts in strong ground motion". Bulletin of the Seismological Society of America, Vol. 96, no. 6, pp. 2090-2102. **[p. 23, 25, 31]**

Graves, R. W. (1998). "3-D finite-difference modelling of the San Andreas fault: source parameterization and ground motion levels". Bulletin of the Seismological Society of America, Vol. 88, pp. 881-897. **[p. 10]**

Graves, R. W. and D. J. Wald (2004). "Observed and simulated ground motions in the San Bernardino basin region for the Hector Mine, California". Bulletin of the Seismological Society of America, Vol. 94, pp. 131-146. **[p. 10]**

Green, A. G., F. M. Campbell, A. E. Kaiser, C. Dorn, S. Carpentier, J. A. Doetsch, H. Horstmeyer, D. Nobes, J. Campbell, M. Finnemore, R. Jongens, F. Ghisetti, A. R. Gorman, R. M. Langridge, and A. F. McClymont (2010). "Seismic reflection images of active faults on New Zealand's South Island", 4th International Conference on Environmental and Engineering Geophysics, Chengdu, China, June 2010. **[p. 46]**

Green, R. A., C. Wood, B. Cox, M. Cubrinovski, L. Wotherspoon, B. Bradley, T. Algie, J. Allen, A. Bradshaw, and G. Rix (2011). "Use of DCP and SASW tests to evaluate liquefaction potential: predictions vs. observations during the recent New Zealand earthquakes". Seismological Research Letters, vol.82, pp. 927-938. **[p. 5, 46]**

Grekova, E. F., M. A. Kulseh and G. C. Herman (2009). "Waves in linear elastic media with microrotations, part 2: Isotropic reduced Cosserat model". Bulletin of the Seismological Society of America, Vol. 99, no. 2B, pp. 1423-1428. **[p. 18]**

Guidotti R., M. Stupazzini, C. Smerzini, R. Paolucci and P. Ramieri (2011). "Numerical Study on the Role of Basin Geometry and Kinematic Seismic Source in 3D Ground Motion Simulation of the 22 February 2011 M_W 6.2 Christchurch Earthquake". Seismological Research Letters, Volume 82, Number 6, pp. 767-782. DOI: 10.1785/gssrl.82.6.767. **[p. 48]**

Gutemberg, B. (1927). "Grundlagen der Erbebenkunde". Univ. Frankfurt a/M,189 pp. **[p. 9]**

Harichandran, R. S. and E. H. Vanmarcke (1984). "Space-time variation of earthquake ground motion". Research Report R 84-12. Department of Civil Engineering, Massachussetts Institute of Technology, Cambridge. **[p. 30, 37, 38]**

Harichandran, R. S. (1991), "Estimating the spatial variation of earthquake ground motion from dense array recordings", Workshop on Spatial Variation of Earthquake Ground Motion 1988, Structural Safety, Vol. 10, p. 219-233. **[p. 28]**

Harris, D. (2006). "Double-slip and spin: dilatant shear in a reduced Cosserat model", in Modern Trends in Geomechanics, Springer Proceedings in Physics, W. Wu and H.-S. Yu (Editors), Vol. 106, Springer, New York, 329-346. **[p. 18]**

Hart, G. C., M. DiJulio and M. Lew (1975). "Torsional response of high rise buildings". J. Struct. Div. ASCE 101, pp. 397-414. **[p. 24]**

Hesthaven, J.S., and C. H. Teng (2000). "Stable spectral methods on tetrahedral elements". SIAM J. Sci. Comput., vol. 21, pp. 2352-2380. **[p. 142]**

Holden, C. (2011). "Kinematic source model of the 22 February 2011 M_W 6.2 Christchurch earthquake using strong motion data". Seismological Research Letters, vol. 82, pp. 783-788. **[p. 56]**

Housner, G. W. and M. D. Trifunac (1967). "Analysis of accelerograms – Parkfield earthquake". Bulletin of the Seismological Society of America, Vol. 57, no. 6, pp. 1193-1220. **[p. 23, 25]**

Huang, B. S. (2003). "Ground rotational motions of the 1991 Chi-Chi, Taiwan, earthquake as inferred from dense array observations". Geophysical Research Letters, vol. 30, no. 6, 1307-1310. **[p. 10, 18, 20, 22]**

Huang, B. S., C. C. Liu, C. R. Lin, C. F. Wu, and W. H. K. Lee (2006). "Measuring mid- and near-field rotational ground motions in Taiwan", a poster presented at the 2006 Fall AGU Meeting, San Francisco. **[p. 18]**

Hudson, D. E. (1983). "Strong Motion Instrumentation Systems". Proc. Golden Anniversary Workshop Strong Motion Seismology, University of Southern California, Los Angeles, California, pp. 73-86. **[p. 12]**

Igel, H., U. Schreiber, A. Flaws, B. Schuberth, A. Velikoseltsev and A. Cochard (2005). "Rotational motions induced by the M 8.1 Tokachi-oki earthquake, September 25, 2003". Geophysical Research Letters 32, L08309. **[p. 10, 17, 133]**

Igel, H., A. Cochard , J. Wassermann, U. Schreiber, A. Velikoseltsev and N. Pham Dinh (2007). "Broadband observations of rotational ground motions", Geophys. J. Int. 168, no. 1, 182-197. **[p. 17]**

Igel, H., M. Käser and M. Stupazzini (2011). "Seismic wave propagation in media with complex geometries, simulation of", in Extreme Environmental Events. Springer, New York, pp. 765-787. **[p. 10, 142, 143]**

Isoyama, R., E. Ishida, K. Yune and T. Shirozu (2000). "Seismic damage estimation procedure for water supply system pipelines," Proceeding of the twelfth World Conference on Earthquake Engineering, Paper No. 1762, 8 pp. **[p. 98]**

Jalali, R., M. D. Trifunac, G. Ghodrati Amiri and M. Zahedi (2007). "Wave-passage effect on strength-reduction factors for design of structures near earthquakes faults". Soil Dynamics and Earthquake Engineering, vol. 27, no. 8, pp. 703-711. **[p. 25]**

Jalali, R. and M. D. Trifunac (2008). "A note on strength reduction factors for design of structures near earthquake faults". Soil Dynamics and Earthquake Engineering, vol. 28, no. 3, pp. 212-222. **[p. 24, 25]**

Jalali R. S. and M. D. Trifunac (2009). "Response Spectra for Near-source, Differential, and Rotational Strong Ground Motion", Bulletin of the Seismological Society of America, Vol. 99, no. 2B, pp. 1404-1415. **[p. 28]**

Jenista, J. (1906-1907). "O seismometrech", Vynélezy a Pokroky, Vol. III, Prague, 10-164. (In Czech, On Seismometers). **[p. 11]**

Kalkan E. and V. Graizer (2007). "Multicomponent ground motion response spectra for coupled horizontal, vertical, angular accelerations, and tilt". Journal of Earthquake Technology, Vol. 44, no.1, pp. 259-284. **[p. 31]**

Kam, W. Y, U Akguzel, and S. Pampanin, (2011). "4 Weeks On: Preliminary Reconnaissance Report from the Christchurch 22 Feb 2011 6.3 M_W Earthquake". http://db.nzsee.org.nz:8080/ en/ web/ chch 2011/ structural/.**[p. 46]**

Kawakami H. and S. Sharma (1999). "Statistical Study of Spatial Variation of Response Spectrum Using Free Field Records of Dense Strong Motion Arrays". Earthquake Engineering and Structural Dynamics, vol. 28, pp. 1273-1294. **[p. 37]**

Kleffmann, S., F. Davey, A. Melhuish, D. Okaya, T. Stern, and the SIGHT Team (1998). "Crustal structure in the central South Island, New Zealand, from the Lake Pukaki seismic experiment", New Zealand Journal of Geology and Geophysics, vol. 41,pp. 39-49. **[p. 49]**

Knupp, P. (2000)."Achieving finite element mesh quality via optimization of the Jacobian matrix norm and associated quantities, Part I", Int. J. Num. Meth. Engr. **[p. 147]**

Komatitsch, D. and J. P. Vilotte (1998). "The spectral element method: an efficient tool to simulate the seismic response of 2D and 3D geological structures". Bulletin of the Seismological Society of America, Vol. 88, pp. 368-392. **[p. 142]**

Komatitsch, D., R. Martin, J. Tromp, M. A. Taylor and B. A. Wingate (2001). "Wave propagation in 2-D elastic media using a spectral element method with triangles and quadrangles". J. Comput. Acous., vol. 9, no.2, pp. 703-718. **[p. 142]**

Komatitsch, D., S. Tsuboi, C. Ji and J. Tromp (2003). "A 14.6 billion degrees of freedom, 5 teraflops, 2.5 terabyte earthquake simulation on the Earth simulator", in Proceedings of the ACM/IEEE Supercomputing SC'2003 Conference, Phoenix, AZ, pp. 4-11. **[p. 142]**

Komatitsch, D., L. Qinya, J. Tromp, P. Suss, C. Stidham and J. H. Shaw (2004). "Simulations of ground motion in the Los Angeles basin based upon the spectral-element method". Bulletin of the Seismological Society of America, Vol. 94, pp. 187-206. **[p. 10, 142]**

Kozak, J. T. (2009). "Tutorial on Earthquake Rotational Effects: Historical Examples". Bulletin of the Seismological Society of America, Vol. 99, no. 2B, pp. 998-1010. May 2009. **[p. 11, 12]**

Kristekova M. et al., (2006) Misfit Criteria for Quantitative Comparison of Seismograms, Bulletin of the Seismological Society of America, Vol. 96, no. 5, pp. 1836-1850. **[p. 151]**

Kulesh, M. (2009). "Waves in linear elastic media withmicrorotations, part 1: Isotropic full Cosserat model". Bulletin of the Seismological Society of America, Vol. 99, no. 2B, pp. 1091-1102. **[p. 18]**

Langston, C. A. (2007). "Wave gradiometry in two dimensions". Bulletin of the Seismological Society of America, Vol. 97, pp. 401-416. **[p. 2]**

Langston, C. A. andC. Liang (2008). "Gradiometry for polarized seismic waves". Journal of Geophysical Reasearch, vol. 113, B08305. **[p. 2]**

Langston, C.A., W. H. K. Lee, C. J. Lin and C. C. Liu (2009). "Seismic wave strain, rotation, and gradiometry for the 4 March 2008 TAIGER explosions". Bulletin of the Seismological Society of America, Vol. 99, no. 2B, pp. 1287-1301. **[p. 70]**

Lavallée, D. and R. J. Archuleta (2003). "Stochastic modelling of slip spatial complexities for the 1979 Imperial Valley, California, earthquake". Geophys. Res. Lett., vol. 30, no.5, p.1245. **[p. 27]**

Lee. S. J., H. W. Chen, Q. Liu, D. Komatitsch, B. S. Huang and J. Tromp (2008). "Three-dimensional simulations of seismic wave propagation in the Taipei basin with realistic topography based upon the spectral-element method". Bulletin of the Seismological Society of America, Vol. 98, no. 1, pp. 253-264. **[p. 142]**

Lee, V. W. and M. D. Trifunac (1985). "Torsional accelerograms". Internationa Journal of Soil Dynamics and Earthquake Engineering, vol. 4, pp. 132-139. **[p. 10, 13, 15, 18, 20, 70]**

Lee, V. W. and M. D. Trifunac (1987). "Rocking strong earthquake accelerations". Internationa Journal of Soil Dynamics and Earthquake Engineering, vol. 6, no. 2, pp. 75-89. **[p. 10, 13, 15, 70]**

Lee, V. W. (2002). "Empirical scaling of strong earthquake ground motion – Part III: Synthetic strong motion". ISET Journal of Earthquake Technology, Paper No. 427, No. 4, pp. 273-310. **[p. 13, 15]**

Lee, V. W. and M. D. Trifunac (2009). "Empirical scaling of rotational spectra of strong earthquake ground motion". Bulletin of the Seismological Society of America, Vol. 99, No. 2B, pp. 1378-1390. **[p. 13, 27, 31]**

Lee, W. H. K. (2009). "A glossary for Rotational Seismology". Bulletin of the Seismological Society of America, Vol. 99, No. 2B, pp. 1082-1090. May 2009. **[p. 1, 17]**

Lee, W. H. K., M. Celebi, M. I. Todorovska and H. Igel (2009a). "Introduction to the Special Issue on Rotational Seismology and Engineering Applications". Bulletin of the Seismological Society of America, Vol. 99, No. 2B, pp. 945-957. May 2009. **[p. 2]**

Lee, W. H. K., B. S. Huang, C. A. Langston, C. J. Lin, C. C. Liu, T. C. Shin, T. L. Teng and C. F. Wu (2009b). "Review: Progress in Rotational Ground-Motion Observations from Explosions and local Earthquakes in Taiwan". Bulletin of the Seismological Society of America, Vol. 99, no. 2B, pp. 958-967. **[p. 5, 9, 20, 21, 22]**

Li, H.-N., L. E. Suarez and M. P. Singh (1997). "Rotational components of earthquake ground motions". Earthquake Engineering and Engineering of Vibrations, vol. 17, pp. 37-50. **[p. 13]**

Li, H.-N., L.-Y. Sun and S.-Y. Wang (2002). "Frequency dispersion characteristics of phase velocities in surface wave for rotational components of seismic motion". Journal of Sound Vibraions, vol. 258, pp. 815-827. **[p. 13, 36]**

Liao, S. and A. Zerva (2006). "Physically compliant, conditionally simulated spatially variable seismic ground motions for performance-based design". Earthquake Engineering and Structural Dynamics, vol. 35, pp. 891–919. **[p. 36]**

Lin, C. J., C. C. Liu and W. H. K. Lee (2009). "Recording rotational and translational ground motions of two TAIGER explosions in northeastern Taiwan on 4 March 2008". Bulletin of the Seismological Society of America, Vol. 99, no. 2B, pp. 1237-1250. **[p. 17, 18, 20]**

Liu, C. C., B. S. Huang, W. H. K. Lee and C. J. Lin (2009). "Observing rotational and translational ground motion at the HGSD station in Taiwan from 2007 to 2008". Bulletin of the Seismological Society of America, Vol. 99, no. 2B, pp. 1228-1236. **[p. 18, 20, 21, 22, 28, 42, 44, 71, 72, 73, 80, 85]**

Long, D. T., S. C. Cox, S. Bannister, M. C. Gerstenberger, and D. Okaya (2003). "Upper crustal structure beneath the eastern Southern Alps and the Mackenzie Basin, New Zealand, derived from seismic reflection data", New Zealand Journal of Geology & Geophysics, vol. 46, pp. 21–39. **[p. 49]**

Luco J, and H. Wong, (1986). "Response of a rigid foundation to a spatially random ground motion". Earthquake Engineering and Structural Dynamics, vol 14, pp. 891–908. **[p. 30, 38]**

Mallet, R. (1862). "Great Neapolitan Earthquake of 1857". Vols. I, II, Chapman and Hall, London. **[p. 11]**

McLeod, D. P., G. E: Stedman, T. H. Webb and K.U. Schreiber (1998). "Comparison of standard and ring laser rotational seismograms". Bulletin of the Seismological Society of America, Vol. 88, pp. 1459-1503. **[p. 17, 133]**

McNamara, D. E. and R. P. Buland (2004). "Ambient Noise Levels in the Continental United States". Bulletin of the Seismological Society of America, Vol. 94, pp. 1517-1527. **[p. 137]**

Melhuish, A., S. Holbroock , F. Davey ,D. Okaya, and T. Stern (2005). "Crustal and upper mantle seismic structure of the Australian Plate, South Island, New Zealand", Tectonophysics, vol. 395, pp. 113–135. **[p. 49]**

Mortimer, N., F. J. Davey, A. Melhuish, J. Yu, and N. J. Godfrey (2002). "Geological interpretation of a deep seismic reflection profile across the Eastern Province and Median Batholith, New Zealand: crustal architecture of an extended Phanerozoic convergent orogen", New Zealand Journal of Geology & Geophysics, vol. 45, pp. 349–363. **[p. 49]**

Niazi, M. (1986). "Inferred displacements, velocities and rotations of a long rigid foundation located at El-Centro differential array site during the 1979 Imperial Valley, California, earthquake". Earthquake Engineering and Structural Dynamics 14, 531-542. **[p. 10, 12, 18, 20]**

Niazi, M. (1990). "Behaviour of peak values and spectral ordinates of near-source strong ground motion over the SMART array". Report no. UCB/EERC 90/17. **[p. 28]**

Nigbor, R. L. (1994). "Six-degree-of-freedom ground motion measurement". Bulletin of the Seismological Society of America, Vol. 84, pp. 1665-1669. **[p. 17, 18, 20]**

Nova, R. and L. Montrasio (1991). "Settlements of shallow foundations on sand", Géotechnique, vol. 15, pp. 243-256. **[p. 100]**

Oliveira, C. S. and B. A. Bolt (1989). "Rotational components of surface strong ground motions". Earthquake Engineering and Structural Dynamics, vol. 18, 517-526. **[p. 10, 12, 18, 20]**

Olsen, K. B., and R. J. Archuleta (1996). "Three-dimensional simulation of earthquakes on the Los Angeles fault system". Bulletin of the Seismological Society of America, Vol. 86, no. 3, pp. 575-596. **[p. 10]**

Olsen, K. B. (2001). "Three-dimensional ground motion simulations for large earthquakes on the San Andreas fault with dynamic and observational constraints". J. Comp. Acoust., vol 9, pp. 1203-1214. **[p. 10]**

R. P. Orense, T. Kiyota, S. Yamada, M. Cubrinovski, Y. Hosono, M. Okamura, and S. Yasuda (2011). "Comparison of Liquefaction Features Observed during the 2010 and 2011 Canterbury Earthquakes". Seismological Research Letters, vol. 82, pp. 905-9018. **[p. 89]**

O'Rourke, M. J. and G. Ayala, (1993). "Pipeline damage due to wave propagation," Journal of Geotechnical Engineering, ASCE, Vol. 119, pp. 1490-1498. **[p. 98]**

O'Rourke, T.D. and S. S. Jeon (1999). "Seismic Zonation for lifelines and utilities," Proceedings of the 6th International Conference on Seismic Zonation, Paper No. 168. **[p. 98]**

O'Rourke, T.D., H.E. Stewart and S.S. Jeon (2001). "Geotechnical aspects of lifeline engineering," Proceedings of the Institution of Civil Engineers, Vol. 149, January 2001, Issue 1, pp. 13-26. **[p. 98]**

Pancha, A., T. H. Webb, G. E: Stedman, D. P. McLeod and K. U. Schreiber (2000). "Ring laser detection of rotation from teleseismic waves". Gephysical Research Letters, vol. 27, pp. 3553-3556. **[p. 17, 134]**

Paolucci, R. (1997). "Simplified evaluation of earthquake induced permanent displacements of shallow foundations". Journal of Earthquake Engineering, vol. 1, pp. 563-579. **[p. 99]**

Paolucci, R., E. Faccioli and F. Maggio (1999). "3D response analysis o fan instrumented hill at Matsuzaki, Japan, by a spectral method". Journal of Seismology, vol. 3, pp. 191-209. **[p. 84]**

Paolucci, R. (2002). "Amplification of earthquake ground motion by steep topographic irregularities", Earthquake Engineering and Structural Dynamics, vol. 31, pp. 1831-1853. **[p. 118]**

Paolucci, R. and C. Smerzini (2008). "Earthquake-induced transient ground strains from dense seismic networks". Earthquake Spectra, vol. 24, no. 2, pp. 453-470. **[p. 18, 19, 20, 38, 80]**

Paolucci, R., F. Pacor, R. Puglia, G. Ameri, C. Cauzzi and M. Massa (2011). "Record Processing in ITACA, the New Italian Strong-Motion Database", "Earthquake Data in Engineering Seismology". Geotechnical, Geological, and Earthquake Engineering, 2011, Volume 14, Part 2, p. 99-113. **[p. 30]**

Peter, D., D. Komatitsch, Y. Luo, R. Martin, N. Le Goff, E. Casarotti, P. Le Loher, F. Magnoni, Q. Liu, C. Blitz, T. Nissen-Meyer, P. Basini and J. Tromp (2011). "Forward and adjoint simulations of seismic wave propagation on fully unstructured hexahedral meshes". Geophysical Journal International, vol. 186, pp. 721-739. **[p. 10, 142]**

Peterson, J. (1993). "Observation and modeling of seismic background noise". U.S. Geol. Surv. Tech. Rept., 93-322, 1-95. **[p. 138]**

Pilz, M., S. Parolai, M. Stupazzini, R. Paolucci and J. Zschau (2011). "Modeling basin effects on earthquake ground motion in the Santiago de Chile basin by a spectral element code". Geophysical Journal International, doi:10.1111/j.1365-246X.2011.05183.x. **[p. 152]**

Pitilakis, K., M. Alexoudi, S. Argyroudis, O. Monge and C. Martin (2006). "Earthquake risk assessment of lifelines". Bulletin of Earthquake Engineering, vol. 4, no.4,pp. 365-390. **[p. 88]**

Pitarka, A., K. Irikura, T. Iwata and H. Sekiguchi (1998). "Three-dimensional simulation of the near-fault ground motion for the 1995 Hyogo-ken Nanbu (Kobe), Japan, earthquake". Bulletin of the Seismological Society of America, Vol. 88, pp. 428-440. **[p. 10]**

Quigley, M., R. Van Dissen, P. Villamor, N. Litchfield, D. Barrell, K. Furlong, T. Stahl, B. Duffy, E. Bilderback, D. Noble, D. Townsend, J. Begg, R. Jongens, W. Ries, J. Claridge, A. Klahn, H. Mackenzie, A. Smith, S. Hornblow, R. Nicol, S. Cox, R. Langridge, and K. Pedley (2010). "Surface rupture of the Greendale fault during the M_W 7.1 Darfield (Canterbury) earthquake, New Zealand: Initial findings". Bulletin of the New Zealand Society for Earthquake Engineering, vol. 43, pp. 236–242. **[p. 46]**

Reid, H. F. (1910). "The mechanics of earthquake" in The California Earthquake of April, 18, 1906, Report of the State Earthquake Investigation Commission, Vol. 2, Carnegie Institution of Washington, 43-47. **[p. 11]**

Reyners, M., and H. Cowan (1993). "The transition from subduction to continental collision: crustal structure in the North Canterbury region, New Zealand", Geophysical Journal International, vol. 115, pp. 1124-1136. **[p. 49]**

Richter, C. F. (1958). "Elementary Seismology". W. H. Freeman, San Francisco, California. **[p. 9]**

Rutenberg, A. and A. C. Heidebrecht (1985). "Response spectra for torsion, rocking, and rigid foundations". Earthquake Engineering and Structural Dynamics, vol. 13, pp. 543-557. **[p. 13]**

Sagnac, M. G. (1913). "La démonstration de l'existence de l'éther lumineaux a travers les mesures d'un intérferomètre en rotation". C. R. l'Acad. Sci., vol. 157, pp. 708-718. **[p. 134]**

Scherwath, M., T. Stern, F. Davey, D. Okaya, W. S. Holbrook, R. Davies, and S. Kleffmann (2003). "Lithospheric structure across oblique continental collision in New Zealand from wide-angle P wave modelling", Journal of Geophysical Research, vol 108, no. B12, 2,566. **[p. 49]**

Schreiber K. U., G. E. Stedman and T. Kluegel (2003), "Earth tide and tilt detection by a ring laser gyroscope", Journal of Geophysical. Research, Vol.108, no. B2, 2132. **[p. 134]**

Schreiber, K. U., A.Velikoseltsev, M. Rothacher, T. Klügel, G. E. Stedman and D. L. Wiltshire (2004a). Direct measurement of diurnal polar motion by ring laser gyroscopes". Journal of Geophysical Research, vol. 109, no. B6, B06405. **[p. 134]**

Schreiber, K. U., A. Velikoseltsev, G. E: Stedman, R. B. Hurst and T. Klügel (2004b). "Large ring laser gyros as high resolution sensors for applications in geoscience". Proc. of the 11th International Conference on Integrated Navigation System, St. Petersburg, 24-26 May 2004, 326-331. **[p. 7, 134, 140]**

Schreiber, K. U., H. Igel, A. Velikoseltsev, A. Flaws, B. Schubert, W. Drewitz and F. Muller (2005). "The GEOsensor project: rotations – a new observable for seismology", in Observation of the Earth System from Space, Springer, New York, pp. 427-447. **[p. 133]**

Schreiber, K. U., G. E. Stedman, H. Igel and A. Flaws (2006). "Ring laser gyroscopes as rotation sensors for seismic wave studies", in Earthquake Source Asymmetry, Structural Media and Rotation Effects, R. Teisseyre, M. Takeo and E. Majewski (Editors), chap. 29, Springer, New York. **[p. 10, 17, 134]**

Schreiber, K. U., J. P. R. Wells and G. E. Stedman (2008). "Noise processes in large ring laser". J. Gen. Relativ. Gravity, vol. 40, no. 5, pp. 935-943. **[p. 137]**

Schreiber, K. U., J. N. Hautmann, A. Velikoseltsev, J. Wassermann, H. Igel, J. Otero, F. Vernon, J. P. R. Wells (2009a), "Ring Laser Measurements of Ground Rotations for Seismology", Bulletin of the Seismological Society of America, Vol. 99, no. 2B, pp. 1190-1198. **[p. 17, 133]**

Schreiber, K. U., A. Velikoseltsev, A. J. Carr, R. Franco-Anaja (2009b), "The Application of Fiber Optic Gyroscopes for the Measurement of Rotations in Structural Engineering", Bulletin of the Seismological Society of America, Vol. 99, no. 2B, pp. 1207-1214. **[p. 134]**

Semblat, J. F., A. M. Duval, P. Dagla (2002). "Seismic site effects in a deep alluvial basins: numerical analysis by the boundary element method". Computers and Geotechnics, vol. 29, no. 7, pp. 573-585. **[p. 118]**

Semblat, J. F., M. Kham, P. Y. Bard (2008). "Seismic wave propagation in alluvial basins and influence of site-city interaction". Bulletin of the Seismological Society of America, vol. 96, no. 6, pp. 2665-2678. **[p. 118]**

Semmens, S., N. D. Perrin, G. Dellow, and R. Van Dissen (2011). "NZS 1170.5:2004 Site subsoil classification of Wellington City", in Proceedings of the Ninth Pacific Conference on Earthquake Engineering, Building an Earthquake-Resilient Society, 14-16 April, 2011, Auckland, New Zealand, paper n. 7. **[p. 55]**

Singh, S. K., M. Santoyo, P. Bodin and J. Gomberg (1997). "Dynamic deformations of shallow sediments in the valley of Mexico, part II: Single-station estimates". Bulletin of the Seismological Society of America, Vol. 87, pp. 540-550. **[p. 18, 20]**

Smerzini C., R. Paolucci and M. Stupazzini (2009a). "Experimental and numerical results on earthquake-induced rotational ground motion". Journal of Earthquake Engineering, vol. 13, no.1, pp. 66-82. **[p. 20]**

Smerzini C., Aviles J., Paolucci R., F. J. Sanchez-Sesma, (2009b). "Effects of underground cavities on surface earthquake ground motion under SH wave propagation". Earthquake Engineering and Structural Dynamics, 38: 1441-1460. **[p. 137]**

Smerzini, C. (2010). "The earthquake source in numerical modeling of seismic wave propagation in heterogenous earth media". PhD dissertation, ROSE School. **[p. 96]**

Smerzini, C., R. Paolucci, and M. Stupazzini (2011). "Comparison of 3D, 2D and 1D numerical approaches to predict long period earthquake ground motion in the Gubbio plain, Central Italy". Bulletin of Earthquake Engineering (June), 1-23. doi 10.1007/s10518-011-9289-8. **[p. 48, 152]**

Smerzini, C. and M. Villani (2012). "Broadband numerical simulations in complex near field geological configurations: the case of the M_W 6.3 2009 L'Aquila earthquake". Submitted for publication at Bulletin of the Seismological Society of America. **[p. 96, 97]**

Spudich, P., L. K. Steck, M. Hellweg, J. B. Fletcher and L. M. Baker (1995). "Transient stresses at Parkfield, California, produced by the M 7.4 Landers earthquake of june 28, 1992: observations from the UPSAR dense seismograph array". Journal of Geophysical Research, vol. 100, no. B1, 675-690. **[p. 10, 12]**

Spudich, P. and J. B. Fletcher (2008). "Observation and prediction of dynamic ground strains, tilts, and torsions caused by the M_W 6.0 2004 Parkfield, California, earthquake and aftershocks derived from UPSAR array observations". Bulletin of the Seismological Society of America, Vol. 98, no. 4, pp. 1898-1914. **[p. 10, 17, 18, 19, 20, 22, 70, 80, 81, 84]**

Stedman, G. E., Z. Li and H. R. Bilger (1995). "Side band analysis and seismic detection in a large ring laser". Applied Optics, vol. 34, pp. 7390-7396. **[p. 17]**

Stupazzini, M., R. Paolucci and H. Igel (2009a). "Near-fault earthquake ground-motion simulation in Grenoble Valley by high-performance spectral element code". Bulletin of the Seismological Society of America, Vol. 99, no. 1, pp. 286-301. **[p. 10, 20, 48, 53, 55, 142, 143, 152]**

Stupazzini, M., J. de la Puente, C. Smerzini, M. Käser, H. Igel, and A. Castellani (2009b). "Study of rotational ground motion in the near-field region". Bulletin of the Seismological Society of America, Vol. 99, no. 2B, pp. 1271-1286. **[p. 17, 18, 19, 20, 22, 70, 79, 80, 84]**

Suryanto, W., H. Igel, J. Wassermann, A. Cochard, B. Schuberth, D. Vollmer, F. Scherbaum, U. Schreiber and A. Velikoseltsev (2006). "First comparison of array-derived rotational ground motions with direct ring laser measurements". Bulletin of the Seismological Society of America, Vol. 96, pp. 2059-2071. **[p. 10, 17, 38, 42]**

Taborda, R. (2010). "Three Dimensional Nonlinear Soil and Site-City Effects in Urban Regions". Dissertations. Paper 6. http://repository.cmu.edu/dissertations/6. **[p. 118]**

Taborda, R. and J. Bielak (2011). "Large-Scale Earthquake Simulation: Computational Seismology and Complex Engineering Systems". Computing in Science and Engineering, vol. 13, no. 4, pp. 14-27. **[p. 118, 121]**

Takeo, M. and H. M. Ito (1997). "What can be learned from rotational motions excited by earthquakes?". Geophysical Journal International 129, 319-329. **[p. 2, 18]**

Takeo, M. (1998). "Ground rotational motions recorded in near-source region." Geophysical Research Letters 25, no. 6, 789-792. **[p. 17, 18, 21]**

Takeo, M. (2009). "Rotational motions observed during an earthquake swarm in April 1998 offshore, Ito, Japan". Bulletin of the Seismological Society of America, Vol. 99, no. 2B, pp. 1457-1467. **[p. 5, 17, 20, 21, 22, 71, 72, 73, 76, 80, 81, 85]**

Taylor, L. M. and D. P. Flanagan (1989). "Pronto 3D-A three-dimensional transient solid dynamics program", SAND87-1912, Sandia National Laboratories. **[p. 147]**

Teisseyre R., and W. Boratynski (2003). "Continua with self-rotation nuclei: evolution of asymmetric fields". Mech. Res. Commun. 30, 235-240. **[p. 18]**

Teisseyre, R., J. Suchcicki, K. P. Teisseyre, J. Wiszniowski and P. Palangio (2003). "Seismic rotation waves: basic elements of theory and recording". Annal. Geofis. 46, 671-685. **[p. 17]**

Teisseyre, R., M. Takeo, and E. Majewski (Editors) (2006). "Earthquake Source Asymmetry, Structural Media and Rotations Effects". Springer Verlag, Berlin-Heidelberg. **[p. 18]**

Teisseyre, R., M. Takeo, and E. Majewski (Editors) (2008). "Physics of Asymmetric Continua: Extreme and Fracture Processes". Springer Verlag, Berlin-Heidelberg. **[p. 18]**

Todorovska, M. I. and M. D. Trifunac (1992). "Effect of input base rocking on the relative response of long buildings embedded foundations". European Earthquake Engineering, vol. 1, pp. 36-46. **[p. 44]**

Todorovska, M. I., and M. D. Trifunac (2008). "Impulse response analysis of the Van Nuys 7-story hotel during 11 earthquakes and earthquake damage detection". Structural Control and Health Monitoring, vol. 15, no.1 pp. 90-116. **[p. 24]**

Tonkin and Taylor Ltd. (2010). "Darfield Earthquake 4 September 2010, Geotechnical Land Damage Assessment & Reinstatement Report", Earthquake Commission. Stage 1 Report for the new Zealand Earthquake Commission. Christchurch, new Zealand, Tonkin & Taylor Ltd. **[p. 46]**

Trifunac, M. D. and D. E. Hudson (1971). "Analysis of the Pacoima Dam accelerogram, San Fernando, California, earthquake of 1971". Bulletin of the Seismological Society of America, Vol. 61, no. 5, pp. 1393-1411. **[p. 23, 25]**

Trifunac, M. D. (1972a). "Stress estimates for San Fernando, California earthquake of February 9, 1971: main event and thirteen aftershocks". Bulletin of the Seismological Society of America, Vol. 62, no. 3, pp. 721-750. **[p. 23]**

Trifunac, M. D. (1972b). "Tectonic stress and source mechanism of the Imperial Valley, California earthquake of 1940". Bulletin of the Seismological Society of America, Vol. 62, no. 5, pp. 1283-1302. **[p. 23]**

Trifunac, M. D. (1982). A note on rotational components of earthquake motions on ground surface for incident body waves". Soil Dynamics and Earthquake Engineering, vol. 1, 11-19. **[p. 10, 12, 13, 14, 15]**

Trifunac, M. D. (1993). "Broad band extension of fourier amplitude spectra of strong motion acceleration". Report CE 93-01. Los Angeles, CA: Department of Civil Engineering, University of Southern California. **[p. 24]**

Trifunac, M. D., M. I. Todorovska and S. S. Ivanovic (1996). "Peak velocities, and peak surface strains during Northridge, California, earthquake of 17 January 1994". Soil Dynamics and Earthquake Engineering, vol. 15, no. 5, pp. 301-310. **[p. 24]**

Trifunac, M. D. (1997). "Differential earthquake motion of building foundations". Journal of Structural Engineering, vol. 4, pp. 414-422. **[p. 25]**

Trifunac, M. D. and M. I. Todorovska (1997a). "Response spectra and differential motion on columns". Earthquake Engineering and Structural Dynamics, vol. 26, no.2, pp. 251-268. **[p. 24]**

Trifunac, M. D. and M. I. Todorovska (1997b). "Northridge, California, earthquake of 17 January 1994: density of pipe breaks and surface strains". Soil Dynamics and Earthquake Engineering, vol. 16, no. 3, pp. 193-207. **[p. 23]**

Trifunac, M. D. (1998). "Stresses and intermediate frequencies of strong motion acceleration". Geofizika, vol. 14, pp. 1-27. **[p. 24]**

Trifunac, M. D. and M. I. Todorovska (1998). "Nonlinear soil response as a natural passive isolation mechanism – the 1994 Northridge, California, Earthquake". Soil Dynamics and Earthquake Engineering, vol. 17, no. 1, pp. 41-51. **[p. 23]**

Trifunac, M. D., M. I. Todorovska and V. W. Lee (1998). "The Rinaldi strong motion accelerogram of the Northridge, California, earthquake of 17 January 1994". Earthquake Spectra, vol. 14, no. 1, pp. 225-239. **[p. 25]**

Trifunac, M. D. and M. I. Todorovska (2001). "A note on the usable dynamic range of accelerographs recording translation". Soil Dynamics and Earthquake Engineering, vol. 21, no. 4, 275-286. **[p. 2, 12, 31]**

Trifunac, M. D. and S. S. Ivanovic (2003). "Analysis of drifts in a seven-story reinforced concrete structure", Dept of Civil Engineering, University of Southern California, los Angeles, California, Report Number CE 03-01. **[p. 3, 22]**

Trifunac, M. D. (2006). "Effects of torsional and rocking excitations on the response of structures", in Earthquake Source Asymmetry, Structural Media and Rotation Effects, R. Teisseyre, M. Takeo and E. Majewski (Editors), Springer, Heidelberg, 569-582. **[p. 3, 23]**

Trifunac, M. D. and V. Gicev (2006). "Response spectra for differential motion of columns, paper II: Out-of-plane response". Soil Dynamics and Earthquake Engineering, vol. 26, no. 12, pp.1149-1160. **[p. 24]**

Trifunac, M. D. (2008). "Buildings as sources of rotational waves", in Physics of Asymmetry, Structural Media and Rotation Effects", R. Teisseyre, M. Takeo and E. Majewski (Editors), Springer, Heidelberg, Germany. **[p. 3, 23]**

Trifunac, M. D. (2009a). "The role of strong motion rotations in the response of structures near earthquake faults". Soil Dynamics and Earthquake Engineering, vol. 29, no. 2, 382-393. **[p. 3, 6, 7, 23, 24, 25, 31, 112, 118, 121, 125]**

Trifunac, M. D. (2009b). "Review: Rotations in structural response". Bulletin of the Seismological Society of America, Vol. 99, no. 2B, pp. 968-979. **[p. 3, 23, 24, 25]**

Tsogka, C. and A. Wirgin (2003). "Simulation of seismic response in an idealized city". Soil Dynamics and Earthquake Engineering, vol. 23, no. 5, pp. 391-402. **[p. 121]**

Vardoulakis, I. (1989). "Shear-banding and liquefaction in granular materials on the basis of a Cosserat continuum theory". Arch. Appl. Mech. (Ingenieur Archiv), 59, no. 2, 106-113. **[p. 18]**

Vos, P. E. J., S. J. Shervin and R. M. Kirby (2010). "From h to p efficiently: implementing finite and spectral hp element methods to achieve optimal performance for low- and high-order discretisations". J. Comput. Phys., vol. 229, pp. 5161-5181. **[p. 142]**

Wald, D. J. and R. W. Graves (1998). "The Los Angeles basin response in simulated and recorded ground motions". Bulletin of the Seismological Society of America, Vol. 88, pp. 337-356. **[p. 10]**

Wang, H., H. Igel, F.Gallovi, A. Cochard and M. Ewald (2008). "Source-related variations of ground motions in 3-D media: application to the Newport-Inglewood fault, Los Angeles basin". International Geophysical Journal, vol. 175, pp. 202-214. **[p. 10]**

Wang, H., H. Igel, F. Gallovic and A. Cochard (2009). "Source and basin effects on rotational ground motions: comparison with translations". Bulletin of the Seismological Society of America, Vol. 99, no. 2B, pp. 1162-1173. **[p. 17, 22, 70, 81, 84]**

Wirgin A., and P. Y. Bard (1996). "Effects of buildings on the duration and amplitude of ground motion in Mexico City". Bulletin of the Seismological Society of America, Vol. 86, no. 3, pp. 914-920. **[p. 121]**

Wu, C. F., W. H. K. Lee, and H. C. Huang (2009). "Array deployment to observe rotational and translational ground motions along the Meishan fault, Taiwan: a progress report". Bulletin of the Seismological Society of America, Vol. 99, no. 2B, pp. 1468-1474. **[p. 18]**

Zembaty, Z., A. Castellani and G. Boffi (1993). "Spectral analysis of the rotational component of earthquake motion". Probabilistic Engineering Mechanics, vol. 8, pp. 5-14. **[p. 13]**

Zembaty, Z. (2004). "Rockburst induced ground motion – a comparative study". Soil Dynamics and Earthquake Engineering, 24, 11-23. **[p. 18]**

Zembaty, Z. (2009). "Tutorial on surface rotations from wave passage effects: stochastic spectral approach". Bulletin of the Seismological Society of America, Vol. 99, no. 2B, pp. 1040-11049. **[p. 12, 17]**

Zerva A. and O. Zhang (1997). "Correlation Patterns in Characteristics of Spatially Variable Seismic Ground Motions". Earthquake Engineering and Structural Dynamics, Vol. 26, pp. 19-39. **[p. 28]**